Breaking the Ice

- Constraining the volatile distribution in protoplanetary disks -

Proefschrift

ter verkrijging van
de graad van doctor aan de Universiteit Leiden,
op gezag van rector magnificus prof.dr.ir. H. Bijl,
volgens besluit van het college voor promoties
te verdedigen op woensdag 23 oktober 2024
klokke 10:00 uur
door

Jan Adriaan Sturm

geboren te Aagtekerke, Nederland
in 1997

Promotor:

Prof. dr. E. F. van Dishoeck

Co-promotor:

Dr. M. K. McClure

Promotiecommissie:

Prof. dr. I. A. G. Snellen	
Prof. dr. S. Viti	
Prof. dr. C. C. Espaillat	Boston University, USA
Dr. L. I. Cleeves	University of Virginia, USA
Dr. S. Krijt	University of Exeter, UK

ISBN: 978-94-6496-208-6

Cover design: Marijn Verschuure

When I consider thy heavens, the work of thy fingers,
the moon and the stars, which thou hast ordained;
What is man, that thou art mindful of him?
and the son of man, that thou visitest him?

– Psalms 8:3–4

Table of contents

1 Introduction **1**
- 1.1 Changing perspectives 1
  - 1.1.1 The divine universe 1
  - 1.1.2 The universe is subject to change 2
  - 1.1.3 Further developments 2
- 1.2 Star formation 3
  - 1.2.1 Initial stages of star formation 4
  - 1.2.2 Gravitational collapse and disk formation 4
  - 1.2.3 Disk structure 5
  - 1.2.4 Planet formation 7
- 1.3 Astrochemistry 9
  - 1.3.1 Chemical evolution 10
    - 1.3.1.1 Chemistry in the ISM 10
    - 1.3.1.2 Inheritance vs. reset 11
  - 1.3.2 Protoplanetary disk chemistry 12
    - 1.3.2.1 Inheritance in planets/comets 12
- 1.4 Ices in protoplanetary disks 13
  - 1.4.1 The role of ices in protoplanetary disk physics 13
  - 1.4.2 The role of ices in protoplanetary disk chemistry 14
- 1.5 Techniques 14
  - 1.5.1 Observations 16
    - 1.5.1.1 Infrared spectroscopy 16
    - 1.5.1.2 Sub-millimeter interferometry 17
  - 1.5.2 Modeling 17
    - 1.5.2.1 Radiative transfer models 17
    - 1.5.2.2 Physical-chemical models 18
- 1.6 This thesis 19
  - 1.6.1 Status quo 19
  - 1.6.2 Breaking the ice 19
  - 1.6.3 Overview of each chapter 20
  - 1.6.4 Summary of the main findings 22
  - 1.6.5 Future outlook 22

2 Tracing pebble drift and trapping using radial carbon depletion profiles in protoplanetary disks **25**
- 2.1 Introduction 27
- 2.2 Observations and data analysis 29
  - 2.2.1 Observations 30
  - 2.2.2 Data analysis 31
  - 2.2.3 Complementary data 32
- 2.3 Observational results 33

2.4 Description of the modeling 36
2.4.1 Disk parameters 37
2.4.2 Stellar parameters 38
2.4.3 Chemical network 38
2.4.4 Radiative transfer 38
2.4.5 Fitting procedure 39
2.4.6 Main sources of uncertainty 39
2.5 Modeling results 40
2.5.1 DR Tau: moderate depletion of carbon and oxygen 41
2.5.2 DO Tau: moderate depletion of carbon and oxygen 44
2.5.3 DL Tau: severe depletion of carbon and oxygen 46
2.5.4 Systematic uncertainty 47
2.6 Discussion 47
2.6.1 Implications of the radial abundance profile 48
2.6.1.1 Dust traps 48
2.6.1.2 Dust retention in smooth, compact systems 51
2.6.2 Evolutionary trend in carbon depletion 52
2.7 Conclusions 53
2.8 Acknowledgements 54
Appendices 55
2.A Observing details 55
2.B pole-on outflow in [C I] 55
2.C Surface density profile DR Tau 55
2.D Channel maps 58

3 Disentangling the protoplanetary disk gas mass and carbon depletion through combined atomic and molecular tracers 65
3.1 Introduction 67
3.2 Observations 69
3.2.1 The LkCa 15 disk 69
3.2.2 Observational details 70
3.2.3 Data analysis 70
3.3 Observational results 72
3.4 Modeling framework 74
3.4.1 Model parameters 74
3.4.2 Chemical networks 75
3.4.3 Modeling approach 77
3.4.3.1 Fitting the dust density distribution 77
3.4.3.2 Fitting the gas density distribution 78
3.5 Results 79
3.5.1 Gas distribution 79
3.5.1.1 HD 79
3.5.1.2 CO isotopologues 83
3.5.1.3 N-bearing species 83
3.5.2 Disentangling gas mass and elemental abundances 84
3.5.2.1 HD 84

3.5.2.2 CO isotopologues 85
3.5.2.3 N-bearing species 85
3.5.2.4 Combining tracers 85
3.5.3 Determination of the C/O ratio 85
3.6 Discussion 86
3.6.1 Comparison with literature gas masses 86
3.6.2 Comparison of HD with observations 87
3.6.3 Modeling of N_2H^+ 87
3.6.4 Scientific implications 88
3.6.4.1 Gas-to-dust ratio 88
3.6.4.2 C/H ratio 88
3.6.4.3 C/O ratio 89
3.7 Conclusions 89
3.8 Acknowledgements 90
Appendices 90
3.A HC_3N detection 90
3.B Modeling robustness 91
3.B.1 Parameter dependence 91
3.B.2 Dust component in cavity 92

4 The edge-on protoplanetary disk HH 48 NE
I. Modeling the geometry and stellar parameters 95
4.1 Introduction 97
4.2 Source and observational data 98
4.2.1 Source description 98
4.2.2 Description of observations 99
4.2.2.1 HST observations 99
4.2.2.2 ALMA observations 100
4.2.2.3 Spectral energy distribution 102
4.3 Modeling 102
4.3.1 Continuum model 102
4.3.1.1 Model setup 102
4.3.1.2 MCMC modeling 104
4.4 Results 107
4.4.1 Stellar parameters 109
4.4.2 Spatial disk parameters 110
4.4.3 Mass 111
4.4.4 Grain properties 112
4.4.5 Cavity 112
4.4.5.1 SED comparison 114
4.4.5.2 Resolved continuum comparison 114
4.4.5.3 Comparison of the gas observation 114
4.4.5.4 Size and depth 115
4.5 Discussion 115
4.5.1 Convergence of fit 116
4.5.2 Grain size distribution 116

4.5.3 Inner cavity 118
4.6 Conclusions 119
4.7 Acknowledgments 120
Appendices 121
4.A Posterior distribution continuum fits 121

5 The edge-on protoplanetary disk HH 48 NE II. Modeling ices and silicates 123
5.1 Introduction 125
5.2 Modeling 126
5.2.1 Continuum model 126
5.2.1.1 Model setup 127
5.2.1.2 Dust scattering 128
5.2.2 Ice distribution 129
5.3 Results 131
5.3.1 Fiducial model 131
5.3.1.1 Integrated optical depths 132
5.3.1.2 Spatially resolved optical depths 134
5.3.2 Sensitivity to parameters 134
5.3.2.1 Sensitivity to abundance 136
5.3.2.2 Sensitivity to the fraction of settled mass 136
5.3.2.3 Sensitivity to the inclination 137
5.3.2.4 Sensitivity to the A_{V} limit 138
5.3.2.5 Sensitivity to the grain size 139
5.3.2.6 Sensitivity to a cavity 139
5.3.2.7 Sensitivity to the total mass 139
5.3.2.8 Sensitivity to the radial size 140
5.3.2.9 Sensitivity to the flaring index 140
5.3.3 Silicate feature 140
5.4 Discussion 141
5.4.1 Constraining the ice abundances 142
5.4.2 Detectability of edge-on disks 143
5.5 Conclusions 144
5.6 Acknowledgments 145
Appendices 146
5.A Comparison between `RADMC-3D` and `Hyperion` 146
5.B Additional material 147

6 A JWST inventory of protoplanetary disk ices. The edge-on protoplanetary disk HH 48 NE, seen with the Ice Age ERS program 153
6.1 Introduction 155
6.2 Observations 158
6.3 Results 159
6.3.1 Gas inventory 161
6.3.2 Ice inventory 162

6.3.2.1 H_2O and NH_3: 3 µm 163
6.3.2.2 CO_2 and $^{13}CO_2$: 4.2 – 4.4 µm 165
6.3.2.3 CO, OCN^-, and OCS: 4.4 – 5 µm 165
6.3.3 Spatial variation in ice features 166
6.3.3.1 Radial variations 167
6.3.3.2 Vertical variations 169
6.4 Discussion 171
6.4.1 Where in the disk do these ice features originate? 172
6.4.2 Optical depths do not trace total ice column in outer disk . 172
6.4.3 Excess ice in disk atmosphere? 174
6.4.4 Implications for the outer disk chemistry 177
6.4.5 Comparison with previous observations 178
6.4.6 Future prospects and outlook 178
6.5 Conclusions 179
6.6 Acknowledgments 180
Appendices 181
6.A CO ro-vibrational gas line fitting 181

7 A JWST/MIRI analysis of the ice distribution and PAH emission in the protoplanetary disk HH 48 NE 185
7.1 Introduction 187
7.2 Description of observations 188
7.3 Observational results 191
7.3.1 PAH emission 191
7.3.2 Ice features 193
7.3.3 Spatially resolved continuum emission in HH 48 NE 193
7.4 Model setup 194
7.4.1 Physical structure 194
7.4.2 Ice distribution 197
7.4.3 PAHs 198
7.5 Modeling results 199
7.5.1 Ice identification 200
7.5.1.1 H_2O 200
7.5.1.2 CO_2 200
7.5.1.3 7 µm region 200
7.5.1.4 NH_3 and CH_3OH 202
7.5.2 Locating the measured ice 202
7.5.2.1 Contribution function 202
7.5.2.2 Locating elevated ices 204
7.6 Discussion 208
7.6.1 PAHs in edge-on protoplanetary disks 208
7.6.2 Ices at high elevation in protoplanetary disks 209
7.6.3 Chemical implications 210
7.6.4 Limitations and future outlook 211
7.6.4.1 Ice observables 212
7.6.4.2 Future prospects 213

7.7 Conclusion 214
7.8 Acknowledgments 215
Appendices 215
7.A Streamer 215
7.B Spectral extraction 216
7.C Model improvements 216

Bibliography **221**

Nederlandse samenvatting **237**

Publications **243**

Curriculum Vitae **247**

Acknowledgements **249**

Chapter 1

Introduction

Life seems repetitive. Days come and go, new generations come and fade, and empires arise and fall. Repetition seems to be even stronger for the universe around us: days, seasons, and Moon cycles repeat endlessly, and stars live billions of years before they eventually die. Most scales in the universe go beyond imagination and most objects do not change significantly over ones lifetime. That is, until one takes a much closer look at the details. The formation of stars and planets occurs over millions of years, a phenomenon that requires an in-depth examination of young star groups to comprehend.

1.1 Changing perspectives

Historically, the progress in the field of astronomy, especially in exploring how stars and planets originate, has been closely linked to innovations in scientific instrumentation. Ancient astronomers such as the Babylonians and Greeks had to rely on imprecise by-eye measurements when studying the universe. Subsequent advancements such as sextants, telescopes, and modern contemporary space telescopes have enabled for much more detailed observations. Consequently, our understanding of our place in the solar system and how it formed and evolved has significantly changed over the years.

1.1.1 The divine universe

The cosmological view in ancient Greece was largely build on the work by Pythagoras (570 – 495 BC). He and his followers structured the movement of the celestial bodies according to mathematical relationships and harmonies, similar to the ratios found in musical intervals. Plato (427 – 348 BC) contemplated the celestial motions and envisioned a cosmos regulated by divine order in his dialogues ‘Phaedo’ and ‘Timaeus’. He regarded the cosmos as a manifestation of perfect Forms ($\iota\delta\acute{\epsilon}\alpha$) or archetypes, which he considered to be eternal and immutable, with the physical world being an imperfect copy. Plato’s cosmology emphasized the role of divine order and the harmony of the cosmos, with the celestial bodies moving in accordance with these Forms. Aristotle (384 – 322 BC) expanded on these ideas in his ‘Physica’ and ‘De Caelo’ from a more empirical standpoint, trying to explain natural phenomena using a geocentric model of the cosmos.

Claudius Ptolemy (100 – 170) refined Aristotle’s model, developing the Ptolemaic system to predict the positions of planets with greater accuracy in his ‘Almagest’. Better observations required him to break with the idea of perfect spheres and harmonics underlying celestial motions and to introduce epicycles and deferents to explain their observed motions. Yet, it was Nicolaus Copernicus (1473 – 1543) who sparked a revolution with his heliocentric model in ‘De revolutionibus orbium coelestium', challenging the entrenched beliefs of his time and reshaping our understanding of the solar system's structure. This shift in paradigm was mainly driven by dissatisfaction with the complexities of the geocentric model, a desire for mathematical elegance, and a reinterpretation of available astronomical observations.

1.1.2 The universe is subject to change

The collaboration between Tycho Brahe (1546 – 1601) and Johannes Kepler (1571 – 1630) furthered our understanding of celestial mechanics. Brahe's meticulous observations, using precise quadrants, sextants, and clocks, provided the data upon which Kepler formulated his laws of planetary motion, describing the elegant dance of the planets around the Sun with unprecedented precision.

Additionally, Brahe refuted the Platonian and Aristotelian belief in an unchanging celestial realm in 'De nova stella' (1573). His measurements indicated that the "new star" that appeared in 1772 (stellae novae, now called supernovae), moved beyond the Moon. This was later confirmed by realizing that the "great comet" that he observed from 1577 – 1578 was not created in the "Earthly sphere", as traditionally assumed, but had to be further than the Moon due to a lack of parallax. The work of Brahe and Kepler laid the groundwork for Isaac Newton's (1642 – 1726) monumental 'Principia Mathematica', which unified celestial and terrestrial mechanics under the laws of gravity and motion.

1.1.3 Further developments

Galileo Galilei (1564 – 1642) was the first to observe the universe with a telescope. Pointing his telescope at the Moon, it became obvious that the Moon was not a translucent and perfect sphere, as Aristotle claimed, and hardly the "first planet, and eternal pearl to magnificently ascend into the heavenly empyrian", as put forth by Dante Alighieri (1265 – 1321) in 'The Divine Comedy'. His observations of the phases of Venus, the moons of Jupiter, and the ring of Venus proved the heliocentric world-view.

Given this new interpretation of the solar system, Emanuel Swedenborg (1688 – 1772) proposed the nebular hypothesis in "Principia Rerum Naturalium". This idea was later elaborated by Immanuel Kant (1724 – 1804) and Pierre-Simon Laplace (1749 – 1827) who described the formation of the solar system from an "urnebel" or rotating disk of gas and dust. Their ideas, combined with advancements in observational techniques, provided new insights into the processes driving star and planet formation within molecular clouds.

In 1774, Friedrich Wilhelm Herschel made a groundbreaking observation of dark patches in the sky within the Scorpio constellation. Struck by the absence of even the faintest star in these regions, he famously exclaimed: "Hier ist wahrhaftig ein Loch im Himmel!" ("Truly, there is a hole in the sky here!"). These enigmatic 'dark clouds' are now known to result from obscuring material, such as molecular gas clouds, whose dust absorbs the light emitted by background stars (e.g., Barnard 1919). Meanwhile, James Clerk Maxwell's (1831 – 1879) equations of electromagnetism paved the way for radio astronomy, a groundbreaking technology that allowed astronomers to study celestial objects beyond the visible spectrum.

This technological breakthrough led to the development of millimeter telescopes and the detection of CO gas in ‘dark clouds’ (Wilson et al. 1970), unveiling the birthplaces of stars and planets hidden within these clouds. Furthermore, the direct observations of exoplanets since 1995 (Mayor & Queloz 1995) have further affirmed the universality of the planet formation process.

As I will show throughout this thesis, the universe, chemistry and planet formation are far less static than we think. The more we focus on the details, the more we see the variation. In the past century, technological advancements have followed each other rapidly, completing our picture of star and planet formation, as discussed in the next section. Through centuries of observation, innovation, and discovery, humanity’s understanding of star and planet formation has evolved, unveiling the intricate processes shaping the cosmos. Each step forward has been propelled by the relentless pursuit of knowledge, driving us ever closer to unlocking the secrets of the celestial origins.

1.2 Star formation

Our path through the history of astronomy concludes that the universe is subject to change and evolution. Galaxies, stars, and planets each have formation mechanisms and limited lifespans. This thesis is dedicated to studying the environment in which planets are formed, known as the protoplanetary disk (Kant’s ‘urnebel’). Yet, the formation of planets is merely one aspect of a larger phenomenon: the birth of stars. Therefore, to delve into the topic of planet formation, it is essential to first grasp the basics of star formation.

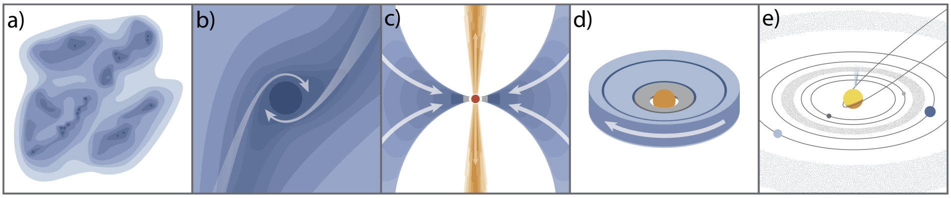

Figure 1.1: Illustration of the various phases involved in the formation of low-mass stars and planets.
a: Stars originate in dense cores within interstellar molecular clouds.
b: Star formation starts when such a dense core starts to collapse under its own gravity.
c: As the contraction advances, the center becomes hot, leading to the creation of a protostar. The accumulation of residual cloud material persists, channeled through a disk that forms due to the cloud’s angular momentum. Rocky protoplanets may start forming here. This phase is also marked by material outflows.
d: After the cloud remnant has been dispersed, the now pre-main sequence star is left with a circumstellar disk. Planets in the disk continue to grow by accreting rocky material and if they grow large enough also gas. The gas in the disk is dispersed after approximately 2 – 10 Myrs, thereby ending the gas accretion onto planets.
e: Rocky and icy planets can keep expanding for an additional 100 Myrs, at the end of which a fully formed planetary system is present. Image credit: K. Peek.

1.2.1 Initial stages of star formation

The space between the stars in the Milky Way is not empty but is filled with a very dilute gas, the so-called interstellar medium (ISM). The ISM is made up predominantly out of hydrogen (H) and helium (He). Trace elements such as carbon (C), oxygen (O), and nitrogen (N) have an elemental abundance that is typically 4 orders of magnitude lower than hydrogen, or 100 ppm (Cardelli et al. 1996; Meyer et al. 1998; Parvathi et al. 2012). The ISM also contains tiny dust grains, constituting approximately 1% of the total mass. These grains, ranging in size from about 0.005 to 1 µm, consist of refractory materials such as silicates and carbonaceous substances (Draine 2003). Elements can be divided into volatiles, those that vaporize at low temperature (like O, C, N) and form ice or gas, and refractories like magnesium, silicon, and iron that are the constituents of dust grains.

The ISM is not evenly distributed over the galaxy but is structured in filaments over an enormous range of scales, from kpc-sized objects associated with spiral arms of the Milky Way (Zucker et al. 2015; Xu et al. 2016) to sub-parsec structures within clouds (Hacar et al. 2013). These filaments are shaped by density and pressure perturbations, gravitational and magnetic fields, and turbulence (Chevance et al. 2023; Hacar et al. 2023). The parts of these filaments that are sufficiently dense ($10^3 - 10^6$ cm^{-3}; compared to $10^{13} - 10^{19}$ cm^{-3} in Earth's atmosphere) and therefore shielded from stellar radiation and cold (10 – 20 K), are called molecular clouds, since volatile species like hydrogen, carbon, oxygen and nitrogen are mostly in molecular form (H_2, H_2O, CO_2, CO, N_2, etc.).

1.2.2 Gravitational collapse and disk formation

Figure 1.1 illustrates the different stages in the star formation process. If molecular clouds get cold enough, gravitational collapse is triggered and a protostar is formed, still embedded in a thick envelope (Jeans 1902; Shu et al. 1987; Lada & Lada 1991). These phases of the star formation process are extremely chaotic (see Fig. 1.2) due to the interaction with the turbulent environment, and often result in the formation of binary or higher-order systems (Jeans 1919; Tobin et al. 2016). Due to the inherited angular momentum from the cloud, contraction and accretion on the central object is only possible if the angular momentum is transported away. Initially, this happens mainly by launching molecular jets and entrained outflow, but eventually results in the formation of a disk (Terebey et al. 1984; Visser et al. 2009; Lebreuilly et al. 2020; Pineda et al. 2023).

At first, these disks are dominated by spiraling infalling material, but if the disk grows sufficiently, the conservation of angular momentum dictates the formation of a rotationally supported disk (Pineda et al. 2023). In rotationally supported disks, accretion happens due to shear friction of the gas. The angular velocity of the gas increases towards to star following Kepler's third law $\Omega_\mathrm{K} = GM_*/r^3$, where G is Newton's gravitational constant, M_* is the mass of the star and r the distance to the star in the disk. This velocity gradient induces viscous friction, which moves angular momentum outwards and allows the transport of material inwards towards the star. Since the infall from the envelope on the disk is efficient, these structures develop rapidly in the first 500 kyr. For low mass stars, the envelope gets destroyed

Figure 1.2: Still taken from the 'STARFORFGE: Anvil of creation' simulation (Grudić et al. 2022). Star formation is not as "clean" as often visualized in schematics, but has in fact ample feedback of surrounding objects' gravity, radiation, jets, magnetic field etc.

eventually due to accretion onto the star, photo-evaporation from the increasing stellar radiation field, or is blown away in disk winds. From that point onward, the disk starts to loose mass because of accretion on the star, photo-evaporation, outflow in the wind, or planet formation. After $\lesssim$10 Myr, the disk gas will disperse (Williams & Cieza 2011; Manara et al. 2023) and a planetary system with a disk with rocky debris remains.

1.2.3 Disk structure

An overview of a general structure of a protoplanetary disk is given in Fig. 1.3. The radial distribution of mass in the disk is often approximated assuming a self-similar viscous disk (Lynden-Bell & Pringle 1974)

$$\Sigma_{\mathrm{gas}} = \Sigma_{\mathrm{c}} \left(\frac{r}{R_{\mathrm{c}}}\right)^{-\gamma} \exp\left[-\left(\frac{r}{R_{\mathrm{c}}}\right)^{2-\gamma}\right], \tag{1.1}$$

where Σ_{c} is the surface density at the characteristic radius R_{c} and $\gamma = 1$. The small dust grains follow the motions and distribution of the gas because they are tightly coupled to the gas via the pressure.

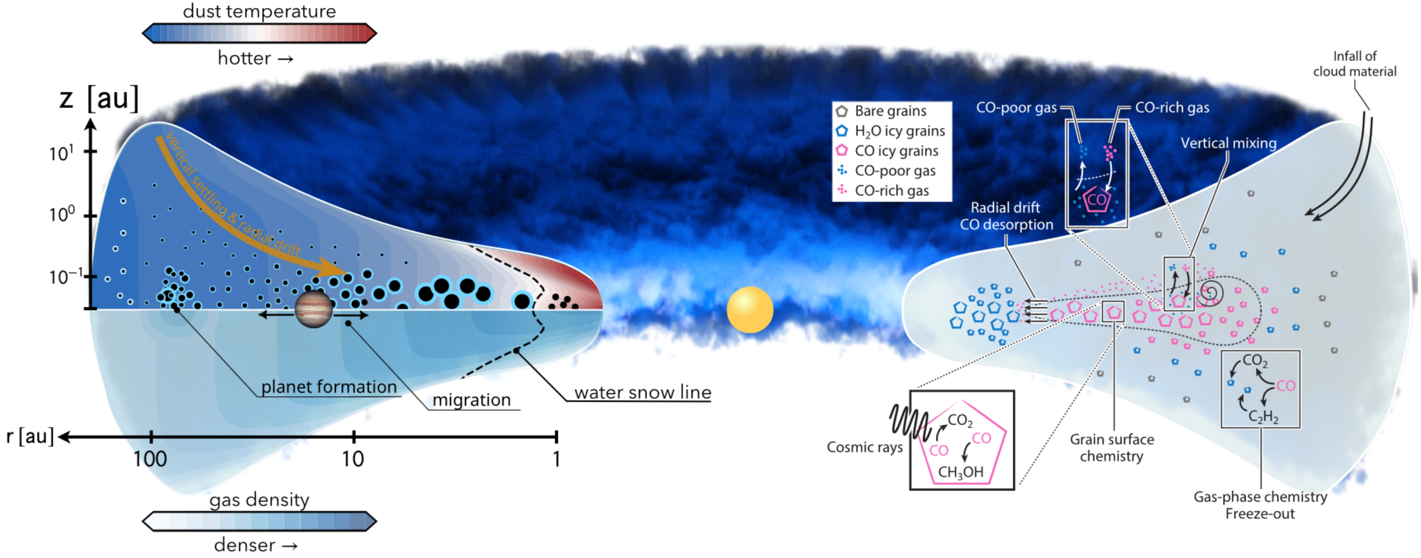
dust temperature
hotter →
z [au]
10^1
10^0
10^{-1}
vertical settling & radial drift
planet formation
migration
water snow line
r [au]
100
10
1
gas density
denser →
Bare grains
H_2O icy grains
CO icy grains
CO-poor gas
CO-rich gas
CO-poor gas
CO-rich gas
Vertical mixing
Infall of cloud material
Radial drift
CO desorption
CO
Cosmic rays
CO_2
CO
CO
CH_3OH
Grain surface chemistry
CO_2
CO
C_2H_2
Gas-phase chemistry
Freeze-out

Figure 1.3: Left: Illustration of the dust temperature and gas density structure in the protoplanetary disks. A sketched distribution of dust particles is shown by the black circles, whose size variation is represented by the symbol size. Bare grains are present within the water snow line (dashed curve), ice-coated grains are contoured in blue. Right: main physico-chemical processes reducing the CO gas abundance in protoplanetary disks, highlighting the three main concurring processes: vertical mixing and grain growth, gas phase chemistry and freeze-out, and grain surface chemistry (adapted from Miotello et al. 2023; Öberg et al. 2023).

The vertical structure of the disk is the result of the radial mass distribution and the disk heating mechanisms. The majority of the heating in the disk is caused by the irradiation of the central star, except for the inner 1 – 5 au where the release of gravitational energy during accretion heats up the gas. This causes a dust temperature structure that increases both inwards and upwards in the directions of higher flux. The gas temperature, T_{gas}, can deviate significantly from the dust temperature in the upper layers of the disk, as a result of additional chemical heating and cooling processes. The vertical structure of the disk is then a result of the balance between internal pressure, P, and gravity and satisfies the condition

$$P = \rho k_{\mathrm{B}} T_{\mathrm{gas}} / \mu \tag{1.2}$$

at all radii, where μ is the mean molecular weight (typically $\sim$2.3).

The inner radius of the dust disk is set by the sublimation temperature of dust, which is approximately 1600 K. Given the luminosity of the central star (L_*), this is approximately at a radius of $0.07 \cdot (L_*/L_\odot)^{1/2}$ au (Monnier & Millan-Gabet 2002). The gas disk extends further in, but its structure is in this regime dominated by the magnetic field and the launching of the jet and outflow (Shu et al. 1994; Calvet & Gullbring 1998; Muzerolle et al. 2004; Bally 2016; Hartmann et al. 2016; McClure 2019). The position and vertical shape of the inner dust rim can have significant effect on the overall disk structure if (part of) the disk is shielded from the stellar radiation (Dullemond et al. 2001; Bosman et al. 2022b). Since the inner disk structure is uncertain, the vertical structure in the outer disk is often approximated by the gas scale height (h) parameterized as

$$h(r) = h_{\mathrm{c}} \left(\frac{r}{R_{\mathrm{c}}} \right)^{\psi}, \tag{1.3}$$

defined by the scale height h_{c} at the characteristic radius with a flaring index ψ and a Gaussian distribution

$$\rho = \frac{\Sigma}{\sqrt{2\pi} r h} \exp\left[-\frac{1}{2} \left(\frac{\pi/2 - \theta}{h} \right)^2 \right]. \tag{1.4}$$

1.2.4 Planet formation

Planet formation is the process of assembling 1000 km-sized solid bodies from dust grains (<1 µm), covering over 13 orders of magnitude in size. During most of the star formation process, grains are tightly coupled to the gas. However, the dense regions of protoplanetary disks allow for additional growth and evolution of the dust. If similar sized dust particles collide with sufficiently low velocity, they could clump together and form a bigger aggregate. The collisional velocity of dust particles in a protoplanetary disk is largely set by the size of the particles and the level of turbulence in the disk. These collisions are studied in laboratories (Blum 2018) and simulations (Birnstiel et al. 2016; Drążkowska et al. 2023).

Initial grain growth is very efficient, but limited to sizes $\lesssim$1 mm. Grains of this size are more likely to bounce or fragment upon collisions than grow, often referred to as the bouncing or fragmentation barrier. Additionally, large grains become decoupled from the gas (Weidenschilling 1977) and, due to friction with the gas, are pushed towards the midplane and eventually drift inwards toward the star. This results in significant dust depletion from the atmosphere when disks get older and more settled (see Fig. 1.3). If pebbles grow larger, they drift inwards so quickly that they would quickly spiral onto the star (Takeuchi & Lin 2002). The most efficient drift is for bodies with a size of 1 m at 1 au, the orbit of the Earth around the Sun. This results essentially in a growth barrier, often referred to as the "meter-barrier".

Due to these growth barriers, the formation of planetesimals in protoplanetary disks appears to be a challenging task in theory, yet observational data indicate that, on average, each star is accompanied by a planetary body (e.g., Kunimoto & Matthews 2020). The presence of numerous planets with a significant gas atmosphere (gas giants) suggests that the largest celestial bodies must have been created early in disks (Tychoniec et al. 2020) that were still abundant in gas (see Fig. 1.4). Although it is feasible to directly collapse planets in gravitationally unstable disks (e.g., Kratter & Lodato 2016), this mechanism fails to account for the formation of terrestrial planets such as the ones within our own solar system. Core accretion and pebble accretion are alternative models for planet formation that are applicable to various types of planets. Both core accretion and pebble accretion require one or more initial seeds for the initiation of planet formation. The streaming instability (initially proposed by Youdin & Goodman 2005) is one of the limited methods to create these seeds, also known as planetesimals. This mechanism is triggered in specific regions in the disk if the gas-to-dust ratio is low (typically $\lesssim 1$) and the back-reaction of the dust onto the gas is so strong that radially drifting grains are collected in that area (Squire & Hopkins 2018; Pan & Yu 2020). These filaments can then collapse to quickly form ∼100 km sized planetesimals.

In the core accretion model, these seeds grow through collisions with each other, whereas in the pebble accretion model, planetesimals initially increase in size by gathering material from the pebble flow passing through the planet's orbit (Johansen & Lambrechts 2017; Ormel 2017; Liu & Ji 2020; Drążkowska et al. 2023). The latter process is more efficient compared to simply accumulating material within the planet's orbit, as the accretion cross-section for pebbles is larger and the pebble reservoir can be significantly larger. Once a planetesimal or planetary core reaches a sufficient size, it begins to accrete directly from the surrounding gas and dust disk, progressing towards becoming an ice or gas giant. Forming planets can migrate through the disk due to planet-disk interactions (Goldreich & Tremaine 1979; Lin & Papaloizou 1985), which means that the observed location of exoplanets does not necessarily reflect the location of their formation. The composition of the gas and solids accreted at this stage plays a crucial role in determining the final atmospheric composition of the planet.

If planets grow big enough they produce a pressure maximum in the disk through tidal torques that halts the radial drift of pebbles (Goldreich & Tremaine 1979; Rosotti et al. 2020). These so-called dust traps are an ideal place to trigger the streaming instability to form additional planets, because of their natural low gas-to-dust ratio. Eventually, giant planets can halt the radial drift so significantly that the region inside their orbit depletes and forms a cavity, the so-called transition disks. Most, if not all, protoplanetary disks show signs of these substructures in observations of their dust disk (e.g., Andrews et al. 2013; Long et al. 2018; Francis & van der Marel 2020). However, not all gaps and rings are necessarily created by planets, other mechanisms are thought to produce pressure maxima as well, for example around molecular snowlines and heat transitions (Zhang et al. 2015; van der Marel et al. 2018).

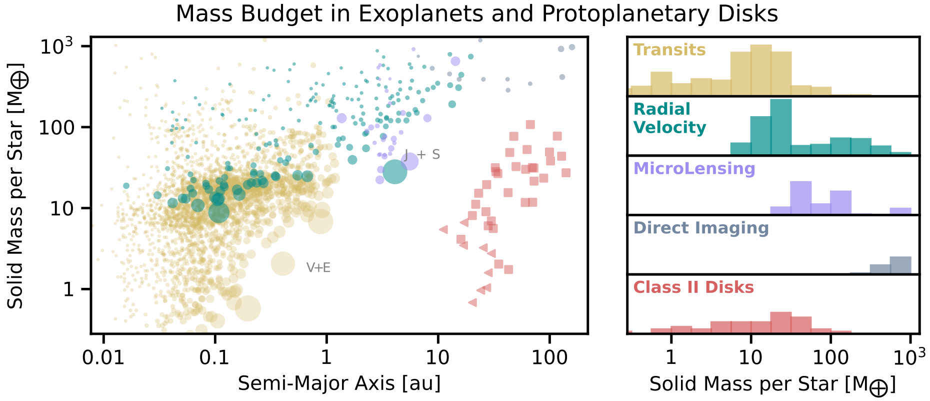

Figure 1.4: Left: The semi-major axis and mass of the observed population of exoplanets and inferred masses from rings in protoplanetary disks. The colors correspond to the categories on the right, showing the distribution of solid mass per star for exoplanets and disks (Figure taken from Drążkowska et al. 2023).

1.3 Astrochemistry

The chemistry of the Interstellar Medium greatly differs from terrestrial chemistry in numerous aspects. The pressure and density in the ISM are orders of magnitude lower, which means that collisional and chemical timescales are long. However, observations still show a wealth of different molecules (Swings & Rosenfeld 1937; Herbst & van Dishoeck 2009; McGuire 2022) that can become rather complex ($>$10 atoms Manigand et al. 2020; Coutens et al. 2022; McGuire 2022). The low temperature in most molecular environments strongly suppresses reactions with energy barriers and almost completely quenches endothermic reactions. Additionally, three-body reactions are rare because of the low density, which means that the only way for exothermic reactions to lose the additional energy is through slow photon radiation processes. Therefore, exothermic reaction products often have no way to dispose of their additional energy, causing the reaction product to break apart. This means that gas-phase reactions often involve ions and radicals and can only produce a select range of molecules (Langer et al. 1997). For example, N_2, CO, HCN can easily form in the gas-phase, but simple molecules like H_2O, CO_2, CH_3OH are difficult to make in large amounts, especially at temperatures $<$400 K (Tielens & Hagen 1982; van Dishoeck et al. 1995).

Additional pathways utilize the surface of dust grains. These surfaces have one less spatial dimension which means that they provide a place where atoms and molecules can concentrate, allowing for more efficient chemistry (Charnley et al. 1992). Additionally, the grain acts as a sink to quickly absorb excess energy in exothermic reactions, making reactions of neutral species possible. Reactions can occur if an atom or molecule from the gas-phase lands directly on a reactant on the grain surface (Eley-Rideal mechanism, Weinberg 1996), or if reactants diffuse over the grain surface (Langmuir-Hinshelwood mechanism; see Cuppen et al. 2017, for a review). In the latter case, the diffusion timescales are related to the binding energy of the atom and the temperature. This means that reactions with light atoms such as hydrogen are preferred at cold temperatures, and larger molecules mostly react with each other at higher temperatures.

The field of astrochemistry is driven by a combination of observations, and crucial laboratory research and quantum calculations to quantify reaction rates, branching ratios, and reaction products. In laboratories, astrophysical conditions are simulated in ultra-high vacuum chambers ($<10^{-11}$ bar), sometimes cooled close to absolute 0 K ($\lesssim -260$ °C) or irradiated by high energy lasers. These reactions are then collected in large databases to make predictions for the abundances of molecules in clouds and protoplanetary disks (e.g., UMIST and KIDA; Wakelam et al. 2012; Millar et al. 2024). See, for example van Dishoeck (2014) or Öberg et al. (2023) for an overview.

1.3.1 Chemical evolution

1.3.1.1 Chemistry in the ISM

In the dilute ISM ($n < 10^2$ cm^{-3}), most elements are in atomic form and often ionized by surrounding ultraviolet (UV) sources. Near the edges of molecular clouds, some molecules may emerge in the gas phase due to the increased density; however, these are continually exposed to an external radiation field from adjacent stars, leading to the photodesorption of any ices. Ice formation initiates in regions sufficiently shielded from the external radiation field by dust, typically at a visible extinction of $A_{\rm V} = 1.5$ mag (i.e., where the external radiation field is diminished by a factor ∼4 Hollenbach et al. 2009; Boogert et al. 2015), which corresponds to regions with a density of $\gtrsim 10^3$ cm^{-3} and $T > 20$ K. This phase includes the formation of simple ices like H_2O, CH_4, CO_2 and NH_3 on dust grains (Tielens & Hagen 1982; Öberg et al. 2011a). Since these molecules are predominantly mixed with H_2O, this phase is generally referred to as the polar phase (see Fig. 1.5). If the density increases and the temperature drops, freezeout rates of CO increase, which adds a layer of CO and CO_2 rich ice on top of the polar layer, the so-called apolar phase, phase 2 in Fig. 1.5. At densities $>10^5$ cm^{-3}, "catastrophic freezeout" of CO allows for the efficient formation of H_2CO and CH_3OH at short timescales (∼10 kyr Cuppen et al. 2009), phase 3 in Fig 1.5. Lab studies have shown that during this time more complex molecules can be formed up to, for example, glycerol (Fedoseev et al. 2017) and ethanol (Bisschop et al. 2007; Qasim et al. 2019), now also observed in clouds (McClure et al. 2023; Rocha et al. 2024). Through these three phases, a complex mixture of ices is formed before the star is born.

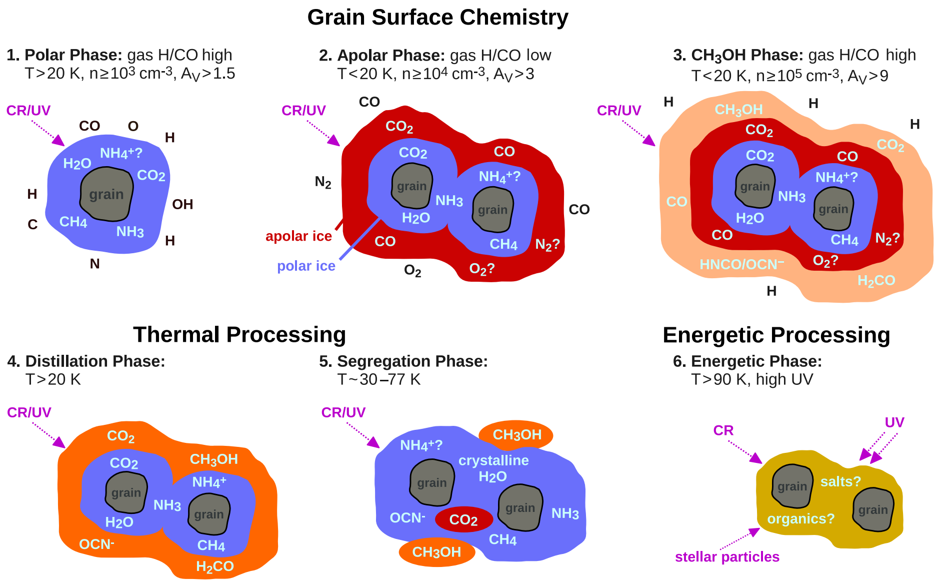
Grain Surface Chemistry
1. Polar Phase: gas H/CO high
T>20 K, n≥10^3 cm^{-3}, A_V>1.5
2. Apolar Phase: gas H/CO low
T<20 K, n≥10^4 cm^{-3}, A_V>3
3. CH_3OH Phase: gas H/CO high
T<20 K, n≥10^5 cm^{-3}, A_V>9
CR/UV
CO
O
H
NH_4^+?
H_2O
CO_2
grain
OH
C
CH_4
NH_3
N
N_2
apolar ice
polar ice
O_2
O_2?
N_2?
CH_3OH
HNCO/OCN^-
H_2CO
Thermal Processing
4. Distillation Phase:
T>20 K
OCN^-
NH_4^+
5. Segregation Phase:
T~30–77 K
crystalline
H_2O
Energetic Processing
6. Energetic Phase:
T>90 K, high UV
CR
UV
salts?
organics?
stellar particles

Figure 1.5: Schematic view of the phases of chemical evolution in the ISM inferred from observations (phases 1 – 3) and the processing in YSO envelopes and disks (phases 3 – 6). Gas phase species participating in grain surface reactions are indicated in red. In phases 1 – 5, the ices experience cosmic ray and UV radiation that only minimally affect the main ice species. As the ice temperature rises (phases 4 and 5), thermal reactions or reactions involving radicals may proceed. Stage 6 is the least observationally constrained. Figure taken from Boogert et al. (2015)

1.3.1.2 Inheritance vs. reset

During the star formation process, the evolution of the ices is dominated by thermal processing. Heating the ice results in the sublimation, segregation, and crystallization of ices, which changes the internal structure of the ices and could result in pockets of pure ice (Ehrenfreund et al. 1997). Additional energetic processing by high-energy particles or UV radiation can lead to additional pathways to form organic material (Boogert et al. 2015).

An important question that currently remains unanswered is how much of the initially formed ice makes its way into protoplanetary disks. During the infall of the envelope and/or protoplanetary disk, the material could heat up significantly in accretion shocks. This could lead to a complete reset if the environment is extreme enough to break down the larger molecules, or alternatively the molecules freeze out again later resulting only in a partial reset (Guilloteau et al. 1992; Guillet et al. 2009). Modeling (Visser et al. 2009; Drążkowska et al. 2016) and observations (Booth et al. 2021) suggest that at least part of the ices makes its way unscathed in protoplanetary disks, but additional observations on a larger sample of sources are required to answer this question in full detail.

1.3.2 Protoplanetary disk chemistry

The chemistry in protoplanetary disks is complex due to several factors. First of all, the steep gradients in temperature and density lead to a wide range of chemical conditions. Moreover, this gives rise to sharp transitions within the disk, where molecules can either exist in the gas phase or become frozen onto the dust grains. These transitions are referred to as snowlines or snow surfaces, named after analogous transitions occurring on mountains as elevation rises. The most prominent snowlines are those from H_2O, CO_2, and CO, which can give rise to significant shifts in the elemental abundances and C/O ratio in the gas and ice phase (Öberg et al. 2011b; Eistrup et al. 2018). If the gas-phase elemental abundance is dominated by oxygen, most of the carbon and oxygen is locked up in relatively inert CO. However, if the C/O ratio gets above unity, the resulting chemistry can change considerably to form for example more hydrocarbons (Bosman et al. 2021b; Cridland et al. 2023; Tabone et al. 2023; Kanwar et al. 2024). Therefore, small hydrocarbons such as C_2H are a good tracer of the C/O ratio in disks.

Additionally, the UV radiation field from the central star is strong in the inner regions and the disk atmosphere but decreases deeper in the disk as a result of shielding from dust and molecules. This results in typical transitions from ionized atoms (C^+) to neutral atoms (C^0) to molecules (CO) in the disk atmosphere (Woitke et al. 2016; Hollenbach & Tielens 1999). The height of these transitions is highly dependent on the source structure, mass, and stellar properties. Deep in the disk, where the temperatures are low (<20 K) and the UV radiation field is diminished by several orders of magnitude, the chemistry is slow and largely driven by cosmic rays and non-energetic processes (Aikawa & Herbst 1999). Cosmic rays are energetic particles and can collide with H_2 to form ${H_2}^+$ and a high-energy electron. ${H_2}^+$ forms ${H_3}^+$ after an additional collision with H_2, which can initiate ion molecule chemistry. Additionally, the high-energy electron collides with other H_2 molecules, inducing electronic transitions that subsequently relax, resulting in the creation of a localized, faint UV field (Prasad & Tarafdar 1983). These UV photons, in turn, generate more radicals, thereby increasing their availability for participation in chemical reactions.

1.3.2.1 Inheritance in planets/comets

It is often assumed that the observed chemical composition of planets is a direct reflection of the chemical composition of the disk (Öberg et al. 2011b). This then could be used to constrain the location of planet formation in the disk. Although there may be some truth to this, the process is somewhat more complex than initially perceived. Planets are thought to form early-on in the star forming sequence (see Sect. 1.2.4), which means that accretion onto the planet happens during all stages of a protoplanetary disk and the chemical history of the system becomes really important. In addition to the evolving protoplanetary disk, the planets migrate through the disk through planet-disk interactions (Sect. 1.2.4), which causes them to accrete from different regions in the disk (Goldreich & Tremaine 1980).

It is also not straight-forward from which vertical layer gas giants planets accrete. Planets are formed at the midplane and start to accrete dust and ice locally. However, if the planet gains enough mass it opens a gap in the dust disk and forms in some cases a circumplanetary disk (CPD). Accretion flows become so complex that accretion from the disk atmosphere can become more important than from the midplane (Morbidelli et al. 2014, Fung & Chiang 2016, Szulágyi et al. 2016, Szulágyi et al. 2022; see Fig. 1.6). During the accretion, the ice composition can be significantly altered after an initial reset of accreted circumstellar ice (Oberg et al. 2023). Sufficiently large planets start to accrete gas as well, which could change the atmospheric composition. This could lead to segregation between the core and the atmosphere which complicates the comparison between observed exo-planet atmospheres and the bulk elemental composition of protoplanetary disks.

1.4 Ices in protoplanetary disks

Ices play a crucial role in protoplanetary disks, as a large portion of the volatile elements are frozen out on dust grains in the cold midplane region of the disk (Pontoppidan et al. 2014; Walsh et al. 2015). Radial and vertical motions of the dust can cause large differences in the overall mass and volatile abundance distributions, which significantly impact the disk physics and chemistry.

1.4.1 The role of ices in protoplanetary disk physics

Ices are thought to play a crucial role in planet formation processes. Figure 1.7 illustrates the most important effect on the disk physics, also known as a "traffic jam". Ices increase the overall solid mass that is available for planet formation (by up to a factor 4 Pontoppidan et al. 2014), and make it more likely that the streaming-instability is triggered. Especially water ice also makes the dust grains more sticky, and allows for more efficient dust growth in the disk. Due to radial drift, the region inside the snowlines is continuously enriched with refractories. After the ices are desorped from the refractory cores, the grains get smaller and potentially break apart causing less efficient radial drift, causing a pile-up or "traffic jam" near the snowline. Additionally, the massive amounts of volatiles that

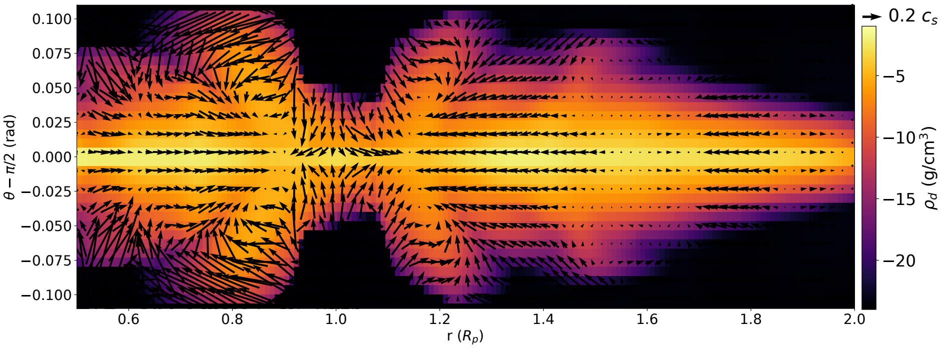

Figure 1.6: Azimuthally averaged velocity structure in the dust normalized to the local sound speed in CPD simulations of a Jupiter-mass planet orbiting at 50 au after 200 planetary orbits. The background colors show dust gas volume density. Figure adapted from Szulágyi et al. (2022).

are released at the snowline cause strong chemical gradients in the disk. Those gaseous volatiles could diffuse outwards again beyond the snowline and create local enhancements in the ice abundance. The result is a pressure bump in the disk and a high dust-to-gas ratio that could directly lead to planet formation via the streaming instability (Drążkowska et al. 2016, 2023).

1.4.2 The role of ices in protoplanetary disk chemistry

As we have shown in Sect. 1.3, grain surface chemistry plays a crucial role in the formation of (complex) molecules in space. However, in turbulent environments like protoplanetary disks, the ice has additional effects on the chemistry as well. Ices constitute a significant fraction of the volatiles and can easily be moved around by turbulence in the gas, grain settling and radial drift. Their critical role in the chemistry was acknowledged after observations of large samples of gaseous CO in protoplanetary disks (see e.g., van Zadelhoff et al. 2001; Dutrey et al. 2003; Chapillon et al. 2008; Favre et al. 2013; Schwarz et al. 2016; Ansdell et al. 2016; Long et al. 2017; Miotello et al. 2017; Ansdell et al. 2018). CO is a molecule with a relatively simple chemistry and is in the gas phase in a large portion of the disk due to its low desorption temperature (20 – 30 K) and therefore often used as a mass tracer. However, the detected number of molecules is often lower than predicted, by up to two orders of magnitude. The most likely explanation to this conundrum is illustrated in the right side of Fig. 1.3 and includes continuous freezeout of CO on dust grains in the upper layers of the disk which subsequently settle to the midplane and radially drift towards the star due to more efficient grain coagulation. Additionally, cold conversion of CO to bigger molecules with a higher desorption temperature (like CO_2 or CH_3OH) contributes as well (Bosman et al. 2018; Trapman et al. 2021). Similar processes are thought to explain the low abundance measurements of other molecules like H_2O (Bergin et al. 2010; Hogerheijde et al. 2011; Du et al. 2017). Depending on the depletion, elemental ratios (like C/O or N/O) that often determine the output of the chemistry, can change significantly in the disk gas.

Apart from depleting volatiles from the gas phase, ices can enhance the volatile gas abundance as well if sufficient material is moved to the inner disk via radial drift (e.g., Zhang et al. 2020a). However, observations have shown increasing evidence that inner disks are more likely depleted in volatiles as well (Bosman & Banzatti 2019; McClure 2019; McClure et al. 2020; Bosman et al. 2021a), suggesting that a large fraction of the icy material is trapped in the outer disk due to dust traps or rapid planetesimal formation (McClure 2019). Clathrate hydrates in the solar system could provide clues for the mechanisms for ice trapping the planet formation process, and are an active field of study in laboratories (Mousis & Schmitt 2008; Dartois 2010, 2021).

1.5 Techniques

Astronomy is driven by technological advancements that allow for observations with increasing detail and models with more calculation steps. This section introduces the instruments and models that are used throughout the thesis.

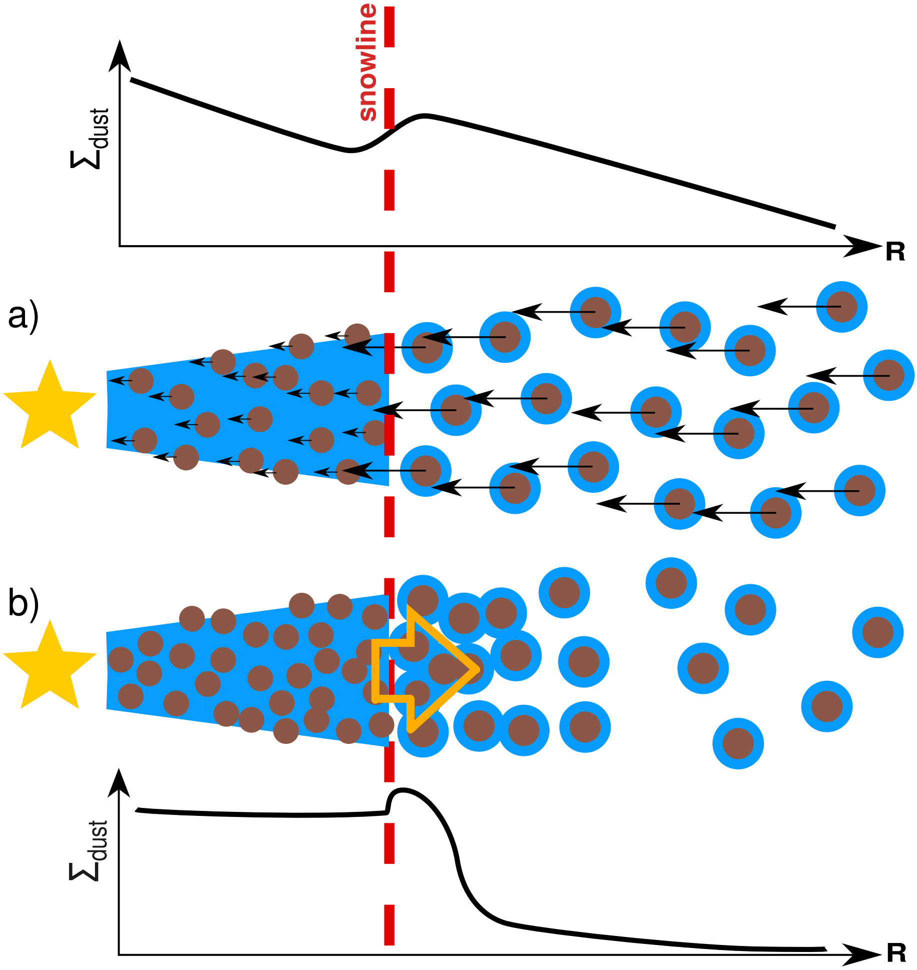

Figure 1.7: This sketch explains the pile-up of ices near the snowline: a) Initially, the solid density is higher outside the snowlines due to the incorporation of ice. Coagulation is more efficient for aggregates that incorporate water ice. Thus, solids grow to larger sizes and drift faster outside of the snow line. The quick drift results in an efficient delivery of material, which does not drift rapidly inside the snowline because of the smaller grain sizes, causing a "traffic jam" and increase the dust concentration in the inner disk. b) The outward diffusion and re-condensation of water vapor locally enhances abundance of solids just outside of the snow line, contributing to the pile-up of icy pebbles. Figure adapted from Drążkowska et al. (2016).

1.5.1 Observations

With telescopes, we observe radiation that could arise from different origins. The most straight-forward radiation is thermal radiation, for example from stars or warm dust. This radiation is transmitted over a large wavelength and energy range, with a peak depending on the temperature according to Wien's law

$$\lambda_{\mathrm{Wien}} = \frac{a}{T} \tag{1.5}$$

with a Wien's displacement constant equal to 2.9 mm K^{-1} and T the temperature. This radiation can be observed either directly or after scattering from dust, similar to how we see the Moon at night.

Atoms and molecules emit too, but this emission is mostly radiated at very specific wavelengths. Atoms have internal electronic transitions that allow for emissions at specific wavelengths if an electron jumps to a less energetic quantum state. Fine structure transitions within electronic ground states occur at visible to far-infrared wavelengths. Molecules radiate emission via vibrational and rotational transitions. Vibrational emission usually occurs at mid-infrared wavelengths (2 – 25 µm) and traces high temperature gas. Rotational emission is less energetic, tracing the cold gas, and usually occurs at millimeter wavelengths. Not all molecules have strong rotational emission spectra, depending on the internal dipole moment. Linearly symmetric or homonuclear molecules like H_2 and CO_2 have no dipole moment and can therefore not be observed at millimeter wavelengths.

The vibrational transitions of molecules in the ice phase are influenced by their chemical environment. Ice features are therefore much broader than gas features, and change depending on the ice mixture. Ices can appear in emission in the far-infrared (see e.g., McClure et al. 2015), but are more often observed in absorption in the mid-infrared. The integrated optical depth of an absorption ice feature is linearly related to the column density of the ice

$$\int \tau d\nu = AN, \tag{1.6}$$

with τ the optical depth, N the column density and A the band strength which is molecule dependent.

1.5.1.1 Infrared spectroscopy

The mid-infrared (2 – 25 µm) is a very interesting wavelength region due to the plethora of molecular vibrational transitions, including ice features. Unfortunately, our own atmosphere is largely opaque at these wavelengths due to, for example, water vapor. Some transparent wavelength windows can be reached from the ground (for example using the Very Large Telescope; VLT), but a space-based telescope is preferred for most observations. Space telescopes are diffraction limited, but are technically challenging due to requirements for the launch. *Infrared Space Observatory* (ISO; 1995 – 1998) and *Spitzer* (2003 – 2020) were the first space telescopes that provided infrared spectra, but with limited sensitivity. The *James Webb Space Telescope* (JWST) is the new flagship of the space fleet. Launched on Christmas 2021, it circles around L2, one of the gravitationally stable orbits around the Sun and the Earth at 1.5 million km. Due to this location it can block the radiation from the Sun and the Earth at all times with its 30 m wide Sun screen. It has four different instrument, each with a different purpose. The Near-InfraRed Spectrograph (NIRSpec) and the Mid-InfraRed Imager (MIRI) are the most frequently used instruments for protoplanetary disk observations. These two spectrographs each can observe spatially resolved spectra of images with at each pixel a spectrum (or spaxel). The observations with these instruments are dominated by warm dust from the inner disk and could detect ices in absorption against this warm continuum, atomic lines and vibrational transitions at medium spectral resolution of $R \sim 2700$.

1.5.1.2 Sub-millimeter interferometry

The (sub-)millimeter is another interesting wavelength range for volatile astrochemistry, due to its vast array of rotational transitions. The (sub-)millimeter is accessible from Earth, but the downside is that at these longer wavelengths the spatial resolution is poor due to the diffraction point spread function that scales as $\theta = \lambda/D$ with λ the observing wavelength and D the diameter of the telescope aperture. Fortunately, the long wavelengths make it possible to measure the phase of the incoming radiation, which allows combining the radiation received with different antennae to simulate a telescope as large as the distance between the antennae. The Atacama Large (sub-)Millimeter Array (ALMA) and NOrthern Extended Millimeter Array (NOEMA) are two of the most state-of-the art interferometers that observe the southern hemisphere and northern hemisphere, respectively. With this technique, we trace cold dust near the midplane of protoplanetary disks and cold gas-phase emission in the disk atmosphere. The long baselines between the 64 ALMA antennae (max 16 km) allow for high angular resolution observations resolving substructure in gas and dust of protoplanetary disks.

1.5.2 Modeling

Observations are critically important. However, interpretation of these observations and determining what physical and chemical properties give rise to these observations, is often far from trivial. Most observations are only a 2D representation of a 4D source; the third spatial dimension and history of the system must be assumed from the 2D representation or comparison with similar objects at other viewing angles or snapshots in time. Ideally, we would calculate analytically what the underlying physics is, but in most cases reality is too complex to study analytically. With numerical models the reality is approximated, which allows us to explore the parameter space in the models. In this thesis we used radiative transfer modeling and physical-chemical modeling which will both be introduced in the following subsections.

1.5.2.1 Radiative transfer models

Radiative transfer models determine the propagation of emitted photons through a dust-rich medium to calculate the temperature and emergent spectrum towards us. They require solving the radiative transfer equation numerically, which is given by

$$\frac{dI_\nu}{ds} = -\alpha_\nu I_\nu + j_\nu + \epsilon_\nu (B_\nu - I_\nu) \tag{1.7}$$

where I_ν is the specific intensity of radiation (energy per unit time, area, solid angle, and frequency interval) along a given direction, s is the distance traveled through the medium, α_ν is the absorption coefficient, representing the fraction of intensity absorbed per unit distance, j_ν is the emission coefficient, representing the amount of radiation emitted per unit volume, solid angle, frequency, and time, ϵ_ν is the emissivity, representing the efficiency of emission relative to a black body. B_ν is the Planck function, describing the intensity of black body radiation at temperature T and frequency ν.

The radiative transfer code that is used in this thesis is `RADMC3D` (Dullemond et al. 2012), which allows for easy setup of density structures (e.g., disks) and energy input sources (e.g., stars). Our model setup follows largely the radiative transfer models developed for the interpretation of *Spitzer* data (Pontoppidan et al. 2005), updated by Ballering et al. (2021). The first step is calculating the temperature in each grid cell of the model, which is done by Monte Carlo simulations that track photon packages through the disk. As the photon packages move through the grid they may scatter off dust grains and thus change their direction according to the particle's scattering properties. They may also get absorbed by the dust, and be re-emitted at a different wavelength, increasing the temperature of the dust in the cell. In very optically thick regions, following the photon package is too time consuming and the escape is simulated with a modified random walk. Subsequently, observations can be mimicked by tracing photon packages that escape the system in a predefined direction (ray-tracing) and convolution with a point spread function.

Radiative transfer modeling requires detailed knowledge of the absorption and scattering properties of the grains. Optical constants of materials are measured in laboratories (Warren 1984; Rocha et al. 2022), and the impact of grain shape, size and mixtures on the scattering properties of particles are simulated using Maxwell's equations for the interaction of light with objects. In the simplest case, perfect spheres are assumed with a range of sizes (Mie theory, Mie 1908). In reality the grains are irregular, porous, and in-homogeneous. Different approximations can be used to correct for the grain shapes and the grain composition, but grain size distributions, composition, and porosity remain one of the most unconstrained properties in models that are often based on large assumptions (Draine 2003; Min et al. 2005, 2007, 2016).

1.5.2.2 Physical-chemical models

The goal of physical-chemical models of protoplanetary disks is to predict the line emission based on the input parameters and to look for trends with the observations. It requires solving the heating-cooling mechanisms in the gas, molecular excitation, and chemistry of the gas at the same time, which all depend on each other. Physical-chemical models like Dust And LInes (DALI; Bruderer et al. 2012; Bruderer 2013, that is used in this thesis, solve these three properties iteratively, starting from the dust temperature from radiative transfer modeling until convergence is reached. Subsequently, the molecular properties can then be used to predict the emission that arises from the molecules and be raytraced to simulate observations. The chemical network is often small to accommodate exploring larger parameter grids and can be changed depending of the project goal.

1.6 This thesis

Ices play a crucial role in both the physics and the chemistry of protoplanetary disks (Sect. 1.4). It is thus crucial to determine the abundance distribution of ices throughout the disk, which still relies heavily on assumptions and theoretical chemical models, lacking direct observational evidence.

1.6.1 Status quo

In the literature, some progress has been made in limiting the characteristics of ices in protoplanetary disks through interpretation of observations. Ice absorption features are observed in scattered light with high-contrast imaging techniques in two face-on disks around Herbig Ae/Be stars (Honda et al. 2009, 2016). These spatially resolved observations provide unique insight in the radial distribution of the ice, but are currently only possible for H_2O ice in bright systems and lack the spectral resolution to study the feature in detail.

Ice emission features in the far infrared have been detected in a couple of instances (Malfait et al. 1998; McClure et al. 2015; Min et al. 2016), but unfortunately no far-infrared observatory will be able to observe those features anytime soon.

The most progress has been made using edge-on disks that often included an envelope (Pontoppidan et al. 2005; Terada et al. 2007; Aikawa et al. 2012; Terada & Tokunaga 2012; Terada et al. 2012; Terada & Tokunaga 2017). Sources with an envelope are generally easier to detect due to their higher luminosity, yet it is challenging to determine the disk's contribution to the total absorption features. Spectra from pure edge-on disks appear dim due to the necessary obscuration of both the star and the inner disk to study the ice's absorption features within the disk (Pontoppidan et al. 2005). Previous space telescopes were therefore not sensitive enough to study the ices in protoplanetary disks in sufficient detail. With the launch of JWST, we are able to observe ices in protoplanetary disks with unprecedented detail and sensitivity.

1.6.2 Breaking the ice

In this thesis, I have explored both indirect (Chapter 2 – 3) and direct methods (Chapter 5 – 7) to probe the abundance and location of ices in protoplanetary disks from observations. Indirect methods involve gas phase observations to probe the effect of moving dust grains on the volatile abundance in different regions of the disk. Direct methods include JWST observations of ice features in edge-on protoplanetary disks. The double meaning of the title of this thesis "Breaking the Ice" refers to the fact that we see many aspects of ice in protoplanetary disks for the first time. With the advent of JWST it is important to get acquainted with ice in protoplanetary disks and to explore what we can constrain from these novel observations. The exploratory study, driven by the Early Release Science program Ice Age on the JWST (Chapter 4 – 7), in particular, has revealed many mechanisms that were unexplored before and has therefore "broken the ice" to allow larger sample studies of edge-on disks with JWST.

1.6.3 Overview of each chapter

Chapter 2 This chapter examines the depletion of gas-phase carbon as a tracer of CO ice freezeout in disks of various ages, employing the first mini-survey of sub-millimeter atomic carbon transitions [C I] conducted with the Atacama Compact Array. Before this work, only two protoplanetary disks had detected [C I] emission at (sub-)millimeter wavelengths, we managed to increase this sample significantly with six more sources. Using physical-chemical models of the expected protoplanetary disk structure, we were able to constrain the C/H abundance in the outer disk of three low-mass sources that all show depletion of gaseous carbon from the disk atmosphere. Including all determined protoplanetary disk carbon abundances in the literature, we find evidence for an evolutionary trend of the C/H abundance, suggesting that gaseous C/H may be a useful proxy for ice build-up in the midplane over time. Comparing our measurements with previous carbon observations tracing the inner disk, we find that most sources have a higher carbon abundance in the inner disk compared to the outer disk, but the correlation with known dust traps in the systems remains unclear.

Chapter 3 The carbon abundance as a proxy for ice freezeout is limited in utility by degeneracy of C/H and the disk gas mass. Therefore, this chapter focuses on a novel method of breaking this degeneracy using the anti-correlation between the CO abundance and the N_2H^+ abundance. The use of the carbon abundance as an indicator for ice freezeout is restricted by the degeneracy between C/H ratios and the disk gas mass. Consequently, this chapter introduces a new approach to resolving the degeneracy between gaseous carbon abundance, C/H, and total gas mass by examining the inverse relationship between CO abundance and N_2H^+ abundance. Using all available ALMA and NOEMA observations of the well known transition disk LkCa 15, we conclude that the disk is only depleted in carbon and oxygen by a factor of a few. Since this young source has a massive cold disk, which should allow for efficient gaseous volatile depletion, we suggest that it is not just the evolving physical structure of the disk, but also the age compared to depletion timescales that sets the overall carbon abundance.

Chapter 4 In this chapter we created a new 3D radiative transfer disk setup using `RADMC3D`, that includes new opacities and scattering prescriptions relative to old *Spitzer* era disk models. We tuned the model to fit HH 48 NE, using *Hubble Space Telescope* (HST), ALMA and photometric data, and explored the impact of disk physical structure on the emergent spectrum. Comparing radiative transfer models with photometric and spatially resolved observations we constrained the source structure, grain size distribution and stellar parameters in the system. We show that the disk atmosphere is depleted in small grains <0.1 µm and that ∼90% of the dust is settled to the midplane. This model acts as a control case for the models presented in Chapter 5 that include ices.

Chapter 5 This chapter expands on the models from Chapter 4 by incorporating ice opacities. We employed a straightforward setup without including chemistry, concentrating on how the source structure affects the emergent spectrum. Utilizing the uncertainties in the source structure established in Chapter 4, we demonstrate that ice abundances can be constrained within a factor of approximately 3, provided certain basic assumptions are valid. This chapter represents an important initial step in leveraging observations of edge-on disks to determine ice properties within disks.

Chapter 6 This chapter presents the first JWST spectrum of ices in a protoplanetary disk that has unprecedented sensitivity. We identified the major ice components H_2O, CO_2, and CO, and multiple weaker signatures from less abundant ices NH_3, OCN^-, and OCS and the $^{13}CO_2$ isotopologue. The nature of the observed absorption features is explored, showing that spatially resolved observations of ices in disks are not easily related to ice column densities due to the source structure and photon scattering. We demonstrate that the radiative transfer in edge-on disks breaks the linear relationship between ice column density and observed optical depth (see Eq. 1.6) and that radiative transfer models are required to constrain the ice abundance. Using the $^{13}CO_2$ isotopologue feature, we were able to constrain the $^{12}CO_2$ column density using the fact that the $^{12}CO_2$ feature is saturated and shows how much of the light actually reaches the icy regions of the disk. H_2O, CO_2, and especially CO are found at high altitude in the disk, suggesting that part of the CO is trapped in less volatile ice like H_2O and CO_2. This entrapment could have important consequences on the positions of snowlines in disks and the composition of exoplanet atmospheres. This chapter marks an important step towards understanding ice observations in edge-on protoplanetary disks and what we can and cannot constrain from them. It makes way for a similar analysis of a larger sample of disks to understand the trends among different sources.

Chapter 7 This chapter presents the JWST MIRI spectrum of ices in the same protoplanetary disk as Chapters 4 – 6, completing the ice inventory that is observable with JWST. We detect CO_2 ice, NH_3 ice and potentially H_2O, NH_4^+ and CH_4 ice. In addition we detect clear PAH features that are usually missing in similar disks at low inclination and suggest that they are localized in the disk. We show that the initial model, constrained pre-JWST, is a good representation of the source in the JWST data and that we can approximately fit the ice features by changing a few key parameters. Using the model we constrained the region in the disk traced with the observations, and confirm that ices need to extend to high elevations to be consistent with observations.

1.6.4 Summary of the main findings

1. It is non-trivial to determine C/H and O/H abundance ratios in protoplanetary disks as these abundances are usually degenerate with the disk mass. Both [C I] and N_2H^+ prove to be good tracers to break the degeneracy with disk mass as they are a sensitive tracer of gaseous C/H abundance in disks (Chapter 2, 3).

2. We observe an evolutionary trend of decreasing gaseous volatile abundance in the outer disk, which suggests an incremental build-up of ice in the midplane as predicted by models. This trend only holds for disks that are cold enough to have a significant region where CO can freeze out (Chapter 2).

3. The radial distribution of carbon shows signs of radial drift and trapping in pressure bumps, but the correlation with observed dust traps at millimeter wavelength is not obvious (Chapter 2).

4. We can constrain the stellar parameters, source structure and grain size distribution of edge-on disks relatively well using a combination of resolved optical and millimeter observations and a photometric SED (Chapter 4). The constraints on the source structure should be good enough to study ice abundances, as long as the ice features do not saturate (Chapter 5).

5. The spatial variations in ice absorption are less easy to interpret than expected. Different line of sights do not necessarily trace different column densities, but rather a different light path through the disk. This implies that radiative transfer models are necessary to deduce spatial information from the observations (Chapter 5, 6, 7).

6. Ices exhibit a high scale height in the HH 48 NE disk, suggesting either continuous recycling of ices from the midplane or the blockage of UV photons by a disk wind. CO ice is trapped in H_2O and/or CO_2 ice, allowing it to endure temperatures above the desorption point of pure CO ice, both higher in the disk and nearer to the star (Chapters 6 and 7).

7. Different ice features trace different regions in the disk, depending on the wavelength and the desorption temperature of the molecule. In general, absorption features at longer wavelengths trace regions closer to the midplane. The bulk of the ices, located in the midplane, are beyond the reach of edge-on disk observations.

1.6.5 Future outlook

Advancements in theory and instrumentation continuously propel the field of star and planet formation forward. As we delve deeper into the details, we find that the formation processes are dynamic and complex, involving system evolution, ongoing transport, recycling, turbulence, and other phenomena.

Given the interplay of these complex processes, the next logical step in constraining the ice abundance distribution and evolution is to increase the sample size to identify statistically significant trends. For indirect methods to constrain ice properties, the ALMA large programs AGE-PRO (PI: K. Zhang) and DECO (PI: L. I. Cleeves), along with the NOEMA large program PRODIGE (PI: D. Semenov), which integrate the methodology from Chapter 3, will provide further insights into the evolution and origin of the gaseous C/H ratio discussed in Chapter 2 and enhance statistical significance.

For direct methods to constrain ice properties, additional edge-on disk observations with JWST are essential to gain insight into the ice abundance distribution. Combining high-resolution ALMA and JWST observations of edge-on systems is necessary to resolve degeneracies in radiative transfer models and to determine the location of the ice relative to the molecular gas layer. Far-infrared probes targeting ice emission features at 40 – 100 µm would significantly extend the regions of the disk currently being studied.

I hope this thesis will serve as an important stepping stone toward understanding the volatile distribution in protoplanetary disks and the resulting planetary composition, advancing our knowledge through the process of “breaking the ice”.

Chapter 2

Tracing pebble drift and trapping using radial carbon depletion profiles in protoplanetary disks

J. A. Sturm, M. K. McClure, D. Harsono, S. Facchini, F. Long,
M. Kama, E. A. Bergin, and E. F. van Dishoeck

A&A 660, A126 (2022)

Abstract

Context. The composition of planets may be largely determined by the chemical processing and accretion of icy pebbles in protoplanetary disks. Recent observations of protoplanetary disks hint at wide-spread depletion of gaseous carbon. The missing volatile carbon is likely frozen in CO and/or CO_2 ice on grains and locked into the disk through pebble trapping in pressure bumps or planetesimals.

Aims. We aim to measure the total elemental C/H ratio in the outer region of seven disks, four of which have been previously shown to be depleted of carbon gas interior to 0.1 au, through near-infrared spectroscopy.

Methods. We present the results of the first successful ACA (Atacama Compact Array) [C I] $J = 1 - 0$ mini-survey of seven protoplanetary disks. Using tailored azimuthally symmetric DALI (Dust And LInes) thermo-chemical disk models, supported by the [C I] $J = 1 - 0$ and resolved CO isotopologue data, we determine the system-averaged elemental volatile carbon abundance in the outer disk of three sources.

Results. Six out of seven sources are detected in [C I] $J = 1 - 0$ with ACA, four of which show a distinct disk component. Based on the modeling we find severe cold gaseous carbon depletion by a factor of 157^{+17}_{-15} in the outer disk of DL Tau and moderate depletion in the outer disks of DR Tau and DO Tau, by factors of 5^{+2}_{-1} and 17^{+3}_{-2}, respectively. The carbon abundance is in general expected to be higher in the inner disk if carbon-rich ices drift on large grains towards the star. Combining the outer and inner disk carbon abundances, we demonstrate definitive evidence for radial drift in the disk of DL Tau, where the existence of multiple dust rings points to either short lived or leaky dust traps. We find dust locking in the compact and smooth disks of DO Tau and DR Tau, hinting at unresolved dust substructure. Comparing our results with inner/outer disk carbon depletion around stars of different ages and luminosities, we identify an observational evolutionary trend in gaseous carbon depletion that is consistent with dynamical models of CO depletion processes.

Conclusions. Transport efficiency of solids in protoplanetary disks can significantly differ from what we expect based on the current resolved substructure in the continuum observations. This has important implications for our understanding of the impact of radial drift and pebble accretion on planetary compositions.

2.1 Introduction

Carbon and oxygen are two of the most abundant elements in interstellar clouds and play a crucial role in the chemistry of star forming regions and planetary atmospheres (Langer 2009; Madhusudhan 2019). If volatile carbon is carried mostly by dust grains, these grains can grow to produce planetesimals rich in complex organic molecule ices, the building blocks of life. CO isotopologue surveys have recently revealed that CO is frequently underabundant by orders of magnitude in the gas-phase in protoplanetary disks of T Tauri stars (van Zadelhoff et al. 2001; Dutrey et al. 2003; Chapillon et al. 2008; Favre et al. 2013; Schwarz et al. 2016; Ansdell et al. 2016, 2018; Long et al. 2017; Miotello et al. 2017). The amount of volatile depletion observed cannot be explained solely by freeze-out, photodissociation or chemical processing in the warm molecular layer (van Zadelhoff et al. 2001; Williams & Best 2014; Miotello et al. 2017; Schwarz et al. 2018; Bosman et al. 2018; Zhang et al. 2019). Detailed analysis of the TW Hya disk, using [C I], HD, CO and C_2H emission, shows that the depletion in CO is related to elemental carbon depletion (Bergin et al. 2013; Kama et al. 2016b; Calahan et al. 2021) and cannot be due to high dust-to-gas ratios only.

The outer disk gas phase carbon depletion can be explained by freeze-out of CO onto dust grains, coupled with a combination of chemical processing into less volatile carbon carrying molecules and dust evolution locking the carbon in the ice on large dust grains in the midplane (Kama et al. 2016b; Krijt et al. 2020). The long timescales for carbon depletion processes are expected to result in stronger depletion, of several orders of magnitude, in older Class II disks (Krijt et al. 2020). Efficient vertical gas mixing is necessary to replenish the CO gas available for freeze-out near the disk midplane, which results eventually in lower carbon abundances in the atmospheric layers of the disk. Large dust grains eventually drift radially inwards towards the central star, due to the gas pressure (Takeuchi & Lin 2002; Trapman et al. 2021). If nothing stops the radial drift, the CO ice is released inside the CO snowline resulting in super-solar C/H ratios as observed in HD 163296 (Zhang et al. 2019, 2020a).

However, Zhang et al. (2019) show that not all protoplanetary disks may have an increase in carbon content inside the CO snowline, as a result of carbon locking into less volatile species in the outer disk. Thus, for example, if CO is processed into CO_2 this carbon will not return to the gas until the CO_2 snowline, which is unresolved in most data. However, the situation may be more complicated than this as a study of accreting T Tauri stars demonstrates that the general trend is that carbon is depleted in the inner disk, which we define as the gas accretion disk inside the dust sublimation radius, typically at 0.01 – 0.1 au; McClure (2019) finds depletion factors ranging between 2 and 25 relative to the diffuse ISM value of 1.35 $\times$ 10^{-4}. The volatile and refractory depletion trend across different atoms in the well studied inner disk of TW Hya (Bosman & Banzatti 2019; McClure et al. 2020) is the inverse of the super solar abundances observed in solar system meteorites (Lodders 2010; Bergin et al. 2015; McClure et al. 2020), which demonstrates that the observed carbon depletion likely results from the trapping of ice-coated rocky pebbles in the outer disk, either in a pressure maximum or in bodies that grow

Table 2.1: Host Stellar Properties

Name (1)	SpT (2)	Age (Myr) (3)	d (pc) (4)	A_V (mag) (5)	L_* ($\mathrm{L}_\odot$) (6)	T_eff (K) (7)	R_* ($\mathrm{R}_\odot$) (8)	M_* ($\mathrm{M}_\odot$) (9)	$\dot{M}$ ($\mathrm{M}_\odot \mathrm{yr}^{-1}$) (10)	V_lsr (km s^{-1}) (11)
DL Tau	K7V	7.8	159 ± 1	1.6	0.37	4060	1.24	0.80	5.8×10^{-8}	6.62 (a)
DO Tau	M0V	2.0	139 ± 1	3.6	0.58	3850	1.72	0.57	6.6×10^{-8}	5.91 (b)
DR Tau	M0V	0.9	195^{+3}_{-2}	2.1	1.12	3850	2.39	0.56	4.8×10^{-7}	9.79 (a)
FZ Tau	M0V	1.1	130 ± 1	6.5	0.93	3850	2.18	0.56	3.5×10^{-7}	6.0 (c)
AS 205 A (d)	K5V	1.1	128 ± 2	2.9	2.14	4266	2.68	0.87	4.0×10^{-8}	4.583 (e)
FM Cha (f)	K7V	5.3	201 ± 6	4.3	0.48	4060	1.40	0.78	8.3×10^{-8}	4.0 (g)
WW Cha (h)	K0V	6.4	190 ± 1	4.1	2.68	5110	2.09	1.65	2.1×10^{-7}	4.3 (g)

Notes. Columns are defined as: (1) Name of the central star, (2) stellar spectral type, (3) stellar age, taken from the evolutionary tracks of Kenyon & Hartmann (1995), (4) distance to the source based on the *Gaia* DR 2 supplemental catalog (Bailer-Jones et al. 2018), (5) extinction along the line of sight, (6) stellar luminosity, (7) effective stellar temperature, (8) stellar radius, (9) stellar mass, (10) stellar mass accretion rate, (11) local standard of rest velocity of the source used in this work, based on literature CO data.

References. All stellar quantities of the sources in Taurus are taken from McClure (2019). (a) Guilloteau et al. (2013), (b) Fernández-López et al. (2020), (c) taken as the velocity of the maximum [C I] cloud absorption, (d) Andrews et al. (2018a), (e) Kurtovic et al. (2018), (f) Manara et al. (2017), (g) Long et al. (2017) and references therein, (h) Manara et al. (2016)

quickly to kilometer-sized planetesimals stopping the radial drift. Since some of the disks in McClure (2019) are compact in the dust and do not show any signs of strong pressure bumps, it is proposed that some of these sources have produced planetesimals via the streaming instability, creating an initial dust trap before any planets have carved a gap. However, the carbon abundance in the outer regions of the disks in the McClure (2019) survey has never been unambiguously determined. Therefore it is still unclear whether the carbon abundance in the outer disk is even lower than the inner disk, as expected based on the models including radial drift, or that the dust is efficiently trapped in dust traps, pebbles and planetesimals.

Observational estimates of the elemental volatile carbon abundance in protoplanetary disks are difficult to constrain. The main gas-phase carbon carriers in the atmospheric layers of protoplanetary disks are C^+, C^0, CO, and CO_2, ordered by increasing shielding from ultraviolet photons (Bruderer et al. 2012; Bergin et al. 2014; Bosman et al. 2018; Krijt et al. 2020). CO is the dominant reservoir in molecular gas in the bulk of the disk, but is not the most accurate probe of the C/H abundance as most isotopologues are optically thick (see e.g. Zhang et al. 2020b; Booth & Ilee 2020) and can be affected by direct photodissociation and freeze-out (Kama et al. 2016a). In the outer and upper regions of the disk where CO and small dust are depleted and the effects of photodissociation are magnified, neutral and ionized carbon become the main carbon reservoirs in the gas. Atomic carbon is not often observed in protoplanetary disks and may have non-disk emission components, but is in combination with spatially resolved CO emission a better tracer of the elemental volatile carbon abundance than CO alone (Kama et al. 2016a).

In this work, we present [C I] observations using the Atacama Compact Array (ACA) of the Atacama Large Millimeter/submillimeter Array (ALMA) in a sample of seven disks, four of which have a known carbon abundance in the inner disk as determined from accreting material emitting in the near-infrared (McClure 2019). Three of these disks were identified as having a dust trap on the basis of their inner disk carbon abundances. The sample, observations, and data analysis are described in Sect. 2.2, the analysis of the observed spectra in Sect. 2.3. Using the atomic carbon emission in combination with archival CO data, we determine a radial profile of the elemental carbon abundance in the three sources with known inner disk carbon abundance. The modeling methodology is described in Sect. 2.4, the results of the modeling in Sect. 2.5 and the implications for the disk chemistry and formation of planetesimals in Sect. 2.6.

2.2 Observations and data analysis

The full sample contains seven well-studied disks, four in Taurus, two in Chamaeleon I, and one in Ophiuchus. The sample was selected to have strong near-infrared permitted C^0 lines tracing the inner disk in either the McClure (2019) data or archival VLT X-shooter spectra. Subsequent criteria were that the sources already have CO isotopologue 12m ALMA observations existent from other programs that could provide additional constraints on our modeling. Table 2.1 lists the properties of the stars in our ALMA sample. Most of the stellar properties are taken from Mc-

Clure (2019). The rest velocities of the sources are taken from high resolution CO data.

2.2.1 Observations

Our ALMA Atacama Compact Array (ACA) Band 8 observations were conducted in August and September of 2018 as program 2017.1.00857.S (PI: M.K. McClure). The continuum emission was recorded in two spectral windows (SPWs), centered on 479.59 GHz and 477.7 GHz respectively, each with a bandwidth of 2.0 GHz. One of the line SPWs was centered on the [C I] $J = 1 - 0$ line at 492.165 GHz, the other line SPW was centered on the CS $J = 10 - 9$ line at 489.755 GHz in an attempt to constrain the sulfur chemistry in the outer disk. The latter emission line is not detected in any of the sources, and hence it is not used in this analysis. The bandwidth of the line SPWs were 250 MHz each, resulting in

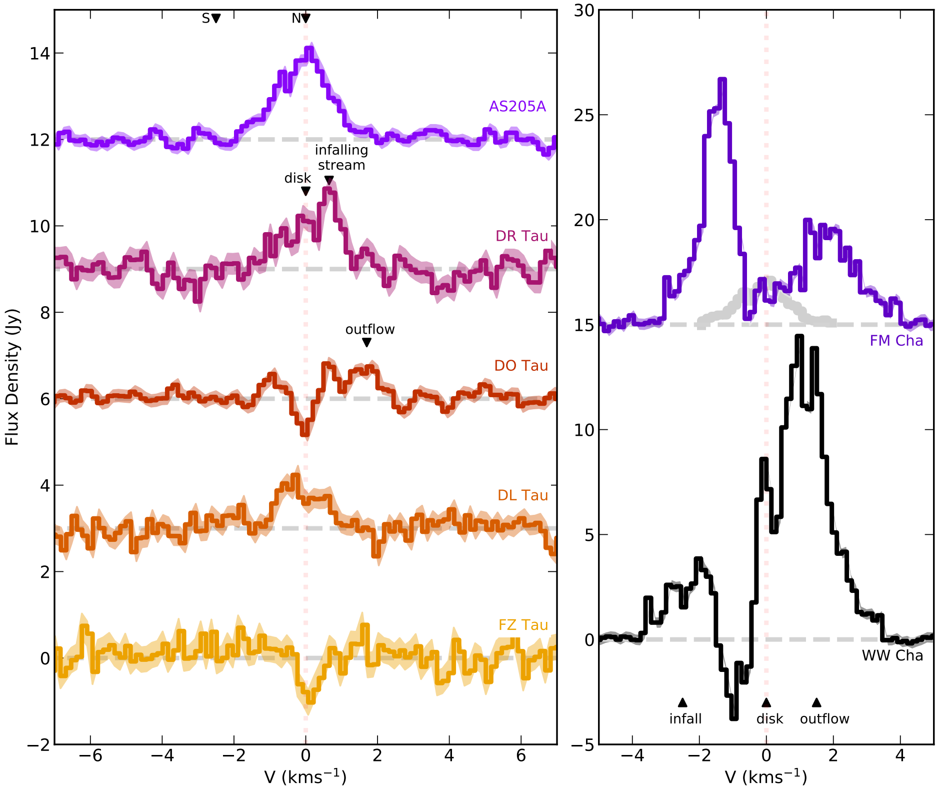

Figure 2.1: Spatially integrated emission spectra of the [C I] $J = 1 - 0$ line at 492.165 GHz for the seven sources in our sample. All the spectra are shifted to their respective local standard of rest velocity (Table 2.1). The shaded region marks the 1σ uncertainty for each source. The spectrum of AS 205 A is shown in gray with FM Cha as a reference of the typical linewidth for a modestly inclined disk. N and S depict the $V_{\rm lsr}$ of AS 205 N and AS 205 S respectively.

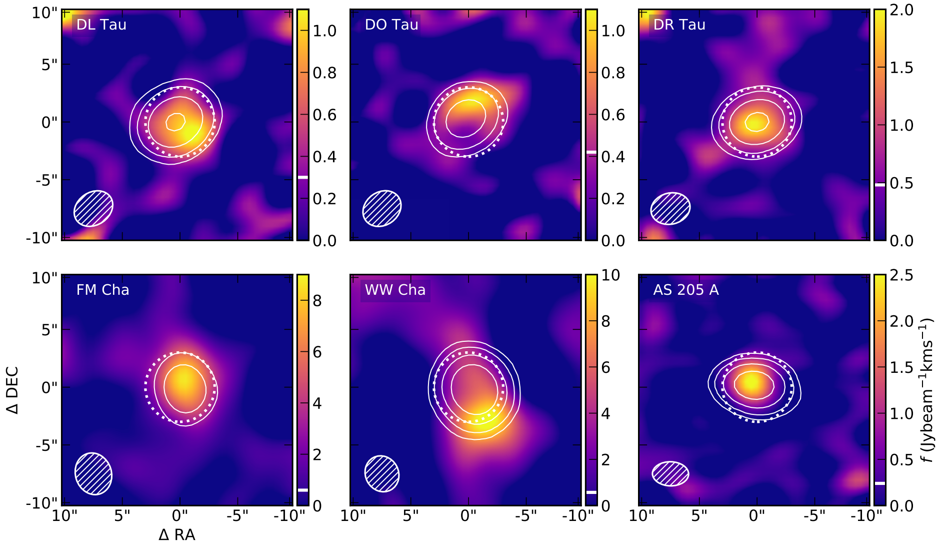

Figure 2.2: Moment zero maps of the [C I] $J = 1 - 0$ emission. Solid white contours show the 0.61 mm continuum at 10, 30, 100, 300 σ respectively. The dashed white contour indicates the region used to extract a spectrum. Beam sizes are shown in the lower left corner of each panel. The 3σ detection limit is illustrated as a white tickmark in the colorbar.

a spectral resolution of 122 kHz or 0.086 km s^{-1}. All disks are unresolved in the beam of the ACA, which is typically $3\farcs5 \times 2\farcs7$.

The selected sample was split into three observing groups, based on their position on the sky and the integration time that was needed to get to the required sensitivity. The sources in Taurus were observed in seven different executions for ~1 – 2 hours integration time per source, the sources in Chamaeleon in five different executions for ~2.5 hours integration time per source and AS 205 A in two different executions for 37 minutes in total. Full details of the observations and used calibrators are summarized in Table 2.A.1.

2.2.2 Data analysis

The data were reduced with the standard ALMA pipeline in `CASA` (McMullin et al. 2007). The sources in Taurus and AS 205 A were calibrated using `CASA` v5.1.1, the sources in Chamaeleon were calibrated with `CASA` v5.4.0. Self-calibration was performed on one of the continuum spectral windows of the combined executions, except for the sources FZ Tau and FM Cha that have a very weak continuum emission (see Table 2.3). The self-calibration tables were then applied to the line SPWs. For the sources that have high enough S/N to apply self-calibration, this procedure provided an improvement in continuum image quality of 50–100% and improved the line peak S/N by ~ 10%. In order to gain S/N in the [C I] $J = 1 - 0$ line, especially for the sources with weak line emission, we rebinned the Measurement Set using the `cvel2` command in `CASA`, reducing the velocity resolution by a factor of ∼2 to 0.15 km s^{-1}.

Table 2.2: Molecular transitions presented in this paper.

Transition	ν (GHz)	E_u (K)	A_{ul} (s^{-1})
[C I] $J = 1 - 0$	492.1607	23.6	7.88×10^{-8}
^{13}CO $J = 2 - 1$	220.3987	15.9	6.08×10^{-7}
^{13}CO $J = 3 - 2$	330.5880	31.7	2.19×10^{-6}
$C^{18}O$ $J = 2 - 1$	219.5604	15.8	6.01×10^{-7}
$C^{18}O$ $J = 3 - 2$	329.3306	31.6	2.17×10^{-6}

Notes. The frequency, energy levels and Einstein A values are adopted from the CDMS database (Müller et al. 2005).

The continuum is subtracted in the uv-plane after deselection of the channels with line emission based on the dirty image. All sources, except FZ Tau where no [C I] $J = 1 - 0$ emission was detected, were imaged using the `tclean` task in `CASA` with Briggs weighting and a robust factor of 0.5. The choice of this robust factor is a trade-off between high sensitivity for the weak lines and a small beam to maximize the ability to discriminate between disk and cloud emission. The emission and absorption features were masked during the imaging procedure using hand-drawn regions in each channel. The line spectra were extracted using a circular mask with a radius of 2″.5, centered on the continuum peak, and are plotted in Fig. 2.1. Continuum fluxes, continuum RMS noise and the final beam size of each source are listed in Table 2.A.1. The disk component of the line flux of the [C I] $J = 1 - 0$ emission was selected based on the literature V_{lsr} values taken from CO emission (Table 2.1) and the modeling.

2.2.3 Complementary data

In addition to the [C I] mini-survey, we analyzed archival ALMA 12m array data of ^{13}CO and $C^{18}O$ emission for the three sources that we modeled and studied in more detail: DR Tau, DO Tau and DL Tau. The details of the different molecular transitions can be found in Table 2.2. The Band 6 CO $J = 2 - 1$ isotopologue data were observed as part of program 2016.1.01164.S (PI: G. J. Herczeg). Details of the data and initial calibration can be found in Long et al. (2019). The ^{13}CO and $C^{18}O$ $J = 2 - 1$ is imaged using natural weighting, with a typical beam-size in the channel maps of 0″.14 × 0″.11 at a velocity resolution of 0.2 km s^{-1}. Spectra were extracted using a circular aperture with a radius of 1″.5 for DL Tau and DR Tau and 1″ for DO Tau.

For DR Tau, we included additional Band 7 CO $J = 3 - 2$ isotopologue data, as part of program 2016.1.00158.S (PI: E.F. van Dishoeck). This data set was calibrated using `CASA` v4.7.3. After the standard pipeline calibration, we performed self-calibration on the continuum and applied the gain solutions to the line channels. The beam-size in the final images is 0″.24 × 0″.20 at a velocity resolution of 0.055 km s^{-1}. Self-calibration on the continuum reduced the noise by a factor of 2 to 0.13 mJy/beam. The total source integrated continuum flux is 333.7 ± 0.2 mJy. The spectrum is extracted using a circular aperture with a radius of $2''$.

2.3 Observational results

Six out of the seven sources are detected in [C I] with high confidence. All spectra are presented in Fig. 2.1. Emission is seen to be within −2 and 2 km s^{-1} for the sources in Taurus and AS 205 A and within −4 and 4 km s^{-1} in the sources in Chamaeleon I. Therefore, we use all channels with a flux density above zero within these limits to construct the moment 0 maps as shown in Fig. 2.2. The integration limits for each source are given in Table 2.3. In most sources where [C I] emission is detected, the emission is either extended or suffers from foreground absorption. Integrated line fluxes, as well as the disk contribution, are listed in Table 2.3. In the forthcoming section, we describe the emission of each source separately.

DR Tau is a relatively young source (0.9 Myr, McClure 2019, see Table 2.1) with a compact, almost face-on disk (dust $R_{\rm out}$ = 54 au, $i = 5.4^{\rm o}$, Long et al. 2019), that has no signs of structure in the millimeter continuum emission image (Long et al. 2019). In the [C I] $J = 1-0$ spectrum, we can identify three different emission components. One emission peak, centered at the cloud velocity, is emission associated with the disk. This emission is single-peaked, as expected on the basis of the low inclination. The disk component is spaced over five channels, which means that the emission is spectrally resolved. The disk has an integrated line flux of 0.92 ± 0.16 Jy km s^{-1}.

On the redshifted side (centered at 0.7 km s^{-1}) of the [C I] $J = 1-0$ spectrum, we detect an additional emission component from a stream of material that is likely infalling. We discuss this extra component further in Sect. 2.5. Some additional emission is observed on the blueshifted side of the spectrum. The [C I] channel maps at this velocity show small extended emission and absorption features (see Fig. 2.D.3), but the spatial resolution is insufficient to see clear structure in the emission.

DO Tau is a 2 Myr old source (see Table 2.1) that harbors a compact dust disk with an outer radius of 37 au and an inclination of 27.6°, without any substructure in the millimeter continuum emission image (Long et al. 2019). This source has a clear detection in [C I] $J = 1-0$, with two peaks separated by an absorption feature at cloud velocity. This absorption feature can be caused by the presence of extended emission in the data beyond the maximum resolvable scale of the interferometer, foreground cloud absorption or a combination of both. The redshifted non-Keplerian emission centered at 1.5 km s^{-1} is connected with extended emission in the channel maps that appears to be co-located with the blueshifted part of the pole-on outflow observed in ^{12}CO (Fernández-López et al. 2020), as illustrated in Appendix 2.B. The moment zero map of DO Tau shows very little emission, due to mostly the foreground cloud. For DO Tau we determine two different fluxes,

Table 2.3: Observed [C I] $J = 1 - 0$ line and continuum fluxes

Source	Total Line Flux (Jy km s^{-1})	Integration limits (km s^{-1})	Flux Disk Component (Jy km s^{-1})	Disk Peak S/N	Line Channel RMS (Jy)	Continuum Flux (mJy)	Continuum S/N
DL Tau	1.36 ± 0.10	-1.0 - 1.0	1.36 ± 0.10	5.59	0.18	889 ± 2.3	387
DO Tau	1.33 ± 0.14	-0.9 - 3.1	1.18 ± 0.10	7.79	0.19	529 ± 2.5	212
DR Tau	2.68 ± 0.16	-1.8 - 1.9	0.92 ± 0.16	4.57	0.23	1008 ± 2.6	388
FZ Tau	<0.87	-	-	-	0.21	51 ± 2.8	18
AS 205 A	3.42 ± 0.08	-2.1 - 2	3.42 ± 0.12	17.06	0.11	1793 ± 2.4	747
FM Cha	23.65 ± 0.20	-3.2 - 3.7	-	-	0.20	204 ± 2.8	73
WW Cha	30.27 ± 0.19	-3.6 - 3.4	-	-	0.18	2662 ± 2.4	1109

Notes. All uncertainties are given as 1σ, upper limits are given as 3σ. Peak S/N is given for the disk component, line RMS is given for the final images over a frequency width of 0.15 km s^{-1}.

dealing differently with the absorption feature. The integrated emission of the disk contribution is 0.59 ± 0.10 Jy km s^{-1}, masking the absorption feature. Assuming a constant flux of 0.6 Jy at velocities where we observe cloud absorption results in an integrated flux of 1.18 ± 0.10 Jy km s^{-1}. The latter approach is more useful in the modeling and is justified based on our modeling and the clean line profiles of the other two sources that have an inclination similar or higher than DO Tau (AS 205 A and DL Tau).

DL Tau is an old source (7.8 Myr, McClure 2019, we discuss its age more specifically in Sect. 2.6.2) and has a large continuum disk with a 95% effective radius of 147 au, an inclination of 27.6° and three dust rings (Long et al. 2018). On-source [C I] emission is detected without any signs of extended emission in the clean channel maps (see Fig. 2.D.1). The spectrum reveals a slightly asymmetric double-peaked Keplerian profile, with the blueshifted peak slightly brighter than the red-shifted emission. The integrated line flux of DL Tau is 1.36 ± 0.10 Jy km s^{-1}. Although the source has a large dust disk, no CO isotopologue emission is detected, suggesting that this source is highly depleted in CO.

FZ Tau is a 0.9 Myr old source (see Table 2.1) with a small (∼10 au Piétu et al. 2014) dust disk and an inclination of $< 70°$. FZ Tau has no detected [C I] $J = 1 - 0$ emission, but does show a similar absorption feature as DO Tau. The angular distance between FZ Tau and DO Tau is small (2.3°), which means that the observed absorption is probably extended cloud absorption. The most likely reason for the non-detection is the small disk size (∼10 au based on the continuum Piétu et al. 2014). FZ Tau has strong near-infrared permitted C^0 emission (McClure 2019) that requires a large enough gas-rich hot region interior to the dust sublimation radius and sufficient UV to photodissociate CO. Unfortunately, the beam dilution is too large to detect the [C I] emission tracing the outer disk using ACA.

WW Cha is a 6.4 Myr old source (see Table 1) with a 135 au structured dust disk at an inclination of 37.2° (Kanagawa et al. 2021). WW Cha has a [C I] spectrum with a classic P-Cygni profile, indicative of an outflow, consisting of a broad intense emission feature on the redshifted side of the spectrum together with a narrower and a weaker absorption feature in the blueshifted emission. Besides the outflow we detect a disk component near the cloud velocity and a ridge of infalling material on the blueshifted side of the spectrum (see also the channel maps in Fig. 2.D.6). The source is known to have a jet (Robberto et al. 2012) and lately confirmed, using VLTI, to be a close binary with a separation of 1.01 au (Anthonioz et al. 2015; GRAVITY Collaboration et al. 2021). The P-Cygni profile could be the result of an outflow caused by the binary interactions with the disk.

FM Cha is 5.3 Myr old source (see Table 1) that harbours a 82 au dust disk at an inclination of 51° (Hendler et al. 2020). FM Cha has a firm detection in [C I] $J = 1 - 0$ with two asymmetric peaks in the spectrum on either side of the systemic velocity. The [C I] line in FM Cha is much broader than in AS 205 A, which we add in grey in Fig. 2.1 for reference, even though both disks have a similar inclination. Most of the emission is extended, contaminated cloud emission at high velocities (> 1 km s^{-1}) relative to the local standard of rest. Although we observe some hints of Keplerian emission close to the source velocity, we cannot constrain the disk contribution in the emission due to the low spatial resolution of the [C I] observations.

AS 205 A is a binary system with a large, 53 au, dust disk to the north (AS 205 N) that is with an inclination of 20.1° relatively face-on, and a small, 24 au, dust disk to the south (AS 205 S) that is inclined at 66.3° (Kurtovic et al. 2018). The system shows a lot of substructures in CO, due to gravitational interaction between the two systems. The distance between the two disks is $1.3''$, which means that the binary system is unresolved in the beam of our observations. The neutral carbon emission is singly peaked, centered on the systemic velocity of the largest disk AS 205 N. The systemic velocity of the secondary star is offset by -2.5 km s^{-1} in CO (Kurtovic et al. 2018), as indicated in Fig. 2.1. There is no significant emission detected at this relative velocity, which means that AS 205 S is not detected and that it is reasonable to assume that all the observed emission comes exclusively from AS 205 N.

Concluding, four disks out of the seven targets have been detected in [C I] $J = 1 - 0$ in this study. In the following we describe the modeling of the three Taurus disks in the sample for which the [C I] $J = 1 - 0$ emission can be easily decomposed. These three sources already have well-determined inner disk C abundance in the literature, which makes them more suitable to study the radial profile of the carbon abundance.

2.4 Description of the modeling

The aim of our modeling was to develop a physical disk model tailored to each source that describes both the dust and the gas structure in each disk. Using this model, we could then determine the volatile carbon abundance in the outer disk by comparing the flux in the [C I] $J = 1 - 0$ observations with a grid of models varying carbon and oxygen abundances. In order to determine the physical structure of the disks, we combined information from the spectral energy distribution (SED) and the outer radii of the disks in ALMA millimeter continuum and CO observations. Although the model may not be unique, it constrains a structure that agrees well with the observations. See Kama et al. (2016a) for a detailed overview of the impact of changes in variables of the physical disk model on the line flux in [C I] $J = 1 - 0$.

The azimuthally symmetric physical-chemical model DALI (Dust And LInes; Bruderer et al. 2012; Bruderer 2013) is used to model the sources using a smooth parameterized gas and dust disk density structure, neglecting all azimuthal substructures, gaps and rings seen in the dust. DL Tau is known to have multiple gaps in the millimeter continuum (Long et al. 2018), but the influence of the millimeter dust on the gas temperature in the outer disk is small (see e.g., Facchini et al. 2018; van der Marel et al. 2018; Alarcón et al. 2020), so it is safe to use a smooth disk density profile to determine the gas temperature and chemistry in the outer disk. Both DO Tau's and DR Tau's disk are smooth in the millimeter dust. DALI first solves the radiative transfer of the continuum based on a dust density structure (Sect. 2.4.1) and an input external radiation field (Sect. 2.4.2) to determine the dust temperature and radiation field from UV to millimeter wavelengths at all locations in the disk. After that, the heating-cooling balance of the gas is solved simultaneously with steady state chemistry in an iterative sequence until convergence is reached. Once the solution is converged, we ray-trace the model in continuum and molecular lines using non-LTE radiative transfer (Sect. 2.4.4).

2.4.1 Disk parameters

The density structure of our model is fully parameterized and is based on a full disk, without inner cavity. We used the standard form of the dust surface density profile of a power law with an outer exponential taper:

$$\Sigma_{\rm dust} = \Sigma_{\rm c} \left(\frac{r}{R_{\rm c}}\right)^{-\gamma} \exp\left[-\left(\frac{r}{R_{\rm c}}\right)^{2-\gamma}\right], \tag{2.1}$$

defined by the surface density $\Sigma_{\rm c}$ at the characteristic radius $R_{\rm c}$, and assuming an initial power-law index $\gamma = 1$. The scale height h at distance r is given by

$$h = h_{\rm c} \left(\frac{r}{R_{\rm c}}\right)^{\psi}, \tag{2.2}$$

defined by the scale height $h_{\rm c}$ at the characteristic radius with a flaring index ψ. The dust was split into two populations, following the approach of D'Alessio et al. (2006), a small dust population which ranges from 0.005 to 1 micron and a large dust population which ranges from 0.005 to 1000 micron. The vertical structure of the small dust grains is

$$\rho_{\rm d,small} = \frac{(1-f)\Sigma_{\rm dust}}{\sqrt{2\pi} r h} \exp\left[-\frac{1}{2}\left(\frac{\pi/2-\theta}{h}\right)^2\right], \tag{2.3}$$

where f is the mass fraction of the large grain distribution, assumed to be 0.99, and θ is the opening angle from the midplane as seen from the central object. The large grains are settled with respect to the full disk height with a factor $\chi \in (0, 1]$, following the same distribution as the small grains (Eq. 2.3) but with f replacing $(1-f)$ and $\chi \times h$ replacing h. The radial distribution of the two dust grain populations is the same, excluding grain evolution processes. The gas density distribution is scaled up from the dust density distribution using the ISM gas-to-dust ratio of 100. The vertical gas structure follows the distribution of the small grains, preserving the global gas-to-dust ratio. We make an initial estimate of the sublimation radius in the disk using Equation 14 in Dullemond et al. (2001). By assuming a dust sublimation temperature of 1500 K, negligible self-irradiation ($H_{\rm rim}/R_{\rm rim}$ «1), and solar units for the luminosity, Equation 14 reduces to $r_{\rm subl}$ [au] $= 0.07$ $(L[L_\odot])^{1/2}$ (see also Monnier & Millan-Gabet 2002). For DO Tau we increased this result to 0.14 au to match the mid-infrared emission from the inner disk, similar to the value found for the Brγ area for DO Tau as determined in Eisner et al. (2014).

2.4.2 Stellar parameters

The stellar spectra are approximated by a perfect blackbody defined by the effective temperature ($T_{\rm eff}$) of each star with an additional component due to accretion, assuming an accretion temperature of 10,000 K of the emitting radiation, using

$$L_{\rm acc}(v) = \pi B_v\left(T_{\rm acc}, v\right) \frac{GM_*\dot{M}}{R_*}\frac{1}{\sigma T_{\rm acc}^4}. \tag{2.4}$$

The observed far infrared luminosity of the sources (Yang et al. 2012) agree within an order of magnitude with this first order approximation.

The properties of all modeled stars are taken from McClure (2019), which uses the procedures from McClure et al. (2013) to derive self-consistent stellar and accretion parameters. We included a X-ray luminosity of 10^{30} erg s^{-1} at a X-ray plasma temperature of 7×10^7 K, and a cosmic ionization rate of 5×10^{-17}s^{-1} incident on the disk surface.

2.4.3 Chemical network

The standard chemical network adopted in DALI is based on UMIST06 (Woodall et al. 2007). This chemical network includes neutral and charged PAHs, 109 molecular species and 1463 reactions. The code includes two-body interactions, freeze-out, photodissociation and -ionization, and thermal- and photo-desorption. There are no grain surface reactions considered, except for the hydrogenation process. It is reasonable to assume that this has no impact on the species that are used in this paper, which trace the atmospheric layers of the disk. For DR Tau and DO Tau we include the full treatment of CO freeze-out and isotope selective processes as described by Miotello et al. (2014, 2016). We adopt fiducial ISM gas-phase elemental carbon and oxygen abundances of C/H = 135 ppm and O/H = 288 ppm, respectively. These values are close to the median abundances observed in translucent interstellar clouds (Cardelli et al. 1996; Meyer et al. 1998; Parvathi et al. 2012) and consistent with the solar values within a factor of a few (Asplund et al. 2009). See Bruderer et al. (2012) for a full justification of these fiducial abundances. In order to make the carbon abundances easy to interpret, we define a carbon depletion factor ($f_{\rm depl}$) as $({\rm C/H})_{\rm ISM}/({\rm C/H})$. When changing the carbon abundance we vary the oxygen abundance such that the C/O ratio stays at the ISM level of 0.47, unless specified differently. Without a similar depletion of oxygen w.r.t. carbon, the neutral atomic carbon abundance would be more strongly dependent on the elemental carbon abundance, as there would be more oxygen available to create CO.

2.4.4 Radiative transfer

After the chemical network has converged to a steady state equilibrium and gas temperature solution, atomic and molecular transitions can be imaged using the ray-tracer in DALI which includes the radiative transfer. The excitation of the line is determined explicitly in a non-LTE fashion, using the collision rate coefficients from the LAMDA database (Schöier et al. 2005; van der Tak et al. 2020). In this step, the sources are projected on the sky using the observed distance, inclination, and position angle given in Table 2.1 and Table 2.4, respectively. For comparison with our observations, we convolved the model with a Gaussian beam with the same shape as the beam of the ALMA observations.

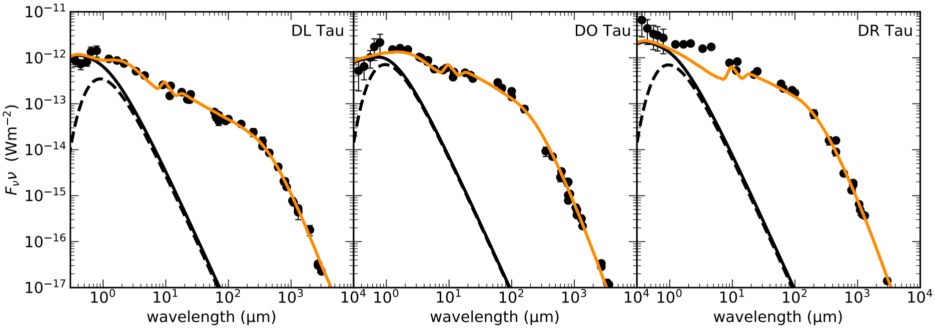

Figure 2.3: SEDs of the three modeled sources with our model fit in orange. The black dots with errorbars represent observations, the dashed black curve denotes the stellar component, the solid black curve is a combination of the stellar component and the UV excess due to accreting material as used in the modeling.

2.4.5 Fitting procedure

In the fitting procedure, we followed a similar approach as Bruderer et al. (2014), creating a physical model that fits the SED through consecutive parameter value refinements, until they converge to a model that is best representative of the source. Using a χ^2 or Markov chain Monte Carlo (MCMC) method was not possible because of the long computation time of the continuum radiative transfer. We used the same characteristic radius (R_c), inclination (i) and position angle (PA) for the gas as observed in high angular resolution dust continuum observations. The gas disk can be significantly larger than expected from millimeter continuum observations if radial drift and grain growth are important in the disk (Facchini et al. 2017; Trapman et al. 2019), but for the sake of simplicity we do not include dust evolution in our modeling. The high spatial resolution sub-millimeter continuum constrains the mass, the characteristic radius (R_c), the inclination (i) and the position angle (PA) of the dust in the disks. Additionally, we look at the spectral line profiles of the CO isotopologue and [C I] emission to further constrain the density and temperature structure of the disks. These properties together constrain Σ_dust, γ, χ, f, h_c and ψ.

2.4.6 Main sources of uncertainty

We stress that the gas phase carbon abundances found in the modeling analysis are subject to a few uncertainties. First, we assume a smooth disk with a system averaged elemental volatile carbon depletion. It is thought that most CO processing preferentially occurs at the deepest, coldest layers (Bosman et al. 2018), while the tracers that we analyze, such as CO and C^0 are known to trace the atmospheric layers of the disk ($z/r > 0.2$ Bruderer et al. 2012). Therefore, both radial and vertical dependence in $(C/H)_{\rm gas}$ can cause discrepancies in the abundance found in the system averaged CO isotopologue and [C I] emission. Based on the carbon abundance measured in the upper layers of the disk, we infer that the bulk of the disk can be depleted in carbon, which is a result from efficient mixing by turbulence. Additionally, abundances of carbon carrying molecules depend on the elemental oxygen abundance in the disk, since an excess in carbon atoms can shift the balance between CO_2, CO, C, and hydrocarbon abundances. Elevated C/O ratios are not uncommon in disks and can arise by a stronger depletion of oxygen, because of freeze-out and processing of CO_2 and H_2O rather than CO (which has been inferred directly from water observations, see Bergin et al. 2010; Hogerheijde et al. 2011; Du et al. 2017) or direct photo-ablation of carbon rich grains (Bosman et al. 2021b). We assumed ISM C/O ratio where possible and discuss a potential elevated C/O ratio in Sect. 2.5.2.

Second, there is an uncertainty in the $(C/H)_{\rm gas}$ found in these three systems, resulting from the uncertainty in the modeling parameters. The biggest sources of uncertainty are the disk mass, $R_{\rm c}$ and the gas-to-dust ratio (Kama et al. 2016a). There are no HD observations of the sources in our sample, which means that there is high uncertainty on the gas disk mass and the gas-to-dust ratio. Based on the few sources that are observed in HD, we do not have reasons to assume that the gas-to-dust ratio in the bulk of the disk is much different from the ISM value of 100 (McClure et al. 2016; Bergin et al. 2016). Kama et al. (2016a) show that an underabundance of gas-phase carbon by an order of magnitude, such as found here, cannot be easily masked by a choice of parameters. Larger depletions will be even more reliably identified.

2.5 Modeling results

Our best-fit results to the SED for the dust density structure are presented in Figure 2.3. All data points in the SEDs are dereddened using the CCM89 extinction curve (Cardelli et al. 1989) for sources with $A_V < 3$ (DR Tau and DL Tau). For DO Tau we used the extinction curve for $0.3 \leq A_k < 1$ from McClure (2009) to correct the emission at wavelengths shorter than 25 micron. This source has $A_{\rm V} = 3.6$ mag (McClure 2019, see Table 2.1), more than the range over which the CCM89 extinction curve is accurate. Reasonable fits are found for the SED, including spatial information from the sub-millimeter continuum. The inferred disk gas masses (Table 2.4) are within a factor of a few of the estimated disk mass based on multi-wavelength continuum observations and assuming a gas-to-dust ratio of 100. See for example Kwon et al. (2015) for DL Tau ($4.1 \pm 0.5 \times 10^{-2}$ $M_\odot$) and DO Tau ($1.4 \pm 0.1 \times 10^{-2}$ $M_\odot$), and Tazzari et al. (2016) for DR Tau ($1.4 \pm 0.4 \times 10^{-2}$ $M_\odot$).

The mid-infrared part of the SED of DR Tau is underestimated by the best representative model. Varying $h_{\rm c}$ between $0.05 - 0.3$, ψ between $0.05 - 0.2$ and $R_{\rm subl}$ between $0.05 - 0.3$ au, we find no plausible configuration of the parameters

Table 2.4: Model parameters

	DL Tau	DO Tau	DR Tau
$R_{\rm subl}$ (au)	0.06	0.13	0.074
γ	1.0	1.0	0.5
χ,f	0.7, 0.99	0.6, 0.99	0.5, 0.99
$R_{\rm c}$ (au)	112.2	34	52
$\Sigma_{\rm c}$ (g cm^{-2})	10	17	20
$h_{\rm c}$,ψ	0.14, 0.07	0.2, 0.14	0.135, 0.1
$\Delta_{\rm gas/dust}$	100	100	100
Gas mass (M$_\odot$)	8.9×10^{-2}	1.4×10^{-2}	2.5×10^{-2}
$L_{\rm X}$ (erg s^{-1})	10^{30}	10^{30}	10^{30}
$T_{\rm X}$ (K)	7.0×10^{7}	7.0×10^{7}	7.0×10^{7}
ζ_{cr} (s^{-1})	5.0×10^{-17}	5.0×10^{-17}	5.0×10^{-17}
i (deg)	45	27.6	5.4
PA (deg)	52.1	170	3.4

Notes. Inclination and position angle of the sources are adopted from high resolution millimeter continuum observations (Long et al. 2019).

that agrees with the inner disk contribution of the SED <10 micron. The strong mid-infrared excess in the SED could be caused by an inner disk gas component that is optically thick to its own radiation, producing continuum emission. Evidence for a gas contribution to the continuum interior to the dust sublimation radius in similar systems can be found in many studies (see e.g., Kraus et al. 2008; Malygin et al. 2014; Lazareff et al. 2017). Since we focus on outer disk tracers, we do not expect the accreting gas column to have a strong influence on the results. Note that our lack of a fit of the inner disk's contribution to the continuum increases the model parameter space for fitting the SED at longer wavelengths.

Figure 2.4 presents the results of the total [C I] $J = 1 - 0$ line flux as function of the elemental gas phase carbon abundance for the three models. Observations are presented as black stars with their corresponding depletion factor and uncertainty in the figure legend. Model carbon abundances are presented as dots at depletion factors of [1, 3, 10, 30, 100, 300]. The derived depletion factor of the sources is the interpolation of the connecting curves with the error set by the measurement error on the [C I] $J = 1 - 0$ flux. A decrease by a factor of ten in the elemental C abundance results typically in a factor of three in the total line flux. The CO emission and spectra will be discussed source individually in the forthcoming sections.

2.5.1 DR Tau: moderate depletion of carbon and oxygen

The results of the line emission fit of DR Tau are presented in Fig. 2.5 for the best-fit model with a carbon depletion factor of 5. A map of the surface brightness of the ^{13}CO $J = 3 - 2$ transition is presented in Fig. 2.6. Using least squares fitting, a Gaussian disk component with an additional Gaussian component centered at

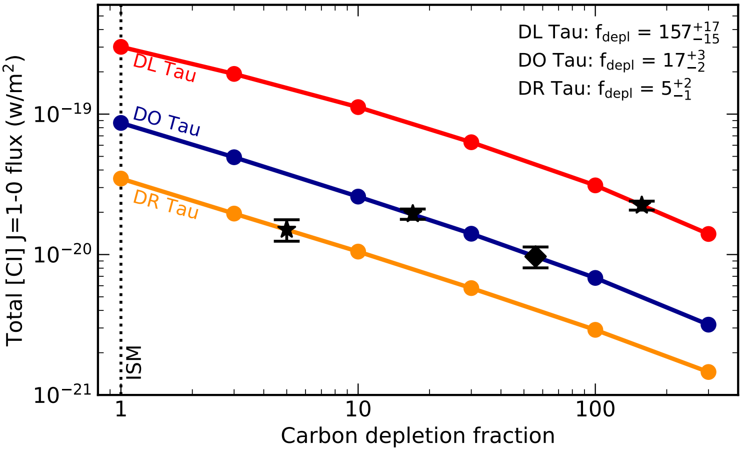

Figure 2.4: The modeling results of the total flux as function of the carbon depletion factor defined as $f_{\mathrm{depl}} = (\mathrm{C/H})/(\mathrm{C/H})_{\mathrm{ISM}}$. Observations are plotted at the interpolated carbon depletion fraction. For DO Tau we plot two values for the total flux, the star is the corrected flux for absorption with a constant value, the diamond is only masked for absorption as discussed in the main text. The derived carbon depletion fraction by interpolation with the model is presented in the top-right corner with errors given by measurement uncertainty of the [C I] observations.

0.7 km s^{-1} accounting for the non-disk emission is fitted to the [C I] and ^{13}CO $J = 3 - 2$ spectra to determine the disk contribution.

The low ratio between the [C I] and CO isotopologue fluxes of the disk could only be explained by assuming $\gamma < 1$. Decreasing γ in the model results in a sharper exponential cut-off from the surface density, which affects the emitting region of the [C I] emission more than the CO emitting layer. Following the approach described in Miotello et al. (2018), we fitted the slope of the emission in the so-called pivot-region of the ^{13}CO and C^{18}O emission where the line is optically thin, but has enough column density to efficiently self-shield against isotope selective processes. We find $\gamma = 0.5$ and $\gamma = 0.8$ for the ^{13}CO and C^{18}O radial intensity profiles, respectively. In the modeling we used $\gamma = 0.5$, which value is consistent with theoretical values for a viscously heated disk (Chambers 2009).

The C^{18}O fluxes together with [C I] provide the strongest constraints on $(\mathrm{C/H})_{\mathrm{gas}}$. Therefore, we include the isotopologue-selective photodissociation of CO (Miotello et al. 2014, 2016), which prevents underestimating $(\mathrm{C/H})_{\mathrm{gas}}$ or the gas mass. We adopt ISM-like ^{13}C and O^{18} abundance ratios of 1.753 ppm and 0.5143 ppm with respect to H (Wilson 1999). A model with (C/H) = 27 ppm, or a depletion factor of 5, reproduces the [C I] emission and most CO isotopologue lines. It overproduces the ^{13}CO $J = 2 - 1$ line by a factor of 3. The modeling suggests similar radial emitting regions for both CO transitions. Using the peak ratio between the ^{13}CO and C^{18}O $J = 2 - 1$ spectra we determine the opacity

Figure 2.5: Emission line profiles of ^{13}CO $J = 2-1$, ^{13}CO $J = 3-2$, C^{18}O $J = 2-1$, C^{18}O $J = 3-2$, and [C I] $J = 1-0$ for DR Tau, with the best fitted model overlaid in color. 1σ error bars are indicated in grey for each spectrum. The data and models of the weak CO isotopologue $J = 2-1$ transitions have been multiplied by a factor of 5 for visualization purposes.

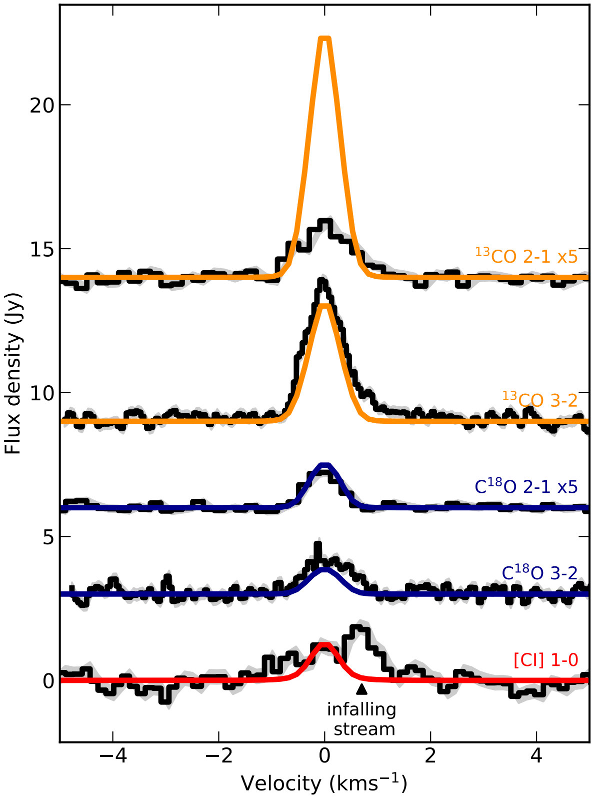

of the line and the corresponding kinetic temperature using Eq. 1 and Eq. 2 from Schwarz et al. (2016). The peak ratio between the two CO isotopologue transitions is only 1.45, while a ratio of 8 is expected based on the ISM abundances of ^{13}C and ^{18}O. This results in an opacity of 9.4 and a temperature of the emitting layer of 42 K. A similar analysis for the CO $J = 3-2$ isotopologue transition results in a peak ratio of 2.85, an opacity of 3.3 and a kinetic temperature of the emitting layer of 30 K. The reason why CO $J = 2-1$ emission seems to be much more optically thick, even though it has a much lower Einstein A coefficient, could be the lack of short spacing in the uv-plane which means that the data is not sensitive to large scale structures that are expected to be more dominant in ^{13}CO than in C^{18}O emission. In depth analysis of the temperature structure of the disk is beyond the scope of this paper. We discuss the CO isotopologue emission and the methods used to constrain γ in more detail in Appendix 2.C.

The best-fit carbon and oxygen abundances are found to be 2.7×10^{-5} and 5.76×10^{-5} which corresponds to a carbon and oxygen deficiency of a factor of 5^{+2}_{-1}. The analysis of the photospheric abundance and the corresponding depletion factor found in the inner disk of DR Tau is 13^{+8}_{-4} (McClure 2019). The low abundance in the inner disk in comparison with the outer disk is consistent with radial trapping of carbon-rich ices beyond the CO snowline. We return to this in Sect. 2.6.

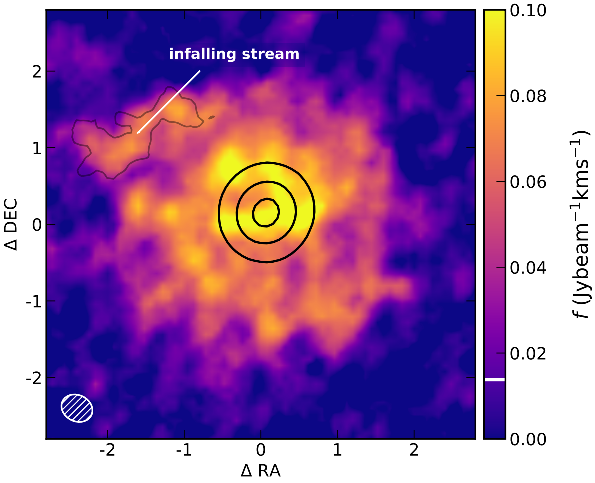

Figure 2.6: Total intensity or moment 0 map of the ^{13}CO $J = 3-2$ emission in DR Tau. The black contours show the continuum emission at 0.8 mm. The grey contours show the residuals after subtracting an azimuthally averaged radial disk profile to highlight the infalling stream. The beam size is shown in the lower left corner.

The non-Keplerian, redshifted emission that is observed in both the [C I] $J = 1-0$ and ^{13}CO $J = 3-2$ spectrum at a velocity of 0.7 km s^{-1} originates likely from the circum-disk material that is also visible in the moment 0 map of the ^{13}CO emission to the northeast (indicated in Fig. 2.6). The high [C I]/^{13}CO $J = 3-2$ flux ratio of this feature suggests that the emission is coming from material that is elevated above the disk surface and thus exposed to a high UV flux. The contaminating material is confined to a single velocity, is not kinematically connected to the disk and may be linked with the late infalling material seen in scattered light observations (Mesa et al. 2022). The C^{18}O $J = 3-2$ line is slightly broader than expected, likely caused by contamination with the same accreting material, but here we do not try to make a two-component fit. Increasing the C/O ratio in a similar manner to our treatment of DO Tau in Sect. 2.5.2 could improve the fit to the ^{13}CO $J = 2-1$ spectrum. However values of up to 3 are insufficient to fit the observed line flux. Furthermore, this would affect the higher S/N ^{13}CO $J = 3-2$emission as well, which is reasonably matched by models with the local interstellar standard C/O.

2.5.2 DO Tau: moderate depletion of carbon and oxygen

The data and best representative modeled spectra for DO Tau are illustrated in Fig. 2.7. We neglected the redshifted excess > 1 km s^{-1} which is associated with a pole-on outflow, as explained in the observation section and illustrated in Appendix 2.B.

The ^{13}CO $J = 2-1$ line is optically thick, with a ratio of 2 with respect to the total C^{18}O $J = 2-1$ flux, while a ratio of 8 is expected based on the relative abundance of the two isotopes in the diffuse ISM. We present two models in Fig. 2.7, one with $f_{\rm depl} = 10$ and an ISM-like C/O ratio and one with $f_{\rm depl} = 20$ and an enhanced C/O ratio of 1. In the later model, oxygen is less abundant with respect to carbon than the first model. If oxygen is less abundant in the model, but the carbon abundance remains constant at ISM level, less CO reacts on the

Figure 2.7: Observations and modeling of DO Tau. Two models are shown, the dashed line is a model with ISM C/O ratio of 0.47 and a carbon depletion factor of 10, the solid line is a model with an enhanced C/O ratio of 1 and a volatile carbon depletion fraction of 20. 1σ errorbars are indicated in grey for each spectrum. The data and models of the ^{13}CO and C^{18}O $J = 2 - 1$ transitions have been multiplied by a factor of 5 and 20, respectively, for visualization purposes.

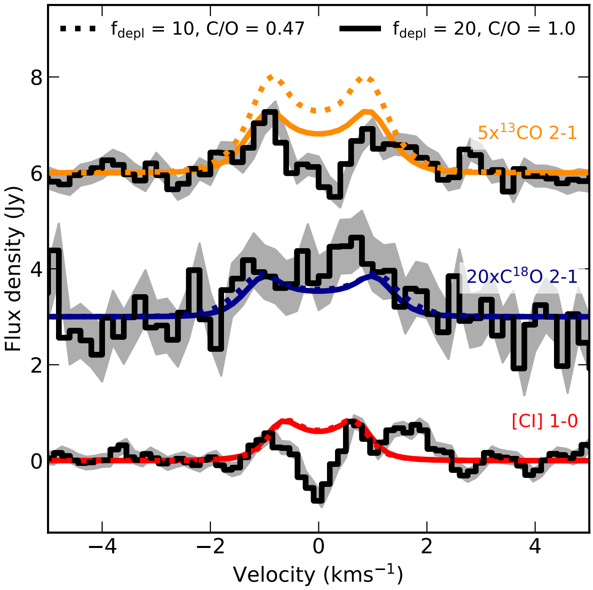

ice with OH to form CO$_2$ and H (e.g., Ioppolo et al. 2011), thus the total CO abundance increases. By using an increased C/O ratio there will be more carbon in atomic state, because there will be more CO in the atmospheric layers to be photodissociated in C^0 and C$^+$ and less oxygen to convert C back in CO. Since ^{13}CO is optically thick, changing the oxygen abundance does not change the total line flux of the model significantly. The best fitted C/O value based on the [C I] and CO isotopologue emission is ~1, which is about twice the ISM value.

C$_2$H can provide much stronger constraints on the C/O ratio than [C I] and CO, as it is predominantly formed in regions where C/O ratios are high (Bergin et al. 2016; Miotello et al. 2019; Bosman et al. 2021b). The observed upper limit of C$_2$H = 73 mJy km s^{-1} found by Bergner et al. (2019) is low compared to the other sources in their sample, and more consistent with C/O close to the ISM value. To prove this we ran an extended chemical model based on the chemical model from Visser et al. (2018) that includes C$_2$H and C$_2$H$_2$ chemistry using the same temperature and density structure as for the atomic carbon and CO emission. We find that for a C/O ratio of 1 and carbon depleted by a factor of 20 with respect to the ISM value, the C$_2$H flux would be 550 mJy km s^{-1}. An ISM-like C/O ratio of 0.47 and a carbon depletion fraction of 10 results in a total flux of 64 mJy km s^{-1}. C$_2$H traces regions in the disks that are closer to the star than [C I], which could mean that the discrepancy is caused by a radially varying C/O ratio in the disk. However, the systematic uncertainty of the models are too large to say anything conclusive about that, and full modeling of C$_2$H is beyond the scope of this paper. Deeper C$_2$H observations are needed to better constrain the C/O ratio. In the rest of this paper we use a C/H ratio that is 17^{+3}_{-2} times lower than the ISM value, set by the carbon abundance grid in Fig. 2.4.

Our carbon abundance in the outer disk of DO Tau is similar to, or higher, than the abundance in the inner disk, which is found to be depleted with gas-phase carbon by a factor of 22^{+20}_{-11} (McClure 2019). This radial pattern is consistent with retaining solids beyond the CO snowline. We return to this in Sect. 2.6.

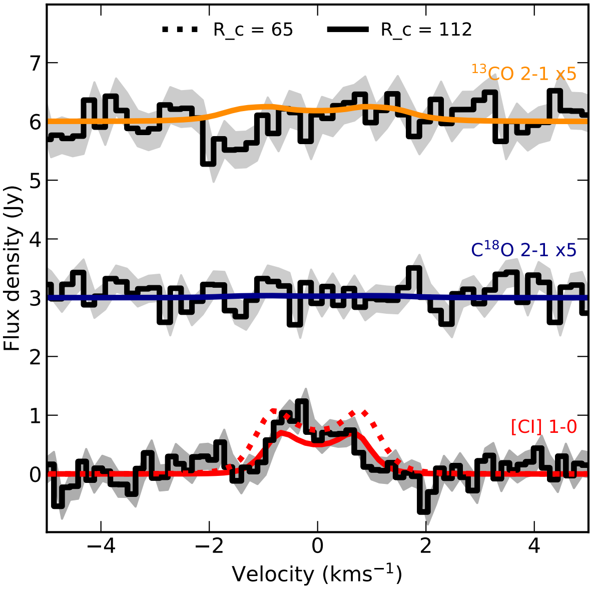

Figure 2.8: Observations and modeling of DL Tau. Two models are plotted, the solid line is a model with $R_c = 112$ au as observed in the dust, the dashed line as a model with $R_c = 65$, which fits the spatially resolved [C I] emission best. Further details can be found in the main text. 1σ errorbars are indicated in grey for each spectrum. The data and models of the weak CO isotopologue $J = 2-1$ transitions have been multiplied by a factor of 5 for visualization purposes.

2.5.3 DL Tau: severe depletion of carbon and oxygen

The data and best representative modeled spectra for DL Tau are illustrated in Fig. 2.8. The [C I] spectrum has a disk component that consists of a clean double-peaked Keplerian profile, without cloud contamination. The two CO isotopologue $J = 2 - 1$ lines are both upper limits, but the upper limits are low, so that they give additional constraints on the gas phase carbon abundance.

The best representative model for DL Tau has $R_c = 112$ au, similar to the value found for the dust disk (Kwon et al. 2015; Long et al. 2019). However, convolving the modeled [C I] emission with the same beam as the observations and comparing the azimuthally averaged radial profiles suggests that the radial extent is two times larger than the ACA beam of $\sim 3''$, while the observations appear as an unresolved point-source down to the same RMS level as the data. The most likely explanation to this dichotomy is that the emission in the outer parts of the disk is buried in the noise. To be consistent with the spatial information of the [C I] emission, we find that R_c has to be smaller than 65 au. The SED constrains the total mass, but does not set limits to R_c. The characteristic radius of the dust is 112 au (Kwon et al. 2015; Long et al. 2019), and the CO outer disk radius is 600 ± 150 au in SMA observations, which is consistent with $R_c = 112$ au. On top of that, a model with $R_c = 112$ au fits the [C I] $J = 1 - 0$ line profile better than a model with the same mass, but with $R_c = 65$ au (see Fig. 2.8). The line profile is, besides the disk mass distribution, also dependent on the mass of the star. There is some uncertainty on the masses of stars, based on their evolutionary track, but the stellar mass would have to be off by a factor of 2 – 3 to fit the Keplerian profile, which is beyond the usually assumed uncertainties for the stellar mass (Baraffe et al. 1998).

For the $R_\mathrm{c} = 112$ au model, we find a best fitting depletion factor of 157^{+17}_{-15}. If the disk were smaller, with $R_\mathrm{c} = 65$, DL Tau would still be depleted in carbon by a factor of 52^{+6}_{-8}. The high depletion value for DL Tau is consistent with the age of the source, as shown by chemical modeling of CO emission (Krijt et al. 2020). We return to this in Sect. 2.6.2. In order to put further constraints to the model for DL Tau and exclude that the disk is depleted in gas, resulting in a small outer gas radius, we need ALMA ^{12}CO and CO isotopologue data and high resolution [C I] observations with more sensitivity in the outer parts of the disk.

2.5.4 Systematic uncertainty

Additional models are presented for the three sources in which the most relevant disk parameters are varied in order to obtain an indication of the systematic uncertainty on the carbon abundance in the modeling, as discussed in their respective subsection. These additional models show that the carbon depletion factor can be trusted within a factor of 3, with the assumption that the gas-to-dust ratio is equal to the canonical value of 100. Kama et al. (2016a) showed how the C/H abundance systematically depends on a large number of other disk parameters, including the dust-to-gas ratio. They found that in the worst case scenario, when taking into account a possibly varying dust-to-gas ratio, the [C I] flux in a disk is robustly sensitive to carbon depletions of at least a factor of 10 in the outer disk. Therefore, we can conclude that the significant carbon depletions in DO Tau and DL Tau are robust to the systematic uncertainties. In contrast, the order of magnitude carbon depletion in DR Tau, while significant under our current model assumption of a gas-to-dust ratio of 100, could be consistent with the ISM carbon abundance if the full range of systematic uncertainties in the DALI models is taken into account.

2.6 Discussion

We present the first successful ALMA mini-survey of neutral carbon to constrain the elemental carbon depletion in the outer disk of a sample of seven T Tauri disks. Two sources in our sample, DR Tau and DO Tau, have moderate depletion of volatile carbon and oxygen in the outer disk, and one source, DL Tau, has severe depletion. The observed sources show two distinct radial carbon abundance behaviors: the moderately depleted sources have carbon abundances in the outer disk that are consistent with the inner disk, while the severely depleted source has a much higher carbon abundance in the inner disk than in the outer disk. This work strengthens the case that some sources are depleted in gas-phase carbon in the outer disk in addition to direct freeze-out and photodissociation of CO. Fig. 2.9 summarizes our results of the carbon abundance in the outer disk compared to the inner disk. We added TW Hya (Zhang et al. 2019; Kama et al. 2016b;

McClure et al. 2020), HD 163296 (Kama et al. 2015; Zhang et al. 2019) and HD 100546 (Kama et al. 2015, 2016b) and a combined point for ten Class 0/I sources (Harsono et al. 2014; Zhang et al. 2020b; Bergner et al. 2020) to the figure for reference. These three sources are the only other sources for which the carbon abundance is determined in both the inner disk and outer disk. For the Herbig Ae/Be stars we make the assumption that the composition of the stellar photosphere is representative of the accreting material in the inner disk, as in Kama et al. (2015).

2.6.1 Implications of the radial abundance profile

Almost all sources with observed elemental carbon abundances have a considerable increase in carbon abundance in the inner disk with respect to the outer disk, except for the two young and compact disks in our sample, DR Tau and DO Tau (see Fig. 2.9). Large dust grains, the formation of which causes gaseous carbon depletion, will eventually drift inwards towards the star, driven by the headwind of the gas that moves slightly sub-Keplerian due to the pressure support. With efficient drifting of dust grains and without any dust trapping, the carbon will be released inside the CO snowline. Any carbon that is processed into less volatile or refractory structures will ultimately sublimate at the dust sublimation rim. The inner disk gas (inside the dust sublimation rim) is constantly replenished with carbon-poor gas from the outer disk, which means that an enhancement there has to be a result of the sublimation of carbon-rich ices as a result of radial drift.

2.6.1.1 Dust traps

Strong pressure maxima and efficient planetesimal formation locations, incorporating the grains in larger bodies, can both stop the grains from radial drifting. DL Tau has three rings in the dust continuum observations that are located outside the CO snowline (Long et al. 2019). Sufficiently large dust grains will be trapped in the pressure maxima at the edge of these gaps, so that those grains remain in the outer disk, but trapped very locally, which means that the CO ice that has formed on these grains cannot efficiently return to the gas phase. The dust trapping in the pressure maxima that are observed in DL Tau are efficient enough to prevent a super-solar carbon abundance in the inner disk contrary to what is observed in the radial CO abundance profiles of other protoplanetary disks like HD 163296 (Zhang et al. 2019, 2020a). However, the fact that we see an enhancement in the inner disk with respect to the outer disk implies that either the traps are “leaky”, i.e., not 100% efficient at trapping dust, or that they formed in a later stage of the disk evolution, i.e., shorter time ago than the viscous time needed to accrete the material from the dust traps to the inner disk, or that carbon depletion mechanisms started later than the viscous time. The last option is unlikely as recent studies pointed out that volatile CO rapidly evolves during the Class I and early Class II stage (Zhang et al. 2020b; Bergner et al. 2020).

The formation of a perfectly efficient dust trap at the CO snowline would prevent depleted carbon in the form of CO ice from entering the gas interior to the CO snowline. However, before it is observable via the near-infrared lines used by McClure (2019) this depleted carbon would still need to viscously accrete from

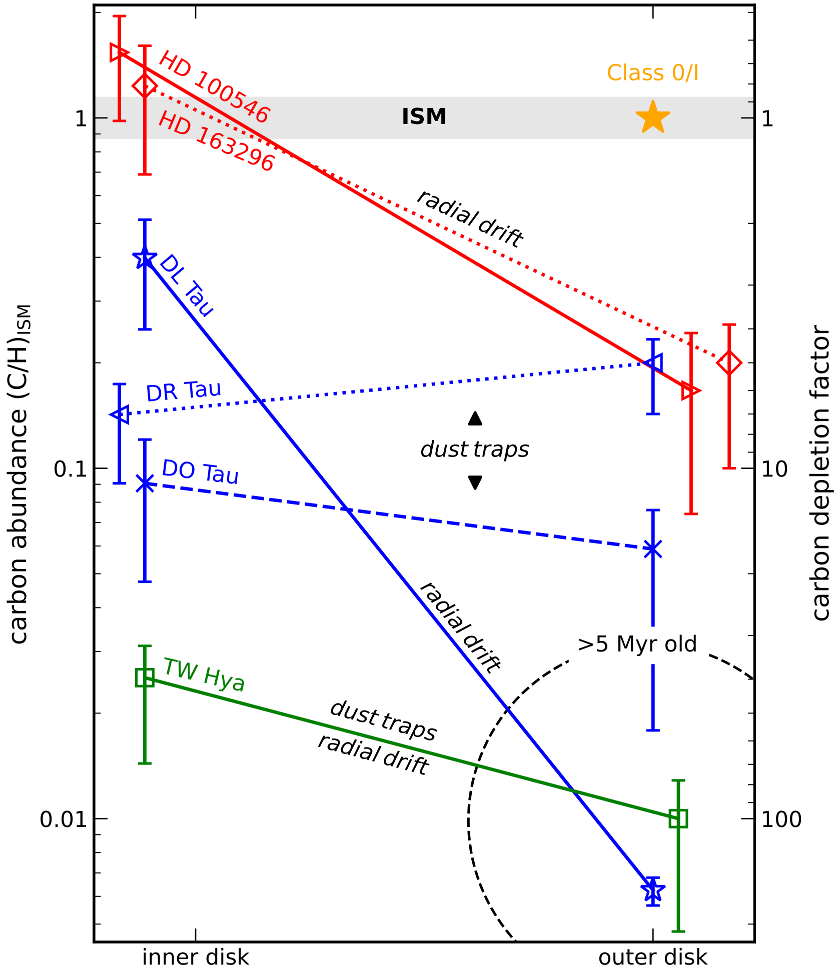

Figure 2.9: Radial profile of the volatile carbon depletion fraction based on one point inside the dust sublimation rim and a disk averaged carbon abundance in the outer disk. The outer depletion fractions of the sources in blue are from this work. Inner disk carbon abundances of these three sources are taken from McClure et al. (2020). We added TW Hya in green (Zhang et al. 2019; Kama et al. 2016b; McClure et al. 2020) and one point in the outer disk for ten Class 0/I sources in yellow (Harsono et al. 2014; Zhang et al. 2020b; Bergner et al. 2020) to illustrate the increase in the level of carbon depletion during the system's evolution. Two herbig Ae/Be stars, HD 163296 (Kama et al. 2015; Zhang et al. 2019) and HD 100546 (Kama et al. 2015, 2016b) are shown in red to complete the picture of carbon depletion that we have. These sources do not follow the evolutionary trend, because they are much warmer.

the CO snowline to ∼0.1 au on a timescale of:

$$t_{visc} = \frac{r^2 \Omega_{\mathrm{K}}}{\alpha c_{\mathrm{s}}^2} \tag{2.5}$$

with Ω_{K} the Keplerian angular velocity and c_{s} the sound speed in the midplane of the disk given by $\sqrt{k_{\mathrm{B}} T/(2.3 m_{\mathrm{p}})}$ with k_{B} the Boltzmann constant, T the midplane temperature, m_{p} the proton mass, and α the viscosity parameter (Shakura & Sunyaev 1973). The innermost gap outside of the CO snowline in DL Tau is located at ∼40 au, and the temperature at the midplane is provided by `DALI`. However, α is not determined directly for DL Tau and is subject to large uncertainty. Observational measurements of α from turbulent broadening of CO $J = 2-1$ emission lines range from $\alpha = 0.08$ in DM Tau to $\alpha < 0.006$ in MWC 480, while theory predicts still lower α around 10^{-4} (Flaherty et al. 2020, and references therein). Using $\alpha = 0.08$ and $\alpha = 0.006$, we find that the formation of the dust trap at the CO snowline should be less than 0.16 − 2.2 Myr ago. This could not explain DL Tau's carbon depleted inner disk if the substructure were formed at the start of the Class II phase (∼7 Myrs ago), as Krijt et al. (2020) showed that for a dust trap with >99% trapping efficiency, the inner disk would be depleted within 3 Myr by more than the factor three with respect to the ISM abundance that is observed in DL Tau. However, if α were <0.003, which still agrees well with the observations, the viscous timescale would be long enough to cover even substructure that has formed right at the start of the Class II phase.

An alternative explanation for the large discrepancy between the carbon abundance in the inner and outer disk is that the dust traps in DL Tau are not 100% efficient in trapping dust. This idea is supported by modeling that shows that low drift efficiency will result in less enhancement in the inner disk (Krijt et al. 2020). McClure et al. (2020) devised a simple analytic model to calculate dust retention efficiencies. The total dust trap efficiency at different positions in the TW Hya disk, based on the distribution of carbon is 99.8%, hence the strong depletion in the inner disk (Fig. 2.9). Following equations 1 − 3 in Appendix C of McClure et al. (2020), we derive a simple expression for the dust trapping efficiency of our disks beyond the inner dust sublimation radius:

$$f_{\mathrm{trap}} = 1 - \frac{X_{\mathrm{g,in}} - X_{\mathrm{g,out}}}{X_{\mathrm{g,ISM}} - X_{\mathrm{g,out}}}, \tag{2.6}$$

where $X_{\mathrm{g,in}}$ is the carbon abundance in the inner disk, $X_{\mathrm{g,out}}$ the carbon abundance in the outer disk and $X_{\mathrm{g,ISM}}$ the carbon abundance in the ISM. Using this formula we find that the dust trap efficiency of the DL Tau disk is 61%, assuming an inner disk abundance that is lower by a factor of 2.5 with respect to the ISM value (McClure 2019). Note that this approximation is highly susceptible to variation in carbon abundance close to the solar value, hence an upper limit. If no carbon depletion is assumed in the inner disk, which is still within the systematic uncertainty of the measurement, then the locking fraction would be 0%.

Long et al. (2020) find low spectral index, $\alpha = 2 - 2.5$, in large regions of the disk of DL Tau by comparing resolved 1.3 mm and 2.9 mm ALMA continuum data. They find similar disk outer radii at both wavelengths and show that this is consistent with a dust evolution model that includes a long lasting pressure bump. A low spectral index is in line with advanced grain evolution, which is also expected based on the evolutionary stage of the source. These authors show also that the spectral index in DL Tau varies only by ∼10% near the pressure maxima, which is in line with the low trapping efficiencies of the dust traps we find in this work. Note, however, that this low variation is a lower limit, since the gaps are unresolved and therefore less pronounced due to beam-smearing.

2.6.1.2 Dust retention in smooth, compact systems

The carbon abundances found for DR Tau and DO Tau are consistent within the observational uncertainties with what is observed in the inner disk, based on the accreting material onto the star (McClure 2019). This implies either that the carbon in ices on dust grains is prevented from drifting towards the star or that the chemistry outpaces the pebble drift by converting CO to less volatile species such as CO_2 and CH_3OH, preventing a resurgence of gas-phase CO just inside the snowline (Krijt et al. 2020). Based on the approximation of the locking fraction in Eq. 2.6, both DR Tau and DO Tau have a trapping efficiency close to 100% (97%, and >100% for DO Tau and DR Tau respectively). Both freeze-out and dust evolution scale with the orbital time scale, which means that carbon is more efficiently depleted closer in to the star, but outside the CO snowline. In extreme scenarios, this could result in a lower abundance in the inner disk than in the disk averaged abundance if radial drift is stopped close to the CO snowline and the inner disk is accreting the gas that is locally highly depleted in carbon just outside the CO snowline. Also, additional dust processing could happen in the $20 - 40$ au between the CO snowline and the inner disk that could influence the carbon abundance. This could be tested by measuring the C/H ratio with JWST or CRIRES+ data in the future. Better resolved radial carbon abundance profiles are necessary to put further constraints on the amount of material that is left behind in the disk to form planets.

There are no signs of dust trapping pressure maxima in the dust continuum images of both DO Tau and DR Tau, often assumed to be a result from planets (Long et al. 2019). However, small substructure will be unresolved in the ∼15 au beam of the continuum observations and the dust is optically thick up to ∼25 au, beyond the CO snowline, which could hide the presence of a gap or dust ring. Future high resolution studies, revolving around substructure near the habiTable zone of compact disks, are necessary to determine whether substructure is exclusively present in extended systems or that compact disks host more substructure than we think. For DR Tau, $R_{\rm gas}/R_{\rm dust} = 3.5$ based on the 95% effective radius of the ^{13}CO $J = 3 - 2$ emission and millimeter continuum, which is close to be a clear sign of dust evolution and radial drift (see Trapman et al. 2019). Considering that the method in Trapman et al. (2019) is based on ^{12}CO observations, which in general has a more extended emitting area than the ^{13}CO for opacity arguments, and the fact that the spatial extent of the CO isotopologue data is slightly larger than can be explained by the modeling (see Appendix 2.C), these systems likely have advanced dust grain evolution and radial drift. This contrast with the radial carbon abundance profile could potentially be explained by dust traps relatively close to the star, not affecting the radial drift in the outer disk. It is also possible that these systems have had efficient radial drift in the past, which is stopped due to recent formation of one or more planetary cores, but not enough to show up in the sub-millimeter continuum.

2.6.2 Evolutionary trend in carbon depletion

Combining all sources of which the carbon abundance in the outer disk is determined using multiple carbon carrying molecules (Fig. 2.9), we find a potential evolutionary trend in the level of elemental gas-phase carbon depletion, similar to those found in CO (Zhang et al. 2020b; Bergner et al. 2020). Recent measurements of $C^{18}O$ in ten Class 0/I sources in multiple star forming regions (shown as a yellow star in Fig. 2.9 Harsono et al. 2014; Zhang et al. 2020b; Bergner et al. 2020) indicate that the youngest sources are not yet depleted in CO, relative to the ISM value, therefore likely not in elemental carbon. As disks age the snowline moves inwards and the vertical snow surface decreases, leading to the presence of a massive cold trap in the outer disk. Any CO that mixes through the dust growth layer or midplane will be lost to never return to the gas. This leads to gas-phase carbon depletion as seen in the outer disks of DO Tau and DR Tau by 1 – 2 Myrs (blue crosses and triangles, respectively in Fig. 2.9). As the disks cool further, and CO-rich icy pebbles drift inward over time, the outer disk becomes increasingly depleted, leading to depletion by up to 2 orders of magnitude within 8 Myrs as in DL Tau and TW Hya (blue stars and green squares, respectively in Fig. 2.9). DL Tau has a similar age and size as TW Hya, and has also an extended ring system, which explains the striking similarity between the two sources in terms of their outer disk carbon depletion. The only dissimilarity arises from the fact that DL Tau is less efficient in trapping dust, resulting in a much larger difference between the inner and outer disk carbon abundances, which we addressed in Sect. 2.6.1.1. TW Hya has an inner cavity (Andrews et al. 2016), which might act as an inner pressure bump that prevents the final drift of pebbles and reduce the carbon enhancement in the inner disk. Similarly old disks around hotter stars, e.g. ∼10 Myr Herbig Ae/Be stars HD 163296 and HD 100546 (red diamonds and triangles, respectively in Fig. 2.9), remain only as depleted as the younger T Tauri disks, possibly due to increased heating and UV radiation from the central star preventing efficient CO ice formation over as large an area as for the T Tauri stars. Larger samples of disks are necessary in order to validate this evolutionary trend.

Calculations of the stellar age can vary considerably depending on the methods used to determine the effective temperature and luminosity to place the sources on evolutionary tracks. The ages for the sources in Taurus that we use here were calculated by McClure (2019) from the Siess et al. (2000a) evolutionary tracks using stellar properties determined self-consistently from near-infrared spectra. The age estimates for DR Tau and DO Tau agree well with the young age of 1 – 2 Myr of the Taurus-Aurigae star forming region (Kenyon & Hartmann 1995), and are close to literature values, 0.37 – 2.8 Myr and 0.37 – 0.93 Myr, respectively (see e.g., Andrews et al. 2013). The age of DL Tau is relatively high for the Taurus-Aurigae star forming region and compared to the literature values of 0.7 – 2.6 Myr (Andrews et al. 2013) and $3.5^{+2.8}_{-1.6}$ Myr (Long et al. 2019). These differences are a result of Andrews et al. (2013) and Long et al. (2019) not taking into account the high veiling of DL Tau (r_J ~2; McClure 2019) when determining the luminosity, namely using a direct fit to the dereddened photometry, that results in overestimating of the stellar luminosity by a factor of 2 and therefore underestimating of the stellar age. Knowing the precise stellar properties is therefore crucial in our understanding of the evolutionary sequence for the outer regions of the disks.

Recent dynamical modeling of CO depletion processes shows that only a combination of chemical processing, freeze-out and sublimation, vapor diffusion, dust and ice dynamics, and pebble formation and dynamics can explain the level of cold, gaseous CO depletion observed in CO surveys (Krijt et al. 2020, 2018). The processes that are involved have in general long timescales, requiring several Myrs to achieve appreciable levels of carbon depletion in the outer regions of a disk. Krijt et al. (2020) find that multiple orders of volatile carbon depletion can only be explained by efficient depletion integrated over at least 3 Myr. Our observations are in line with this modeling, and show that the high level of outer disk carbon depletion of DL Tau and TW Hya is likely due to the fact that more volatile CO has had the chance to freeze out and be locked up in more complex molecules, in large dust grains or transported away from the outer disk by radial drift.

A secondary impacting mechanism on the level of depletion may be the size of the disks, either set by evolutionary or mass arguments. The carbon depletion mechanism is thought to be more efficient in disks with a larger freeze-out zone. HD 100546 and HD 163296 both have no strong carbon depletion, even though the properties of the disk are similar to TW Hya and both sources may be even older than TW Hya (Kama et al. 2016b). However, these two sources are much warmer because of the bright star in the centre, hence they have a small region where CO can freeze out. Similarly, DO Tau and DR Tau are both compact, thus have a relatively small volume beyond the CO snowline where CO freeze-out may occur. Future observations and modeling are needed to get a better understanding of the carbon depletion processes during the different stages of evolution of the disk.

2.7 Conclusions

In this paper, we present observations and modeling of the main gas-phase carbon carriers in protoplanetary disk atmospheres, C^0 and CO isotopologues. We observed a sample of seven disks around T Tauri stars in [C I]. Six out of the seven sources have a firm detection in [C I], in four of the spectra we can constrain the disk component. Three of the sources are modeled with the thermo-chemical disk model `DALI` to determine the C/H ratio in the outer disk. We can conclude the following

- We find depletion factors in gas-phase elemental carbon abundance of 5^{+2}_{-1}, 17^{+39}_{-7} and 157^{+17}_{-15} for the outer disks of DR Tau, DO Tau and DL Tau, respectively.

- DL Tau is much more depleted in carbon in the outer disk than in the inner disk, following a similar pattern as observed in other disks. This is likely the result of advanced grain evolution, efficient radial drift and little locking of carbon in the outer disk. We propose that either the substructure formed later than the viscous time, or that the dust rings observed in the millimeter continuum images of this disk are leaky, i.e., have $<100\%$ efficiency in trapping dust.

- DO Tau and DR Tau show, within the systematic error, similar depletion in volatile carbon in the outer disk as in the inner disk that indicates very efficient dust trapping in the outer disk. Though both disks do not show any dust substructures from current high resolution millimeter continuum observations, our radial carbon abundance profiles suggest the presence of small scale pressure maxima in the inner disk of these compact dust disks. In addition, these systems could have had efficient planetesimal formation that stopped most of the radially drifting dust grains.

- Combining all literature volatile carbon depletion factors in inner and outer disks of T Tauri stars, we find hints for an evolutionary trend in carbon depletion that is consistent with CO isotopologue studies and dynamical models of CO depletion processes that show increasing depletion for older sources.

Expanding the number of points in the radial profiles of carbon depletion will be crucial to understand where the dust is locked up in the disk, potentially in the form of small planetesimals. Future higher spatial resolution observations of the [C I] $J = 1 - 0$ line, in combination with high resolution CO and continuum data, have the potential to be one of the few ways to probe directly the formation of small planetesimals in T Tauri disks.

2.8 Acknowledgements

This paper makes use of the following ALMA data: ADS/JAO.ALMA#2017.1.00857.S, ADS/JAO.ALMA#2016.1.00158.S, ADS/JAO.ALMA#2016.1.01164.S, ALMA is a partner-ship of ESO (representing its member states), NSF (USA), and NINS (Japan), together with NRC (Canada) and NSC and ASIAA (Taiwan), in cooperation with the Republic of Chile. The Joint ALMA Observatory is operated by ESO, AUI/NRAO, and NAOJ. We thank the referee for comments that helped to improve the manuscript.

Appendix

2.A Observing details

In Table 2.A.1 we present the observing log of the [C I] observations.

2.B pole-on outflow in [C I]

The redshifted excess emission in the spectrum of DO Tau (see Fig. 2.1) originates from an off-center, spatially resolved ring of emission, likely emitted from the pole-on outflow that is also observed in CO (Fernández-López et al. 2020). Some of the channels at this velocity are presented in Fig. 2.B.1. The white ellipse in this figure marks the best-fit ellipse to the pole-on outflow observed in ^{12}CO ($B_\mathrm{maj} = 3''$, $B_\mathrm{min} = 2''$, PA = 167°) by Fernández-López et al. (2020). Studying the outflow in detail is beyond the scope of this paper; additional research to the nature of the wind and its impact on the disk dynamics is necessary.

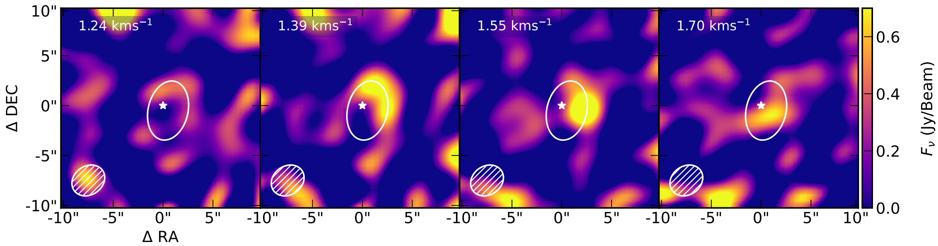

Figure 2.B.1: Channelmaps of the [C I] $J = 1 - 0$ emission of the non-Keplerian redshifted component in DO Tau. Channel velocities are relative to the cloud velocity. The white ellipse denote the best-fit ellipse to the pole-on outflow observed in CO ($B_\mathrm{maj} = 3''$, $B_\mathrm{min} = 2''$, PA = 167° (Fernández-López et al. 2020)). The arc-like emission shares striking similarity with the observed pole-on outflow observed in CO.

2.C Surface density profile DR Tau

DR Tau is a very complex source with a lot of substructure in the different gas tracers. We explored a range of modeling parameters that fit the SED reasonably well, but all of the models have their own caveats. Here we present some additional models to give a feeling for the uncertainty in carbon abundance of this source-specific model. Unfortunately, there is no archival high resolution ^{12}CO data available and the isotopologues ^{13}CO and C^{18}O $J = 2 - 1$ are too weak to determine the spatial scale of the gas disk, as the outer regions of the disk are not detected with high confidence. This means that the spatial information we have of DR Tau is limited. In Fig. 2.C.1 A. we present the azimuthally averaged radial profile of the normalized flux of the ^{13}CO $J = 3 - 2$ emission, together with a small grid of models. In Fig. 2.C.2 we present the corresponding emission spectra of the different transitions. We lowered the carbon abundance to match the modeled [C I] line flux with our observations. Our fiducial model has $R_\mathrm{c} =$

Table 2.A.1: ALMA Observing Log

Execution blocks (UTC Time) (1)	N_{ant} (2)	Calibrators (3)	Targets (4)	Integration time (s) (5)	Beam ($''$) (6)
2018 Aug 17	9	J0440+1437	DL Tau	5080	3.6 × 2.8
2018 Aug 28	11	J0510+1800	DO Tau	5291	3.5 × 2.9
2018 Sep 3	11	J0522-3627	DR Tau	3387	3.4 × 2.7
2018 Sep 4	10		FZ Tau	4656	3.6 × 2.7
2018 Sep 5	10				
2018 Sep 11	12				
2018 Sep 12	11				
2018 Aug 25	10	J0522-3627	FM Cha	8376	3.7 × 3.1
2018 Sep 18	12	J1058-8003	WW Cha	8528	3.2 × 2.9
2018 Sep 19	11	J1145-6954			
2018 Sep 19	11				
2018 Sep 20	11				
2018 Sep 22					
2018 Sep 9	10	J1256-0547	AS 205 A	2238	3.1 × 2.1
2018 Sep 10	11	J1553-2422			
		J1517-2422			

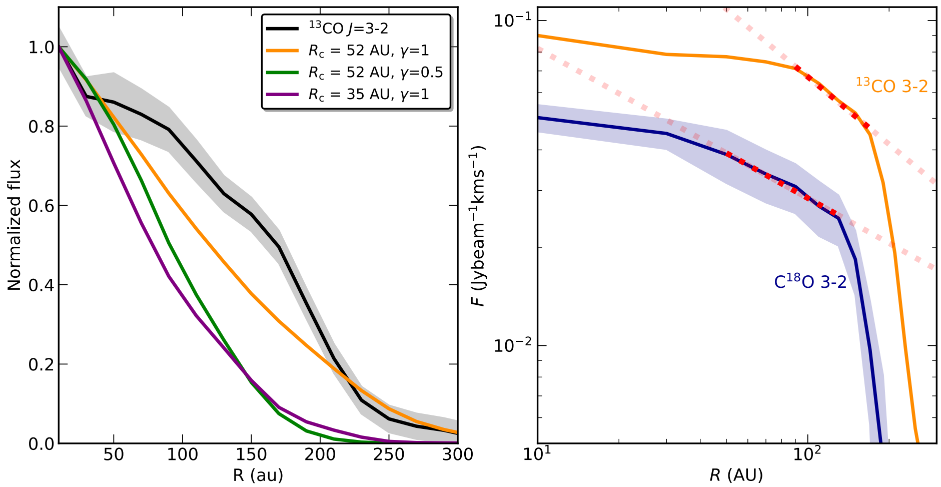

Figure 2.C.1: Left: Radial profile of the ^{13}CO data in black with three models varying R_c and γ convolved with a gaussian beam, similar to the observations. Parameters that are changed with respect to the fiducial model used in the main text are denoted in the legend. The shaded region marks the 1σ uncertainty on the azimuthal average of the data. Right: Radial profile of the ^{13}CO (orange) and C^{18}O emission (blue) in DR Tau. The dotted lines are a linear fit in log-log space. The fit is only performed in the pivot-region (bold dotted line) where the line is optically thin, but with enough column density to efficiently self-shield. The shaded regions mark the 1σ uncertainty on the azimuthal average of the data.

52 au, similar to the continuum observations, and $\gamma = 1$. This model fits the spatial extent of the ^{13}CO emission (Fig. 2.C.1 A) reasonably well, but under-predicts the line fluxes of most CO isotopologue transitions (Fig. 2.C.2). Using this model we find volatile outer disks carbon depletion fractions up to 50 to match the [C I] $J = 1 - 0$ observations, while a depletion fraction of 5 suffices to fit the CO isotopologue transitions.

Following the procedure described in Miotello et al. (2018), we fitted a powerlaw surface density profile in the so called pivot-region of the radial profile of the CO isotopologue $J = 3 - 2$ emission, where the line is optically thin, but has enough column density that isotope selective processes are not a dominant factor. We present the results of this fit in Fig. 2.C.1 B. For ^{13}CO we performed a linear least-squares fit between 75 – 175 au. For C^{18}O the pivot region extends from 30 – 150 au. We find $\gamma = 0.5$ and $\gamma = 0.7$ for ^{13}CO and C^{18}O, respectively, strengthening the case that $\gamma < 1$ for DR Tau.

The best representative model of the line fluxes, presented in the main text, has $\gamma = 0.5$ and $R_c = 52$ au, with the same mass and geometry as the fiducial model. This model has a smaller spatial extent than the ^{13}CO observations (Fig. 2.C.1 A), but fits both the CO isotopologue data as well as the [C I] line fluxes (Fig. 2.5). We tested a model with $\gamma = 1$ and a smaller disk, $R_c = 35$ au, that matches the spatial distribution of the CO isotopologue emission of the model with $\gamma =$

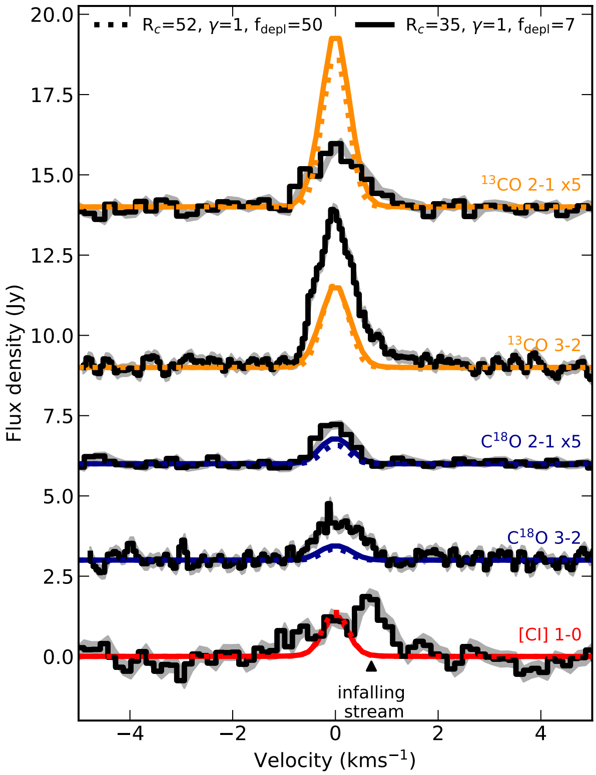

Figure 2.C.2: Line profiles for DR Tau, same as Fig. 2.7, but with changes in $\gamma = 1$ and $R_\mathrm{c} = 35$, respectively, as indicated in the Figure legend.

0.5 and $R_\mathrm{c} = 52$ au, but this model underproduces the CO isotopologue emission with respect to the [C I] emission, similar as the fiducial model. The fit could be improved in the future by using a different sized gas disk than the dust disk, as follows from observations, which is beyond the scope of this paper.

In all possible models that we analyzed the ^{13}CO $J = 2 - 1$ flux is over-predicted by a factor of a few, which is probably due to the low UV-sampling at shorter baselines of the data. We neglect this line further in our modeling. In the main text we used the model that is closest to the continuum observations and reproduced the line emission spectra best. The effect of under-predicting the size of the disk, if any, could be that the disk is more depleted in volatile carbon than assumed in the text, but less than $f_\mathrm{depl} = 50$.

2.D Channel maps

In Fig. 2.D.1 – Fig. 2.D.4 we present the channel maps of the [C I] observations for each source.

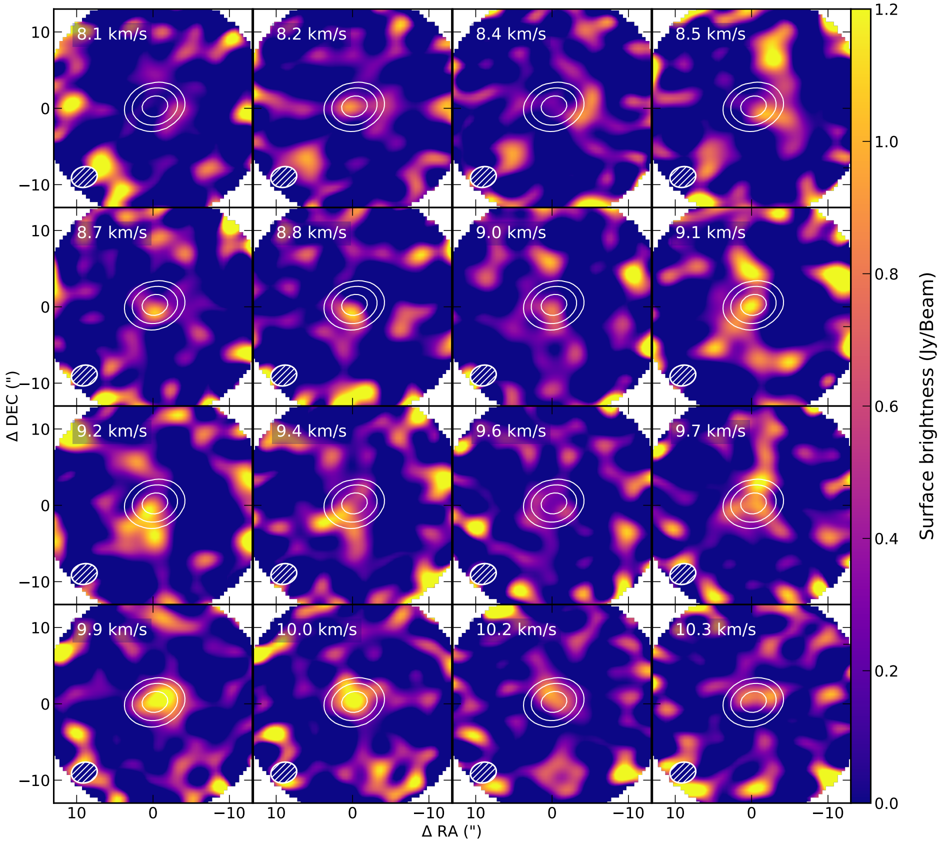

Figure 2.D.1: Primary beam corrected channel maps of the [C I] emission in DR Tau. Solid white contours show the millimeter continuum at 10, 50, and 200 σ, respectively.

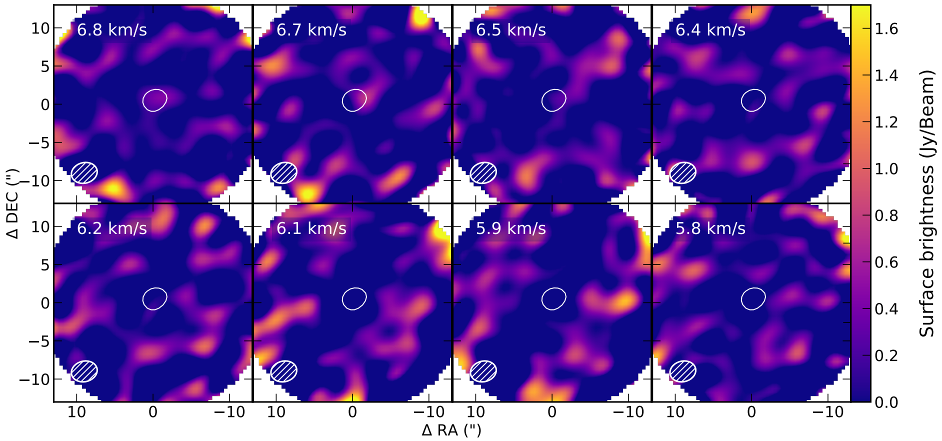

Figure 2.D.2: Same as Fig. 2.D.1 for FZ Tau.

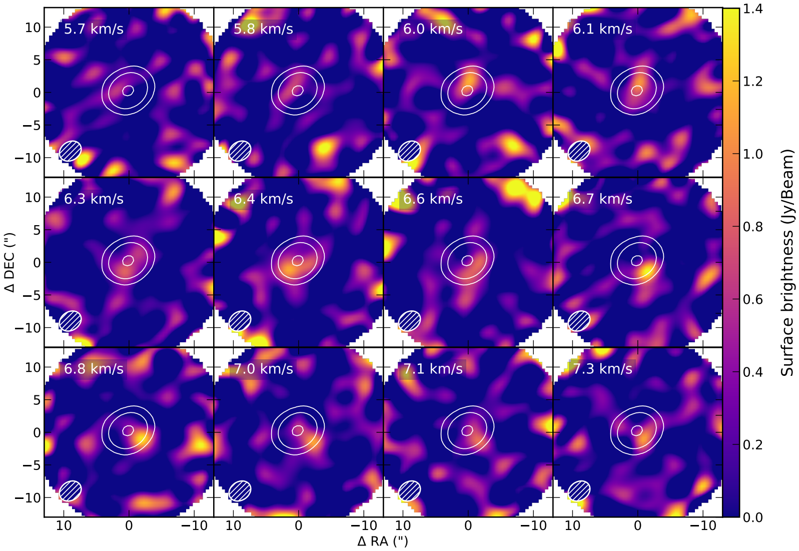

Figure 2.D.3: Same as Fig. 2.D.1 for DL Tau.

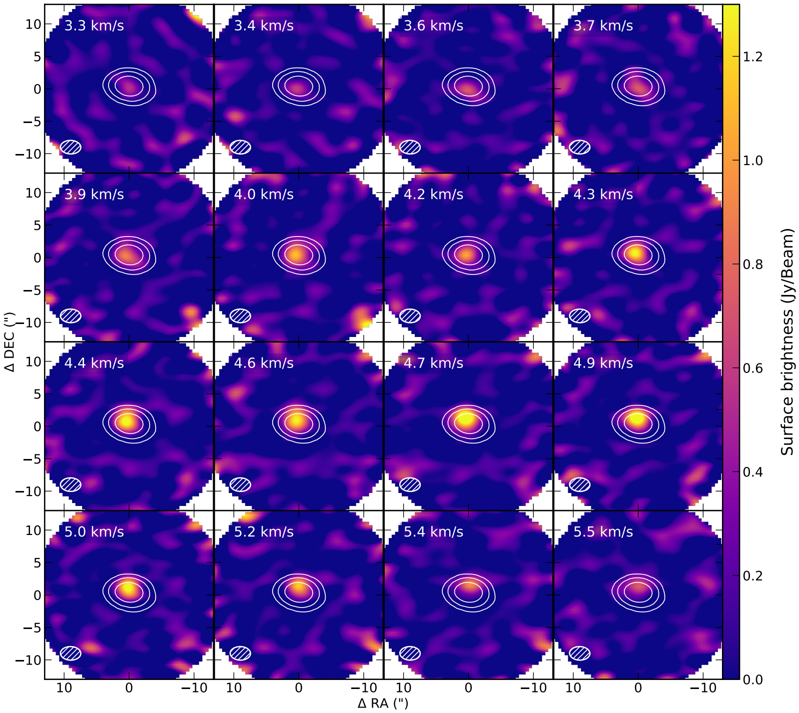

Figure 2.D.4: Same as Fig. 2.D.1 for AS 205 A.

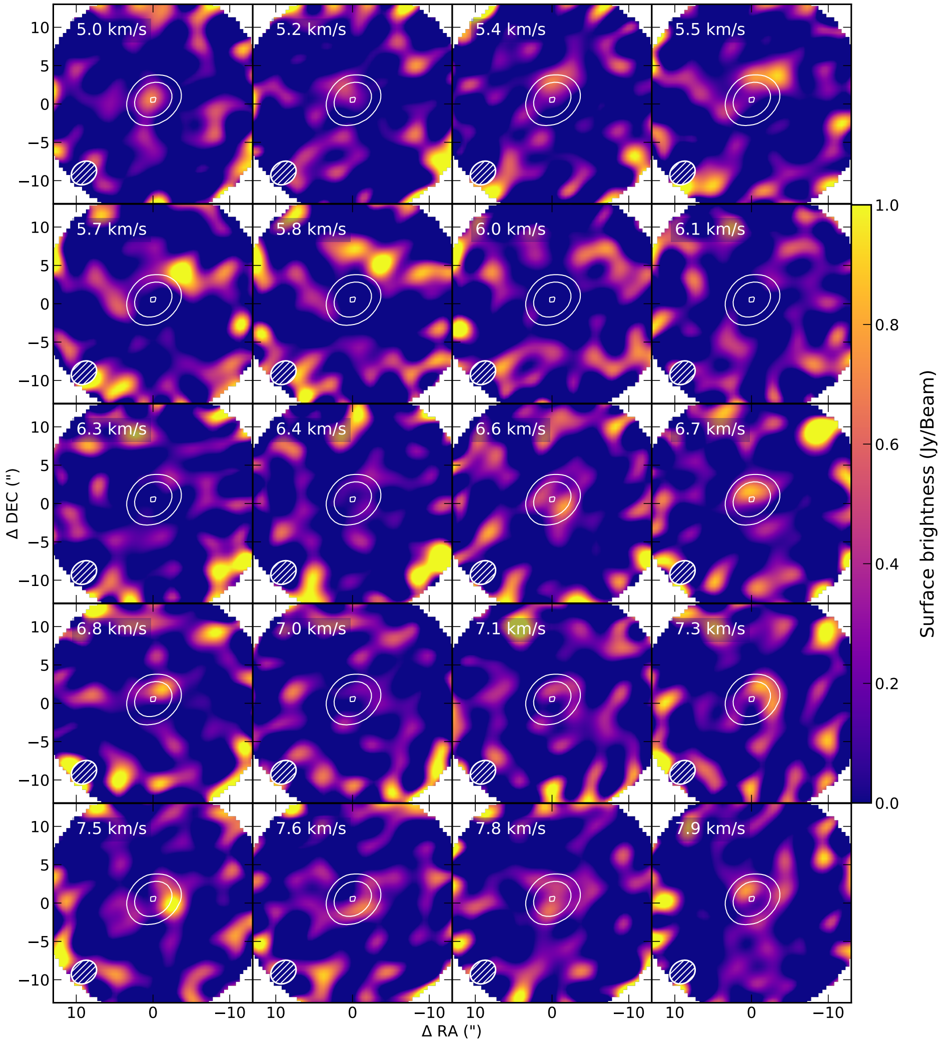

Figure 2.D.5: Same as Fig. 2.D.1 for DO Tau.

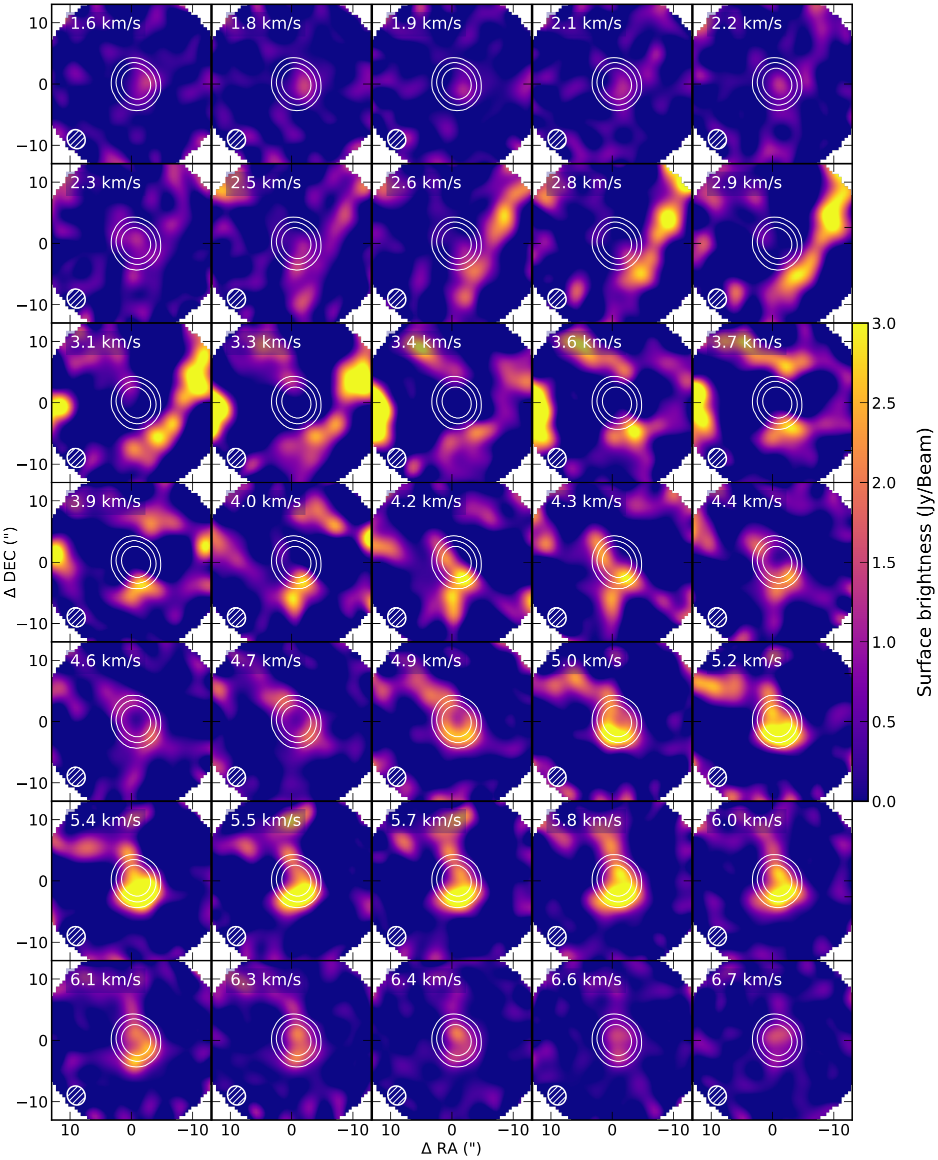

Figure 2.D.6: Same as Fig. 2.D.1 for WW Cha.

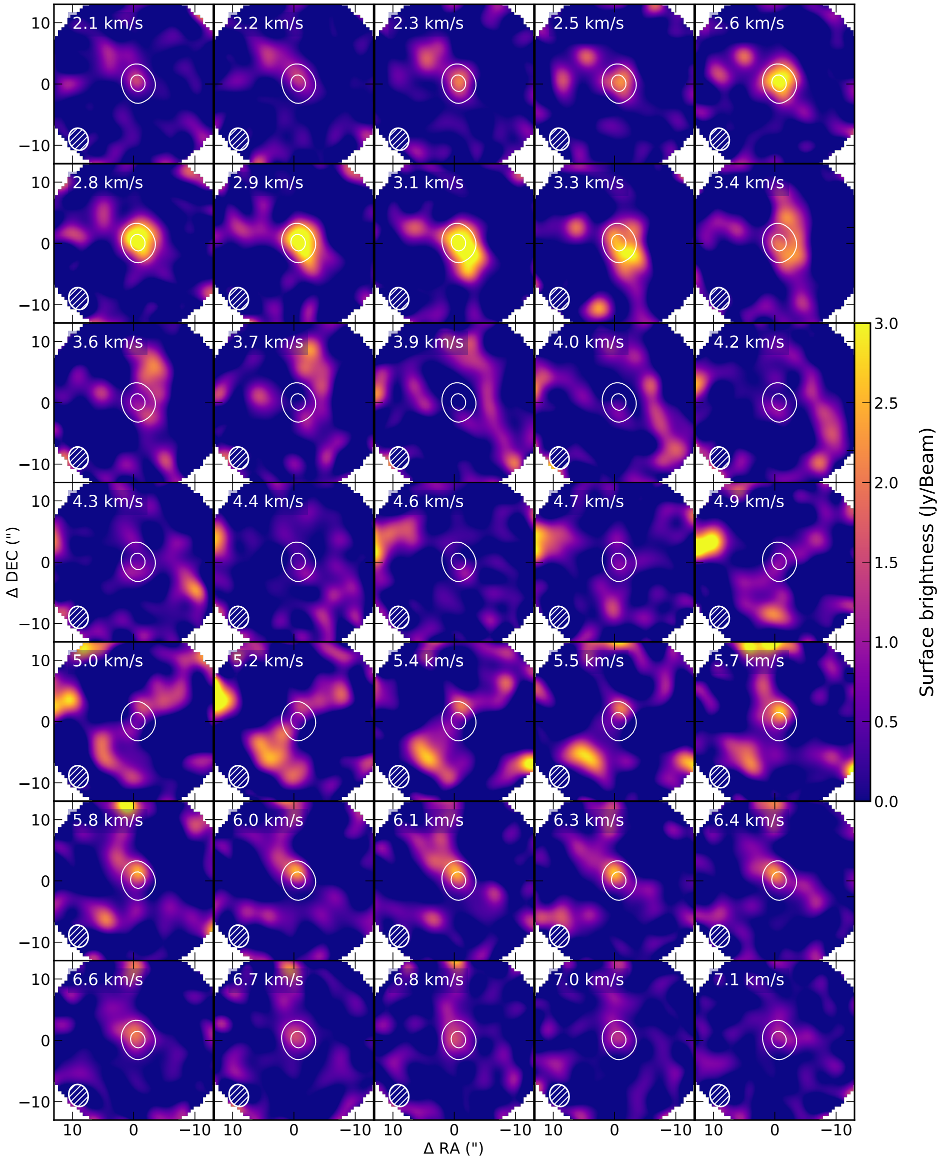

Figure 2.D.7: Same as Fig. 2.D.1 for FM Cha.

Chapter 3

Disentangling the protoplanetary disk gas mass and carbon depletion through combined atomic and molecular tracers

J.A. Sturm, A.S. Booth, M.K. McClure, M. Leemker, and
E.F. van Dishoeck

A&A 670, A12 (2023)

Abstract

Context. The total disk gas mass and elemental C, N, and O composition of protoplanetary disks are crucial ingredients for improving our understanding of planetary formation. Measuring the gas mass is complicated, since H_2 cannot be detected in the cold bulk of the disk and the elemental abundances with respect to hydrogen are degenerate with gas mass in all disk models.

Aims. We aim to determine the gas mass and elemental abundances ratios C/H and O/H in the transition disk around LkCa 15, one of the few disks for which HD data are available, in combination with as many chemical tracers as possible.

Methods. We present new NOrthern Extended Millimeter Array observations of CO, ^{13}CO, C^{18}O, and optically thin C^{17}O $J = 2-1$ lines, along with high angular-resolution Atacama Large Millimeter Array millimeter continuum and CO data to construct a representative model of LkCa 15. Using a grid of 60 azimuthally symmetric thermo-chemical DALI disk models, we translated the observed fluxes to elemental abundances and constrained the best-fitting parameter space of the disk gas mass.

Results. The transitions that constrain the gas mass and carbon abundance the most are C^{17}O $J = 2-1$, N_2H^+ $J = 3-2$ and HD $J = 1-0$. Using these three molecules, we find that the gas mass in the LkCa 15 disk is $M_{\rm g} = 0.01^{+0.01}_{-0.004}$ M$_\odot$, which is a factor of 6 lower than previous estimations. This value is consistent with cosmic ray ionization rates between 10^{-16} – 10^{-18} s^{-1}, where 10^{-18} s^{-1} is a lower limit based on the HD upper limit. The carbon abundance is C/H $= (3 \pm 1.5) \times 10^{-5}$, implying a moderate depletion of elemental carbon by a factor of 3 – 9. All other analyzed transitions also agree with these numbers, within a modeling uncertainty of a factor of 2. Using the resolved C_2H image we find a C/O ratio of $\sim$1, which is consistent with literature values of H_2O depletion in this disk. The absence of severe carbon depletion in the LkCa 15 disk is consistent with the young age of the disk, but stands in contrast to the higher levels of depletion seen in older cold transition disks.

Conclusions. Combining optically thin CO isotopologue lines with N_2H^+ is promising with regard to breaking the degeneracy between gas mass and CO abundance. The moderate level of depletion for this source with a cold, but young disk, suggests that long carbon transformation timescales contribute to the evolutionary trend seen in the level of carbon depletion among disk populations, rather than evolving temperature effects and presence of dust traps alone. HD observations remain important for determining the disk's gas mass.

3.1 Introduction

The total mass of a protoplanetary disk is one of its most significant properties. The disk mass sets the potential for planet formation at different evolutionary stages and it is a fundamental input for models of the disk chemical inventory, planetary formation, and planet-disk interactions (see e.g., Lissauer & Stevenson 2007; Mordasini et al. 2012). In contrast to the dust mass, which can be relatively well constrained by the spectral energy distribution and resolved mm continuum observations (Hildebrand 1983), the gas mass is much harder to determine. Over 99% of the gas resides in H_2 and He, which cannot be directly observed in the bulk of the disk due to lack of a dipole moment. Hydrogen deuteride (HD) is emitted from the warmer atmospheric layers in the disk and can be used to determine the gas mass within a factor of a 2 (Favre et al. 2013; McClure et al. 2016; Trapman et al. 2017). However, only a handful of the most massive sources have obtained a detection of the HD $J = 1 - 0$ line, using far-infrared *Herschel* observations (Bergin et al. 2013; McClure et al. 2016), and unless a far-infrared facility is selected for NASA's upcoming probe class mission, no instruments will be able to target HD in the near future. For several massive disks, *Herschel* HD upper limits can provide additional constraints on the gas mass (Kama et al. 2020).

Carbon monoxide (CO), the second most abundant molecule in disks, is often used to trace the disk mass using a scaling factor to find the total gas mass. Early studies of a few disks have found unexpectedly weak CO emission (van Zadelhoff et al. 2001; Dutrey et al. 2003; Chapillon et al. 2008; Favre et al. 2013). Recent large surveys in the nearby low-mass star-forming regions Lupus and Chamaeleon (Ansdell et al. 2016, 2018; Long et al. 2017; Miotello et al. 2017) have suggested that weak CO emission is common and that CO might be one to two orders of magnitude less abundant in protoplanetary disks than the canonical interstellar medium (ISM) value of $C/H = 1.35 \times 10^{-4}$. This depletion is greater than the amount of depletion expected purely from freeze-out and photo-dissociation. Carbon monoxide is thought to be stored in ices on large dust grains in the midplane and out of reach of chemical equilibrium, which could result in low elemental C/H and O/H abundances in the gas, as compared to the ISM value (see e.g., Kama et al. 2016b; Sturm et al. 2022). These elemental ratios are very important for the disk chemistry and understanding the mechanisms that set these values is crucial for understanding the formation of habiTable planets.

Assessing the degree of CO depletion is complicated by several factors. First, CO depletion is thought to be a combination of dust grain growth, radial and vertical dust dynamics, CO freeze-out, and the chemical processing of CO (van Zadelhoff et al. 2001; Williams & Best 2014; Miotello et al. 2017; Booth et al. 2017; Schwarz et al. 2018; Bosman et al. 2018; Krijt et al. 2018; Zhang et al. 2019; Krijt et al. 2020). Second, recent studies that observed the rare isotopologues $^{13}C^{18}O$ (Zhang et al. 2020a) and $^{13}C^{17}O$ (Booth et al. 2019) show that even $C^{18}O$ lines can be optically thick in the densest, innermost regions of the disk, attributed to enhanced abundances due to radial drift of ice rich material on large dust grains within the snowline. Third, the C/O ratio in the gas is thought to be radially varying between 1 at large radii and ∼0.47 at small radii because of the freeze-out of key C and O bearing species such as H_2O, CO and CO_2 (Öberg et al. 2011b; Eistrup et al. 2016). Additional elevation is inferred in a number of disks by the strong lines of small carbon chains such as C_2H and C_3H_2 that require C/O ratios of 1.5 – 2 to form efficiently (Bergin et al. 2016; Miotello et al. 2019; Bergner et al. 2019; Ilee et al. 2021; Bosman et al. 2021a). The elevated C/O ratio could be a result of the observed gas phase depletion of H_2O and CO_2 (Bergin et al. 2010; Hogerheijde et al. 2011; Du et al. 2017; Bosman et al. 2017). Potentially direct photo-ablation of carbon rich grains can also contribute (Bosman et al. 2021b). The C/O ratio in the planetary birth environment is one of the key ingredients in models of planetary atmospheres. A slight increase in C/O ratio in a typical hot Jupiter atmosphere changes abundances of key carbon-bearing species such as CH_4 and C_2H_2 by multiple orders of magnitude (Lodders 2010; Madhusudhan 2019).

Nitrogen bearing molecules are proposed to be good candidate gas mass tracers, since the main molecular carrier of N, N_2, has such a low freeze-out temperature that the depletion of nitrogen is likely to be less severe than that of oxygen and carbon (Tafalla & Santiago 2004; Cleeves et al. 2018; Visser et al. 2018). A smaller fraction of the total amount of nitrogen is contained in meteorites and comets, which suggests that less material is depleted from the gas phase by freeze-out and further processing on the grains (see more details in Bergin et al. 2015; Anderson et al. 2019). Since N_2 cannot be observed directly under typical disk conditions by lack of a dipole moment, much less abundant species such as HCN, CN, and N_2H^+ are necessary for probing the disk mass. However, most of these molecular abundances are dependent on the C/H abundance in the disk. As for N_2H^+, which is observed in a large number of disks (Öberg et al. 2010, 2011c; Qi et al. 2019),

Table 3.1: LkCa 15 source properties

Parameter	Symbol		Value
Right Ascension	RA (J2000)		04:39:17.8
Declination	DEC (J2000)		+22:21:03.21
Distance	d	(pc)	157.2
Spectral type	SpT		K5
Age	t	(Myr)	2 (0.9 – 4.3)
Effective Temperature	T_{eff}	(K)	4730
Stellar Luminosity	$L_\star$	($L_\odot$)	1.04
Stellar Radius	$R_\star$	($R_\odot$)	1.0
Stellar Mass	$M_\star$	($M_\odot$)	1.03
Mass accretion rate	$\log_{10}\dot{M}$	($M_\odot$ yr^{-1})	−8.7
Visible Extinction	A_{V}	(mag)	1.5
Inclination	i	(deg)	55
Position Angle	PA	(deg)	60
Systemic velocity	v_{sys}	(km s^{-1})	6.1

References. Espaillat et al. (2010); van der Marel et al. (2015); Pegues et al. (2020); Gaia Collaboration et al. (2021)

it is the most promising candidate as it does not contain a carbon atom, but it is destroyed by proton transfer in the vicinity of gaseous CO (van 't Hoff et al. 2017; Anderson et al. 2019). Anderson et al. (2019, 2022) have shown, based on a small survey of N_2H^+ emission lines, that N_2H^+ can be used in combination with $C^{18}O$ to constrain the carbon abundance and total gas mass, which was confirmed in the recent modeling work of Trapman et al. (2022), comparing the outcome with established HD modeling. No single molecule is an optimum tracer, but here we investigate whether a combination of these molecules would work best to disentangle the gas mass from the elemental abundance determination.

This paper is organized as follows. In Sects. 3.2 and 3.3, we present the object of study, LkCa 15, along with previous works on measuring the gas mass in this system and new findings. Section 3.4 summarizes the physical-chemical modeling framework. In Section 3.5, we compare the results of a range of possible modeling parameters with the data. In Sect. 3.6, we discuss the results and present our conclusions.

3.2 Observations

3.2.1 The LkCa 15 disk

In this paper, we focus on one specific source, LkCa 15, which is one of the few disks for which observations in many gas mass tracers exist, including an HD upper limit. Comparing multiple proposed gas mass tracers and the C/O ratio tracer C_2H, we aim to constrain the gas mass and C/H and O/H abundances in the bulk of the disk. LkCa 15 is a relatively young (~2 Myr old Andrews et al. 2018b) T Tauri star located at a distance of 157.2 pc, as determined by *Gaia* (Gaia Collaboration et al. 2016, 2021) in the Taurus star forming region. It has a well-studied transition disk, with a dust disk cavity of ~50 − 65 au, where the millimeter sized dust grains are depleted (e.g., Piétu et al. 2006; Isella et al. 2012; Facchini et al. 2020). Most of the millimeter dust continuum is emitted from two bright rings between 50 − 150 au. Micron-sized dust grains are observed in scattered light observations in an inner disk inside the dust gap up to ~30 au (Oh et al. 2016; Thalmann et al. 2016). Spatial segregation in dust sizes supports the presence of a massive planet orbiting at ~40 au (Pinilla et al. 2012; Facchini et al. 2020). There has been speculation about the existence of multiple planets inside the cavity based on asymmetric emission in scattered light and Hα emission (Kraus & Ireland 2012; Sallum et al. 2015), but these were later shown to be likely due to disk features (Thalmann et al. 2016; Currie et al. 2019). The gas disk extends out to ~1000 au (Jin et al. 2019) and has a significantly smaller cavity than the one found in the dust at 15 – 40 au (van der Marel et al. 2015; Jin et al. 2019; Leemker et al. 2022a).

Previous estimates of the mass in the LkCa 15 disk were based on the SED and the millimeter dust continuum (~0.06 $M_\odot$ Isella et al. 2012; van der Marel et al. 2015; Facchini et al. 2020) and a combination of the SED and the upper limit from the HD $J = 1 - 0$ line, which gives 0.062 $M_\odot$ (McClure et al. 2016). Jin et al. (2019) used optically thick CO and ^{13}CO lines and the assumption of a gas-to-dust ratio of 1000 and a constant CO/H_2 abundance of 1.4×10^{-4} to find a gas mass of $\sim$0.1 $M_\odot$. Facchini et al. (2020) found an upper limit of the gas-to-dust ratio using stability arguments against gravitational collapse of 62 and 68 in the two bright dust continuum rings, respectively, containing the bulk of the total dust mass.

3.2.2 Observational details

We present new NOEMA (NOrthern Extended Millimeter Array) observations targeting the optically thin $^{13}C^{18}O$ and $C^{17}O$ $J = 2{-}1$ lines, ^{13}CO, $C^{18}O$, and CN. These new NOEMA observations combined with a large number of high-resolution archival ALMA CO isotopologue observations, N_2H^+ and C_2H emission, and a HD upper limit allow us to study the possible gas mass range and composition of LkCa15 in much more detail, breaking the degeneracy between the disk gas mass and C/H and O/H abundances.

The new NOEMA observations were taken on the 26 and 27 of November 2020. All nine antennae were used with baselines ranging from 32 to 344 m. Three calibrators were used, 0507+179, LKHA101, and 3C84 to correct, respectively, the phase, amplitude, and flux and radio interference. We integrated for 7.5 hours on-source, resulting in a sensitivity of 40 mJy/Beam at a velocity resolution of 0.2 km s^{-1}. Imaging was done using `CASA` v5.4.0. (McMullin et al. 2007) using Briggs weighting and a robust factor of 0.5. The resolution of the final images is typically $1''.1 \times 0''.7$ or $\sim$150 au at the distance of LkCa 15. Observational details are given in Table 3.2.

Additionally, this project makes use of data from various archival ALMA programs, which are summarized in Table 3.2. We include high-resolution CO $J = 2-1$, ^{13}CO $J = 2-1$ and $C^{18}O$ $J = 2-1$ lines to constrain the radial profile of the CO emission, ^{13}CO $J = 6-5$ to further constrain the temperature profile (Leemker et al. 2022a), and C_2H to constrain the C/O ratio in the disk. CO isotopologue ALMA data were self-calibrated in CASA and CLEANed using a Keplerian mask. Further details of the data and initial calibration are described in Leemker et al. (2022a). C_2H ALMA observations and reduction are described in more detail in Bergner et al. (2019). N_2H^+ observations are described in Qi et al. (2019), and are consistent with those reported in Loomis et al. (2020). The upper limit for HD $J = 1-0$ is taken at 3σ from *Herschel* data (McClure et al. 2016). The properties of all emission lines and an overview of the observations are presented in Table 3.2.

3.2.3 Data analysis

Integrated emission or moment 0 maps were created for all NOEMA lines and CO isotopologue ALMA data by integrating over the emission inside the same Keplerian mask that is used in the CLEANing process, set by the source parameters given in Table 3.1 and restricted to $\pm$4 km s^{-1} from the source velocity. The moment 0 maps are presented in Fig. 3.1, together with the ^{12}CO $J = 2-1$ and continuum images of the ALMA Band 6 data for comparison. Integrated line fluxes are determined using a mask extending to $6''.5$ or $\sim$1000 au in radius and are presented in Table 3.2 and are shown in black in the right panel of Fig. 3.2.

Table 3.2: LkCa 15 line properties

Line	Telescope	Program ID	Integrated flux (Jy km s^{-1})	Beam size ($''$)	Beam PA ($^\circ$)	ν (GHz)	$E_{\rm u}$ (K)	$\log_{10}A_{\rm ul}$ (s^{-1})
^{12}CO $J = 2-1$	ALMA	2018.1.01255.S	16 ± 2	0.34 × 0.25	-9.7	230.538	16.6	-6.16050
^{13}CO $J = 2-1$	NOEMA	S20AT	5.0 ± 0.5	1.13 × 0.73	20.4	220.399	15.9	-6.51752
^{13}CO $J = 2-1$	ALMA	2018.1.00945.S	5.5 ± 0.5	0.35 × 0.25	26.7			
^{13}CO $J = 6-5$	ALMA	2017.1.00727.S	8.3 ± 0.9	0.32 × 0.30	-31.2	661.067	111.1	-5.02695
C^{18}O $J = 2-1$	NOEMA	S20AT	1.1 ± 0.1	1.14 × 0.74	20.4	219.560	15.8	-6.22103
C^{18}O $J = 2-1$	ALMA	2017.1.00727.S	1.0 ± 0.1	0.36 × 0.27	26.6			
C^{17}O $J = 2-1$	NOEMA	S20AT	0.36 ± 0.07	1.13 × 0.72	20.9	224.714	16.2	-6.19211
^{13}C^{18}O $J = 2-1$	NOEMA	S20AT	<0.17	1.17 × 0.78	21.5	209.419	15.1	-6.28123
CN $N = 2-1$, $J = \frac{5}{2}-\frac{3}{2}$	NOEMA	S20AT	8.1 ± 0.8	1.12 × 0.72	20.9	226.876	16.3	-3.94188
C_2H $N = 3-2$, $J = \frac{5}{2}-\frac{3}{2}$	ALMA	2016.1.00627.S	1.7 ± 0.2	0.59 × 0.49	-26.3	262.1	25.2	-4.31202
C_2H $N = 3-2$, $J = \frac{7}{2}-\frac{5}{2}$	ALMA	2016.1.00627.S	2.4 ± 0.3	0.59 × 0.49	-26.3	262.0	25.2	-4.27528
N_2H^+ $J = 3-2$	ALMA	2015.1.00678.S	1.82 ± 0.02	0.32 × 0.29	-23.0	279.511	26.8	-2.86895
HD $J = 1-0$	*Herschel*	-	< 19.1	6.6	-	2674.99	128.4	-7.26648

Notes: Flux errors include 10% calibration error.

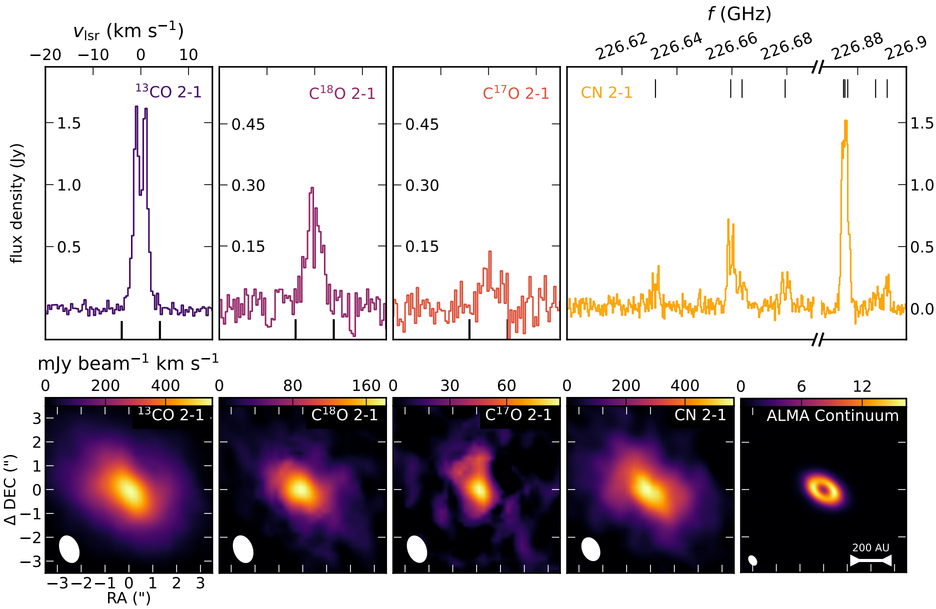

Figure 3.1: Disk-integrated spectra (top) and total intensity or moment 0 maps of the new emission lines (bottom) obtained with NOEMA at $1''.1 \times 0''.7$. ALMA band 6 continuum data at $0''.3 \times 0''.3$ are shown for comparison. Integration limits for the moment 0 maps are indicated with black tickmarks in the bottom at −4 and 4 km s^{-1}. Robustly detected CN hyper-fine structure lines are indicated in the top right panel with black tick marks. For each moment 0 map, the beam is shown as a white ellipse in the lower left corner.

All moment 0 maps are deprojected and averaged along azimuth using the geometrical source properties given in Table 3.1. We chose the source center for each molecule as the pixel (typically 1/5 of the beam) with the peak flux or, in case the cavity is resolved, the pixel with the lowest flux inside the cavity. The source center is shifted with maximum $0''.1$ from the reference position, which is a result of the observed eccentric inner disk (Thalmann et al. 2016; Oh et al. 2016), the high inclination (55°) of the main disk and the different observing dates. The radial profiles are presented in Fig. 3.2 as black lines, the 1σ uncertainty is masked around the curves. We include the radial profile of the C_2H emission from Bergner et al. (2019) and the N_2H^+ from (Qi et al. 2019). The radial profile of the continuum from Facchini et al. (2020) is included in Fig. 3.3.

3.3 Observational results

All targeted CO isotopologues, except for $^{13}C^{18}O$ $J = 2-1$, were detected. The spectra of all detected emission lines are presented in the top panel of Fig. 3.1. Here, $C^{17}O$ $J = 2-1$ is robustly detected with NOEMA at a S/N of 6. The $^{13}C^{18}O$ $J = 2-1$ line is not detected so we listed the 3σ upper limit in Ta-

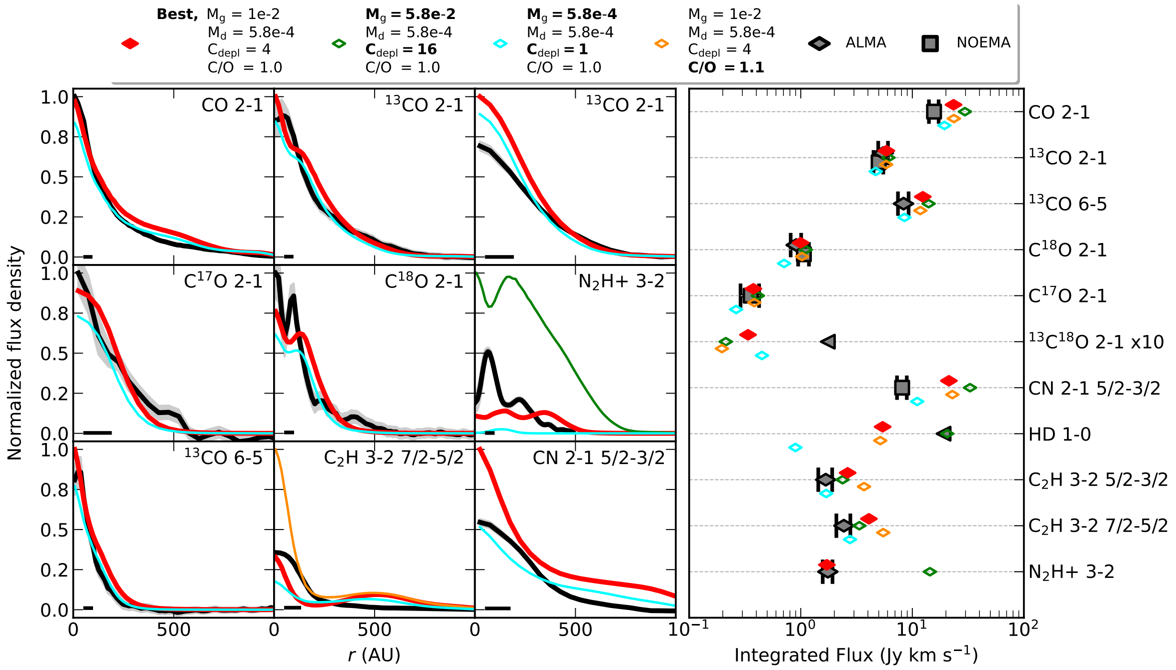

Figure 3.2: Azimuthally averaged radial profiles of the different gas tracers used in this work (left). Data are shown as black lines with shaded 1σ uncertainty and normalized to the brightest point for visualization purposes. The full width at half maximum of the beams is shown as a black horizontal line in the lower left-hand corner. The best-fitting model with a gas mass of 0.012 $M_\odot$ and a factor of 4 in carbon depletion is overplotted in red. The blue line shows the same model but with a lower gas-to-dust ratio, resulting in a gas mass of $4 \times 10^{-4} M_\odot$, and no carbon depletion. This model reproduces the optically thick CN and CO lines somewhat better, but underproduces the optically thin N_2H^+ line. The orange line illustrates the C_2H radial profile for an increased C/O ratio of 1.1. With C/O > 1 excess carbon, not in CO, changes the carbon chemistry completely. Integrated line flux of the various emission lines analyzed in this paper (right). Black squares represent the observed line fluxes of NOEMA data, black diamonds represent the observed line fluxes of ALMA data, black triangles denote upper limits, taken at 3σ. Colored diamonds show the results for the same models as in the left panel.

ble 3.2. The upper limit for ^{13}C^{18}O results in a minimum C^{17}O/^{13}C^{18}O ratio of 4.6, compared with the elemental abundance ratio of 24. The observed ^{13}CO and C^{18}O $J = 2-1$ disk integrated fluxes in the NOEMA and ALMA observations agree well with each other. In addition we detect 8 hyper-fine CN $N = 2-1$ lines that we combine into one single image. Based on the ratio of the hyper-fine lines we find that the emission is optically thick for the blended lines at 226.87 GHz and 226.66 GHz, but optically thin for the other lines.

Most of the observed CO isotopologue lines are centrally peaked, without resolving the inner cavity. The inner cavity is resolved in the ^{13}CO $J = 2-1$ and C^{18}O $J = 2-1$ ALMA data, lately confirmed by Leemker et al. (2022a) using ^{13}CO $J = 2-1$ data with higher spatial resolution and using the high velocity line wings that trace regions closer in to the star than the spatial resolution of the data (Bosman et al. 2021c). The CN emission is centrally peaked and extends out to 1000 au, similar to the ^{12}CO data.

3.4 Modeling framework

Our aim is to distentangle the gas mass and elemental abundances C/H and O/H in LkCa 15. For that purpose we made a representative model of LkCa 15 using the azimuthally symmetric physical-chemical model Dust And LInes (DALI; Bruderer et al. 2012; Bruderer 2013). To find the best representative geometry, density structure, and composition of the LkCa 15 disk, we combined information from the spectral energy distribution (SED), high-resolution ALMA continuum observations, the emission lines discussed in Sect. 3.2.2 and observables from scattered light observations, as well as near-infrared spectra from the Infrared Telescope Facility (IRTF) facility using SpeX (Espaillat et al. 2010).

3.4.1 Model parameters

The first step in our modeling was to set up a geometrical density structure including all radiation sources that is consistent with the data. For the dust density structure we adopted a fully parametrized surface density profile with a power law surface density dependence on radius (r) and an exponential outer taper:

$$\Sigma_{\rm dust} = \frac{\Sigma_{\rm c}}{\epsilon}\left(\frac{r}{R_{\rm c}}\right)^{-\gamma} \exp\left[-\left(\frac{r}{R_{\rm c}}\right)^{2-\gamma}\right], \tag{3.1}$$

where $\Sigma_{\rm c}$ is the surface density at the characteristic radius, $R_{\rm c}$, γ the power law index, and ϵ the gas-to-dust ratio. Following the approach of D'Alessio et al. (2006), we split the dust into a small dust population which ranges from 0.005 to 1 µm and a large dust population which includes the small dust sizes, but extends to 1000 µm. To calculate the opacities we assume a standard ISM dust composition following Weingartner & Draine (2001), combined using Mie theory, consistent with Andrews et al. (2011). We also included polycyclic aromatic hydrocarbons (PAHs), assumed to be 0.1% of the ISM abundance following Geers et al. (2006). The small dust grains follow an exponential dependence on the height in the disk, given by:

$$\rho_{\mathrm{d,small}} = \frac{(1-f_\ell)\Sigma_{\mathrm{dust}}}{\sqrt{2\pi}rh}\exp\left[-\frac{1}{2}\left(\frac{\pi/2-\theta}{h}\right)^2\right], \tag{3.2}$$

where θ is the opening angle from the midplane as seen from the center, h is the scale height defined by $h = h_{\mathrm{c}}\,(r/R_{\mathrm{c}})^{\psi}$, and f_ℓ is the mass fraction of large grains. We parametrized dust settling by replacing the scale height of the large grains by χh, so that only a fraction $1-f_\ell$ of the grains is distributed throughout the height in the disk. We fixed χ at 0.2 and f_ℓ at 0.98, adopted from McClure et al. (2016) (see also Andrews et al. 2011). The gas surface density follows the same radial and vertical distribution as the small dust grain population, but scaled by the total gas-to-dust ratio, which we take initially at 100. Within the dust sublimation radius, both dust and gas surface density are set to zero. To include a cavity in the dust and gas we scaled the dust and gas surface density profiles independent from each other inside a given radius, R_{gap}, with respect to the distribution given in Eq. 3.2 and with constant scaling factors, δ_{d} and δ_{g}. To account for the three rings observed in the high-resolution continuum images (Facchini et al. 2020), we scaled up the dust density distribution in three intervals (see Fig. 3.3 for a visualization of the density distribution of the dust and gas).

The stellar spectrum is approximated as a blackbody with temperature $T_{\mathrm{eff}} =$ 4730 K. We added an additional UV component to account for gas accretion using a plasma temperature (T_{acc}) of 10,000 K, with a luminosity given by:

$$L_{\mathrm{acc}}(v) = \pi B_v\left(T_{\mathrm{acc}}, v\right)\frac{GM_*\dot{M}}{R_*}\frac{1}{\sigma T_{\mathrm{acc}}^4}, \tag{3.3}$$

where $B_v\left(T_{\mathrm{acc}}, v\right)$ is Planck's law for blackbody radiation, M_* is the stellar mass, R_* is the stellar radius and $\dot{M}$ the mass accretion rate. We adopted stellar parameters from Espaillat et al. (2010) and Pegues et al. (2020), given in Table 3.1 resulting in $\mathrm{L_{UV}} = 0.06\ \mathrm{L_\odot}$. We note that the observed values of $\dot{M}$ are uncertain up to an order of magnitude and can change over time. We included X-rays assuming an X-ray luminosity of 10^{30} erg s^{-1} at a plasma temperature of 7×10^7 K. The cosmic ionization rate incident on the surface of the disk is set to 5×10^{-17} s^{-1}.

Using the sources of radiation and the density structure described in Sect. 3.4.1, we determined the dust temperature and continuum mean intensity in each grid cell using a Monte-Carlo approach, where photon packages are started randomly from the star, dust grains, or the background.

3.4.2 Chemical networks

The gas temperature is iteratively solved together with the chemistry, since the gas temperature is dependent on the abundance and excitation of different coolants in the disk. We used two different chemical networks in DALI to cover both the isotope selective processes of CO and proper treatment of C$_2$H and CN. For the CO isotopologue emission we used the HD chemistry described in , but adapted it to the reduced CO isotopologue network described in Miotello et al. (2016) rather than the full network described in Miotello et al. (2014) to save computation time. This network includes HD, D, HD$^+$, D$^+$, ^{13}CO, C^{18}O, C^{17}O, and ^{13}C^{18}O as

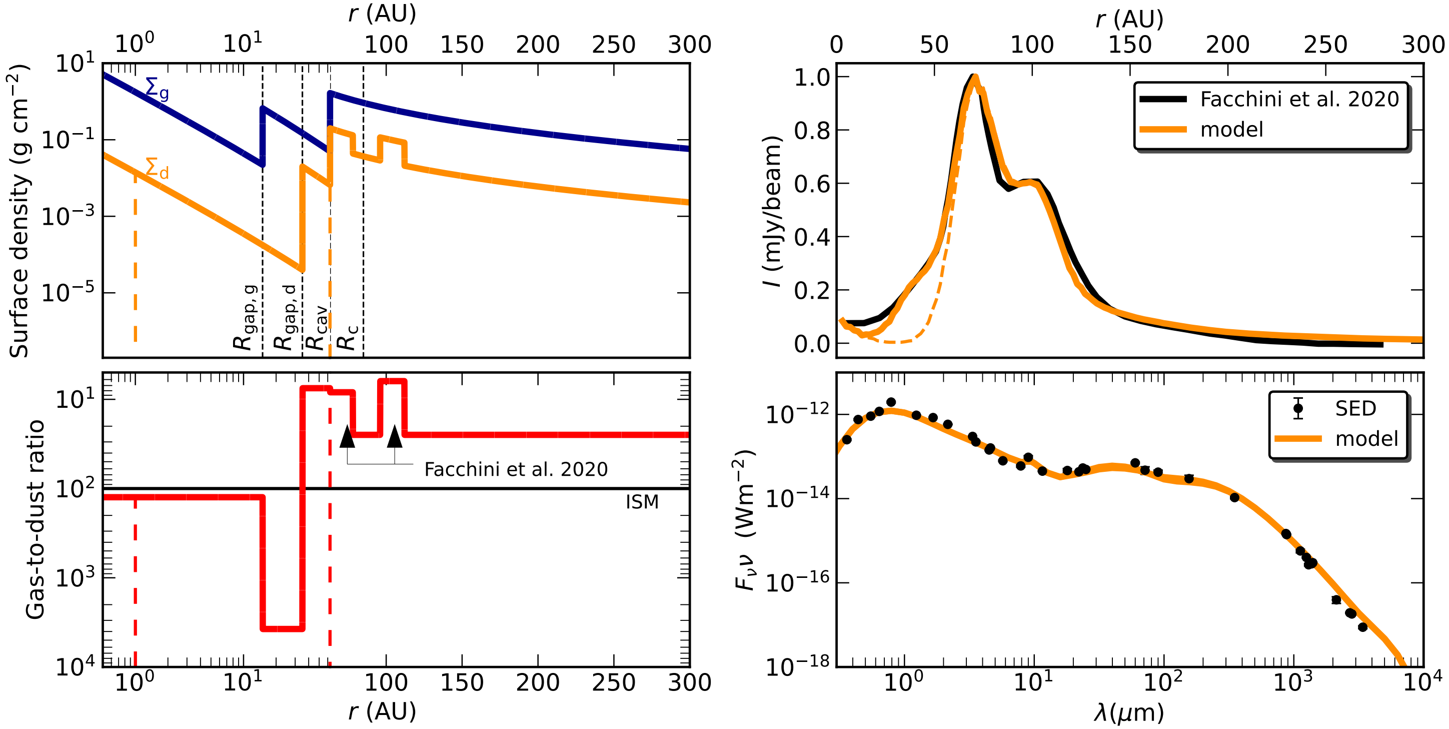

Figure 3.3: Setup of the DALI model for LkCa 15, Top-left: Normalized surface density of the dust (orange) and gas (blue) as function of radius, Bottom-left: Gas-to-dust ratio as function of radius in the fiducial model, this is a direct consequence of the used gas and dust surface density profiles shown in the top left panel, Top-right: Radial profile of the continuum observations (black) and the model (orange) normalized to 1, Bottom-right: Observed SED in black with the modeled continuum fluxes in orange. Dashed lines show the setup for the same model with cleared cavity, discussed in Appendix 3.B.

separate species, resulting in a total of 189 species and 5789 reactions (compared to 280 species and 9789 reactions in Trapman et al. 2017). For CN and C_2H we used the expanded network described in Cazzoletti et al. (2018) and Visser et al. (2018). Nitrogen isotopes are not considered. Reaction types include standard gas-phase reactions, photoionization and -dissociation, X-ray and cosmic ray induced reactions, freeze-out and (non-) thermal desorption, PAH and small grain charge exchange, as well as hydrogenation and reactions with vibrationally excited H_2 (H_2^*). Details of these reactions are described in Bruderer et al. (2012), Trapman et al. (2017), and Visser et al. (2018).

We adopted fiducial ISM gas-phase volatile elemental carbon, oxygen, and nitrogen abundances of $C/H = 135$ ppm, $O/H = 288$ ppm, and $N/H = 21.4$ ppm, respectively (Cardelli et al. 1996; Meyer et al. 1998; Parvathi et al. 2012), and ^{13}C, ^{18}O, ^{17}O abundance ratios of 77, 560, and 1792 with respect to their most abundant isotopes (Cardelli et al. 1996; Meyer et al. 1998; Parvathi et al. 2012; Wilson 1999). All volatile carbon, oxygen, and nitrogen starts in atomic form in the gas, but can cycle between gas and ice. The chemistry is run time dependently for 1 Myr. Most line strengths do not change when run in steady-state mode, because the surface layer dominates the abundance of these molecules where the chemistry is fast and emission is not sensitive to the time step.

N_2H^+ is modeled using a separate, simple chemical network described in van 't Hoff et al. (2017) for a better treatment of the charge distribution. This network focuses specifically on the ionization balance between ${H_3}^+$, N_2H^+, and HCO^+, including freeze-out, thermal desorption, and photodissociation of CO and N_2. Using this simplified network has the advantage of being easier to understand the ionization balance, while using the same temperature structure and CO and N_2 abundances as in the complete model.

After the chemistry is converged, the model is ray-traced in the analyzed transition lines and at 200 continuum wavelengths from 0.1 − 10,000 µm. Following a similar approach as described in Sect. 3.2.2, we created moment 0 maps and radial profiles for each of the model lines.

3.4.3 Modeling approach

Initially we fit the disk parameters by eye in a logical order, that we describe in the following sections, so that they converge to a model that best represents the available data. The large number of parameters and the computational time of the models make it impossible to use χ^2 fitting or Monte Carlo processes on the whole parameter space. This means that it is not possible to derive formal uncertainties of model parameters and to determine correlations or degeneracies between parameters. The final best fit parameters are summarized in Table 3.3.

3.4.3.1 Fitting the dust density distribution

The first step was to find a dust density distribution that agrees well with the data. For that purpose we compared the modeled continuum spectrum with the observed SED and the radial profile of the modeled emission to the radial profile of the high-resolution 1.35 mm continuum data (Facchini et al. 2020). The SED is taken from Andrews et al. (2013) and dereddened using the CCM89 extinction

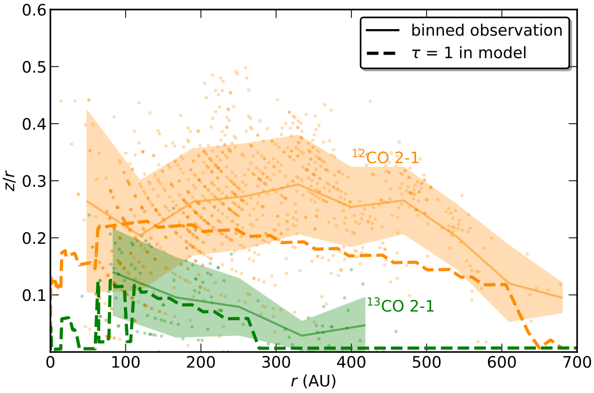

Figure 3.4: Emitting heights of the ^{12}CO (orange) and ^{13}CO (blue) $J = 2-1$ emission, taken from Leemker et al. (2022a). Scattered points represent the emitting height for each channel, whereas the solid line represents a radially binned average with 1σ error. The dashed line shows the height of the $\tau = 1$ line in the DALI model. The disk is flat in both the observations as well as the model.

curve (Cardelli et al. 1989) and the observed visible extinction A_V=1.5 (Espaillat et al. 2010). As a starting point we used the model by van der Marel et al. (2015), but updated to the new *Gaia* DR 3 distances and most recent observations. We first fit the aspect ratio, h_c, by matching the model with the observations at the base height of the silicate feature at 10 µm, assuming grain size distributions given in Sect. 3.4.1. This aspect ratio agrees well with the observed emitting heights of the optically thick CO and ^{13}CO lines (see Fig. 3.4). Subsequently, we fit the dust gap radius based on the radial profile of the continuum observations, using an inner disk that extends to 35 au as revealed by scattered light observations (Oh et al. 2016; Thalmann et al. 2016). We then varied the flaring index, ψ, and the dust depletion in the gap, δ_d, to roughly fit the SED and continuum radial profile. The flaring index is low, $\psi = 0.075$, consistent with a flat disk. The dust mass is fixed to 5.8×10^{-4} M$_\odot$ based on the lower limit from the continuum observations (Isella et al. 2012). This dust mass agrees well with the slope of the SED beyond 1 mm (see Fig. 3.3), given the adopted grain size distributions and ISM-like grain composition. We included three rings to account for the observed continuum rings, and varied the height of these to match the radial profile of the continuum observations. The way these dust rings are treated results in a decreased model gas-to-dust ratio in these rings, consistent with the upper limits of 68 and 62 constrained by Facchini et al. (2020). The cavity is not completely empty in our model, to account for the third continuum ring inside the dust cavity observed in the 1.3 mm continuum. Clearing a large cavity from dust between 35 and 63 au (dashed lines in Fig. 3.3) does not significantly change the gas temperature structure and has no significant effect on the line emission, as we show in Appendix 3.B (see also the discussion in van der Marel et al. 2015). The parameters of the most representative model are listed in Table 3.3.

3.4.3.2 Fitting the gas density distribution

The second step in constraining the model is determining the gas density distribution, with γ and R_c constrained by the CO isotopologue lines. For that purpose we ran a grid of models ranging between 50 au $< R_c <$ 150 au and $0.5 < \gamma <$

4 and took the parameters that reproduced the radial profiles of the CO isotopologue lines the best beyond 200 au. The gas gap is constrained by high-resolution ^{13}CO and C^{18}O observations with ALMA. The gas surface density inside the gap at 15 au ($\sim$0.1 g cm^{-1}; see Fig. 3.3) is consistent with upper limits on the total column density determined using C^{18}O (Leemker et al. 2022a), but is an order of magnitude higher than the column density upper limit inside 0.3 au determined from ro-vibrational CO upper limits (Salyk et al. 2009). Lowering the gas surface density in the gap further results in underproducing C^{17}O and ^{12}CO inside the gas gap. We find that LkCa 15 is a large, flat, massive disk with significant structure inside 100 au in both gas and dust.

We used the C$_2$H flux to determine the C/O ratio in the disk. The elemental carbon depletion and gas mass are then based on the CO isotopologue data, N$_2$H$^+$, CN, and the HD upper limit. To study the degeneracy between the carbon abundance and the gas mass, we run a grid with models for gas-to-dust ratios of [205, 100, 63, 39, 25, 15, 10, 4, 2, 1] and carbon depletion factors [1, 2, 4, 8, 16, 32]. This results in a range of gas masses between 0.1 M$_\odot$ and 5×10^{-4} M$_\odot$. We keep the dust mass fixed at a value of 5.8×10^{-4} M$_\odot$. We allowed a modeled emission line uncertainty by a factor of 2 to find a confined region where the model is consistent with the data. Confining the region to the model uncertainties circumvents the dependence of the best fit on the S/N of the lines, since the brightest lines (e.g., CO and CN) are not the most sensitive to variations in gas mass and carbon abundance. The choice of a factor of 2 is motivated by an earlier work from Kama et al. (2016a), where the authors varied the most impactful modeling parameters to determine the effect on the total line flux for CO and isotopologues. Also, Bruderer et al. (2012) and Bruderer (2013), in their benchmark of the DALI model, found deviations in flux within a factor of two compared to similar modeling codes due to uncertainties in the reaction rates and desorption temperatures. The geometrical structure of the disk is constrained in this work due to the wealth of data available for LkCa 15. More specific uncertainties and the dependence of the molecular emission flux on important parameters are described in Sect. 3.6. In Appendix 3.B, we present the result of variations in key parameters and their influence on the total line flux.

3.5 Results

3.5.1 Gas distribution

Figure 3.2 presents the radial profiles and the total fluxes of the best-fitting model. We find that a characteristic radius of $R_\mathrm{c} = 85$ au and $\gamma = 1.5$ fit the emission best at large radii.

3.5.1.1 HD

The HD $J = 1 - 0$ emission in the model is confined to the inner region < 200 au (see Fig. 3.5), where the gas temperature is high enough ($30 - 70$ K, see also Trapman et al. 2017) to populate the higher levels. This relatively small emitting region is a direct result of the flat geometry of the disk, which means that regions further out in the disk are relatively cool. This makes the total HD $J = 1 - 0$

Table 3.3: LkCa 15 best-fit model parameters

Parameter	Symbol		Value
Dust sublimation radius	$R_{\rm subl}$	(au)	0.08
Outer grid radius	$R_{\rm out}$	(au)	1000
Characteristic scale height	$h_{\rm c}$		0.08
Flaring index	ψ		0.075
Characteristic radius	$R_{\rm c}$	(au)	85
Density power law coefficient	γ		1.4
Settling parameter	χ		0.2
Mass fraction large grains	f_ℓ		0.98
Gas surface density	$\Sigma_{\rm c}$	**(g cm^{-2})**	**2.7**
Total gas mass	$M_{\rm g}$	**(M$_\odot$)**	**1.2** $\times 10^{-2}$
Gas-to-dust ratio	**gdr**		**15**
Total dust mass	$M_{\rm d}$	(M$_\odot$)	5.8×10^{-4}
Dust gap radius	$R_{\rm gap,d}$	(au)	35
Dust gap depth	$\delta_{\rm d}$		2×10^{-4}
Gas gap radius	$R_{\rm gap,g}$	(au)	15
Gas gap depth	$\delta_{\rm g}$		1×10^{-4}
Cavity radius	$R_{\rm cav}$	(au)	63
Dust cavity depth	$\delta_{\rm cav,d}$		1×10^{-1}
Gas cavity depth	$\delta_{\rm cav,g}$		3×10^{-2}
Ring 1	$R_{\rm ring1}$	(au)	63 – 78
Scaling in ring 1	δ_{r1}		3
Ring 2	$R_{\rm ring2}$	(au)	96 – 112
Scaling in ring 2	δ_{r2}		4
X-ray luminosity	$L_{\rm X}$	(erg s^{-1})	1×10^{30}
X-ray temperature	$T_{\rm X}$	(K)	7×10^{7}
Cosmic ray ionization rate	ζ	(s^{-1})	5×10^{-17}
Carbon abundance	C/H		3.4×10^{-5}
Oxygen abundance	O/H		3.4×10^{-5}
C/O ratio	C/O		1

Notes. bold text indicates the parameters that are varied in the 2D grid

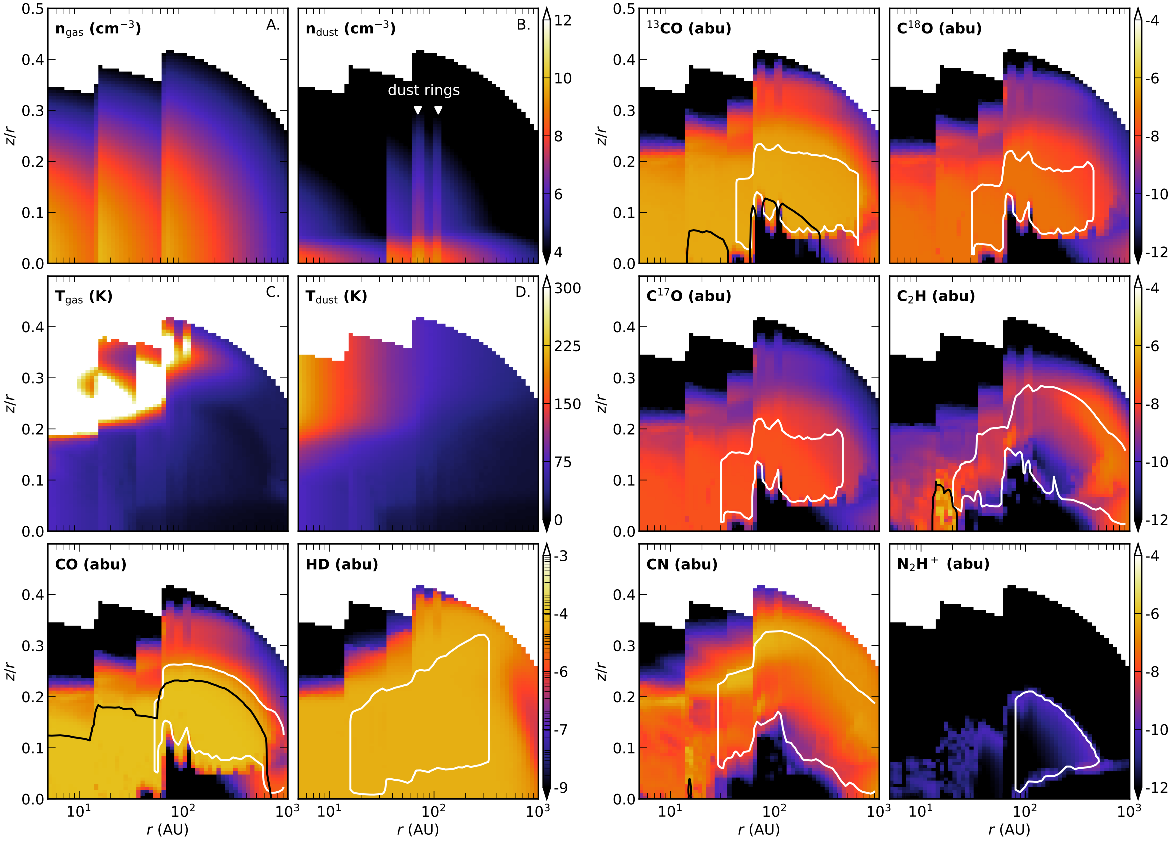

Figure 3.5: Overview of the DALI model output. The four panels left top (A. – D.) present the gas and dust density structure and the gas and dust temperature, respectively. The other panels present the molecular abundances of the molecular transitions in the most representative DALI model, assuming a gas-to-dust ratio of 25 and a carbon depletion factor of 4. The white contours represent the region where 95% of the emission originates, the black lines show the $\tau = 1$ surface for the optically thick emission lines.

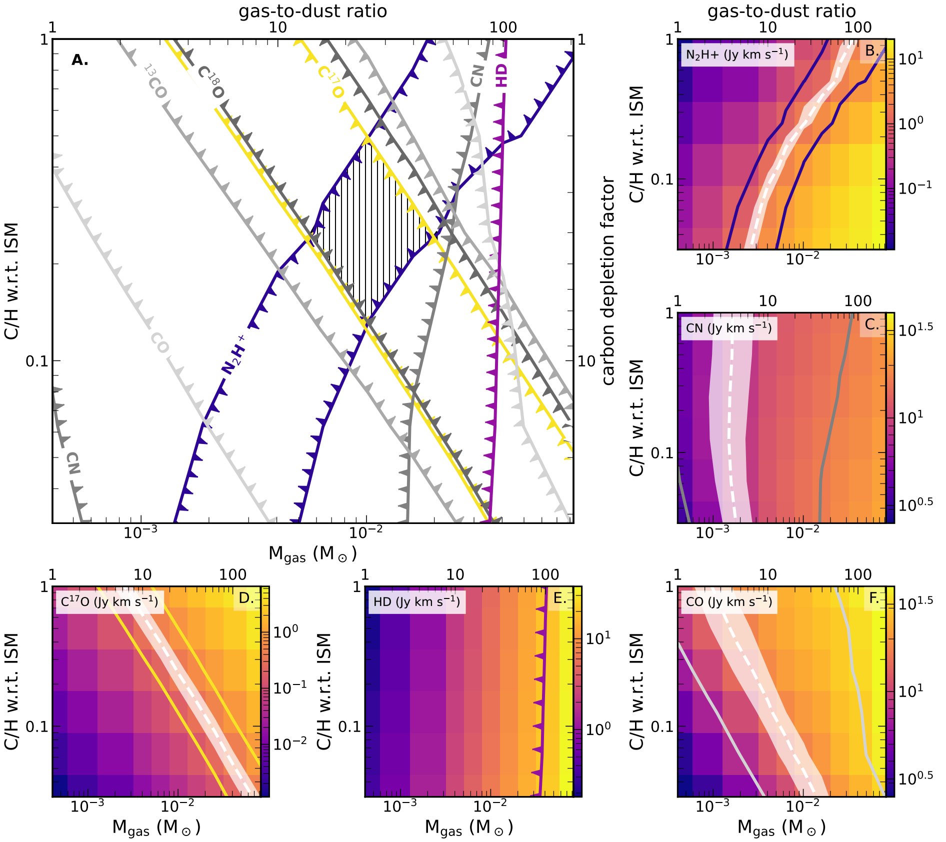

Figure 3.6: Results of the 10 × 6 model grid with carbon abundance versus disk gas mass. Panel A shows the limits on C/H and M_{gas} for each emission line, assuming a model uncertainty of a factor of 2. The hashed region denotes the parameter space that matches with all the observed emission lines. Panels B. – F. show the line flux of key C/H abundance and gas mass tracers N_2H^+, CN, $C^{17}O$, HD, and ^{12}CO, respectively, for the same grid of models. The white contours depict the observed flux with observational uncertainty in shaded region. The colored contours mark an average deviation of the model by a factor of 2, the same as in the main panel. The HD observation denotes an upper limit.

flux susceptible to temperature variations inside the cavity at 63 au and changes in the level of gas depletion with respect to the dust.

3.5.1.2 CO isotopologues

Using the high-resolution CO isotopologue data, we find that the gap inside 35 au is less depleted in gas than in dust, but a significant gas depletion of a factor of 3×10^{-2} throughout the cavity is necessary to explain the central dip observed in ^{13}CO and C^{18}O. The inner disk inside 15 au is depleted further in gas up to a factor 10^{-3} (see Fig. 3.3). This is consistent with earlier findings in Leemker et al. (2022a); they report a gas cavity size ∼15 au based on the line wings and radial profile of high S/N CO isotopologue data. The two steps in gas depletion (see the top-left panel of Fig. 3.3) that were necessary to fit the CO lines could be a result of gradual gas depletion inside the cavity.

The best-fitting model reproduces ^{13}CO $J = 2-1$, C^{18}O $J = 2-1$, C^{17}O $J = 2-1$ and ^{13}CO $J = 6-5$ within the 1σ error at most radii. The ^{13}CO and C^{18}O emission is predicted to be moderately optically thick in the region just outside the gas cavity, but the C^{17}O emission is optically thin throughout the disk. This is consistent with the observations that show that the disk integrated C^{18}O/C^{17}O ratio of 3.1 is consistent with the expected ISM abundance ratio of 3.2. The models are unable to reproduce the small bump at 500 au observed in both the C^{17}O and C^{18}O radial profiles (see Fig. 3.2). This enhancement may be caused by non-thermal desorption processes of CO from the ice due to enhanced UV penetration or a slight change in C/H ratio as a result of infalling pristine material.

The ^{12}CO line is highly optically thick throughout the largest part of the disk (see Fig. 3.5) and thus primarily sensitive to temperature. Our model reproduces the radial profile of this line and is consistent with the vast size of the disk (see Fig. 3.2). The ^{12}CO model is somewhat too bright in the outer regions of the disk between 300 – 700 au, by about a factor of 1.5. The largest recovered angular scale of the ^{12}CO data is r ∼600 au, which likely explains part of the flux that is missing in the outer regions. Changing the geometry (i.e., h_c and ψ) does not change the temperature structure sufficiently. The disk is flat (see Fig. 3.4), and changing h_c will only marginally affect the temperature of the highest layers in the disk where the CO and CN emission originate. Lowering the gas mass of the system lowers the height of the emitting layer and results in less flux contribution across the disk, matching the data better. Altering the settling parameters χ or f_ℓ (see Eq. 3.2), as suggested by McClure et al. (2016), changes the temperature in the upper layers and would allow for better fitting of ^{12}CO. However, this results in decreased temperatures that would lead to unrealistically low CO isotopologue fluxes, even with increased values for γ and ISM C/H abundance.

3.5.1.3 N-bearing species

The N_2H^+ emission is confined to the inner 300 au and is in general well reproduced by the model. N_2H^+ is predominantly formed in regions where the N_2 abundance dominates the CO abundance, for example, as a result of differences in their desorption temperature or photo-dissociation rate. Qi et al. (2019) show that the emission can be separated in an extended component, attributed to the small layer between the (vertical) N_2 and CO snow surfaces, and an additional ring at ∼50 au due to the difference between the (radial) N_2 and CO snowline. The ring at ∼50 au is underproduced in our model (see Fig. 3.2), which is likely because of the steep temperature gradient just outside the cavity. The difference in desorption temperature between N_2 and CO is only 3 – 7 K (Bisschop et al. 2006) which means that the location of the CO and N_2 snowline cannot be determined accurate enough due to the uncertainty in the temperature structure and cavity properties of the system. Using the location of the brightest ring in the N_2H^+ emission, Qi et al. (2019) find that the midplane CO snowline is located at 58^{+6}_{-10} au. This value is consistent with the location of the midplane CO snowline in our model. Assuming a CO freeze-out temperature of 20 K we find that the snowline in our model is located at 66 au, just outside the cavity. Additional X-ray ionization close to the star, which is not taken into account in our modeling, and a locally decreased CO abundance closer to the snowline (see Krijt et al. 2020) could also partially explain the differences between the observations and our model.

The CN emission is moderately optically thick in some of the hyper-fine structure lines, especially in the strongest blended lines. The best-fitting model roughly follows the shape of the radial distribution (see Fig. 3.2), but the modeled total flux is too high by nearly a factor of 2. Such a difference is entirely consistent with uncertainties in chemical reaction rate coefficients of the outer disk nitrogen chemistry. Changing the nitrogen abundance in the outer disk does not have a large effect on the CN abundance (see Fig. 3.B.1) and there is no clear physical reason to assume that the nitrogen abundance is lower than the ISM value (see also). A low gas mass is able to reproduce the CN line, as we show in Fig. 3.2. Other important parameters have hardly any effect due to the high elevation of the emitting layer in the disk (see App. 3.B). The CN emission is located mainly between a height of $z/r = 0.2 - 0.3$, higher than the other tracers analyzed in this work.

3.5.2 Disentangling gas mass and elemental abundances

The gas mass and elemental abundances are interdependent for most tracers. For optically thin CO isotopologues, for example, one determines the total CO mass rather than either the CO abundance or gas mass. To break this degeneracy we ran a grid of 60 models with varying mass and carbon abundance, as described in Sect. 3.4.3.2. In Fig. 3.6, we present the integrated line flux of the key molecules for these models with disk gas mass ranging from 0.1 $M_\odot$ – 5×10^{-4} $M_\odot$ and system-wide volatile carbon depletion between 1 and 32 with respect to the ISM. We overplot the observed total line fluxes as a dashed white line and colored contours at a factor of 2 for comparison. The colored regions are combined in the main panel for easy comparison of the molecules.

3.5.2.1 HD

The HD flux is independent of the carbon abundance, as expected, and changes almost directly proportional with the disk gas mass. This indicates that changes in temperature corresponding to the variations in the gas mass do not have strong influence on the emitting region of HD. The observed upper limit of HD constrains the gas mass to be lower than 0.05 $M_\odot$, which gives reliable evidence that the total disk gas mass is lower than expected from the total dust mass ($5.8\times10^{-4}M_\odot$) and the canonical ISM value for the gas-to-dust ratio of 100.

3.5.2.2 CO isotopologues

$C^{17}O$ has a near-linear relationship between carbon abundance and gas mass, which indicates that the emission is fully determined by the total CO mass in the system. The other CO isotopologue emission lines follow similar trends as $C^{17}O$, but are slightly less sensitive to changes in gas mass, as these lines are optically thick at least in some parts of the disk. The optically thick ^{12}CO line prefers lower gas masses, for which the emitting surface moves to colder layers deeper inside the disk, decreasing the modeled flux at larger radii (see Sect. 3.5.1). The total flux of ^{12}CO changes by less than an order of magnitude over the two orders of magnitude in gas mass, which shows that the temperature dependence of the optically thick tracers is much less sensitive to the gas mass than the density dependence of the optically thin tracers.

3.5.2.3 N-bearing species

We find that the N_2H^+ emission is strongly dependent on the total gas mass in the system, changing almost in direct proportion with it. N_2H^+ behaves opposite to CO: it increases in line strength by lower carbon abundances due to less competition with CO for ${H_3}^+$, and less conversion from N_2H^+ to HCO^+ by direct reaction with CO. The CN flux varies by only a factor of ~3 over two orders of magnitude change in gas mass and is roughly independent of the carbon abundance.

3.5.2.4 Combining tracers

Without a robust detection of HD, it is not possible to determine either the C/H abundance or the gas mass because all known other tracers vary as function of both quantities. The optically thick tracers CO and CN could in principle be used, but their dependence on the temperature is weak, and the temperature structure is less constrained in the models than the density distribution. However, combining the different tracers (Fig. 3.6) we find a confined region in the modeling parameter space, $M_{\rm g} = 0.01^{+0.01}_{-0.004}$ $M_\odot$; $C/H = 3 \pm 1.5 \times 10^{-5}$, that agrees within a factor of 2 with the CO isotopologue fluxes, HD upper limit, CN and N_2H^+. All optically thin tracers are consistent within the observational uncertainty, assuming the usual 10% calibration error.

3.5.3 Determination of the C/O ratio

The C_2H $N = 3 - 2$ transition changes as function of carbon abundance, but is also prone to variations in the C/O ratio. For that reason we leave this species out of the analysis for the carbon abundance in Fig. 3.6. However, we can use C_2H to deduce the C/O ratio in the system and determine the O/H abundance. We find that the integrated line flux of the C_2H $N = 3 - 2$ transition in our model is not very sensitive to the C/O ratio (see Fig. 3.2) compared to other sources (see e.g., Bosman et al. 2021a). A change in C/O ratio from ISM level (~0.47) to unity changes the total C_2H emission by only a factor of 2, but a little bit of excess carbon, not locked up in CO, (i.e., C/O ratio of 1.1) would make a difference (see Fig. 3.2) since this changes the carbon chemistry considerably. The bulk of the C_2H emission in our model originates from a region at 250 − 750 au, that is contributing less prominently in the observed azimuthally averaged radial profile. The maximum resolvable scale of r ~600 au for that data set should be large enough to pick up this emission in the disk. Changing the C/O ratio in the model mainly has an impact on the emission inside 200 au. With an ISM-like C/O ratio, we underproduce the C_2H emission at $r < 200$ au with an order of magnitude (see Fig. 3.2). To determine the C/O ratio, we ran a grid of models varying the C/O ratio by depleting more oxygen in a range between 0.47 and 1.5. This procedure is repeated for a more massive model (green line in Fig. 3.2). An elevated C/O ratio ~1 matches consistently the centrally peaked emission component, which means that the volatile elemental oxygen abundance in the best-fitting model, 3.4×10^{-5}, is depleted by a factor of 8 with respect to the ISM in the best-fitting model.

3.6 Discussion

3.6.1 Comparison with literature gas masses

Previously, the gas mass of LkCa 15 has been inferred from dust continuum observations (Isella et al. 2012), optically thick ^{12}CO and ^{13}CO emission (Jin et al. 2019) and the HD upper limit (McClure et al. 2016). We find with our method a gas mass of $M_{\mathrm{g}} = 0.01^{+0.01}_{-0.004}$ $\mathrm{M}_{\odot}$. This value agrees with the high-resolution continuum observations and observed dust mass, but the total mass of the system is lower than values usually assumed in the literature due to the lower gas-to-dust ratio. We find that the gas mass of LkCa 15 is an order of magnitude lower than the value previously reported in Jin et al. (2019).

There are three key differences between the models described in Jin et al. (2019) and those presented in this work. The first is the assumed density structure in radial and vertical direction. Our models follow the standard formulation for viscous disks with a power law and exponential taper (see Eq. 3.1) and a Gaussian vertical distribution (see Eq. 3.2). Jin et al. (2019) neglect the exponential taper and solve the hydrostatic equation to find a self-consistent vertical density structure. Neglecting the exponential taper leads to very high values of the power law index; they find $\gamma = 4$, compared to our $\gamma = 1.5$. They show that using lower values for γ, which reproduces their ^{13}CO emission but not ^{12}CO, leads to values for the gas mass that are consistent with that found in this work.

The second difference is the temperature structure. Jin et al. (2019) mainly analyze the optically thick ^{12}CO $J = 3 - 2$ emission that traces the temperature structure rather than the density structure in the disk, which is much less sensitive to the mass than optically thin tracers (see Fig. 3.6). Furthermore, their temperature structure is calculated only by the dust grains and the hydrostatic equation, neglecting any gas heating by the photo-electric effect or cooling by collisions. This leads to an nonphysical, almost vertically isothermal temperature structure and a midplane CO snowline at 300 au that is inconsistent with observations described in Sect. 3.5.1 which put the CO snowline at 60 au.

The third difference is the chemistry that is included. Jin et al. (2019) used a parametrized CO abundance structure assuming a CO abundance of 1.4×10^{-4}, including freeze-out and photo-dissociation, but neglecting any CO chemistry, self-shielding and depletion. With this chemical approach and the adopted gas temperature structure they need to vary the ^{12}C/^{13}C ratio radially by almost four orders of magnitude to reproduce both the ^{12}CO and ^{13}CO emission profiles. The strength of this work is that we reproduce self-consistently the total flux and radial emission profiles of optically thick CO, many optically thin CO isotopologue lines, C_2H, and N_2H^+ in addition to taking the HD upper limit into account.

3.6.2 Comparison of HD with observations

The mass upper limit from HD that we find in this work is more constraining than previous models by McClure et al. (2016). With new evidence from the interferometric data analyzed in this paper, we use a more extended disk structure with a lower average gas temperature. High angular resolution continuum observations have additionally moved the continuum cavity radius further outwards from 39 au to 63 au, which has significant effect on the heating in the region where most HD emission originates (<250 au). The chemical modeling of HD is determined self-consistently with the other chemistry and we include the continuum rings that are important for the temperature balance in the HD emitting region. We show that the present *Herschel* upper limit to HD is less constraining for disentangling the gas mass from the elemental C and O abundances than the CO isotopologues and N_2H^+. However, a robust detection, which would be constraining, would only require a sensitivity ten times better than that of the Herschel observation that yielded the upper limit used here (McClure et al. 2016). A 3σ detection would require a channel rms of $6.3{\times}10^{-19}$ W m^{-2} µm^{-1}.

3.6.3 Modeling of N_2H^+

N_2H^+ is often raised as a potential mass and CO abundance degeneracy breaker, because of its inverse trend with the CO abundance. We retrieve similar trends for LkCa 15 as described in Anderson et al. (2019) and confirmed by Trapman et al. (2022) and Anderson et al. (2022). High N_2H^+ fluxes are found for models with a high gas mass and low carbon abundance, though the observed N_2H^+ flux in this particular case is consistent with moderate depletion and a low gas mass.

The largest uncertainties on the N_2H^+ modeling are the total ionization and the volatile nitrogen abundance. In our modeling, we assume that the ionization is dominated by cosmic rays. The N_2H^+ flux over two observed epochs is similar (Qi et al. 2019; Loomis et al. 2020), which is consistent with ionization set primarily by cosmic rays rather than by (variable) X-rays, which can lead to variations in HCO^+ and N_2H^+ strength (Cleeves et al. 2017). The value for ζ assumed in this work is on the high end for protoplanetary disks. Running a small grid of models with different values for ζ we find that a change by one order of magnitude in ζ leads to a change in N_2H^+ flux by a factor of 3 (see Appendix 3.B), which is consistent with the theoretical $\sqrt{\zeta}$ relation. Our assumed uncertainty on the modeling is consistent with CR ionization rates between 10^{-16} – 10^{-18} s^{-1}. The minimum CR ionization rate that is still consistent with the HD upper limit is

10^{-18} s^{-1}, assuming ISM N/H abundance. Future observations of HCO^+ will help to determine the ionization level in the disk and decrease the uncertainty on the disk gas mass.

As explained in Sect. 3.1, nitrogen is thought to be less affected by volatile depletion processes than carbon and oxygen. Unfortunately, there are no other nitrogen carrying molecules that could constrain the nitrogen abundance and give a handle on the uncertainty of the abundance in the disk. However, using the strict upper limit on the gas mass for the HD observations, we can determine lower limits on the nitrogen abundance based on the N_2H^+ flux, which is sensitive to the nitrogen abundance (see also App. 3.B). Varying the nitrogen abundance between 100 – 0.1 ppm for CR ionization rates 5×10^{-17} and $1 \times 10^{-18} s^{-1}$ gives strict lower limits of 3.8 and 17 ppm on the N/H ratio, respectively, using the gas mass upper limit from the HD observations and corresponding carbon abundance.

3.6.4 Scientific implications

3.6.4.1 Gas-to-dust ratio

Our inferred gas mass for the LkCa 15 disk from thorough modeling of many molecular transitions, including $C^{17}O$ $J = 2-1$, N_2H^+ $J = 3-2$ and the HD $J = 1 - 0$ upper limit is $M_g = 0.01^{+0.01}_{-0.004}$ $M_\odot$. These values correspond to a midplane gas-to-dust ratio of 10 – 50 with locally very low gas-to-dust ratios <10 as a result of the two bright continuum rings attributed with dust traps. Low gas-to-dust ratios in the two continuum rings are consistent with stability related arguments (Facchini et al. 2020). The large amount of dust and the vicinity of the midplane CO snowline just outside the cavity at 63 au (see Fig. 3.5) makes this region very suitable for triggering streaming instabilities (see e.g., Bai & Stone 2010).

3.6.4.2 C/H ratio

Multiple studies find observational evidence for an increase in volatile depletion (on top of the standard freeze-out and photo-dissociation processes) with the age of the system (Bergner et al. 2020; Zhang et al. 2020b; Sturm et al. 2022). The moderate level of carbon depletion, by a factor $f_{\rm depl} = 3 - 9$ with respect to the ISM, that we find for LkCa 15, follows this trend given the young age of the system (2; 0.9 – 4.3 Myr Pegues et al. 2020). Younger stars typically have higher accretion rates, emit stronger in ultra-violet wavelengths and therefore have warmer disks than older sources. The disk temperature structure is thought to play an important role in setting the CO abundance and C/O ratio in the disk, as it determines the size of the region in the disk where CO can freeze out (van der Marel et al. 2021).

However, LkCa 15 could be considered a typical “cold transition disk”, with a large dust mass in regions where CO could freeze out and at least one dust trap beyond the CO snowline that potentially halts the radial drift of CO rich ice. This implies that the level of CO depletion in cold disks might be the result of accumulative conversion of CO on longer timescales, resulting in the evolutionary trend seen in the observations of T Tauri stars. This is in line with modeling of CO conversion and locking up in pebbles that typically happen at timescales of $\sim 10^5 - 10^6$ year (see e.g., Krijt et al. 2020).

3.6.4.3 C/O ratio

The observed C_2H flux in LkCa 15 is consistent with a C/O ratio of ∼1. This value is in agreement with the O/H ratio inferred from deep *Herschel* observations that, unexpectedly, do not find any water emission in LkCa 15 (Du et al. 2017). The water could be hidden if it is only frozen out in parts of the disk with millimeter emission, but it is likely for water to be depleted by a factor of at least 5 − 10 throughout the whole disk, similar to the explanation of the observed flux in HD 100546 and the upper limits of the full sample of the water in star-forming regions with *Herschel* (WISH) sample, resulting in elevated C/O ratios (Du et al. 2017; van Dishoeck et al. 2021a), (see also Pirovano et al. 2022). Comparison with rotational water lines would be very interesting, but was not possible in this case, as there are no observations in HDO and the disk is too cold for observations of the $H_2^{18}O$ line at 203 GHz. The C/O ratio of 1 that we find for LkCa 15 is low compared to other sources like TW Hya C/O = 1.5 − 2 (Kama et al. 2016b). A possible limitation of the C/O elevation is efficient vertical mixing stirring up oxygen rich ice to warmer regions in the disk where it releases oxygen to the gas.

Bergner et al. (2019) find that either high UV penetration or a high level of CO depletion is necessary inside 200 au to explain the centrally peaked C_2H emission component, and low level CO depletion beyond 200 au to explain the extended emission. We show that a constant level of carbon depletion $f_{\rm depl} = 3 - 9$ reproduces both features in our model. A combination of the very flat geometry and deep inner gas cavity enables deep UV penetration. Together with an elevated C/O ratio this produces enough C_2H flux in the inner regions of the disk, without the need for additional carbon depletion.

3.7 Conclusions

Determining the gas mass and volatile elemental abundances of C and O in protoplanetary disks is crucial in our understanding of planet formation. In this work we present new NOEMA observations of LkCa 15 in the CO isotopologues $C^{17}O$, $C^{18}O$, ^{13}CO, and CN. Combining these observations with archival N_2H^+, C_2H, and HD data and high-resolution CO isotopologue data we constrain the gas mass and C/H and O/H abundances in the disk using physical-chemical modeling. We summarize our findings below:

- Using optically thick CO and optically thin CO isotopologue lines, we are able to construct a model that reproduces all analyzed disk integrated emission fluxes within a factor of 2. The radial profiles of continuum and emission lines are reproduced by the model in all cases.

- Using the combination of N_2H^+, $C^{17}O$ and the HD upper limit, we constrained the gas mass of LkCa 15 to be $M_{\rm g} = 0.01^{+0.01}_{-0.004}$ $M_\odot$, compared with $M_{\rm d} = 5.8 \times 10^{-4}$ $M_\odot$. This is consistent with cosmic ray ionization rates between 10^{-16} – 10^{-18} s^{-1}, where 10^{-18} s^{-1} is a lower limit based on the HD upper limit. This gas mass implies that the average gas-to-dust ratio in the system is lower than the canonical value of 100, which means that this particular system could be efficient in producing planetesimals via the streaming instability, especially at the location of the dust traps.

- The CO gas abundance relative to H_2 is only moderately reduced compared with the ISM in the LkCa 15 disk by a factor between 3 – 9. This reduced depletion of elemental carbon is consistent with the age of the system, but contrast with the higher levels of depletion seen in older cold transition disks. This contrast suggests that the long timescales for CO transformation and locking up in pebbles contribute to the variation in the level of carbon depletion seen in T Tauri stars at different stages in their evolution.
- The C_2H emission in the LkCa 15 disk is consistent with a C/O ratio around unity in the bulk of the disk. These findings agree with the non-detection of water in deep *Herschel* observations. Given that the LkCa 15 disk is one of the brightest sources in C_2H, this proves that not all sources with high C_2H flux require C/O ratios significantly higher than unity.

We find that a combination of CO isotopologues, N-bearing species, and C_2H provides good constraints on protoplanetary disk masses, the volatile C/H abundance, and the C/O ratio. Far-infrared HD detections, and complimentary ionization tracers like HCO^+ would greatly strengthen the mass constraints.

3.8 Acknowledgements

This paper makes use of the following ALMA data: 2018.1.01255.S 2018.1.00945.S 2017.1.00727.S 2016.1.00627.S 2015.1.00657.S ALMA is a partner-ship of ESO (representing its member states), NSF (USA), and NINS (Japan), together with NRC (Canada) and NSC and ASIAA (Taiwan), in cooperation with the Republic of Chile. The Joint ALMA Observatory is operated by ESO, auI/NRAO, and NAOJ. This paper is based on observations carried out under project number S20AT with the IRAM Interferometer NOEMA. IRAM is supported by INSU/CNRS (France), MPG (Germany) and IGN (Spain). M.L. acknowledges support from the Dutch Research Council (NWO) grant 618.000.001. Astrochemistry in Leiden is supported by the Netherlands Research School for Astronomy (NOVA), by funding from the European Research Council (ERC) under the European Union's Horizon 2020 research and innovation programme (grant agreement No. 101019751 MOLDISK). We thank the IRAM staff member Orsolya Feher for assistance of observations and data calibrations.

Appendix

3.A HC_3N detection

We also report the detection of HC_3N in the LkCa 15 disk. We identified the HC_3N $J = 23-22$ transition at a rest frequency of 209.230234 GHz with an upper energy level of 120.5 K (Endres et al. 2016) using matched filter analysis (see Loomis et al. 2018). Using a Keplerian mask set by the source properties given in Table 3.1, the response reached a significance of 4.6 at the correct frequency for the HC_3N $J = 23-22$ transition. The stacked HC_3N $J = 31-30$, $J = 32-31$ and $J = 33-32$

transitions were reported as a potential marginal detection in (Loomis et al. 2020). In Fig. 3.A.1 we show the impulse response spectrum with a 100 au Keplerian mask which reaches a peak of 4.6σ. The line is imaged using natural weighting, and at a channel width of 1 km s^{-1} the line reached a peak of 26.8 mJy/beam with a S/N ratio of 4.5. In Fig. 3.A.1 we show the Keplerian masked integrated intensity map which highlights that the emission is compact and mostly within one beam. The integrated flux of the line is 0.18 Jy km s^{-1}, which results in an average column density of $1-5\times10^{13}$ cm^{-2} assuming a range of excitation temperatures between $30-60$ K (similar to that found in Ilee et al. 2021) and an emitting area of 1 beam. This number is consistent with disk-integrated column densities found in the large program Molecules with ALMA at Planet-forming Scales (MAPS), where they find column densities ranging from $2-8\ \times10^{13}$ cm^{-2} in a range of rotational temperatures between $30-60$ K in the sources MWC 480, HD 163296, AS 209 and GM aur. The abundance of HC_3N in disk models has been shown to vary with C/O ratio (Le Gal et al. 2019). Therefore, the detection of HC_3N in the LkCa 15 disk is consistent with the strong C_2H line fluxes and elevated C/O ratio with respect to the ISM.

3.B Modeling robustness

The effect of the C/O ratio, C/H abundance and the gas mass on the model is discussed in detail in Sect. 3.5. In this section the effect of other parameters such as the N/H abundance, ζ, f_ℓ and the extra dust in the cavity is investigated.

3.B.1 Parameter dependence

The results for a grid with varying specific model parameters are presented in Fig. 3.B.1. We vary the nitrogen abundance between $10^{-4}-10^{-7}$, ζ between $10^{-16}-10^{-19}$ s^{-1} and f_ℓ between 0.99 and 0.5. Variations in the nitrogen abundance have no effect on the CO lines as these abundances are constrained by the

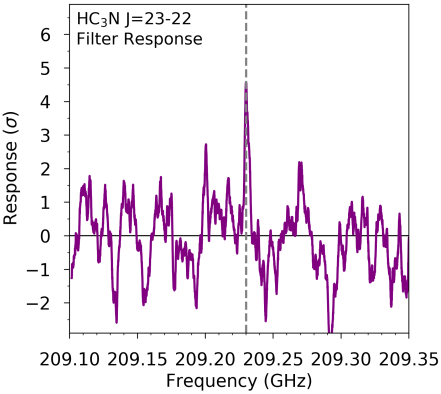

Figure 3.A.1: Left: filter response for a Keplerian mask, the HC_3N $J=23-22$ transition is marked with a dashed line. Right: Keplerian masked integrated intensity map. The beam is shown in the bottom left corner.

availability of oxygen for C/O = 1. CN depends moderately on the nitrogen abundance, changing only a factor of two over 4 orders of magnitude difference in C/N. This means that CN is not a dominant carrier of N but that its abundance is set by other quantities such as the UV flux. The N_2H^+ emission is very sensitive to the nitrogen abundance, as the CO/N_2 ratio has to be low to form N_2H^+ efficiently (see the discussion in Sect. 3.5.1.3). Unfortunately, we do not have the tools to determine the N/H abundance separately, considering CN is not sensitive to the N/H abundance. Nitrogen is thought to be less depleted than carbon (Bergin et al. 2015; Cleeves et al. 2018; Visser et al. 2018), given that the level of carbon depletion is low in this system the assumption of ISM level N/H is valid, but requires additional attention in the future.

Changing ζ has only effect on the optically thin CO lines as the rare CO isotopologues are less efficient in self-shielding against destruction. The ionization balance in the disk is mainly set by ζ, which results in a moderate dependence of N_2H^+ on ζ as discussed in Sect. 3.6.3.

Lowering f_ℓ will impact the vertical temperature structure as more surface area per dust mass unit is moved to the upper layers of the disk. High values for the large grain fractions are motivated by studies that find that mm-size dust can form on timescales of 10^5 yr (Ubach et al. 2012; Birnstiel et al. 2016). Lower values of f_ℓ are one of the only options to decrease the CN and ^{12}CO flux and would increase the mass upper limit of the HD emission as it decreases the size of the HD emitting region. However, the effect on CN and ^{12}CO is small and physical values $f_\ell < 0.9$ result in underproducing the CO isotopologue emission even taking higher C/H abundances and gas masses into account.

3.B.2 Dust component in cavity

Motivated by the millimeter dust continuum observations presented in Facchini et al. (2020) we included a small contribution of dust inside the cavity to improve the fit on the millimeter continuum radial profile (see Fig. 3.3). This third dust ring could be a result of diffusing small grains inside the cavity or a planet. In the bottom panel of Fig. 3.B.1 we compare the model fluxes with a model that uses the conventional transition disk setup with a cleared cavity and a small 1 au inner disk (following the dashed line in Fig. 3.3). The dust surface density in the cavity in our fiducial model does not have a significant effect on the disk integrated line fluxes.

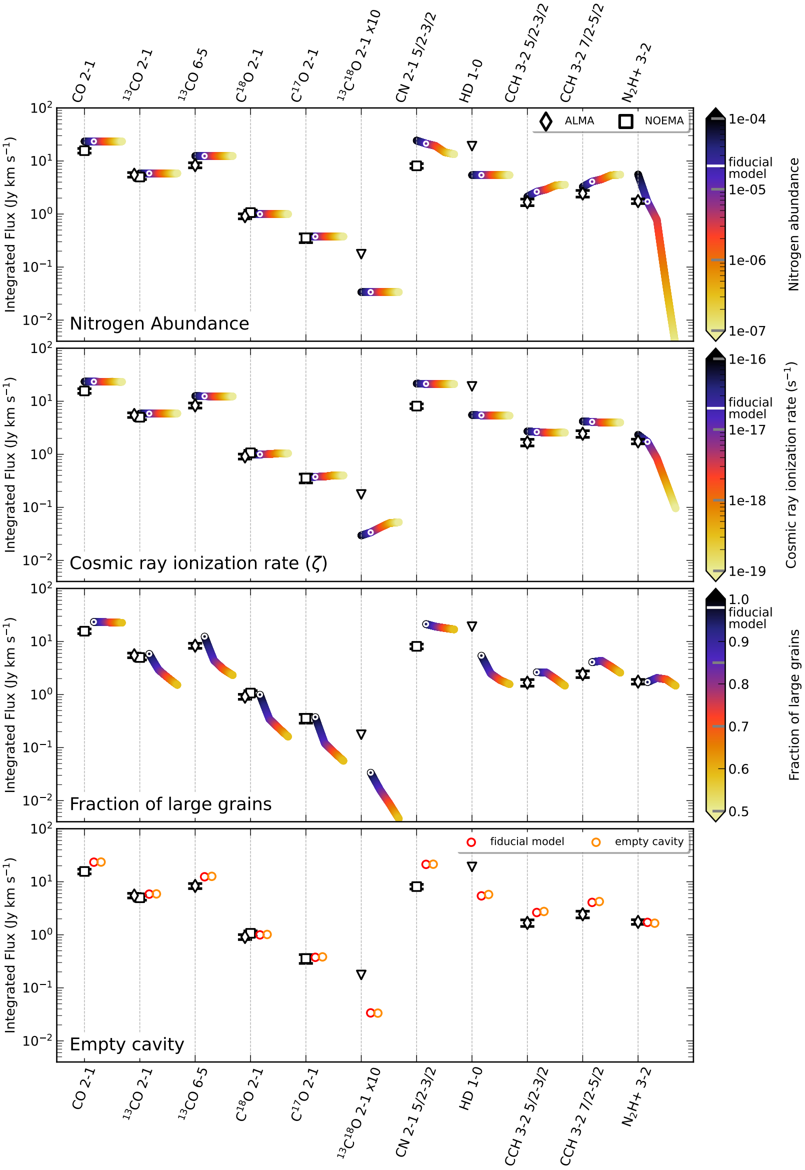

Figure 3.B.1: Total flux dependencies of the various molecules on the main parameters in the model. From top to bottom: Nitrogen abundance, cosmic ray ionization rate ζ, fraction of settled large grains f_ℓ. Data grid points and the fiducial model are shown in the color bar as grey and white tickmarks, respectively. The color bars represent interpolated values between these models. The fiducial model is shown in the plots as a white dot. The bottom panel shows the result for a similar model as the fiducial model, but with a cleared cavity between 1 – 63 au (see Fig. 3.3). Note that the fiducial model is the same as the “best” model in Fig. 3.2.

Chapter 4

The edge-on protoplanetary disk HH 48 NE
I. Modeling the geometry and stellar parameters

J. A. Sturm, M. K. McClure, C. J. Law, D. Harsono, J. B. Bergner,
E. Dartois, M. N. Drozdovskaya, S. Ioppolo, K. I. Öberg,
M. E. Palumbo, Y. J. Pendleton, W. R. M. Rocha, H. Terada, and
R. G. Urso

A&A 677, A17 (2023)

Abstract

Context. Observations of edge-on disks are an important tool for constraining general protoplanetary disk properties that cannot be determined in any other way. However, most radiative transfer models cannot simultaneously reproduce the spectral energy distributions (SEDs) and resolved scattered light and submillimeter observations of these systems because the geometry and dust properties are different at different wavelengths.

Aims. We simultaneously constrain the geometry of the edge-on protoplanetary disk HH 48 NE and the characteristics of the host star. HH 48 NE is part of the JWST early-release science program Ice Age. This work serves as a stepping stone toward a better understanding of the physical structure of the disk and of the icy chemistry in this particular source. This type of modeling lays the groundwork for studying other edge-on sources that are to be observed with the JWST.

Methods. We fit a parameterized dust model to HH 48 NE by coupling the radiative transfer code `RADMC-3D` and a Markov chain Monte Carlo framework. The dust structure was fit independently to a compiled SED, a scattered light image at 0.8 µm, and an ALMA dust continuum observation at 890 µm.

Results. We find that 90% of the dust mass in HH 48 NE is settled to the disk midplane. This is less than in average disks. The atmospheric layers of the disk also exclusively contain large grains (0.3 – 10 µm). The exclusion of small grains in the upper atmosphere likely has important consequences for the chemistry because high-energy photons can penetrate very deeply. The addition of a relatively large cavity (∼50 au in radius) is necessary to explain the strong mid-infrared emission and to fit the scattered light and continuum observations simultaneously.

4.1 Introduction

Protoplanetary disks that are viewed at high inclination to the line of sight provide a unique opportunity to study the physical structures and processes that give rise to the formation of planets. In these systems, the cold outer disk occults both the star and the warm inner disk. This reveals the optical and infrared emission in scattered light from small dust grains in the upper disk layers, as resolved in a limited number of Hubble Space Telescope observations (Padgett et al. 1999) and ground-based telescopes. Since the scattered light is highly sensitive to the grain properties, these observations can be used to infer the grain size distributions and bulk composition (Pontoppidan et al. 2005, 2007). At submillimeter wavelengths, the vertical distributions of gas and millimeter-sized dust can be resolved with Atacama Large (sub-)Millimeter Array (ALMA), for example, which allows direct observations of the temperature structure of the gas, of the CO snowline in disk atmospheres, and of dynamical dust processes such as settling and radial drift (Dutrey et al. 2017; Podio et al. 2020; Teague et al. 2020; Flores et al. 2021; Villenave et al. 2022). The combination of these resolved infrared and submillimeter observations allows deriving these fundamental physical quantities directly, without the integrated optical depth effects seen in face-on disks.

Although the resolved observations may be more straightforward, the modeling of edge-on disks presents three unique challenges. First, the stellar light is blocked, which means that the stellar properties for any given disk are generally poorly constrained. Second, the inner disk midplane is also occulted, which hides potential radial structure that might impact the physical structure of the disk. Several studies have found suggestive evidence for hidden cavities or gaps in edge-on disks using submillimeter observations, but the impact of this on the spectral energy distribution (SED) is unclear (Sauter et al. 2009; Madlener et al. 2012). Third, the infrared and submillimeter emissions trace very different regions of the disk and are impacted by the details of the dust-gas dynamics in the vertical and radial directions. This means that modeling multiwavelength observations including scattered light observations and resolved millimeter emission often converges to different physical models for the individual observables, or does not match the SED (Wolff et al. 2017, 2021). Furthermore, the scattered light continuum emission may involve complicated anisotropic radiative transfer from stellar radiation due to the nontrivial scattering functions as well as mid-infrared radiation from the warm inner disk (Pontoppidan et al. 2007).

In this paper, we solve these challenges using multiwavelength observations and modeling to find a model that reproduces all key observables. We focus on the edge-on protoplanetary disk HH 48 NE in the Chamaeleon I molecular cloud, which is part of the *James Webb* Space Telescope (JWST) early-release science program Ice Age (proposal ID: 1309, PI: McClure). This disk is spatially resolved by the HST (Stapelfeldt et al. 2014) and by ALMA (Villenave et al. 2020), which allows us to determine the disk geometry and the dynamical stellar mass. This paper serves as a stepping stone toward understanding upcoming resolved JWST ice observations of HH 48 NE in the mid-infrared and is the first in a short series of papers. In this series, we combine our knowledge of the disk geometry and radiative transfer to robustly quantify future inferences from mid-infrared ice observations. In this first paper (Paper I) of the series, we introduce the source and constrain the stellar properties and disk geometry. In Sturm et al. (2023d, Paper II), we use the constraints from this work on the source structure to model the icy composition of HH 48 NE and determine how well we can constrain the chemistry from resolved and unresolved scattered light observations. In later papers, we will present resolved observations and compare them with our models to ultimately measure the ice chemistry in planet-forming regions in the disk and explore what determines the chemical composition of planetary atmospheres and surfaces.

The structure of this paper is as follows: We introduce the HH 48 source and existing observations that are used for a comparison to the models in Sect. 4.2. We then describe the model setup and the fitting procedures we used in Sect. 4.3. In Sect. 4.4 we present the fitting results, which we discuss in detail in Sect. 4.5. Sect. 4.6 summarizes the results and contains our conclusions.

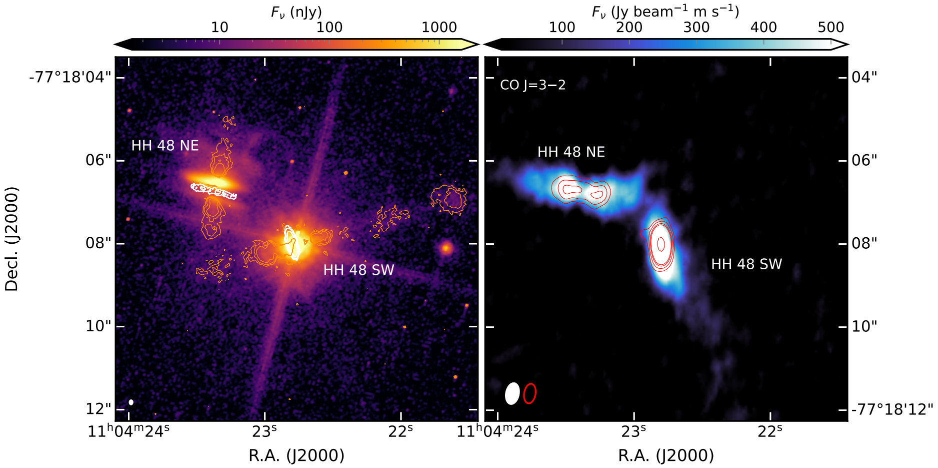

Figure 4.1: Overview of the HH 48 system.
Left: Scattered light observations of HH 48 with HST at 0.8 μm on a logarithmic scale to highlight the weak features. The jets observed with HST at 0.6 μm are overlaid in orange, and the ALMA Band 6 continuum (1.3 mm) is overlaid in white. The beam of the ALMA Band 6 observations (0″.10×0″.07) is shown in the lower left corner.
Right: The integrated CO $J = 3 - 2$ emission in HH 48, with Band 7 continuum (0.89 mm) contours overlaid in red. The beams of both observations (0″.51×0″.31) are shown in the lower left corner.

4.2 Source and observational data

4.2.1 Source description

HH 48 (R.A.: $11^{\mathrm{h}}04^{\mathrm{m}}22.8^{\mathrm{s}}$, Decl.: -77°18′08″.0) is a binary system of protostars in the Chamaeleon I star-forming region, with a close to edge-on disk around the northeast protostar and a less strongly inclined disk around the southwest source (see Fig. 4.1). The separation between the two protostars is a projected distance of 2.″3 (425 au). In this work, we focus on the northeast component of the binary, which is referred to as HH 48 NE. HH 48 is located at a distance of 185 pc according to recent *Gaia* measurements (Gaia Collaboration et al. 2016, 2021) of HH 48 SW, and we assumed that HH 48 NE has the same distance. The HH 48 NE disk appears asymmetric in scattered light observations, and its bipolar jet is tilted with respect to the polar axis of the disk midplane by 6°, as observed at optical wavelengths (Stapelfeldt et al. 2014, and see Fig. 4.1). The disk has a sharp cutoff in millimeter continuum emission ($\Delta r/r = 0.4 \pm 0.1$; Villenave et al. 2020) and the gas disk is distorted (see Fig. 4.1). Taken together, this indicates that the disks of the two young systems likely interact with each other.

Little else is known about the system, including its central star and the protoplanetary disk. In the literature, only spectral types for the combined system are found because the separation between the two sources is small. Luhman (2007) reported a K7 spectral type star, which is consistent with an effective temperature of 4000 K. The local visual extinction ($A_{\rm V}$) in the region was estimated to be ∼3 mag based on *Gaia* estimates of nearby background stars (Gaia Collaboration et al. 2021). The inclination of the disk is currently not well constrained. Villenave et al. (2020) reported a lower limit of 68° based on the radial and vertical extent of the disk in the millimeter continuum. No attempts have been published to constrain the inclination from scattered light observations.

4.2.2 Description of observations

The primary constraints on the physical properties and geometry of HH 48 NE are provided by archival HST scattered light observations, ALMA observations, and the SED. In the following sections, we introduce each of these observations.

4.2.2.1 HST observations

The HST observations were obtained using the Advanced Camera for Surveys (ACS) in a single orbit and were first described in Stapelfeldt et al. (2014) (GO program 12514; PI: Stapelfeldt). For comparison with the model, we selected the exposure with the F814W filter at 0.8 µm because this image has the best trade-off between high spatial resolution and the signal-to-noise ratio (S/N), and it is least contaminated by the jet. The pipeline-calibrated observations were taken from the Mikulski Archive for Space Telescopes (MAST). The diffuse local background in the science frame was subtracted by taking the median in an angular mask around the source at a distance of 2″ between position angles (PAs) [−40°,10°] to avoid any contamination by the diffraction spikes and jet emission of the SW companion (see Fig. 4.1). The scattered light observations are presented in Fig. 4.1.

The scattered light observations reveal the two surfaces of the disk separated by the dark lane that is typical for close to edge-on protoplanetary disks. The intensity of the lower half of the disk is weaker by a factor of ∼10 than that of the upper half of the disk, which indicates that the source is inclined by less than 90°. The disk extends radially to 1.″3, or 240 au. The west side of the disk is brighter in the lower surface, which is likely a result of disk asymmetries caused by the companion. The jet of HH 48 NE is detected in optical light (0.6 µm), but is not significantly detected at 0.8 µm. This is likely a result of the strong [O I] lines in the (0.6 µm) filter that trace the jet outflow. No direct starlight is visible at 0.8 µm, which allows us to place tight constraints on the flaring, mass, and inclination of the disk.

4.2.2.2 ALMA observations

Observational details and imaging

We obtained ALMA archival data (2016.1.00460.S; PI: Ménard) of the HH 48 system. These data consist of observations of CO $J = 3-2$ and the 0.89 mm continuum in ALMA Band 7. See Villenave et al. (2020) for a detailed description of the observational setup and details.

The continuum observations were taken from the supplemental data products in Villenave et al. (2020). For the CO gas observations, we recalibrated the data using the ALMA calibration pipeline in CASA `v5.4.0` (McMullin et al. 2007). We then self-calibrated the 0.89 mm continuum using two rounds of phase self-calibration, with solution intervals of 60s and 18s, respectively. The resulting calibration solutions were then applied to the full visibilities before we subtracted the continuum with a zeroth-order polynomial using the `uvcontsub` task.

We then switched to CASA `v6.3.0` for all subsequent imaging. We used `tclean` to produce images of CO $J = 3-2$ with a Briggs `robust` weighting of -2 (uniform weighting) to achieve the highest possible angular resolution. All images were made using the multiscale deconvolver with pixel scales of [0,5,10,25] and CLEANed down to a 4σ level, where σ was the RMS measured from the dirty image. This resulted in a beam of $0''.51\times0''.31$, PA= -11.2° for the CO $J = 3-2$ image. The CO $J = 3-2$ image cubes had a channel spacing of 0.21 km s^{-1} and a root mean square (RMS) value of 23 mJy beam^{-1}channel^{-1}. The right panel in Fig. 4.1 shows the 0.89 mm continuum image and the zeroth-moment maps for CO $J = 3-2$. The CO zeroth-moment map was generated using `bettermoments` (Teague & Foreman-Mackey 2018) with a 2σ clipping. Our reprocessed continuum and that of Villenave et al. (2020) were consistent, so we just opted to use their data.

Additional continuum observations of HH 48 in Band 6 (2019.1.01792.S; PI: Mardones) were obtained from the ALMA archive. These data were observed on 19 September 2021 at a wavelength of 1.3 mm. The observations were carried out in two execution blocks for a total on-source integration time of 2910 s. In the first execution, 42 antennas were used with projected baseline lengths ranging from 15 to 3697 m. In the second execution, 34 antennas were used with baselines ranging from 47 to 8547 m. The observations were taken in the time-division mode, which means that any line emission was unresolved in the ∼40 km s^{-1} wide channels. The data were calibrated using the CASA pipeline `v6.2.1` and self-calibrated using three rounds of phase-only solutions (60s, 30s, and 15s). The continuum image was made by combining the four spectral windows with a Briggs `robust` weighting of 0.5 for a trade-off between sensitivity and angular resolution. This resulted in a beam of $0''.10\times0''.07$, PA= -1.2° with an RMS of 0.07 mJy km s^{-1}channel^{-1}. The left panel in Fig. 4.1 shows the 1.3 mm continuum image on top of the scattered

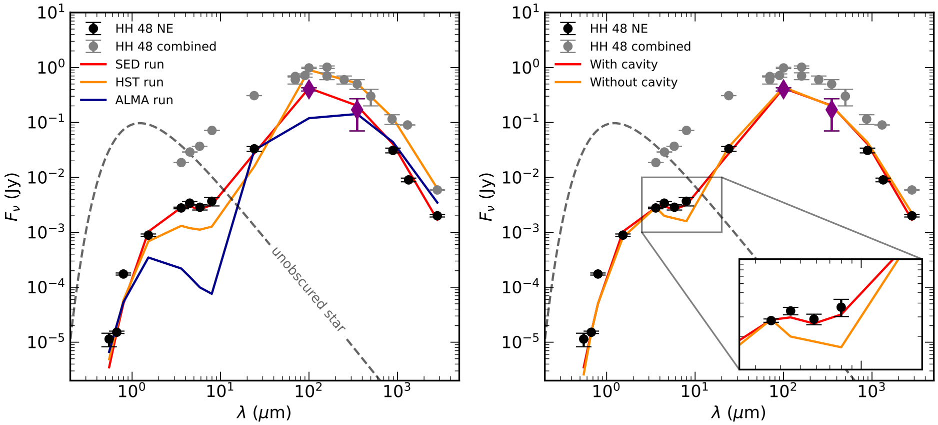

Figure 4.2: Comparison between the observed and modeled spectral energy distributions of HH 48 NE.
Left: Observed SED of HH 48 NE (black) and observations for the two components of the binary system combined (gray). The flux values for HH 48 NE are listed in Table 4.1. The colored lines show the results of the three different MCMC runs described in Sect. 4.3. The dashed gray line shows the 4155 K stellar input spectrum scaled to a distance of 185 pc. The purple diamonds mark the two points that are scaled from the combined spectrum, as explained in the main text.
Right: Comparison of the best-fitting model in the SED runs with and without a cavity.

light observations.

Gas and dust morphologies

The ALMA observations include the NE and SW components of the HH 48 system, which are both detected in CO $J = 3-2$ and continuum emission. The SW source is considerably brighter than the NE source in both line emission and continuum. HH 48 SW has a diffuse tail of low-intensity CO emission that extends $\sim 4 - 5''$ toward the southwest (see Fig. 4.1). However, as HH 48 NE is the primary focus of this paper, further exploration of HH 48 SW is left to future work.

HH 48 NE shows a clear disk-like morphology with evidence of possible radial substructure in both continuum and CO line emission. A few suggestive emission minima and maxima are visible in Fig. 4.1. In the 0.9 and 1.3 mm continuum observations, the disk is resolved along the radial direction with a major axis size of $1''.7$ (310 au at the distance of HH 48 NE), but is unresolved along the vertical direction. The beam of the observations is elongated in the North-South direction due to the southern position of HH 48 on the sky. The size of the CO gas disk extends 2.4 times further than the Band 7 continuum, with radii that enclose 95% of the effective flux of $1''.7$ and $0''.7$, respectively. The CO shows a nonaxisymmetric feature at the western edge of the NE source. At the current resolution of the ALMA observations, it is particularly difficult to discern the origin of this CO feature, which might be the physical disk structure (i.e., a warp), an elevated CO emitting surface (e.g., Law et al. 2021), or dynamical interactions between the outer edges of the NE and SW sources.

4.2.2.3 Spectral energy distribution

The SED was carefully compiled from the literature using observations that resolved the NE and SW components (Fig. 4.2; Table 4.1). All observations with a beam larger than twice the distance between the two sources in the binary (i.e., $>4''.6$) are dominated by the southwest component and should therefore be taken as upper limits. We included observations taken by *Gaia*, the HST, *Spitzer*, and ALMA. Unfortunately, the SED has a gap between 24 and 890 µm, where photometry of the combined system was taken at a resolution that was insufficient to separate the binary pair. No observatory is currently able to observe at this wavelength, so we were forced to scale the combined photometry to account for the NE component. In this part of the spectrum, the continuum mainly corresponds to thermal emission from the cold dust in the outer disk. From 890 – 2800 µm, the flux ratio of the two components remains approximately the same. Therefore, we assumed the same fraction of flux (F_ν = HH 48 NE / HH 48 combined) as was measured at 890 µm for the 100 and 300 µm observations and scaled the *Herschel* intensities by this factor. The addition of these wavelength points, although with intensities including a higher error bar, are essential to discard models with SEDs that significantly deviate in this wavelength range. In Fig. 4.2 we also show the observed fluxes of the two sources combined, which must not be exceeded by either of the binary components. The uncertainties on all data points were increased to 5% to account for short-term variability that often occurs in young systems like these (Espaillat et al. 2019; Zsidi et al. 2022).

4.3 Modeling

4.3.1 Continuum model

Our modeling was based on the full anisotropic scattering radiative transfer capabilities of `RADMC-3D` (Dullemond et al. 2012). The specific steps of our modeling and fitting procedure are described in the following sections.

4.3.1.1 Model setup

The model setup we used was fully parameterized, assuming an azimuthally symmetric disk with a power-law density structure and an exponential outer taper (Lynden-Bell & Pringle 1974),

$$\Sigma_{\mathrm{dust}} = \frac{\Sigma_{\mathrm{c}}}{\epsilon}\left(\frac{r}{R_{\mathrm{c}}}\right)^{-\gamma} \exp\left[-\left(\frac{r}{R_{\mathrm{c}}}\right)^{2-\gamma}\right], \tag{4.1}$$

where Σ_{c} is the surface density at the characteristic radius, R_{c}, γ is the power-law index, and ϵ is the gas-to-dust ratio. The inner radius of the disk was set to the sublimation radius, approximated by $r_{\mathrm{subl}} = 0.07\sqrt{L_{\mathrm{s}}/L_{\odot}}$, and the outer radius of the grid was set to 300 au ($1''.6$). The stellar input spectrum was approximated by a blackbody with temperature (T_{s}) scaled to the stellar luminosity (L_{s}).

Table 4.1: SED of HH 48 NE.

λ (µm)	F_ν (mJy)	Observatory	Angular resolution	Reference
0.55	0.011 ± 0.003	HST / ACS	0.″10	Robberto et al. (2012)
0.67	0.015 ± 0.0008	*Gaia* Band G	0.″14	Gaia Collaboration et al. (2021)
0.79	0.174 ± 0.009	HST / ACS	0.″07	This work
1.53	0.89 ± 0.04	HST / WFC3	0.″13	This work
3.59	2.8 ± 0.1	*Spitzer* / IRAC	0.″9	Dunham et al. (2016)
4.48	3.4 ± 0.3	*Spitzer* / IRAC	1.″1	Dunham et al. (2016)
5.84	2.9 ± 0.3	*Spitzer* / IRAC	1.″4	Dunham et al. (2016)
7.96	3.7 ± 0.7	*Spitzer* / IRAC	1.″9	Dunham et al. (2016)
24.1	33 ± 3	*Spitzer* / MIPS	5.″8	Dunham et al. (2016)
100	400 ± 30	*Herschel* / PACS	5.″9	scaled from Winston et al. (2012)
350	170 ± 100	*Herschel* / PACS	21″	scaled from Marton et al. (2017)
890	31 ± 3	ALMA	0.″4	Villenave et al. (2020)
1339	7 ± 0.7	ALMA	0.″1	This work
2828	2 ± 0.1	ALMA	2.″3	Dunham et al. (2016)

The height of the disk is described by

$$h = h_{\rm c} \left(\frac{r}{R_{\rm c}} \right)^{\psi} , \tag{4.2}$$

where h is the aspect ratio, $h_{\rm c}$ is the aspect ratio at the characteristic radius, and ψ is the flaring index. The dust density has a vertical Gaussian distribution,

$$\rho_{\rm d} = \frac{\Sigma_{\rm dust}}{\sqrt{2\pi} r h} \exp \left[-\frac{1}{2} \left(\frac{\pi/2 - \theta}{h} \right)^2 \right] , \tag{4.3}$$

where θ is the opening angle from the midplane as seen from the central star.

We adopted the canonical gas-to-dust ratio of 100 to scale between the total disk mass and the total mass in dust grains. Dust settling was parameterized by separating the total dust mass over two dust populations: one population of small grains covering the full vertical extent of the disk, and another population with large grains that was limited in height to $X \cdot h$ with $X \in [0, 1]$. The minimum grain size and maximum grain size of the small dust population were allowed to vary to simulate variations in grain growth. The minimum grain size of the large dust population was fixed to the minimum size of the small dust population, and the maximum grain size of the large dust population was fixed to 1 mm. The two dust populations followed a power-law size distribution with a fixed slope of -3.5. The fraction of the total dust mass that resides in the large dust population was defined as f_ℓ. We assumed a grain composition consistent with inter stellar matter (ISM) dust, consisting of 85% amorphous pyroxene $\rm Mg_{0.8}Fe_{0.2}SiO_3$, 15% amorphous carbon, and a porosity of 25% (see, e.g., Weingartner & Draine 2001 and Andrews et al. 2011 for an observational justification of these fixed parameters).

The dust and ice opacities were calculated using `OpTool` (Dominik et al. 2021), using the distribution of hollow spheres (DHS; Min et al. 2005) approach to account for grain shape effects. We used the full anisotropic scattering capabilities of `RADMC-3D` because isotropic scattering assumptions can have a significant impact on the amount of observed scattered light in the near- to mid-infrared (Pontoppidan et al. 2007).

The ALMA continuum and CO gas observations suggest that the system has an inner cavity, which we discuss in more detail in Sect. 4.4.5. To account for this in the models, we removed dust and gas inside $R_{\rm cav}$ by multiplying the surface density by a constant factor $\delta_{\rm cav}$, following the approach taken in Madlener et al. (2012), to simulate the removal of gas and dust in the inner disk region.

In total, we have 14 free parameters that were varied to find the best-fitting model for HH 48 NE: Two stellar parameters ($L_{\rm s}$, $T_{\rm s}$), six geometric parameters ($R_{\rm c}$, $h_{\rm c}$, ψ, i, γ, $M_{\rm gas}$), four parameters describing the two dust populations (f_ℓ, X, $a_{\rm min}$, $a_{\rm max}$), and two variables describing the cavity ($R_{\rm cav}$ and $\delta_{\rm cav}$).

4.3.1.2 MCMC modeling

To find a model that represents HH 48 NE the best, we applied Markov chain Monte Carlo (MCMC) modeling on resolved observations of the disk in scattered light, the highest S/N ALMA Band 7 millimeter continuum, and the SED. MCMC is a method for sampling from probability distributions with an unknown normalization constant to converge to a global minimum in the difference between a model and observations. Since we explored a highly degenerate multiparameter space, we used a parallel tempered approach (Earl & Deem 2005). In parallel tempered MCMC, multiple runs sample from the probability distribution at the same time, each with a different measure (temperature) of how likely low-probability regions in the probability distribution will be crossed. By occasionally exchanging states between these different runs, the chain of interest is less likely to remain stuck in local minima of the probability space. We used the `python` MCMC implementation `emcee` (Foreman-Mackey et al. 2013), using two different likelihood temperatures in the parallel tempered approach.

We used three observables on wich we evaluated our model: a complete SED from 0.5 – 3000 µm (see Fig. 4.2), HST scattered light observation at 0.8 µm (see Fig. 4.1, left panel), and ALMA continuum observation at 890 µm (see Fig. 4.1, right panel). We only used the ALMA Band 7 continuum data because data set has the highest S/N, but we compare the Band 6 continuum data extensively to the model outcome in Sect. 4.4.5. Combining the different observables in one evaluation at every step in the Markov process is nontrivial because the sources of uncertainty are different in each step. Weighting the importance of the individual χ^2 values is therefore not straightforward. For the easiest understanding of the likelihood of each data set given by our model, we conducted three independent MCMC runs with one of the observables as input. We refer to these MCMC runs as the SED run, the HST run, and the ALMA run. An additional MCMC fit on the SED was performed without a cavity in the model for a comparison with the runs with the cavity, and to gauge how robust the different parameters are. We refer to this run as the SED run without a cavity.

The models were evaluated using a χ^2 value,

$$\chi^2(\boldsymbol{m}) = \sum_{i=1}^{N} \frac{(\mu_i(\boldsymbol{m}) - O_i)^2}{\sigma_i^2}, \tag{4.4}$$

where N is the number of observables, μ_i is the modeled observable, O_i is the data points, and σ_i^2 is the corresponding error estimate. The log-likelihood in `emcee` was set to

$$\mathcal{L} = -\frac{1}{2}\left(\chi^2 + \sum_{i=1}^{N} \ln\left(\sigma_i^2\right) + N\ln(2\pi)\right) \tag{4.5}$$

(Wolff et al. 2017).

For the SED runs, evaluating χ^2 is straightforward because we can directly compare the total flux in the model with the observations and their respective uncertainty. The modeled SEDs were corrected for foreground visual extinction. The A_V value was treated as an independent parameter that was determined after every run by reducing the χ^2_SED value to a minimum assuming $A_\mathrm{V} \geq 0$ mag. The correction functions were taken from Cardelli et al. (1989) if A_V <3 mag and from McClure (2009) otherwise. For the HST and ALMA runs, we convolved the ray-traced 2D images with a Gaussian beam/point spread function (PSF) similar to

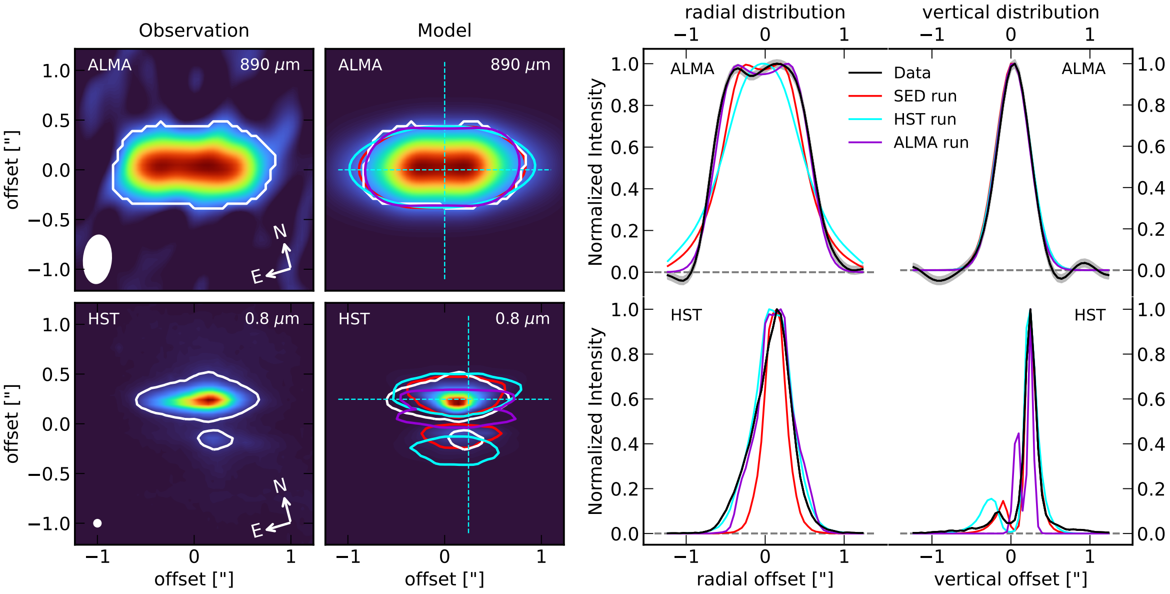

Figure 4.3: Comparison between the ALMA (890 μm, *top*) and HST (0.8 μm, *bottom*) observations with the ray-traced model.
Far left: Observations of HH 48 NE normalized to the peak emission. The size of the beam/PSF is indicated in the bottom left corner. The white lines trace the 5σ contours of the observations.
Center left: Best-fitting model at the same wavelengths as the observation, convolved with a model of the beam or PSF. The colored lines trace the same value relative to the peak flux, as the 5σ contour of the observation in the model images for the SED run (red), the HST run (cyan), and the ALMA run (purple). The dashed cyan line illustrates the position of the radial and vertical cuts shown in the right panel.
Center right: Radial cut through the observations (black) and the three models using the SED (red), the resolved HST observation (cyan), the ALMA observation (purple) (see Sect. 4.3). The radial cuts are normalized to their respective peak flux.
Far right: Normalized vertical cut through the data and models as for the radial distribution. The vertical cut through the HST observations is 0″.25 off-center to obtain the highest S/N of the lower lobe.

that of the observations and rebinned the images to the same resolution as the observations. After this, we used an autocorrelation to find the optimal position of the model. The χ^2 value was then determined over the pixels in the region with a 5σ detection in the data (white contours in Fig. 4.3) to avoid overfitting on noise features. The images were normalized to the peak flux in the observations and models to focus on the spatial distribution without the total flux at only one wavelength in the fit (as opposed to the SED run, which fit the total flux from 0.5 – 3000 µm).

We let 200 walkers (more than ten times the number of free parameters) explore the parameter space for 500 steps in each of the three different runs, resulting in 2×10^5 models per run. A physically motivated prior was applied to the parameter space, which means that we rejected models that were not feasible given our knowledge of the general population of T Tauri stars to avoid long run-times and to facilitate convergence. The priors were uniform distributions within the ranges given in Table 4.2. The disk mass, cavity depletion, grain sizes, and settling fraction were sampled logarithmically to support the variations of many orders of magnitude that are physically possible. The starting position of each of the walkers was randomly sampled using a uniform distribution in a region around a selected model that fit the SED reasonably well. The walkers quickly spread out to sample every corner of the parameter space. The first 100 steps were considered the burn-in stage and were not taken into account for the statistics.

4.4 Results

The results of the individual runs are summarized in Table 4.2, and the uncertainties are given by the 16th and 84th percentiles. The full posterior distributions can be found in Appendix 4.A. The MCMC runs converge to a very similar model in terms of physical parameters and geometry.

In the next section, we describe the results from the four independent MCMC runs on the SED, the HST observation in scattered light, and the ALMA observation of the warm dust continuum. We selected of the best-fitting representative (all parameters within 1σ) models out of each run for a comparison with the data, and we discuss the import of each of the parameters on the geometry and dust distribution of the HH 48 NE disk. The choice of parameters for the best model in each run is indicated in Fig. 4.A.1 and given in Table 4.2 with the corresponding χ^2 value on each observable. The simulated observations are compared to the data in Fig. 4.2 and Fig. 4.3. In the ideal case, all MCMC runs would end in the same place in the parameter space, but this is unrealistic because each of the observables is sensitive to a different subset of the free parameters and because the parameterized model does not account for local changes in surface density, settling, or radial drift, for instance. The benefit of having separate runs for the different observables is that we can provide our own weights for the constraints of the different runs. In this particular case, the outcomes of the different MCMC runs are consistent with each other within the error bars for most parameters (see Table 4.2). The best-fitting model from the SED run was taken as the overall best fit to the data and will be used as a fiducial model in the ice analysis in

Table 4.2: Results of the MCMC modeling for the four runs described in Sect. 4.3.

Parameter	Prior	SED run	HST run	ALMA run	SED no cavity
L_s ($\mathrm{L}_\odot$)	[0.1, 3]	**0.41** $0.44^{+0.11}_{-0.09}$	**0.51** $0.48^{+0.08}_{-0.07}$	**0.58** $0.55^{+0.17}_{-0.17}$	**0.54** $0.50^{+0.10}_{-0.07}$
T_s (K)	[2000, 6000]	**4155** 4500^{+570}_{-557}	**4496** 4176^{+407}_{-643}	**4025** 4357^{+701}_{-764}	**3091** 3463^{+593}_{-593}
R_c (au)	[25, 150]	**87** 88^{+29}_{-25}	**105** 95^{+13}_{-15}	**52** 57^{+14}_{-13}	**86** 90^{+14}_{-14}
h_c	[0.01, 0.4]	**0.24** $0.23^{+0.04}_{-0.05}$	**0.18** $0.19^{+0.02}_{-0.02}$	**0.05** $0.14^{+0.07}_{-0.05}$	**0.21** $0.21^{+0.05}_{-0.03}$
ψ	[0.01, 0.5]	**0.13** $0.16^{+0.04}_{-0.04}$	**0.22** $0.22^{+0.03}_{-0.03}$	**0.25** $0.20^{+0.07}_{-0.04}$	**0.19** $0.20^{+0.03}_{-0.04}$
i (°)	[65, 90]	**82.3** $83.5^{+3.7}_{-2.7}$	**83.5** 83.3 ± 1.1	**88.1** $88.1^{+0.6}_{-1.2}$	**83** $82.1^{+2.2}_{-2.7}$
γ	[0.3, 3]	**0.81** $0.77^{+0.25}_{-0.24}$	**0.89** $0.98^{+0.16}_{-0.18}$	**0.32** $0.48^{+0.12}_{-0.10}$	**0.93** $0.84^{+0.20}_{-0.30}$
$\log(M_\mathrm{gas}$ ($\mathrm{M}_\odot$))	[−4, −1]	**−2.57** $-2.58^{+0.09}_{-0.08}$	**−1.89** $-2.02^{+0.19}_{-0.22}$	**−2.1** $-2.47^{+0.37}_{-0.38}$	**−2.56** $-2.60^{+0.12}_{-0.13}$
$\log(1 - f_\ell)$	[−4, 0]	**−0.94** $1.09^{+0.15}_{-0.17}$	**−0.97** $-0.92^{+0.16}_{-0.19}$	**−1.92** $-1.76^{+0.47}_{-0.72}$	**−1.07** $-1.03^{+0.13}_{-0.13}$
X	[0.01, 0.5]	**0.2** $0.24^{+0.08}_{-0.09}$	**0.27** $0.26^{+0.06}_{-0.05}$	**0.47** $0.27^{+0.08}_{-0.09}$	**0.26** $0.26^{+0.05}_{-0.05}$
$\log(a_\mathrm{max}$ (µm))	[−2, 1]	**0.83** 0.92 ± 0.22	**0.93** 0.88 ± 0.17	**1.1** $1.07^{+0.28}_{-0.22}$	**1.0** $1.10^{+0.29}_{-0.20}$
$\log(a_\mathrm{min}$ (µm))	[−3, 0]	**−0.37** $-0.41^{+0.11}_{-0.09}$	**−0.44** $-0.45^{+0.06}_{-0.04}$	**−0.62** $-0.59^{+0.14}_{-0.27}$	**−0.49** $-0.42^{+0.09}_{-0.06}$
R_cav (au)	[0, 100]	**55** 53^{+14}_{-16}	**42.8** 52^{+17}_{-9}	**80** 74^{+5}_{-10}	-
$\log(\delta_\mathrm{cav})$	[−4, 0]	**−1.8** $-1.70^{+0.47}_{-0.42}$	**−1.76** $-1.77^{+0.19}_{-0.28}$	**−1.5** $-1.67^{+0.24}_{-0.19}$	-
χ^2_SED		46	*3270*	*1109*	88
χ^2_{HST}		*25345*	8842	*40559*	*22595*
χ^2_ALMA		*3737*	*5742*	839	*9497*
A_V		5.1	5.1	5.3	4.9

Notes. The values in bolt are the best-fitting model in that particular run, the values on the right are the median value of the distribution with the 16th and 84th percentiles of the posterior distribution as error. The evaluation (χ^2 value) of the best-fitting model in each run is given for each observable, with the evaluations that are not used in the optimization in italic. Note that the A_V is not sampled like the other parameters, but determined after each run by reducing χ^2_SED to a minimum.

Paper II. This specific model was chosen as it fits the photometric data points in the mid-infrared (see Fig. 4.2), which is crucial for modeling the ices in Paper II and for the comparison with JWST data in later papers. It also reproduces the main features of the ALMA and HST observations (see Fig. 4.3).

4.4.1 Stellar parameters

The best fit stellar parameters are consistent with the K7 spectral type in the literature for the combined system (Luhman 2007). We find a slightly higher mean stellar effective temperature than the typical temperature of ∼4000 K for a K7 star (Pickles 1998), but the uncertainty on the temperature is significant (10 – 15%) in each of the runs. The luminosity is well constrained at 0.4 ± 0.1 $L_{\odot}$ but is partly degenerate with the foreground extinction (A_V) that could not be constrained from other observations due to the obscuration of the star. The visual extinction from foreground clouds is ∼5 in the best-fitting model, which is consistent with *Gaia* measurements of the extinction toward nearby stars.

To better constrain the stellar parameters of HH 48 NE, we applied dynamical mass fitting to the CO $J = 3-2$ rotation map. CO rotation maps can be used to derive the dynamical mass of the HH 48 NE disk, assuming that the gas is in Keplerian rotation around the central star. We generated a rotation map of CO $J = 3-2$ using the quadratic method of `bettermoments` and excluded regions in which the peak intensities were lower than three times the RMS. Fig. 4.4 shows the resulting map. We then fit this rotation map with `eddy` (Teague 2019), which uses the `emcee` (Foreman-Mackey et al. 2013) Python code for MCMC fitting. We used 64 walkers to explore the posterior distributions of the free parameters, which take 500 steps to burn in and an additional 500 steps to sample the posterior distribution function.

We considered only two free parameters for modeling the Keplerian velocity fields: the stellar host mass (M_*), and the systemic velocity (v_{lsr}). Due to difficulties in interpreting the source morphology, as noted in Sect. 4.2.2.2, and the relatively large and asymmetric beam size, we fixed the coordinates of the disk center, which were visually estimated from the CO $J = 3-2$ map. We adopted the best-fit model inclination value of 82.3°. The estimates of M_* were found to be particularly sensitive to the choice of PA, which is again difficult to constrain due to uncertainties in the gas structure of HH 48 NE and the significant non-Keplerian gas motions, as labeled in Fig. 4.4. We thus ran fits with a range of plausible PA values between 80 – 95° in increments of 2.5°. We note that when we adopted the PA value of 75° derived from the continuum in Villenave et al. (2020), a nonconverging fit resulted, which again suggests that HH 48 NE likely has a complex gas and dust structure that is only marginally resolved in the current ALMA observations.

Overall, we find best-fit velocity fields consistent with a v_{lsr} of $\sim 4.4 - 4.9$ km s^{-1} and a stellar host mass of $\sim 1 - 1.4$ $M_{\odot}$. Statistical uncertainties on any individual fit are ∼20 – 40%, which do not include the systematic uncertainties on each fixed parameter. Fig. 4.4 shows a representative fit to the rotation map. Higher angular resolution observations of gas in the HH 48 system would greatly alleviate these difficulties and allow for a significantly more robust dynamical mass determination.

With the modeled evolutionary tracks, we determined whether the combination of stellar parameters we found was theoretically feasible. Siess et al. (2000b) modeled the physical evolution of protostars using the `Grenoble` stellar evolution code in an extensive grid of initial conditions and listed the main stellar properties as a function of time (mass, luminosity, temperature, etc.). Using their evolutionary tracks for solar metallicity, we find that the luminosity (0.41 $L_\odot$) and temperature (4070 K) of the best-fitting model from the SED run are consistent, within the uncertainty of the MCMC runs, with the dynamical mass. These values agree with the literature K7 spectral type, as we discuss further in Sect. 4.5.1.

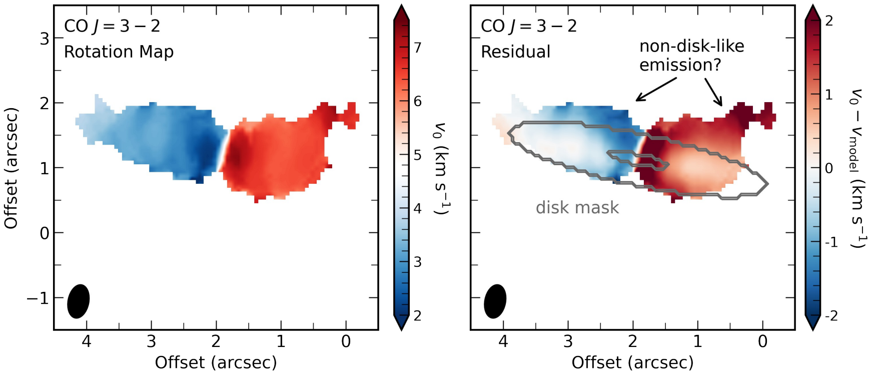

Figure 4.4: Dynamical mass fitting of HH 48 NE.
Left: Rotation map of the ALMA CO $J = 3-2$ observations in HH 48 NE. The spatial offset on the axes is with respect to the telescope pointing (HH 48 SW; R.A.: 166.0953°, Decl.: -77.30207°). The beam size is shown as a black ellipse in the bottom left corner ($0\farcs51 \times 0\farcs31$).
Right: Residuals after subtracting the model from the observations. The gray ellipses indicate the regions we used for the fitting. The innermost two beams were masked to avoid confusion from beam dilution, and the outer radius was visually determined to avoid non-disk-like emission.

4.4.2 Spatial disk parameters

The disk in HH 48 NE has a characteristic radius of ~90 au, with a power-law density index slightly lower than the canonical value of 1. The physical disk size estimate is 30% smaller in the ALMA run than in the SED and HST runs, with a best-fitting $R_{\rm c} = 57^{+14}_{-13}$ au and $\gamma = 0.5 \pm 0.1$, compared to $R_{\rm c} = 95^{+13}_{-15}$ au and $\gamma = 1.0 \pm 0.2$ in the HST observation. The disk appears similarly extended in the ALMA continuum image compared to the scattered light observations (see Fig. 4.1), but with a very steep outer cutoff ($\Delta r/r = 0.4 \pm 0.1$; Villenave et al. 2020). In the model, we show that the disk might be significantly smaller in the millimeter continuum than in the scattered light observations when radiative transfer and optical depth effects are taken into account. This is consistent with most observations of protoplanetary disks (Villenave et al. 2020), and it may be due to radial drift of the largest dust grains. It might also arise because small dust grains follow the gas interaction between the two components (see Fig. 4.1).

The disk is moderately thick with an aspect ratio, h_c, of $0.2 - 0.25$ and a flaring index, ψ, of $0.15 - 0.2$. These values are constrained the most by the HST run, but agree within the error bars with the SED and ALMA runs. h_c and the settling height X are degenerate in the ALMA run because the millimeter continuum wavelengths trace the largest grains that only exist in the large-grain population that is settled with a constant X with respect to the height of the small dust grains and gas. By comparing the outcomes of the SED and HST runs, both of which trace small grains and can therefore constrain the aspect ratio better, we can conclude that the large millimeter-sized grains are settled to 20-25% of the disk scale height. The mass fraction of grains that is settled to the midplane is discussed in Sect. 4.4.4.

The disk is found to be inclined at 82 – 84° from the SED and HST runs. The ALMA MCMC run suggests a higher inclination of 88°, but these high inclinations clearly contradict the scattered light observations (see Fig. 4.3). A similar anomaly has been seen in the extensive modeling of Oph 163131 by Wolff et al. (2021), who reported a similar offset in inclination between the scattered light observations and the ALMA continuum (which was subsequently resolved by observations at a higher angular resolution; Villenave et al. 2022). Because the ALMA image is not resolved in the vertical direction and is only resolved with four to five beams along the radial direction, it is hard to break the degeneracies between the inclination and several other parameters such as h_c and R_c (see Appendix 4.A). In the end, we find that an inclination of ∼83° is more probable based on the appearance of the disk in scattered light, and this inclination reproduces the ALMA image relatively well (see Fig. 4.3).

4.4.3 Mass

The total mass of the disk is determined from the MCMC runs to be $2.5 - 10\times10^{-3}$ $\mathrm{M}_\odot$, assuming a gas-to-dust ratio of 100. The disk mass and fraction of large grains are directly proportional with each other in the ALMA run (see Appendix 4.A) because the ALMA observations only trace the large grains. The mass found in the ALMA run is consistent with the SED run within the systematic error when a best-fit value of $f_\ell = 0.9$ is used. The mass estimate we found based on the HST run is four times higher than the values found in the ALMA and SED runs. High density is needed to explain the broad radial emission seen in scattered light. The SED run fits the west wing of the upper surface in the scattered light image reasonably well (Fig. 4.3), but fails to fit the asymmetric extension on the east side of the disk. However, the higher total disk mass clearly contradicts the SED (see Fig. 4.2), which is visible as an underprediction of flux in the near- and mid-infrared and as an excess of flux at millimeter wavelengths. Therefore, the lower mass estimate is more probable.

Using the continuum flux at 0.89 mm (Villenave et al. 2020) and 2.8 mm (Dunham et al. 2016), we compared these values to the lower limit of the total disk mass from the observed millimeter flux using

$$M_{\mathrm{gas}} = 100\frac{d^2 S_\nu}{B_\nu(T_{\mathrm{d}})\kappa_\nu}, \tag{4.6}$$

where d is the distance, $B_\nu(T_{\mathrm{d}})$ is the Planck function at the isothermal temperature T_{d}, taken as 20 K, κ_ν is the dust opacity at the observed frequency, and the factor 100 is used to convert dust mass into total disk mass. Using our opacities for the large dust grain population, we find an opacity of 9.1 cm^2 g^{-1} and 2.3 cm^2 g^{-1}, corresponding to a mass estimate of $1.2 \pm 0.1\times10^{-3}$ M$_\odot$ and $2.4 \pm 0.3\times10^{-3}$ M$_\odot$ for the observations at 0.89 mm and 2.8 mm, respectively. The mass estimate at 0.89 mm is significantly lower than the estimate at 2.8 mm, which indicates that the observations at 0.89 mm are still optically thick and that we do not trace the full column of dust. Because the column densities along the line of sight increase with inclination, this is not surprising for a disk this massive (see also the discussion in Villenave et al. 2020). The mass we find in the MCMC runs agrees with these direct estimates when the bulk of the disk is assumed to be optically thin at 2.8 mm.

4.4.4 Grain properties

The minimum grain size of the small dust distribution is constrained to be 0.2 – 0.4 µm, excluding nanometer-sized dust grains in the disk atmosphere completely. The maximum grain size of the small dust distribution is constrained to be 8 – 12 µm. The small grain size distribution is best constrained by the mid-infrared part of the SED (5 – 100 µm) and the scattered light observations. The posterior distribution in the ALMA run is much broader because the millimeter wavelength radiation is only changed via the disk temperature structure when the grain size distribution is varied, rather than directly via the scattering properties. However, the estimates based on ALMA agree well with the HST and SED runs.

We consistently find that about 90% of the dust mass is settled toward the midplane in large grains at a maximum height of 20 – 25% of the small grains (see Sect. 4.4.2 for the discussion of the settling height). Both the SED and the HST observations are extremely sensitive to the amount of settling, resulting in small uncertainties on the number of small grains in the disk atmosphere. At inclinations $<85°$, the disk needs to be vertically extended and to have a sufficient number of small dust grains in the upper layers of the disk to block direct lines of sight or strong forward scattering from the star. More dust settling hence quickly results in a strong central peak in the synthesized scattered light image. This is not observed in the HST observation (see also Fig. 5 in Paper II).

4.4.5 Cavity

A cavity must be included in the model to fit all three observables at the same time. To show this, we ran an additional MCMC fit on the SED without a cavity (last column in Table 4.2), and we show the SED of the resulting best-fit model in Fig. 4.2.

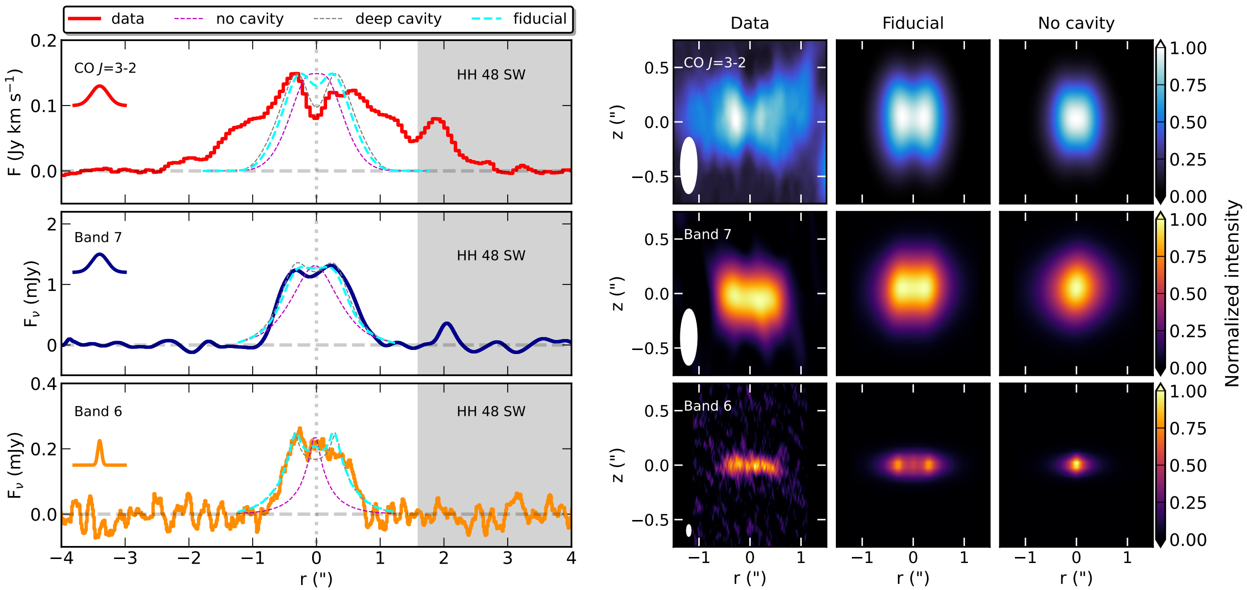

Figure 4.5: Observed radial profiles of CO and millimeter continuum from ALMA observations compared to models with and without a cavity.
Left: radial profile of the CO $J = 3-2$ integrated emission map (red, top), Band 7 continuum (blue, middle), and Band 6 continuum (orange, bottom). The beam size of the observations in the radial direction is illustrated with a black Gaussian profile in the upper left corner. The modeled emission is shown with a dashed line and is normalized to the peak of the observed profile. The best-fitting or fiducial model is shown in cyan, the best-fitting model without a cavity is shown in purple, a similar model to the best model, but with a cavity that is 100 times more depleted in gas, and dust is shown in gray. The position of HH 48 SW is marked with a gray shaded area.
Right: 2D maps of the CO $J = 3-2$ integrated emission (top), Band 7 continuum (middle), and Band 6 continuum (bottom). Images are rotated by 12 degrees so that the disk is aligned horizontally. From left to right: Observations, overall best-fitting model, and best-fitting model without a cavity. The beam sizes of the observations are shown in the lower left corner.

4.4.5.1 SED comparison

The modeled SEDs of the runs with and without a cavity look largely the same, but the mid-infrared flux is underestimated in the model without a cavity. The cavity decreases the amount of warm dust in the inner regions of the disk, but photons from the warm inner disk regions can escape much easier because the density is significantly lower. These photons can then again scatter at the surface into our line of sight. Since scattering of dust-emitted photons dominates the observed flux in the mid-infrared (2 – 15 µm) and this process is more efficient at longer wavelengths, where a larger part of the inner disk is optically thin, the cavity effectively boosts the flux at mid-infrared wavelengths (2 – 15 µm) compared to optical wavelengths (0.4 – 0.8 µm). This allows combinations of parameters that fit both the optical wavelengths and the mid-infrared wavelengths in the SED.

The parameters of the SED without a cavity largely agree with the SED run with a cavity (see Table 4.2), but this run prefers a significantly cooler star (3500 K) with a lower level of visual extinction to compensate for the flux deficit in the mid-infrared. This lower temperature contradicts the measured dynamical mass and is still not able to account fully for the excess flux between 2 – 15 µm (see Fig. 4.2).

4.4.5.2 Resolved continuum comparison

Additionally, the steep radial profile with a dip in the continuum detected at 3σ (see Fig. 4.5) suggests that the inner region of the disk is either depleted in solids or is inclined close to 90° and thus is optically thick (Villenave et al. 2020). Since the latter is excluded by the HST and SED runs, it is likely that these signatures are due to an inner cavity. The model of the SED run without a cavity has a strongly centrally peaked radial profile in ALMA and does not reproduce the $1''$ emission plateau and potential dip at the center (see Fig. 4.5). We would like to note that the effect of the cavity in the HST image is small because of the high optical depth at visible wavelengths.

The ALMA Band 6 (1.3 mm) continuum lacks any obvious cavity, which sets clear limits on the size and depth of the cavity. Our best-fitting model reproduces the size of the radial extent in the ALMA Band 6 continuum, as well as the emission plateau of $\sim 1''$. Models without a cavity and similar inclinations are centrally peaked and do not result in the flat profile that we observed in the ALMA Band 6 and Band 7 continuum. Only very high inclinations would be an option (see the discussion in Villenave et al. 2020), but they are excluded by the SED and scattered light observations. As a next step, an inner disk or a radius-dependent dust depletion factor inside the cavity might be included in order to produce a better combined fit to the Band 6 and Band 7 data. This is beyond the scope of this paper, however.

4.4.5.3 Comparison of the gas observation

Last, the CO $J = 3 - 2$ line emission reveals a 50% dip at a position similar to that seen in the dust continuum (see Fig. 4.5), and this can only be reproduced when a cavity is included or when the foreground cloud contributes significantly to the observations. Since the foreground visual extinction is low (A_{V} ~5 mag) and a similar dip is not observed toward HH 48 SW, the latter is unlikely. To estimate the depth of the cavity in the gas, we added CO gas to the model at a number abundance of 10^{-4} with respect to H nuclei. To mimic freeze-out, we removed all CO gas from disk regions that were colder than 20 K, the typical desorption temperature of CO. Photodissociation was approximated by removing all CO at gas densities lower than 10^7 cm^{-3}. The CO level populations were determined in `RADMC-3D` using a nonlocal thermal equilibrium large velocity gradient approach assuming that the gas temperature is the same as the dust temperature. The CO $J = 3-2$ line was then ray-traced at a velocity resolution of 0.5 km s^{-1}. This simple approach is not meant to build the perfect gas model of HH 48 NE because it has severe limitations and crude approximations, but should only be considered as a quick comparison.

We show the integrated emission of the modeled CO $J = 3–2$ line with its radial profile in Fig. 4.5. The radial profile of the best-fitting model has a clear dip at the center, similar to the observations. The dip is not as deep as in the observations, which could be due to the fact that we assumed the gas temperature to be the same as the dust temperature, which is no longer true in a cavity (Bruderer 2013; Leemker et al. 2022b). Decreasing the amount of material in the cavity by two additional orders of magnitude does reproduce the depth of the gas cavity (gray line in Fig. 4.5), but is a poorer fit to the continuum and has a significant impact on the SED. The best-fitting model without a cavity does not reproduce the observed radial profile and is strongly centrally peaked. Hence, the gas observations show additional evidence that the disk likely is depleted in dust and gas in a central region of the disk. The modeled emission agrees with the observations in the inner 1″, but fails to reproduce the wings that extend beyond the size of the disk in millimeter emission. The gas in the disk extends farther out than the dust, which is likely a result of radial drift (see, e.g., Andrews et al. 2011; Trapman et al. 2019).

4.4.5.4 Size and depth

The cavity is constrained to be 50 – 70 au, where dust is depleted by two orders of magnitude. An empty cavity results in an underestimation of the mid-infrared part of the SED, so some warm dust must be available in the inner cavity. However, it is impossible to distinguish between a depleted but not empty cavity and a fully depleted cavity with a small inner disk with sufficiently warm dust. The cavity appears larger in the millimeter observations (74^{+5}_{-10} au) than in the SED and HST observations (∼50 au), which may be partly attributed to the poor spatial resolution of the latter observations. However, this may also be partly due to radial dust segregation if the small dust grains follow the gas further into the cavity than the large dust grains. Similar dissimilarities between the scattered light observations and millimeter continuum are seen in almost all transition disks (Villenave et al. 2019; Sturm et al. 2023a; van der Marel 2022; Benisty et al. 2022).

4.5 Discussion

The source structure of HH 48 NE is in many ways in line with our current understanding of protoplanetary disk physics. The height, mass, and radial extent of the disk suggest that HH 48 NE has a typical T Tauri disk that would not stand out of the population of observed protoplanetary disks at lower inclination (see, e.g., Ansdell et al. 2016; Manara et al. 2023). Cavities are relatively common in Class II disks (see, e.g., van der Marel & Mulders 2021). The two main differences between this disk and the average disk are its relatively low-mass fraction of settled large dust grains and high inclination. Previous infrared surveys of disks in Chamaeleon I reported that between 99% and 99.9% of the dust mass in the upper layers of the disk had settled to the midplane (Manoj et al. 2011), consistent with disks in other 1 – 3 Myr old molecular clouds such as Taurus and rho Ophiuchus (Furlan et al. 2011; McClure et al. 2010). In contrast, only 90% of the dust has settled in the disk around HH 48 NE. Based on the paucity of bona fide edge-on disk detections, we speculate that the known edge-on disks might be detectable because they possess the combination of (at most) moderate dust settling and high inclination. We address this question in Paper II and discuss the implications of our concordant best-fitting model for the disk physical properties below (see also the recent paper by Angelo et al. 2023).

4.5.1 Convergence of fit

Multiwavelength dust fitting including the SED and resolved observations often leads to discrepancies in which the scattered light observations push the model geometry in a different direction than either the continuum observations or the SED, for example (see, e.g., Wolff et al. 2017, 2021). Therefore, more complicated attempts such as using a staggered Markov chain (Madlener et al. 2012) or covariance matrices (Wolff et al. 2017) are explored in the literature, each with their promises and limitations. We have shown that three separate MCMC runs on the SED, scattered light HST observations, and millimeter-continuum ALMA observations converge to a model that reproduces these three observables to a reasonable extent. Additionally, we show in Fig. 4.6 that the temperature and luminosity in the best-fitting model are in line with the measured dynamical mass of the system, and the age spread in the Chamaeleon I star-forming region (4 - -5 Myr is on the old end of the age spread in the Chamaeleon I star-forming region; Galli et al. 2021). For this reason, we kept the procedure as simple as possible, without combining the different observations. As we have shown in Sect. 4.4, individual differences between the outputs of the runs can provide insight into the effects of dust dynamics on differently sized grains. In principle, radial segregation of grain sizes and/or radial drift in the model could be accounted for, but this would introduce additional free parameters and would complicate the MCMC fits while the data may not have high enough S/N and/or spatial resolution to definitively draw conclusions on the differences between large and small grains.

4.5.2 Grain size distribution

The dust grains in the atmospheric layers of the disk in HH 48 NE are constrained to have a size between 0.3 and 10 µm. The minimum grain size found in the disk is much larger than in the ISM dust distribution (typically 0.005 µm). This result is consistent with previous findings of Pontoppidan et al. (2007), showing that the high mid-infrared scattered light continuum in the Flying Saucer can only be explained by a dust distribution in the disk atmosphere with large grains (0.25 – 16 µm). Our result is also consistent with previous simple comparisons of opacities

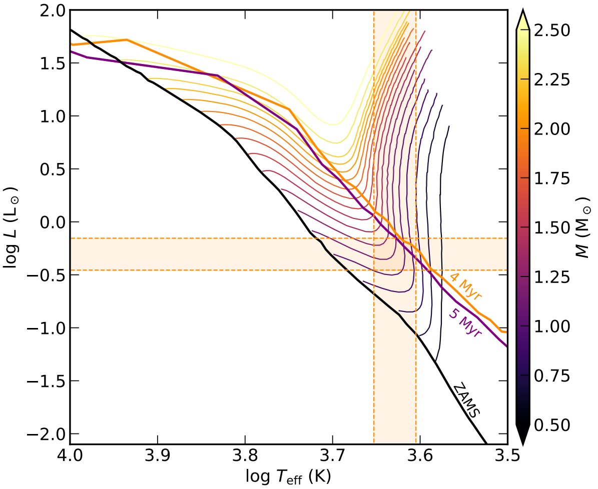

Figure 4.6: Hertzsprung-Russel diagram with stellar tracks from Siess et al. (2000b) for stellar masses from 0.5 – 2.5 M$_\odot$. The orange and purple lines denote the 4 and 5 Myr isochrones. The crosshair points at the range of effective temperature and luminosity found in the MCMC runs, which agrees well with a ~1 M$_\odot$ star derived from the dynamical fits to the CO emission.

with single-grain sizes to *Spitzer*/IRS observations of the silicate feature at 10 µm. Olofsson et al. (2009) find that the observed silicate features in a large (96) sample of T Tauri disks are mainly produced by micrometer-sized grains. They show that there cannot be a large number of submicrometer-sized dust grains in the disk atmosphere because their emission would overwhelm the few large grains. Additionally, Tazaki et al. (2021) reported evidence for grains greater than micrometers in the upper layers of the HD 142527 disk with an independent method, using resolved H_2O ice observations in coronagraphic imaging of scattered light (see also Honda et al. 2009). The grain size limits are on the high end compared to the range found using the SEDs of 30 well-known (low-inclination) protoplanetary disks (Kaeufer et al. 2023). Kaeufer et al. (2023) used a Bayesian analysis to determine accurate parameter values with their uncertainties, and found a minimum grain size of typically 0.01 – 0.2 µm and a maximum grain size of typically 1 – 9 µm.

Grains larger than 1 µm are thought to settle quickly to the midplane ($<10^5$ yr; Dullemond & Dominik 2004) in the relevant regions (<100 au) because of the frictional force between the Keplerian orbit of the grain and the slightly sub-Keplerian orbit of the gas because of the pressure support. Together with the very low levels of turbulence in lower disk regions (e.g., Pinte et al. 2016; Villenave et al. 2022; Flaherty et al. 2020, and the references therein), this means that some mechanism has to segregate dust vertically and prevent the micrometer-sized dust grains from settling to the midplane or replenishes the micrometer-sized dust grains via grain-grain fragmentation, but does not affect the millimeter-sized dust grains observed with ALMA. Some theoretical sources of turbulence can cause efficient vertical mixing, but do not reach all the way to the midplane (zombie vortex instability; Barranco et al. 2018; see also Lesur et al. 2022). This particular source of turbulence is likely available in the strongly stratified regions of all protoplanetary disks as long as there is modest grain settling and/or growth (Barranco et al. 2018; Lesur et al. 2022). Only non-physically fast cooling and a high viscosity are known to suppress the instability (Lesur & Latter 2016). Mechanisms such as these are a promising solution to the micrometer-sized dust grains in the upper layers of the disk, but need to be studied further in simulations to determine whether any direct observational signatures can serve as proof of their existence.

In addition, there has to be a mechanism that efficiently removes submicrometer grains from the disk atmosphere, but leaves approximately micrometer sized dust grains in the upper disk. This could be possible if growth timescales for these small grains are significantly shorter than the fragmentation timescales (see, e.g., Birnstiel et al. 2011; Windmark et al. 2012). This would require low levels of turbulence, or porous fluffy grains that easily stick together to form larger grains (Birnstiel et al. 2011). Because no ice is available in the disk atmospheres to make the grains stickier due to the extreme temperatures and UV irradiation, this would require that the products of grain-grain fragmentation are inherently porous and fluffy. An additional hypothesis is that the smallest dust grains can be lifted from the surface by disk winds, while the larger grains are too heavy to be carried away (Olofsson et al. 2009; Booth & Clarke 2021). Disk winds might be a ubiquitous driving mechanism for accretion in T Tauri protoplanetary disks (see, e.g., Tabone et al. 2022) and may be launched from a substantial fraction of the disk surface (Tabone et al. 2020). Dust lifting by the wind is only efficient for smaller dust grains (<1 µm) and might significantly deplete the small-dust population if it is sustained for timescales of millions of years (Booth & Clarke 2021). Understanding the vertical dust segregation could be a key element in understanding the origin of turbulence in protoplanetary disks and the weight-lifting capabilities of disk winds.

The exclusion of small nanometer-sized grains from the upper atmosphere of the disk has strong implications for the disk chemistry. In many chemical disk models, the minimum grain size distribution is taken to be the same as for ISM grains (∼5 nm) (e.g., Bruderer et al. 2012; Walsh et al. 2015). When the average surface area of dust grains in the disk atmosphere were decreased, a higher degree of UV radiation in the deeper disk layers would result. An excess of UV radiation enhances photodissociation and photodesorption processes that ultimately result in a very rich chemistry (Bergner et al. 2019, 2021; Calahan et al. 2023).

4.5.3 Inner cavity

We have shown that HH 48 NE likely has an inner cavity in the disk in both gas and dust of ∼50 au. Similar cavities are found in a relatively large number of face-on disks (transition disks) (∼10%; Ercolano & Pascucci 2017), but have not been directly observed in edge-on protoplanetary disks so far. The radial structure of some of the disks in the large sample of Villenave et al. (2020) suggests that radial substructure is present in edge-on disks. However, detailed multiwavelength modeling is necessary to exclude increased dust opacity due to high inclinations in combination with a high disk mass as an alternative explanation for disks with a flat radial flux distribution or central dip. The inclusion of a cavity in our model is crucial to fit the SED in the mid-infrared. The cavity allows photons emitted by warm dust in the innermost region of the disk to escape if they have an ideal angle to scatter along our line of sight. Similar conclusions are drawn from optical and near-infrared observations (see Benisty et al. 2022, for a review) and also lead to a distinction of Herbig Ae/Be stars into group I and group II sources. Group I includes the sources with high levels of optical scattering due to large inner cavities, and group II includes the sources without a cavity and much lower levels of scattering.

Without a cavity, we would need to add a 1400 K blackbody to the source spectrum in a similar way as Pontoppidan et al. (2007) to mimic the increasing amount of photons originating from the inner disk regions. Adding a 1400 K blackbody manually solves the discrepancy in the SED fit but is not self-consistent because the 1400 K emission is thought to arise from the inner disk, not from the central star. The difference in solid angle between a stellar point source with an additional 1400 K component and warm inner disk could result in crucial differences when ice features in the mid-infrared are to be modeled because the mid-infrared continuum would be dominated by photons that scatter off of the disk that are produced in the warm inner disk, not in the star itself (see Appendix A in Paper II). We showed that our model is self-consistent and naturally reproduces the flux in the mid-infrared.

Additional research, preferably with higher angular resolution ALMA data, is necessary to determine whether the unnoticed existence of a cavity can resolve this issue in more sources. In edge-on disks, many of the smaller cavities or rings will be hidden behind the optically thick dust in the midplane, and a multiwavelength analysis is necessary to constrain it. In the specific case of the Flying Saucer, where a similar deficit in mid-infrared flux is found as in our model without a cavity (Pontoppidan et al. 2007), the continuum indicates a double-peaked continuum in the radial direction (Guilloteau et al. 2016), even though the dip is weaker and less well resolved than in HH 48. Additional detailed multiwavelength studies of other edge-on disks are necessary to determine whether more of them harbor a cavity.

4.6 Conclusions

We have developed a disk model using the radiative transfer code `RADMC-3D`, which includes anisotropic scattering. We ran MCMC fits to HST observations, ALMA observations, and the SED for HH 48 NE to constrain the geometry and physical features of this edge-on Class II system. We can conclude the following:

- The best-fitting model (SED run) reproduces both the spatially resolved features of the emission in scattered light observations, millimeter dust continuum observations, CO gas observations, and the SED.

- HH 48 NE is a K7 star with a mass of $1 - 1.4$ $M_\odot$, an effective temperature of $\sim$4150 K, and a luminosity of $\sim$0.4 $L_\odot$. These values agree with the estimated age of the Chamaeleon I star-forming region following evolutionary stellar tracks from the literature.

- HH 48 NE is a typical T Tauri disk in many ways, but stands out due to the lack of small ($<$0.3 µm) grains in the disk atmosphere. Mechanisms that remove the small dust grains can be the result of efficient sticking of the smallest grains, or of lifting in large-scale disk winds. The exclusion of small grains may have a major impact on the chemistry in the disk because UV radiation can likely penetrate much deeper into the disk because the average surface area of the grains is smaller.

- The disk in HH 48 NE likely has a ∼50 au inner cavity in gas and dust that is mostly invisible due to optically thick dust. The cavity boosts the mid-infrared emission in the SED and allows for a unique model that is consistent with the scattered light observations and the millimeter continuum observations at the same time.

Understanding the mechanisms that set grain size distributions and physical properties of protoplanetary disks is crucial. Edge-on disks can be a unique tool for constraining some parameters that are hard to constrain in less strongly inclined disks, such as dust settling and the grain size distribution.

4.7 Acknowledgments

We would like to thank the anonymous referee for suggestions that improved the manuscript. We also thank Ewine van Dishoeck for useful discussions and constructive comments on the manuscript. Astrochemistry in Leiden is supported by the Netherlands Research School for Astronomy (NOVA), by funding from the European Research Council (ERC) under the European Union's Horizon 2020 research and innovation programme (grant agreement No. 101019751 MOLDISK). M.K.M. acknowledges financial support from the Dutch Research Council (NWO; grant VI.Veni.192.241). D.H. is supported by Center for Informatics and Computation in Astronomy (CICA) grant and grant number 110J0353I9 from the Ministry of Education of Taiwan. DH acknowledges support from the National Technology and Science Council of Taiwan through grant number 111B3005191. M.N.D. acknowledges the Swiss National Science Foundation (SNSF) Ambizione grant no. 180079, the Center for Space and Habitability (CSH) Fellowship, and the IAU Gruber Foundation Fellowship.

This paper makes use of the following ALMA data: ADS/JAO.ALMA#2016.1.00460.S, ADS/JAO.ALMA#2019.1.01792.S. ALMA is a partnership of ESO (representing its member states), NSF (USA) and NINS (Japan), together with NRC (Canada), MOST and ASIAA (Taiwan), and KASI (Republic of Korea), in cooperation with the Republic of Chile. The Joint ALMA Observatory is operated by ESO, auI/NRAO and NAOJ. The National Radio Astronomy Observatory is a facility of the National Science Foundation operated under cooperative agreement by Associated Universities, Inc.

This work makes use of the following software: `numpy` (van der Walt et al. 2011), `matplotlib` (Hunter 2007), `astropy` (Astropy Collaboration et al. 2013, 2018), `bettermoments` (Teague & Foreman-Mackey 2018), CASA (McMullin et al. 2007), `eddy` (Teague 2019), `emcee` (Foreman-Mackey et al. 2013), `OpTool` (Dominik et al. 2021), `RADMC-3D` (Dullemond et al. 2012).

Appendix

4.A Posterior distribution continuum fits

In Figure 4.A.1 we present the posterior distribution of the three independent runs using the SED, the resolved scattered light observation, and the resolved millimeter continuum observations. In Figure 4.A.2 we present the posterior distribution of the SED run without a cavity, the physical parameters of which overall agree well with the SED run with a cavity.

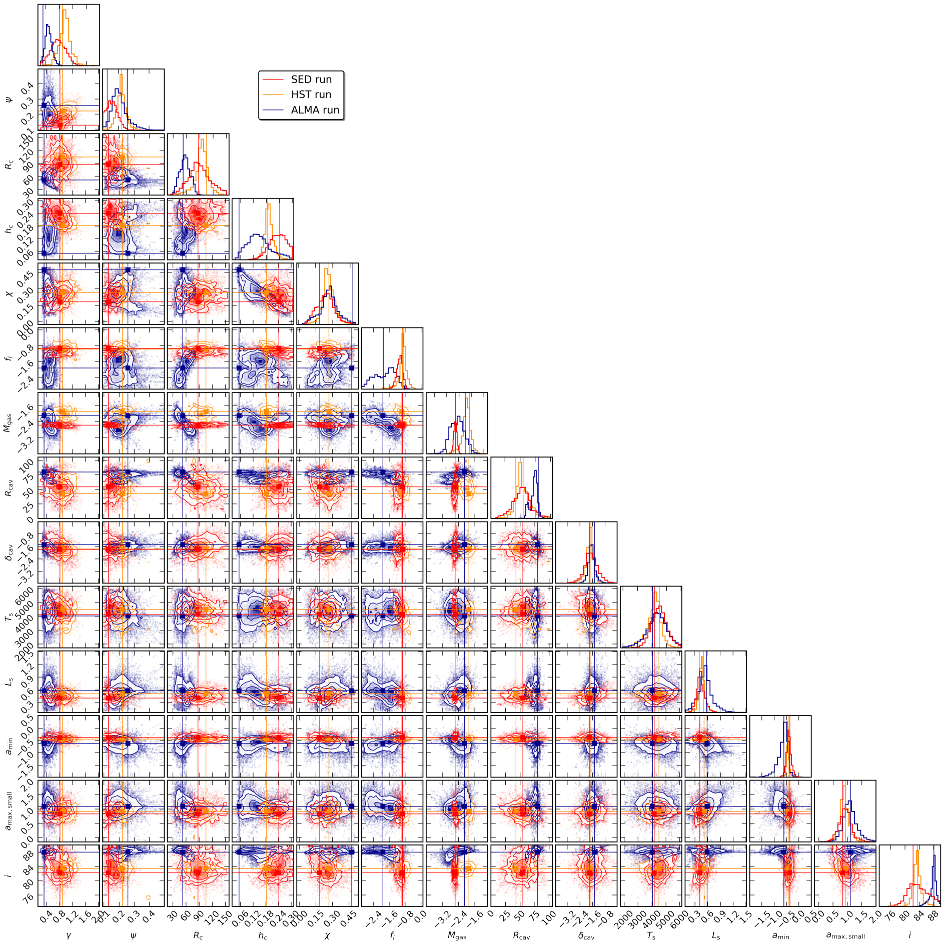

Figure 4.A.1: Posterior distributions of the three different MCMC runs. The SED run is shown in red, the HST run is plotted in orange, and the ALMA run is shown in blue. The median value for each parameter and the 16% and 84% confidence intervals are given in Table 4.2.

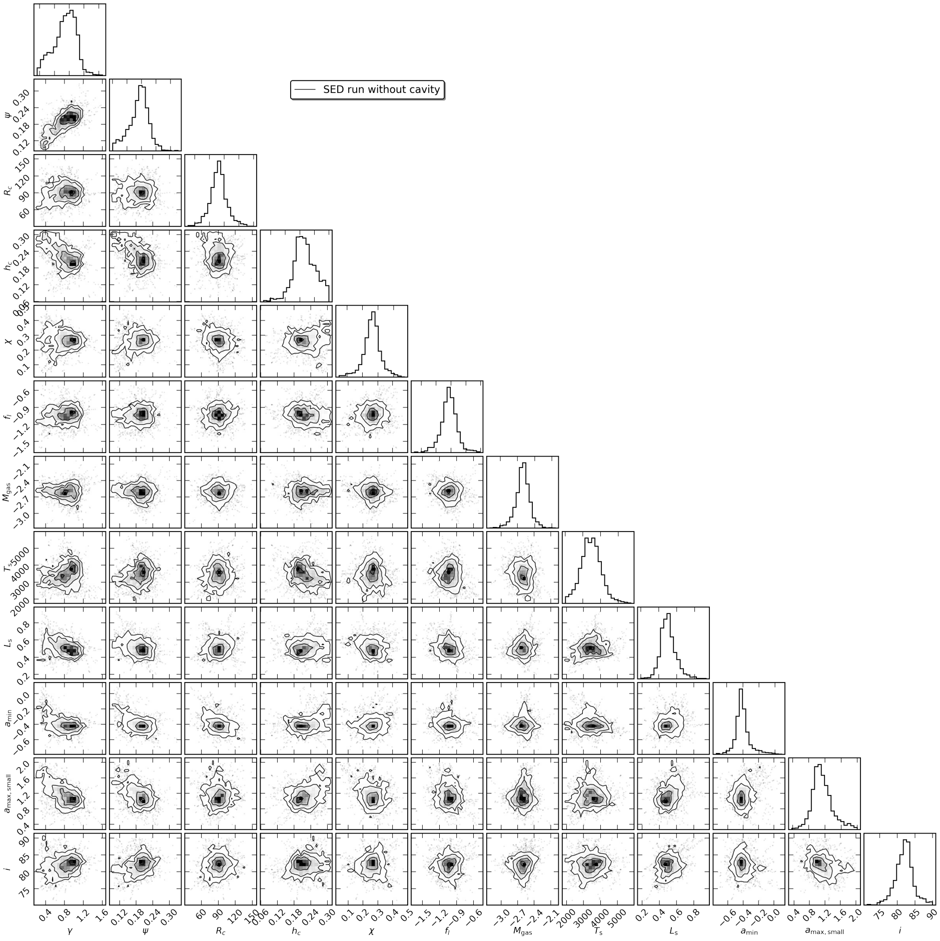

Figure 4.A.2: Posterior distribution of the SED run without a cavity. The median value for each parameter and the 16% and 84% confidence intervals are given in Table 4.2.

Chapter 5

The edge-on protoplanetary disk HH 48 NE II. Modeling ices and silicates

J.A. Sturm, M.K. McClure, J.B. Bergner, D. Harsono, E. Dartois,
M.N. Drozdovskaya, S. Ioppolo, K.I. Öberg, C.J. Law,
M.E. Palumbo, Y.J. Pendleton, W.R.M. Rocha, H. Terada, and R.G.
Urso

A&A 677, A18 (2023)

Abstract

Context. The abundance and distribution of ice in protoplanetary disks is critical for an understanding of the link between the composition of circumstellar matter and the composition of exoplanets. Edge-on protoplanetary disks are a useful tool for constraining this ice composition and its location in the disk because the spectral signatures of the ice can be observed in absorption against the continuum emission that arises from the warmer regions in the central disk.

Aims. The aim of this work is to model ice absorption features in protoplanetary disks and to determine how well the abundance of the main ice species throughout the disk can be determined within the uncertainty of the physical parameter space. The edge-on protoplanetary disk around HH 48 NE, a target of the *James Webb* Space Telescope Early Release program Ice Age, is used as a reference system.

Methods. We used the full anisotropic scattering capabilities of the radiative transfer code `RADMC-3D` to ray-trace the mid-infrared continuum. Using a constant parameterized ice abundance, we added ice opacities to the dust opacity in regions in which the disk was cold enough for the main carbon, oxygen, and nitrogen carriers to freeze out.

Results. The global abundance relative to the dust content of the main ice carriers in HH 48 NE can be determined within a factor of 3 when the uncertainty of the physical parameters is taken into account. Ice features in protoplanetary disks can be saturated at an optical depth of $\lesssim$1 due to local saturation. Ices are observed at various heights in the disk model, but in this model, spatial information is lost for features at wavelengths >7 µm when observing with *James Webb* Space Telescope because the angular resolution decreases towards longer wavelengths. Spatially observed ice optical depths cannot be directly related to column densities, as would be the case for direct absorption against a bright continuum source, because of radiative transfer effects. Vertical snowlines will not be a clear transition because the height of the snow surface increases radially, but their location may be constrained from observations using radiative transfer modeling. Radial snowlines are not really accessible. Not only the ice abundance, but also the inclination, the settling, the grain size distribution, and the disk mass have a strong impact on the observed ice absorption features in disks. Relative changes in the ice abundance can only be inferred from observations if the source structure is well constrained.

5.1 Introduction

Ices constitute the bulk reservoir of volatiles such as C, N, and O in cold protoplanetary disks (Pontoppidan et al. 2014) and are thought to be the carriers and precursors of astrophysically complex organic molecules (Boogert et al. 2015). Ices on dust grains and the macromolecular residues formed from their processing in space environments are often recognized as important carriers of organic compounds of astrobiological relevance (e.g., Baratta et al. 2019; Johansen et al. 2021; Sossi et al. 2022). It is crucial to investigate the processing of small molecules, such as CO and CO_2, and the origin of the diversity of complex organics in planet-forming regions in protoplanetary disks to understand the origin of the chemical complexity in planets.

Previously, the thermal snow surfaces of the molecules CO, CS, and H_2O have been traced directly in protoplanetary disks using observations of their gas emission lines (Qi et al. 2013; Pinte et al. 2018; van't Hoff et al. 2020; Podio et al. 2020). Ices have also been traced indirectly in studies focusing on radial transport of volatiles that are frozen out on large dust grains in the disk midplane (Zhang et al. 2020a; Sturm et al. 2022) and through their physical imprint on the grain properties (Banzatti & Pontoppidan 2015; Cieza et al. 2016). H_2O ice is observed directly toward multiple Class II disks (e.g., Terada et al. 2007; Aikawa et al. 2012; Terada & Tokunaga 2012; McClure et al. 2015; Terada & Tokunaga 2017) using ground-based observations of the Infrared Camera and Spectrograph (IRCS) on the Subaru telescope and the AKARI and Herschel space telescopes. However, until the advent of the recently launched *James Webb* Space Telescope (JWST), direct observations of ices other than H_2O in disks were hardly possible because Earth's atmosphere efficiently absorbs radiation at these wavelengths, and previous space-based instruments lacked enough sensitivity and spatial resolution. CO_2, and tentatively CO, ice features have been detected previously in a handful of edge-on Class II disks with the AKARI space telescope (Aikawa et al. 2012). Other ices have been observed toward multiple young class 0/I protostars with edge-on disks (e.g., Pontoppidan et al. 2005 and Aikawa et al. 2012) , but it is hard to determine the fraction of ices the disk in these systems that contributes to the absorption bands because the ice absorption can be dominated by the envelope and foreground cloud.

Observations with the JWST Near Infrared Spectrograph (NIRSpec, 0.6 – 5.3 µm; Jakobsen et al. 2022a) and Mid-InfraRed Instrument (MIRI, 4.9 – 28.1 µm; Rieke et al. 2015a) of the later-stage edge-on disks (>2 Myr), where the envelope has long dissipated, will shed light on the composition of ices in protoplanetary disks and on their spatial distribution in the disk. The space-based JWST is sensitive enough to observe many more ice species in protoplanetary disks and has the resolving capability to spatially constrain absorption strengths throughout the disk. However, detailed modeling of these edge-on disks is necessary to interpret what the observations reveal about the physical and chemical structure of these disks. Ices in edge-on protoplanetary disks are revealed in absorption against the continuum of the inner disk and/or the scattered light. Stellar photons and photons emitted from warm dust in the (<5 au) inner regions of the disk are both emitted or scattered off small dust grains on the surface of the outer disk, and they are absorbed at specific wavelengths by ices located in the cold regions in the disk (see Appendix 5.A for a detailed breakdown of the observed continuum emission). For a sketch of the basic principles, we refer to Fig. 3 in Terada et al. (2007).

Ballering et al. (2021) used advanced chemical modeling to show that the main ice species could likely be detected with JWST. Their work focused on the observability of chemical differences with the current generation of observatories and reported that the strength of the absorption features might reveal whether the ices are inherited from the protostellar phase or are formed after a molecular reset upon entering the disk. Arabhavi et al. (2022) implemented ice opacities in the protoplanetary disk model (ProDiMo) and studied the impact of the chemistry and ice distribution on the dust grains on the spectral ice features in the JWST wavelength range. Dartois et al. (2022) modeled the influence of grain growth on the spectroscopic profiles of the ice features in dense clouds and disk observations. In this work, we extend the modeling analysis of ices in protoplanetary disks and focus on how the physical disk parameters affect the JWST spectra in edge-on protoplanetary disks. We also quantify how robustly we can constrain ice abundances.

While we apply our modeling to one specific disk, HH 48 NE, this work can readily be generalized to all edge-on disks. HH 48 NE is part of the JWST early-release science program Ice Age (proposal ID: 1309, PI: McClure), which studies the evolution of ices during star formation from dark clouds (McClure et al. 2023) until protoplanetary disks. The disk geometry and stellar parameters are explored in Paper I of this paper series (Sturm et al. 2023e). HH 48 NE is a nearly edge-on disk that was first observed with Hubble Space Telescope (HST) (Stapelfeldt et al. 2014) and subsequently with Atacama Large (sub-)Millimeter Array (ALMA) (Villenave et al. 2020). In Paper I, we showed that the spectrum is consistent with a stellar spectral type K7, and a luminosity of 0.4 $L_\odot$. The 200 au scattered light disk is inclined at 82.3° and likely has a 55 au cavity in which dust is depleted by two orders of magnitude.

In this work, we use a simple parameterized abundance structure for the main ice species H_2O, CO, CO_2, NH_3, CH_4, and CH_3OH to reveal the physical parameters of the disk that are required to assess the ice abundances and chemistry, and how accurately we can constrain the chemistry in HH 48 NE given the uncertainty in the disk geometry. The structure of this paper is as follows: We first describe our model setup in Sect. 5.2. In Sect. 5.3 we present the ice spectrum in the fiducial model and the sensitivity of the ice features to various parameters. In Sect. 5.4 we discuss the implications of these results in the analysis of HH 48 NE and edge-on disks in general. Sect. 5.5 summarizes the results and gives our final conclusions.

5.2 Modeling

5.2.1 Continuum model

Our modeling is based on the full anisotropic scattering radiative transfer capabilities of `RADMC-3D` (Dullemond et al. 2012). In the first stage, the temperature

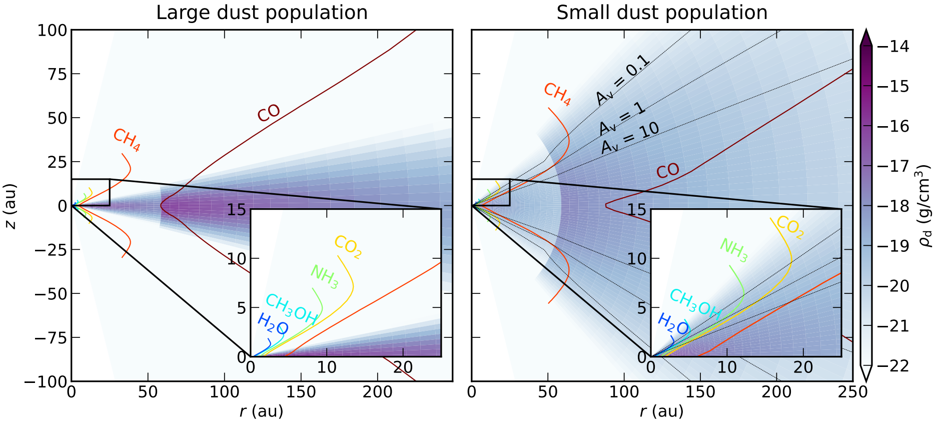

Figure 5.1: Dust density setup in the model of the large dust population (left) and small dust population (right). The colored contours follow the dust temperature at which the considered molecules freeze out according to their desorption temperature given in Table 5.2. The dotted black lines denote a visual extinction (A_v) of 0.1, 1, and 10 mag as measured from the stellar position. The onset of ice formation is set to $A_v < 1.5$ mag in the fiducial model.

is determined, after which we distribute the ices in cold disk regions and ray-trace the model to simulate observations. The specific steps of our modeling procedure are described in the following sections. All parameters are adopted from the best-fitting model in Paper I, which reproduces the spectral energy distribution well. They are listed in Table 5.1.

5.2.1.1 Model setup

The model setup we used is fully parameterized, assuming an azimuthally symmetric disk with a power-law density structure and an exponential outer taper (Lynden-Bell & Pringle 1974),

$$\Sigma_{\rm dust} = \frac{\Sigma_{\rm c}}{\epsilon}\left(\frac{r}{R_{\rm c}}\right)^{-\gamma} \exp\left[-\left(\frac{r}{R_{\rm c}}\right)^{2-\gamma}\right], \tag{5.1}$$

where r is the radial distance to the star in the plane of the disk in au, $\Sigma_{\rm c}$ is the surface density at the characteristic radius $R_{\rm c}$ in g cm^{-2}, γ is the power-law index, and ϵ is the gas-to-dust ratio.

The height of the disk is described by

$$h = h_{\rm c}\left(\frac{r}{R_{\rm c}}\right)^{\psi}, \tag{5.2}$$

where h is the aspect ratio, $h_{\rm c}$ is the aspect ratio at the characteristic radius, and ψ is the flaring index. The dust has a vertical Gaussian distribution,

$$\rho_{\rm d} = \frac{\Sigma_{\rm dust}}{\sqrt{2\pi}rh} \exp\left[-\frac{1}{2}\left(\frac{\pi/2-\theta}{h}\right)^2\right], \tag{5.3}$$

Table 5.1: Properties of the fiducial model constrained by extensive MCMC fitting using the spectral energy distribution and resolved HST and ALMA observations in Paper I.

parameter (unit)	value
L_s ($\mathrm{L}_\odot$)	0.41
T_s (K)	4155
R_c (au)	87
h_c	0.24
ψ	0.13
i (°)	82.3
γ	0.81
M_gas ($\mathrm{M}_\odot$)	2.7×10^{-3}
f_ℓ	0.89
$\times$	0.2
a_min (µm)	0.4
$a_\mathrm{max,s}$ (µm)	7
$a_\mathrm{max,l}$ (µm)	1000
R_cav (au)	55
δ_cav	1.6×10^{-2}

where θ is the opening angle from the midplane as seen from the central star. The dust sublimation radius is determined using $r_\mathrm{in} = 0.07\sqrt{L/L_\odot}$, assuming a dust sublimation temperature of 1600 K, which corresponds to 0.045 au.

Dust settling is parameterized by introducing a second dust population containing large grains that is limited in height to Xh, where X is a constant between 0 and 1. The mass fraction of the total dust mass that resides in the large grain population is defined as f_ℓ. We assumed a grain composition consistent with inter stellar matter (ISM) dust, consisting of a mass fraction of 85% amorphous pyroxene $\mathrm{Mg_{0.8}Fe_{0.2}SiO_3}$, 15% amorphous carbon, and a porosity of 25%. The two dust populations follow a power-law size distribution with a fixed slope of −3.5 (see, e.g., Weingartner & Draine (2001) and Andrews et al. (2011) for an observational justification of these parameters). The grain size limits of the small dust population are $a_\mathrm{min} = 0.4$ µm and $a_\mathrm{max} = 7$ µm, as determined with Markov chain Monte Carlo (MCMC) fits using the spectral energy distribution (SED) and the resolved HST and ALMA observations in Paper I. The minimum grain size of the large dust population is the same as the minimum size of the small dust population. The maximum grain size of the large dust population is adopted to be 1 mm. Dust and ice opacities were calculated with `OpTool` (Dominik et al. 2021), using the distribution of hollow spheres (DHS; Min et al. 2005) approach to account for grain shape effects. The phase function was truncated at 3°, which means that forward scattering within this range was treated as if the photon package did not have any interaction with the grain at all.

5.2.1.2 Dust scattering

We used the full anisotropic scattering capabilities of `RADMC-3D` because isotropic scattering assumptions can have a significant impact on the amount of observed scattered light in the near- to mid-infrared (Pontoppidan et al. 2007). Additionally,

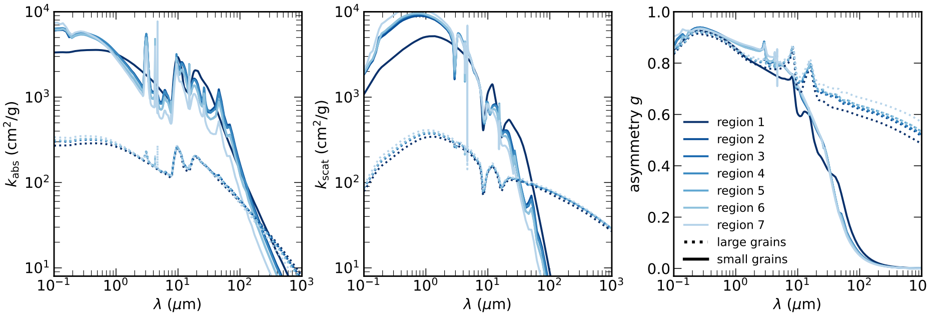

Figure 5.2: Opacities used for the seven different regions in the disk. Left: Absorption opacity. Center: Effective scattering opacity. Right: Asymmetry parameter g. The regions are numbered with decreasing desorption temperature, as further specified in Table 5.2.

the direction from which the scattered light originates is important for modeling the ices in the disk. The spectral range in which most ice absorption features occur is dominated by scattered light that is emitted in the warm inner region of the disk and scattered off in the outer disk (see Fig. 5.A.1). As the ices are localized in the lower layers in the disk, directional dependence is critically important for the amount of light that is absorbed by the ices.

5.2.2 Ice distribution

To evaluate the ices in the model, we assumed a constant molecular abundance throughout the disk to separate the effect on the ice features of physical disk parameters from chemistry. The molecular abundances were adopted from the initial abundances in the inheritance model in Ballering et al. (2021) based on dark cloud ice surveys (Öberg et al. 2011b; Boogert et al. 2015) to facilitate the comparison

Table 5.2: Adopted ice properties: Desorption temperature (taken as the recommended peak desorption temperature in Minissale et al. (2022) under high-density conditions), abundance with respect to total H (Ballering et al. 2021), molecular weight, disk regions in which the ice is distributed and references for the optical constants. Disk regions are numbered from warm to cold in steps of one ice component.

Opacity	T_{des} (K)	X/H (ppm)	M_n	Deposited in disk region	Reference optical constants
Dust	1600	-	-	[1, 2, 3, 4, 5, 6, 7]	
H_2O	155	80	18	[2, 3, 4, 5, 6, 7]	Warren & Brandt (2008)
CH_3OH	128	4.8	32	[3, 4, 5, 6, 7]	Gerakines & Hudson (2020)
NH_3	96	4.8	17	[4, 5, 6, 7]	Martonchik et al. (1984)
CO_2	80	22.4	44	[5, 6, 7]	Warren (1986)
CH_4	47	3.60	16	[6, 7]	Gerakines & Hudson (2020)
CO	20	99.2	28	[7]	Palumbo et al. (2006)

between their approach and ours. All molecules were assumed to be frozen out when the dust temperature was below the desorption temperature of that particular species (see Table 5.2 for details). The ice was limited vertically by a visual extinction (A_V) limit from the star, supported by both dark cloud observations (Boogert et al. 2015) and protoplanetary disk models (Visser et al. 2018; Arabhavi et al. 2022). This limit was set to $A_V = 1.5$ mag in the fiducial model based on the lower limit at which ices are observed in dark clouds toward background stars (Boogert et al. 2015). We did not include a background radiation field because no early spectral type stars lie in the vicinity of HH 48. For sources with a strong background radiation field, the ice can be photo-desorbed in a significant area of the disk because this radiation will encounter the cold translucent parts of the disk first. Future JWST observations of ices in a larger sample of protoplanetary disks will shed more light on the effect of the external radiation field on ices in disks.

To ray-trace the ice features and to time and efficiently compute in `RADMC-3D`, we divided the disk into seven regions, one for each considered ice species. To do this, we added ices toward cooler regions in the disk based on their respective absorption temperature (see Table 5.2 and Fig. 5.1). The average density of the dust and ice composite was then calculated in every region using

$$\rho_{\rm ice} = \rho_{\rm gas} \frac{x_{\rm ice} M_{\rm ice}}{x_{\rm gas} M_{\rm gas}}, \tag{5.4}$$

where x is the abundance, and M the mean molecular weight. The gas predominantly consists of H_2 and He and has an abundance of $x_{\rm gas} = 0.64$ and a mean molecular weight of 2.44.

The ice is distributed throughout the small and large grain population according to their surface area, following the description in Ballering et al. (2021),

$$f_{{\rm ice}\ ,\ell} = \frac{f_{{\rm dust},\ell}}{\sqrt{a_{{\rm max},\ell}/a_{\rm max,s}}\,(1 - f_{{\rm dust},\ell}) + f_{{\rm dust},\ell}}, \tag{5.5}$$

where $a_{\rm max,s}$ is the maximum grain size of the small dust population, $a_{{\rm max},\ell}$ is the maximum grain size of the large dust population, and $f_{{\rm dust},\ell}$ is the mass fraction of grains in the large dust population. In each of the two dust populations, the ice is distributed throughout the grains assuming a constant core-mantle mass ratio. This approach is consistent with dust grains that are a coagulation of small dust grains covered in ice and for preferred freezeout on large grains due to a lower surface energy barrier (Powell et al. 2022). We would like to note that the choice of ice partitioning for large grains does not significantly influence the results because most ice absorption occurs in the optically thin upper regions of the disk where the large dust population is excluded by settling. A distribution throughout the grains assuming a constant mantle thickness in the small dust population would have a significant effect, as was shown recently by Arabhavi et al. (2022).

Table 5.2 lists the laboratory-measured ice optical constants we used for the opacity calculation, which are available through `OpTool`. We mixed the optical constants together in each of the regions using the Bruggeman rule (Bruggeman 1935), assuming homogeneous mixing of the ice components in an icy mantle on top of the dust core. We assumed only pure ice components, measured at a singular temperature (see Table 5.2 for the references), and thus did not take into account how the precise shape of the feature and peak position vary with temperature and the ice matrix. A more detailed analysis on the shape of the absorption features and the dependence on the chemical environment in protoplanetary disks will be given in a forthcoming paper.

We used a well-sampled grid of 200 × 100 × 25 cells in radial, vertical, and azimuthal directions and used 10^8 photons ($\tau_{\rm peak}$ ~0.1) to determine the temperature structure in the model. After deposition of the ices, we repeated the temperature calculation to ensure that adding the reflective layer to the opacities did not change the internal temperature in the model. In theory, multiple iterations might be made over the ice deposition and temperature calculations to ensure that the regions in which the ice are distributed are determined accurately. However, to limit the computing time, we ignored the small deviations in deposition area. The temperature differences between different iterations are small and converge rapidly (Arabhavi et al. 2022).

In Fig. 5.2 we present the opacities in the seven different regions for the small and large grain population. In addition to molecular ice bands that arise over relatively narrow wavelength ranges, the ice addition slightly modifies the overall shape of the continuum. The total opacity of the small grains dominates that of the large grains at shorter wavelengths, while the large grains dominate at longer wavelengths.

The model is ray-traced at 309 wavelengths that were selected to resolve the mid-infrared ice features. For the ray-tracing, we used 10^7 photon packages per frame, with image dimensions of 300 pixels in size and a pixel size of 2 au. The 2D images were then convolved with an oversampled instrumental point spread function (PSF) for NIRSpec (<5 µm) or MIRI (>5 µm) using the `Python` package `WebbPSF` (Perrin et al. 2012) to create mock observations that can directly be compared with the observed data.

5.3 Results

We discuss the results of the ice modeling. We first discuss the specifics of the different ice species in the fiducial model. After this, we present various grids, for which we change one physical parameter at a time to determine the sensitivity of the optical depth of the ice features to the physical parameters and to which extent we can spatially constrain ice abundances in the disk.

5.3.1 Fiducial model

In Fig. 5.3 we present the mid-infrared spectrum of the fiducial model and compare it to the observations in the four *Spitzer*/IRAC bands and to the dust-only model. Adding ices to the model has a minor effect on the continuum with respect to the dust-only model because of the addition of the ice scattering opacities (see also Fig. 5.2). The modeled spectrum is a good fit overall to the photometric data points in the considered spectral range.

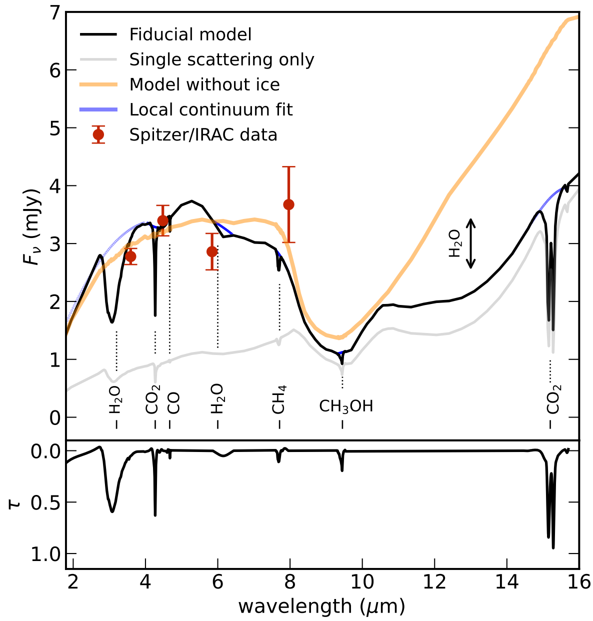

Figure 5.3: Integrated spectrum of the fiducial model, with photometric data points (red circles) and the best-fitting dust-only model (orange line) for reference. The local continuum used to calculate the optical depths of the sharp ice features is shown in blue. The fiducial model excluding double scattering is shown in gray. The lower panel shows the optical depth of the analyzed ice features in the fiducial spectrum.

5.3.1.1 Integrated optical depths

We fit a local continuum around the main ice absorption features using several wavelength points just outside the (known ab initio) absorption features and a second-order polynomial fit (see Fig. 5.3), and converted the spectrum into a logarithmic ice optical depth using

$$\tau = -\ln\left(\frac{F_\nu}{F_{\nu,\mathrm{cont}}}\right). \tag{5.6}$$

The prominent H_2O ice feature at 3 µm has a peak optical depth of 0.6 in the integrated spectrum (see Fig. 5.3). The feature has a minor contribution from CH_4, CH_3OH, and NH_3 in the model compared to the H_2O O-H stretching mode. The CO_2 features at 4.26 and 15.2 µm are also present in the spectrum, with a similar strength as the 3 µm H_2O ice feature. The feature at 15.2 µm is double peaked, as expected for a pure CO_2 ice (Warren 1986). The addition of a component of CO_2 in polar mixtures will change the shape of this feature drastically, but this will be discussed in a forthcoming paper. The CO feature at 4.7 µm has a peak optical depth of 0.07. Additional ice features in the spectrum are the CH_4 feature at 7.7 µm and the CH_3OH feature at 9.4 µm. The strength of these features is comparable to that of the CO feature. The spectrum is dominated by photons that encountered multiple scattering events (compared with the gray line in Fig. 5.3). The ice features in the scattering-dominated part of the spectrum (<10 µm) are substantially weaker when single scattering alone is considered because singly scattered photons will be scattered from a warm layer high up in the disk.

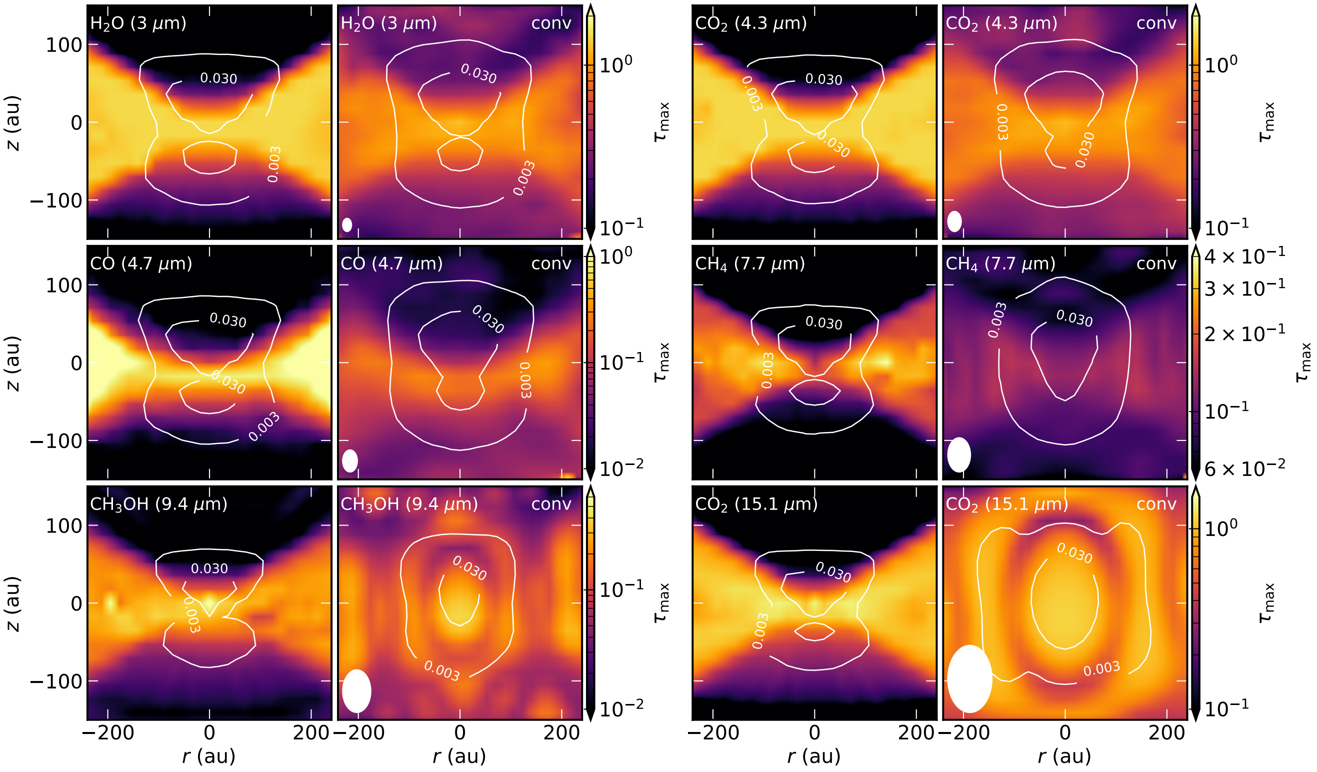

Figure 5.4: Expected peak optical depth for the six main ice absorption features as a function of disk radius and height toward HH 48 NE. The left columns show the optical depth in the model at similar pixel resolution as NIRSpec and MIRI. The right columns show the same after convolving the model with an instrumental PSF of NIRSpec (<5 µm) or MIRI (>5 µm). The FWHM of the PSF is shown in the lower left corner. The white contours show the local continuum at 0.003 and 0.030 mJy for reference. 30 μJy is the typical 3σ sensitivity of a JWST/ NIRSpec exposure of ~1 hour. The color scales are different for each ice feature.

5.3.1.2 Spatially resolved optical depths

We determined the optical depth of the ice features as a function of disk radius and height at a similar pixel scale as that of the NIRSpec and MIRI instruments (Fig. 5.4). We convolved the simulated observations with a NIRSpec or MIRI PSF, depending on the wavelength, and compared it to the original model (second and fourth column). After convolving with an instrumental PSF, the vertical changes are smoothed out over a larger area, lowering the peak optical depths up to a factor of two. The smallest resolvable scale at 4 µm (see Fig. 5.4) is ∼20 au, while the resolvable scale at 15 µm is ∼90 au. This means that at the MIRI longer wavelengths the disk will not be resolved into a lower and upper lobe.

Fig. 5.4 illustrates that the H_2O ice feature at 3 µm is expected to be present throughout the disk. The optical depth of the H_2O ice feature clearly varies with the height in the disk, ranging from an optical depth of 1 at the midplane to 0.3 in the upper layers in the disk. The dark lane is offset from the midplane because of the 82.3° inclination, so that the strongest absorption features are found slightly below the central disk midplane. In the dark lane, where the dust column density is highest and temperatures are low, we trace a higher column density of ice. The optical depth of the water ice features is therefore higher there than in the disk atmosphere.

Radial variations in peak optical depth are small in the model. Even though the continuum changes over two orders of magnitude, the ice column density decreases rapidly with radius and the optical depth is not saturated. This is in contrast to dark cloud ice observations, where in general the ice column density is probed directly, and it illustrates the importance of radiative transfer for understanding edge-on disk ice absorption. The small radial variations in optical depth show that most absorption occurs in the outer disk regions that are similarly crossed by light from all lines of sight.

The CO_2 ice features at 4.3 µm and 15.1 µm are predicted to absorb in similar regions of the disk as the water ice (Fig. 5.4). For the ice features at wavelengths >7 µm, it will be impossible to see vertical changes because of the extent of the instrumental PSF. CO is only available near the disk midplane because the ice is vertically limited by the temperature structure in the disk (see Fig. 5.1). The CO ice feature is strongest in the lower surface of the disk, but we note that the absorption in the upper surface of the disk contributes equally to the integrated spectrum because the continuum in the upper surface is stronger (see Fig. 5.B.1). The vertical CO snowline is resolved in the upper surface of the disk, but the edge is smoothed out due to radiative transfer effects and PSF smoothing.

5.3.2 Sensitivity to parameters

In Fig. 5.5 we present the modeled spectra for a range of parameters compared to the fiducial model that best resembles the currently available continuum observations (see Paper I for details). The evolution of the integrated peak optical depth with these parameters is presented in Fig. 5.6. These peak optical depths are dominated by the disk regions with highest continuum values (see Fig. 5.B.1), however. To compare the models at different disk locations more universally, we summed all emission in a radial slab at seven different heights in the disk and show

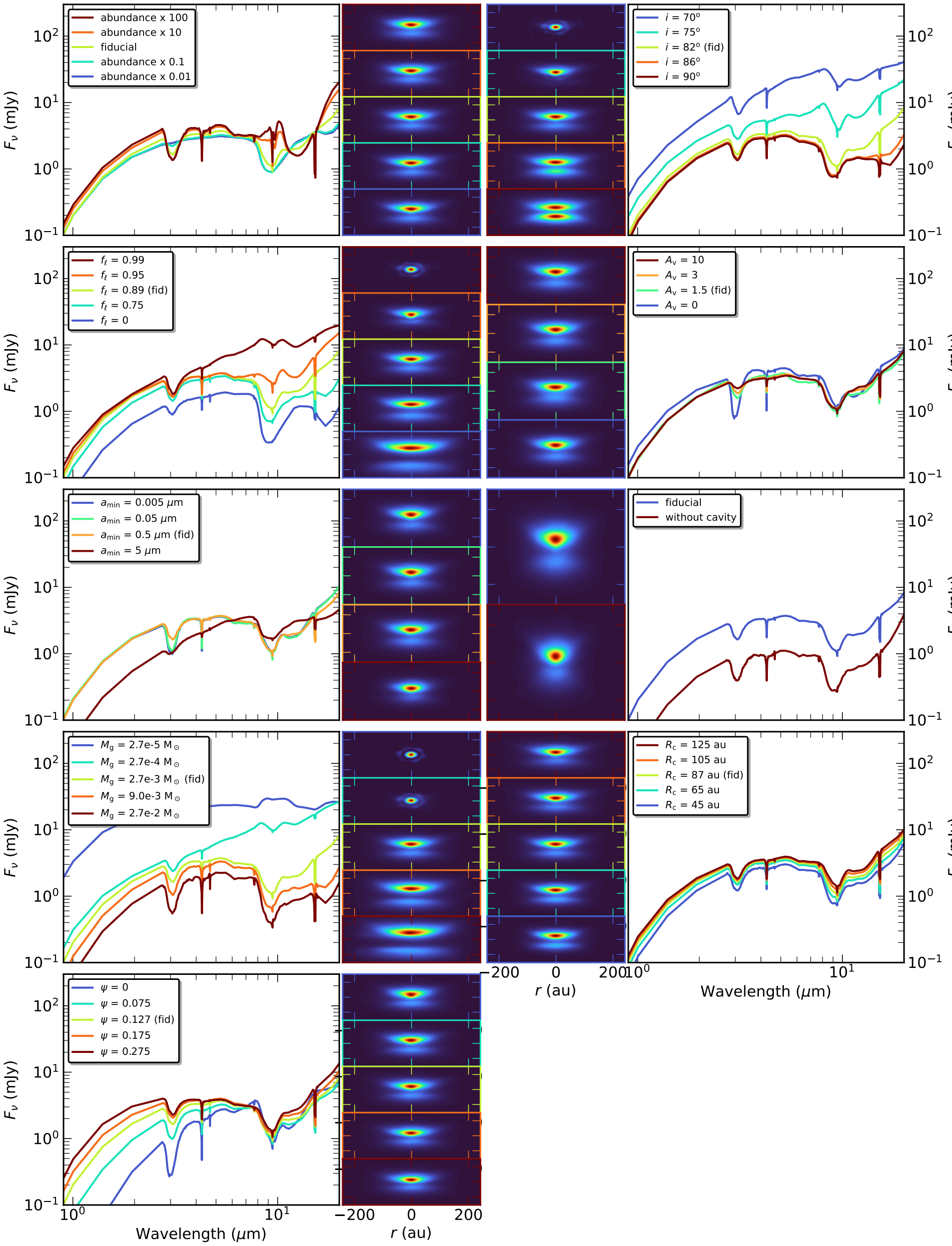

Figure 5.5: Sensitivity of the mid-infrared spectrum to various parameters of the model, stated in the legend (large panels). Appearance of the disk in scattered light at 4 μm, convolved with the NIRSpec PSF (small panels). The panels are labeled with the same color as the legend and show to which extent changes in these parameters will be visible in the NIRSpec images. The vertical ticks indicate ± 100 au.

the optical depth in Figs. 5.B.2, 5.B.3, and 5.B.4.

5.3.2.1 Sensitivity to abundance

We varied the abundance of all molecules by two orders of magnitude from the fiducial model in nine logarithmic steps while keeping the total amount of mass the same. Fig. 5.5 shows the integrated spectra, and the spatially resolved results are shown in Fig. 5.B.2. In a direct observation of ice against a background source instead of a scattering continuum, we would expect a peak optical depth that is directly proportional to the abundance because the ice column density is thought to scale linearly with optical depth. In the limit of low ice abundances (lower than the ISM abundance) we recover the same trend for edge-on protoplanetary disks (see the large panel in Fig. 5.6). However, this slope flattens toward high abundances for all ice species before reaching total saturation of the absorption feature (see Fig. 5.5). This is likely a result of local saturation, meaning that the ice absorption features are saturated at the position in the disk in which the ice absorbs the light, but that additional light from the same line of sight contributes to the total flux that is not saturated because it is scattered through disk regions with less ice. The result is that low ice abundances can be inferred with great accuracy, but for abundances greater than ten times this low abundance, the ISM abundance can only be constrained with a lower limit. The optical depth of CO_2, H_2O, and CH_3OH can reach higher values than CH_4 and CO because their freeze-out region is larger and therefore their absolute absorption is higher. The maximum optical depth can vary from source to source depending on the scattering continuum and source structure.

5.3.2.2 Sensitivity to the fraction of settled mass

The amount of settling (expressed as the mass fraction in large settled grains: f_ℓ, with the corresponding fraction of material left in the atmosphere: $1 - f_\ell$) has a direct effect on the height of the scattering surface in the disk, which is defined as the height at which the disk becomes optically thick to stellar light at each wavelength. This in turn determines which part of the disk will absorb the scattered light from the star and the warm inner disk and thus the depth of the ice absorption features. We changed the amount of settled dust mass in the model setup from 0 to 99% in five steps (see Figs. 5.5, 5.B.2) to determine how this affects the ice spectrum. $f_\ell = 0$ implies that the disk contains no grains larger than 7 µm, which means that the longer wavelengths for that model miss an important emission contribution.

Settling has a major impact on the scattered light images and on the scattering continuum. Less settling means that the upper and lower emission surfaces of the disk extend farther out in height and that the width of the dark lane increases. This is a direct result of the height of the scattering surface, which increases if the number of small grains in the disk atmosphere increases. Disks with $f_\ell >99\%$ do not fully shield the star at an inclination of 82.3°, and the source appears as a point source. Since the settling has a major effect on the resolved scattered light observations, the JWST observations provide tight constraints on the number of small dust grains in the disk atmosphere.

The ice features are strongly affected by the amount of settling (see Fig. 5.6). Multiple effects are at play at the same time, which results in a complicated dependence that is different for every ice feature. The amount of settled dust mass changes the position of the scattering surface, as explained earlier, which affects the amount of cold material below the scattering surface. This effect is visible in Fig. 5.6 as a general increase in the strength of the ice features toward less settled disks up to an order of magnitude due to an increased column density of cold material below the scattering surface. However, for all molecules except CO, the optical depth decreases again for $f_\ell \gtrsim 0.9$. This turnover is due to a directional effect in which the light is scattered more through the disk surface rather than through the cold midplane. The same effect creates the increased width of the dark lane for a less settled disk. Additionally, the upper layers of the disk become increasingly optically thin due to the settling of material, which allows for more direct stellar light or singly scattered light that traces a smaller column of ice. The h$_2$o feature at 3 µm does not follow the trend up in opacity from $f_\ell = 0.99$ to $f_\ell = 0.9$, which is likely because h$_2$o has a high desorption temperature and thus is available throughout the disk. This feature at a relatively short wavelength is also less affected by direct stellar light.

5.3.2.3 Sensitivity to the inclination

In previous works, it has been shown that the inclination can have a strong effect on the visibility of the ices in the disk (e.g., Terada & Tokunaga 2017; Ballering et al. 2021). We varied the inclination of our model from 60° to 90° in eight steps to determine the impact on the absorption features in HH 48 NE.

We show in Fig. 5.5 that the total spectrum of the disk changes over an order of magnitude, but the optical depth of the ice features is not very sensitive to the inclination for most ice species (see Fig. 5.6) as long as the disk is sufficiently edge-on to block direct lines of sight to the star ($i > 70°$; see Fig. 5.3). This is consistent with previous modeling work that showed little variation in ice optical depths >80° (Pontoppidan et al. 2005), although that model predicts significantly more absorption close to the critical inclination of 70°. This difference is likely a result of the differences between the model setups, as Pontoppidan et al. (2005) did not include any settling of large grains nor an A_v threshold for UV photodissociation of ices, which results in a larger amount of ice in the atmospheric layers that is traced in disks at an inclination of ∼70° compared to our model. The sharp transition around i ∼70° is confirmed observationally using all known water ice detections in protoplanetary disks (Terada & Tokunaga 2017). The CO ice feature in the integrated spectrum increases by an order of magnitude from 70 to 90°. This occurs primarily because at low inclination, the scattered light continuum does not reach the coldest regions in the midplane of the disk along the line of sight, but will only probe the ice in layers higher up in the disk.

At lower inclinations, the upper surface of the disk absorbs significantly less in the H_2O, CO_2 , and CO features than the lower surface (see Fig. 5.B.2). The asymmetry between absorption depth in the upper half versus the lower half could thus be a direct probe of the disk inclination. For low inclinations (<75°), the peak of the absorption features shifts to longer wavelengths, which is seen in all main ice features (see Fig. 5.B.2). At these inclinations, the ice scattering opacity plays an important role and causes shifts in the peak position and changes in the absorption profiles. In extreme cases, this results in absorption features with a wing in emission in CO_2 (Dartois et al. 2022).

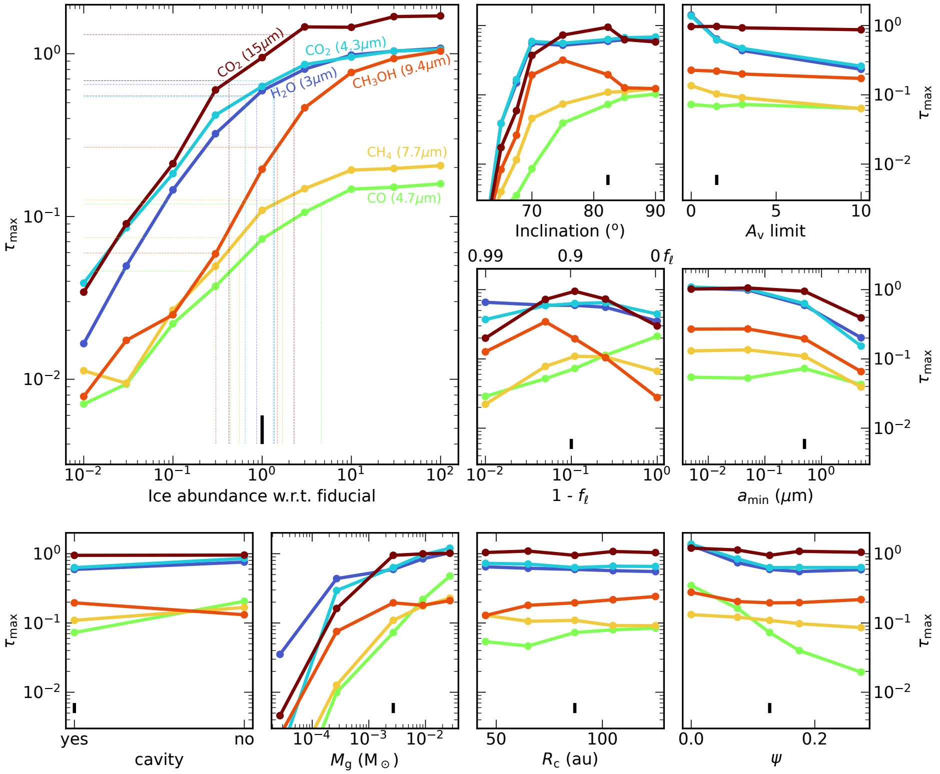

Figure 5.6: Sensitivity to various parameters of the maximum optical depth of the six main ice features. The vertical black line is the fiducial model. The dotted lines in the large panel indicate the uncertainty of the peak optical depth (horizontal) and corresponding abundance (vertical) when taking the uncertainty of all parameters into account. The varied parameters are the ice abundance, the inclination, the A_V limit, the mass fraction of small grains expressed as $1 - f_\ell$, the minimum grain size, the existence of a cavity, the disk mass, and the characteristic disk radius. A typical deep observation of the JWST has a contrast ratio of 300 on the continuum (i.e., S/N = 300), which translates into a 3σ peak optical depth of $\sim 10^{-2}$.

5.3.2.4 Sensitivity to the A_V limit

As mentioned in Sect. 5.2, we added a physically motivated A_V limit to the height in the disk at which ice is allowed to form on the dust grains (see Fig. 5.1). Above this limit, ices will be easily desorbed by nonthermal processes under the intense irradiation of high-energy stellar photons (Boogert et al. 2015; Arabhavi et al. 2022). We varied the A_V limit from the fiducial value of 1.5 to 0, 3, and 10 mag.

Without an A_V limit, the optical depth of H_2O and CO_2 remains fairly constant over the height of the disk, even up to 90 au from the disk midplane (Fig. 5.B.3). With the A_V limit in place, there is less absorption of H_2O and CO_2 (Fig. 5.6), and a larger variation with height (see Fig. 5.B.3). The A_V limit has no effect on the CO absorption because the regions in which the disk is cold enough for CO to freeze out are already lower than the A_V limit (see Fig. 5.1) and the effect on the continuum is minor (Fig. 5.5). The ice features are not sensitive to small variations in the limit that is used. The peak of the absorption features moves with increasing A_V limit to longer wavelengths. This is the case for the H_2O, the CO_2, and the silicate feature (see Sect. 5.3.3 for more details).

5.3.2.5 Sensitivity to the grain size

To determine the sensitivity of the ice features to the grain size distribution, we changed the minimum grain size from the fiducial model of 0.5 µm by extending it to smaller grains. The absorption features of most ice features, except CO, are slightly stronger when we include small grains up to the canonical value of ISM grains, 0.005 µm, but there is no significant difference between a minimum grain size of 0.005 µm and 0.05 µm. Ices on large grains are partly invisible, as shown in previous studies (e.g., Dartois et al. 2022). Including more small grains will therefore boost the fraction of observed ice, hence the optical depth. Any addition of grains smaller than 1 µm is enough to dominate the absorption, and including more small dust grains does not change the optical depths of the ice significantly. If only grains larger than 5 µm are used, the optical depth changes significantly by a factor of $\sim$5 (see Fig. 5.6).

5.3.2.6 Sensitivity to a cavity

To determine the effect of a cavity on the spectrum, we ran the same model as the fiducial model, but without a dust depletion inside the cavity. The integrated continuum is suppressed by a factor of $3 - 4$ (see Fig. 5.5), but the cavity has a negligible effect on the H_2O and CO_2 ice features (see Fig. 5.6). This indicates that most absorption occurs in the outer regions of the disk and that the cavity does not have a significant effect on the region in which the warm dust emission is scattered in the disk, as long as there is warm material in the inner disk. The CO feature at 4.67 µm does change by a factor of 3, which is considerable given that a similar boost could result from an elevated abundance by an order of magnitude.

5.3.2.7 Sensitivity to the total mass

The disk mass was varied over four orders of magnitude from $3\times10^{-5} - 3\times10^{-2}$ $M_\odot$ while keeping the gas-to-dust ratio constant. We would like to note that a lower disk mass therefore decreases the ice column densities, similar to the ice abundance grid, but also has a significant effect on the scattering continuum (see Fig. 5.5). Ice absorption features are sensitive to the order-of-magnitude changes, but only the features at wavelengths <5 µm change significantly if the mass increases by an order of magnitude. By changing the disk mass, the temperature structure changes, as does the column density of the material and the height of the emitting layer. The latter two dominate in the impact on the ice features. This results in a weaker change in the features at longer wavelengths, partly due to the local saturation explained in Sect. 5.3.2.2. This is especially true for the methanol feature at 9.4 µm and the CO_2 feature at 15.2 µm. The CO_2 feature at 4.27 µm is much more affected than the CO_2 feature at 15.2 µm, which could serve as a direct probe of the disk mass. However, the feature at 15.2 µm can changes considerably in shape if the CO_2 is in different ice matrices.

5.3.2.8 Sensitivity to the radial size

The physical size of the disk can play a major role in setting its temperature structure. We varied one of the parameters that determines the radial extent of the disk, R_c, between 45 and 125 au. Although the effect on the continuum is significant (Fig. 5.5), the ice optical depths do not change significantly (Fig. 5.6). We would like to note that for models with a small R_c, the 55 au cavity pushes material outward to sustain the same disk mass as the fiducial model. Increasingly small disks without a cavity are expected to show variations due to changes in the area below the snow surfaces.

5.3.2.9 Sensitivity to the flaring index

We varied ψ from a flat disk ($\psi = 0$) to an extremely flared disk ($\psi = 0.275$) in five steps $\psi \in [0, 0.075, 0.127, 0.175, 0.275]$. The flaring has only a minor effect on the ice features in the MIRI wavelength regime, but the optical depth of the ice features <5 µm increases for a flatter disk. The flaring of the disk (ψ) changes the temperature structure in the disk and directly affects the angle of the scattering surface toward the midplane. For disks with less flaring, this angle is smaller, and thus more light will reach the ice-rich regions of the disk. This effect is strongest for the CO ice feature at 4.7 µm because CO ice is only located near the midplane.

5.3.3 Silicate feature

Not only the ice absorption features, but also the shape and strength of the silicate feature at 10 µm are affected by the physical parameters of the disk model (see Figs. 5.B.2 and 5.B.4). In the fiducial model, the silicate feature is only seen in absorption, unlike the typical emission feature seen in disks with an inclination <70° (Olofsson et al. 2009). Absorption of the silicate feature arises when the scattering surface is high up in the disk and the light has to pass through a large column of cold dust in the outer disk.

The silicate feature is very sensitive to the inclination. For inclinations <75°, an emission component is seen in addition to the silicates in absorption, and at even lower inclinations, the silicate feature appears only in emission. Very settled disks also show a silicate feature in emission because the scattering surface is low in the disk, which means that the warm dust above the scattering surface significantly adds emission to the spectrum. These changes also affect the determined CH_3OH optical depths (see Fig. 5.6). The silicate feature varies in strength with varying ice abundance, and it is even seen in emission when the ice coating on the grains is thick enough.

Changes in the shape of the silicate absorption feature are observed in *Spitzer* IRS spectra toward edge-on protoplanetary disks. For comparison, we retrieved low-resolution spectra from the CASSIS archive (Lebouteiller et al. 2011) of the edge-on disks Tau 042021 and ESO-Ha 569 (see Fig. 5.7). The optical depth of the silicate feature was determined with a linear fit using data points between (5,6) and (11,14) µm and Eq. 5.6. The silicate feature in ESO-Ha 569 has a clear emission component around 8 µm, while the feature in Tau 042021 has only a component in absorption. Without detailed modeling of the sources, we overplot the model for HH 48 NE at an inclination of 90° and 75°. The inclination of these sources can roughly be inferred from their silicate feature alone because ESO-Ha 569 is inclined at ∼83° (Wolff et al. 2017), while Tau 042021 is inclined at 88° (Villenave et al. 2020). The differences in inclinations are exaggerated because of the differences in mass and settling of the two disks and HH 48 NE. An estimate of the dust mass is necessary to use this approach in observations, for example, from millimeter continuum observations. The shape and strength of the silicate feature can be crucial to break parameter degeneracies and help interpreting the ice observations.

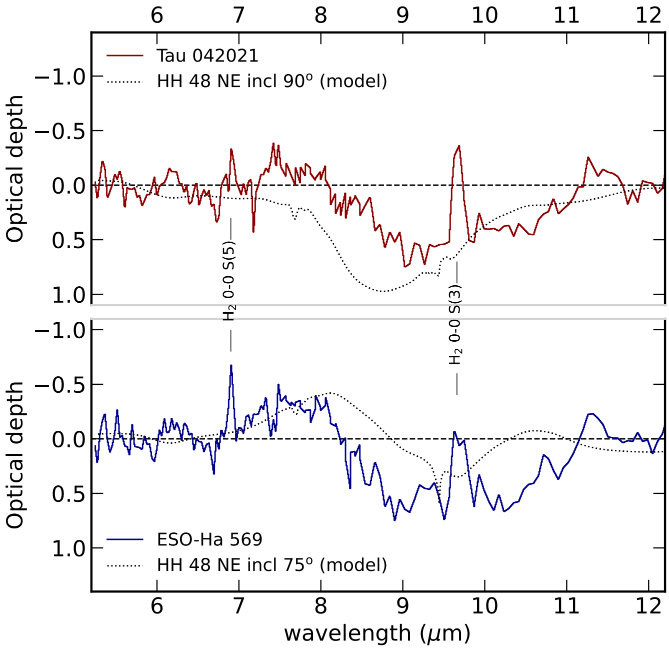

Figure 5.7: Optical depth of the silicate feature in *Spitzer* spectra for Tau 042021 and ESO-Ha 569. The black lines show the optical depth of the silicate features in a model inclined at 90° and 75°. The shape of the silicate feature clearly is a function of inclination and disk mass.

5.4 Discussion

The high sensitivity and resolution of the JWST will provide spatially resolved measurements of ices in Class II protoplanetary disks. These observational data can only be properly interpreted with detailed modeling. This is especially true for edge-on disks because the ice absorption features are highly dependent on the physical source structure and are not easy to interpret. We have explored the effect of various parameters on the optical depth of the ice that can be directly compared to observations to interpret the results.

5.4.1 Constraining the ice abundances

We investigated the impact of various physical disk parameters on the optical depth of the main ice features in protoplanetary disks. We find that the molecular abundance and disk mass have the strongest effect on the observed ice features, which results primarily from a reduction of the absolute column density of ice. The optical depth increases monotonically with the abundance for all ice features, but the exact shape is dependent on the source structure and wavelength. Two other important parameters are the inclination and the amount of grain growth and settling. These parameters can change the optical depths in the same order of magnitude as the chemical abundance. It is hence crucial to have a well-constrained physical disk model to constrain the ice abundances from observations.

This work is the first to convolve the model with an instrumental PSF to determine whether we can resolve vertical changes in the ice abundance. HH 48 NE should be resolved sufficiently within the NIRSpec range to constrain vertical abundance gradients due to temperature, irradiation, and chemistry. At wavelengths >7 µm, the vertical dependences are no longer resolved because the size of the PSF increases. The vertical extent of the CO and CO_2 snowline might therefore be observable in the derived observed optical depths, although the transition will be smooth because the elevation of the snow surface increases radially outward. The PSF side lobes can induce significant artifact ice-feature signatures throughout the disk, even in regions in which direct ray-tracing of the model without convolution of a PSF shows no sign of ices (e.g., at 100 au in Fig. 5.4). Since the radial dependence of the optical depth of the ice is largely insensitive to the disk geometry and most absorption occurs in the outer regions of the disk, it will be difficult to infer radial snowlines or abundance variations in radial direction because all photons originate from central regions in the disk, which means that all photons that are scattered in our direction have encountered a wide range of radii regardless of the line of sight they appear to come from. We would like to note that RADMC-3D uses long characteristic radiative transfer for the image reconstruction, which in general is more expensive, but gives the most accurate results. We tested another radiative transfer approach that combines both long characteristics and short characteristics radiative transfer, `Hyperion` (Robitaille 2011), which gives identical results (see Appendix 5.A for more details).

We have shown that the optical depth of the ice features increases monotonically with abundance, but an accurate estimate of the source inclination, the amount of settling, and the disk mass is required to determine the conversion factor. The maximum optical depth that can be reached in our models is ∼1 even at very high ice abundances and column densities. This illustrates that the ice features may be locally saturated in the disk, but that at least one-third of the light is scattered through the ice-free upper layers of the disk before it is scattered in our direction from a layer deeper down in the disk. The optical depths of the ice that we find in our model are relatively high compared to earlier work by Ballering et al. (2021) and Arabhavi et al. (2022). In contrast to these works, we expect to find CO in the integrated NIRSpec spectra and deeper CO_2 ice features. Ballering et al. (2021) used a standard model with a high disk mass and complex gas-grain chemistry in the same radiative transfer code `RADMC-3D`. Their continuum for an inclination of 85° is similar to our spectrum, but their silicate feature is in emission even at an inclination of 90°. The water-ice feature in their spectrum is of similar strength as in our model, but the other species compared to water ice are much weaker. The final abundances in their inheritance model are very similar to our input abundance and are fairly constant with height and radius. The differences between their expected strength of the ice absorption features and this work are therefore largely a result of the geometry of the fiducial disk model. The observed optical depths toward the Class I disk in Pontoppidan et al. (2005) are much deeper than our model, but they show that most ices are located in the envelope surrounding the disk, and only 50% of H_2O and CO_2 and none of the CO ice are located in the disk. Because HH 48 NE is a more evolved disk without a thick envelope, absorption from cloud ice does not play a significant role.

In Sect. 5.3.2 we showed that global ice abundances can be inferred from spatially integrated observations when the settling, inclination, and disk mass are known. In the case of HH 48 NE, these three parameters are well constrained (see Paper I; Sturm et al. 2023e). By treating the uncertainties as independent from each other, we can derive a first-order estimate of the uncertainty on the measured ice abundances from the parameter variation in Fig. 5.6. We determined the uncertainty on the optical depth expected from the 1σ uncertainty interval via interpolation for each of the considered parameters. By combining the uncertainties using $\sigma_{\mathrm{tot}}^2 = \sum_{\mathrm{p}} \sigma_{\mathrm{p}}^2$, we determined the uncertainty on the molecular abundance for each ice feature (see the vertical lines in the top left panel of Fig. 5.6). The uncertainty on the ice abundances is typically a factor of 2, and only the CO abundance is uncertain to a factor of 3.

5.4.2 Detectability of edge-on disks

Highly inclined disks ($i > 70°$) are statistically less often detected than their less inclined counterparts (Luhman et al. 2008; Rodgers-Lee et al. 2014). Based on this parameter study, we identify several potential explanations for this trend.

First, edge-on disks are often selected based on their SEDs and are then confirmed with scattered light imaging or resolved millimeter continuum observations. Edge-on disks typically have a high infrared excess and a characteristic dip in the mid-infrared because the silicate feature is in absorption. The spectra of these disks can look similar to those of transition disks, which show a comparable dip in the mid-infrared that is caused by a lack of warm material in the inner disk regions (van der Marel et al. 2022), or to those of Class I sources that recieve less stellar contribution to their SED as well. We have shown that edge-on disks with a high level of settling or with an inclination of <85° may instead show a silicate feature in emission, which means that these objects may not be recognized as edge-on disks until they are observed at high angular resolution. Complete sample studies at high angular resolution with ALMA or scattered light observatories are hence necessary to increase the fraction of detected edge-on disks. Unfortunately, very high angular resolution is necessary to determine highly inclined sources directly from the observations (Villenave et al. 2020), and the observed samples of disks in scattered light are far from complete.

Second, the radial substructure might be important for detecting edge-on disks.

The HH 48 NE model without a cavity has a scattered light continuum that is lower by a factor of 3 to 4, which makes the disk harder to detect (see Fig. 5.5). With a cavity, the mid-infrared is boosted by the structural changes in the disk density profile.

Third, in many instances, we find that the disk disappears due to a lack of contrast between the star and the disk (see Fig. 5.5). This is especially true for disks with a high level of settling, a low inclination, or a low disk mass. This results in an observation bias because the average observed disk mass for edge-on disks ($>$25.6 $M_\oplus$ Villenave et al. 2020) is higher than the mean dust mass distribution of the full Taurus and Lupus disk populations (15 $M_\oplus$ Andrews et al. 2013; Ansdell et al. 2016), especially when we take into account that edge-on disks are much more likely to be optically thick (Villenave et al. 2020). Without sufficient material in the upper layers of the disk to block direct lines of sight to the star, it will be impossible to detect these disks in scattered light without a coronagraph (see also Wolff et al. 2017). The recent work by Angelo et al. (2023) comes to similar conclusions using a simulated population of edge-on protoplanetary disks.

5.5 Conclusions

We have set up a disk model using the radiative transfer code `RADMC-3D` that includes anisotropic scattering and opacities of the six most important ice species. The sensitivity of the optical depth of the main ice features to various physical parameters was explored to determine how well chemical abundances can be constrained in the disk. We conclude the following:

- The main ice species, H_2O and CO_2, are likely detectable in JWST data of edge-on protoplanetary disks. Weaker features such as those from CO, CH_4, CH_3OH, and NH_3 require a high inclination and a low amount of settling to be observed.

- The optical depth of the ice features in protoplanetary disks changes monotonically, but non-linearly with ice abundance, and is saturated at an optical depth $\lesssim$1 due to the effect of local saturation. A detailed modeling of the source structure is necessary to infer the chemical effects in the disk. The abundances in the HH 48 NE disk can be constrained to within a factor of 3 with respect to the dust content when the current uncertainty on the disk geometry is taken into account.

- Vertical ice abundance gradients are detectable in the NIRSpec range (H_2O, CO_2, and CO), but the resolved optical depths are not linearly related to the ice column density along the line of sight. For wavelengths longer than 7 µm, resolved maps will be dominated by PSF residuals that are due to the large angular scale of the PSF.

- The shape of the silicate feature and the comparison between the two CO_2 bands at 4.3 and 15.1 µm might help to break the degeneracy between the total solid mass and the ice-to-rock ratio.

- The low detection rate of edge-on disks can be explained by a combination of silicate features that appear in emission at inclinations <85°, radial substructure that is necessary to boost the mid-infrared continuum, and the need for a large amount of dust high up in the disk to block direct lines of sight toward the star.

We have shown that the JWST will be able to observe spatially resolved ice features in protoplanetary disks. In-depth modeling of the ice chemistry, disk geometry, and radiative transfer is crucial to interpret forthcoming observations of the JWST ERS program IceAge and edge-on disks in general.

5.6 Acknowledgments

We would like to thank the anonymous referee for suggestions that improved the manuscript. We also thank Ewine van Dishoeck for useful discussions and constructive comments on the manuscript. Astrochemistry in Leiden is supported by the Netherlands Research School for Astronomy (NOVA), by funding from the European Research Council (ERC) under the European Union's Horizon 2020 research and innovation programme (grant agreement No. 101019751 MOLDISK). M.K.M. acknowledges financial support from the Dutch Research Council (NWO; grant VI.Veni.192.241). D.H. is supported by Center for Informatics and Computation in Astronomy (CICA) grant and grant number 110J0353I9 from the Ministry of Education of Taiwan. DH acknowledges support from the National Technology and Science Council of Taiwan through grant number 111B3005191. M.N.D. acknowledges the Swiss National Science Foundation (SNSF) Ambizione grant no. 180079, the Center for Space and Habitability (CSH) Fellowship, and the IAU Gruber Foundation Fellowship.

This work makes use of the following software: `numpy` (van der Walt et al. 2011), `matplotlib` (Hunter 2007), `astropy` (Astropy Collaboration et al. 2013, 2018), `OpTool` (Dominik et al. 2021), `RADMC-3D` (Dullemond et al. 2012), `Hyperion` (Robitaille 2011), `WebbPSF` (Perrin et al. 2012).

Appendix

5.A Comparison between `RADMC-3D` and `Hyperion`

Figure 5.A.1: Comparison between ray-traced spectra by `RADMC-3D` and `Hyperion`. The top panel shows the SEDs for `Hyperion` and `RADMC-3D`. The colored lines show the contribution to the total spectrum of scattered stellar light (red), scattered light from warm dust (blue), and direct light from warm dust (orange). The direct stellar light component is negligible and is therefore not shown in this plot. The bottom panel shows the normalized difference between the two total outputs of the two codes. The dashed lines indicates the standard deviation of the difference, which is 5%.

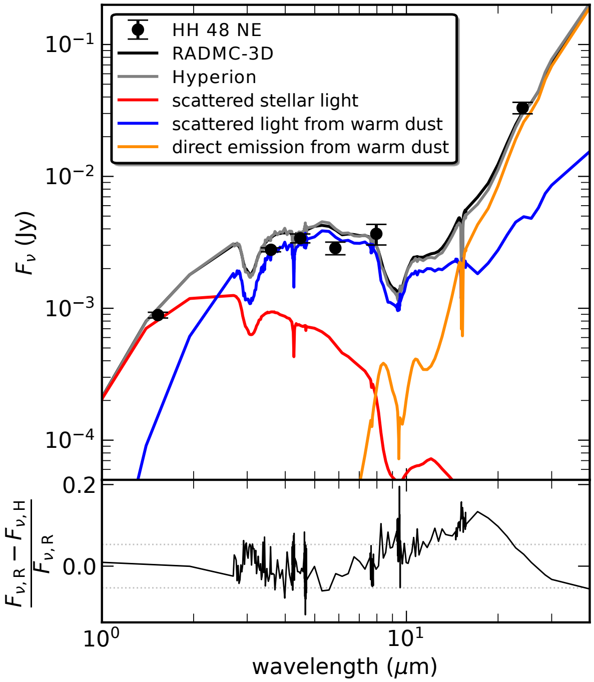

As a validation of the suitability of `RADMC-3D` for full anisotropic scattering in edge-on disk models, we ran the best-fitting model once with the radiative transfer code `Hyperion` (Robitaille 2011). `Hyperion` treats scattering internally differently. It traces each individual photon package from the source to the destination. The benefit of this is that multiple inclinations can be ray-traced at once and that the final spectrum can be dissected into four components: direct stellar light, scattered stellar light, direct dust emission, and scattered light from warm dust (see Fig. 5.A.1). The downside is that the code is very demanding in terms of computing time and computer RAM (>500 Gb; hence only possible on high-performance clusters). The relative difference between the final output of the two codes is less than 20% everywhere in the spectrum, does not increase in the ice absorption features, and has a standard deviation of 5%. With this comparison, we demonstrate that the output can be trusted independent of the radiative transfer code that is used. In the spectral region in which the important ice absorption features are located, the continuum is dominated by the dust scattering by half an order of magnitude over direct source scattering at short wavelengths and dust emission at long wavelengths.

5.B Additional material

In Fig. 5.B.1 we present the spatially resolved optical depth of the ice features, similar to Fig. 5.4, but weighted with the continuum emission. The maps show how much the different disk regions contribute to the disk integrated spectrum. In all absorption features, only a few pixels determine the optical depth of the ice in the disk-integrated spectrum.

Spatially resolved observations are necessary to trace any variations in abundance directly. In Figs. 5.B.2, 5.B.3, and 5.B.4, we present the vertically resolved optical depth of the main ice absorption features as function of the same parameters as in Sect. 5.3.2

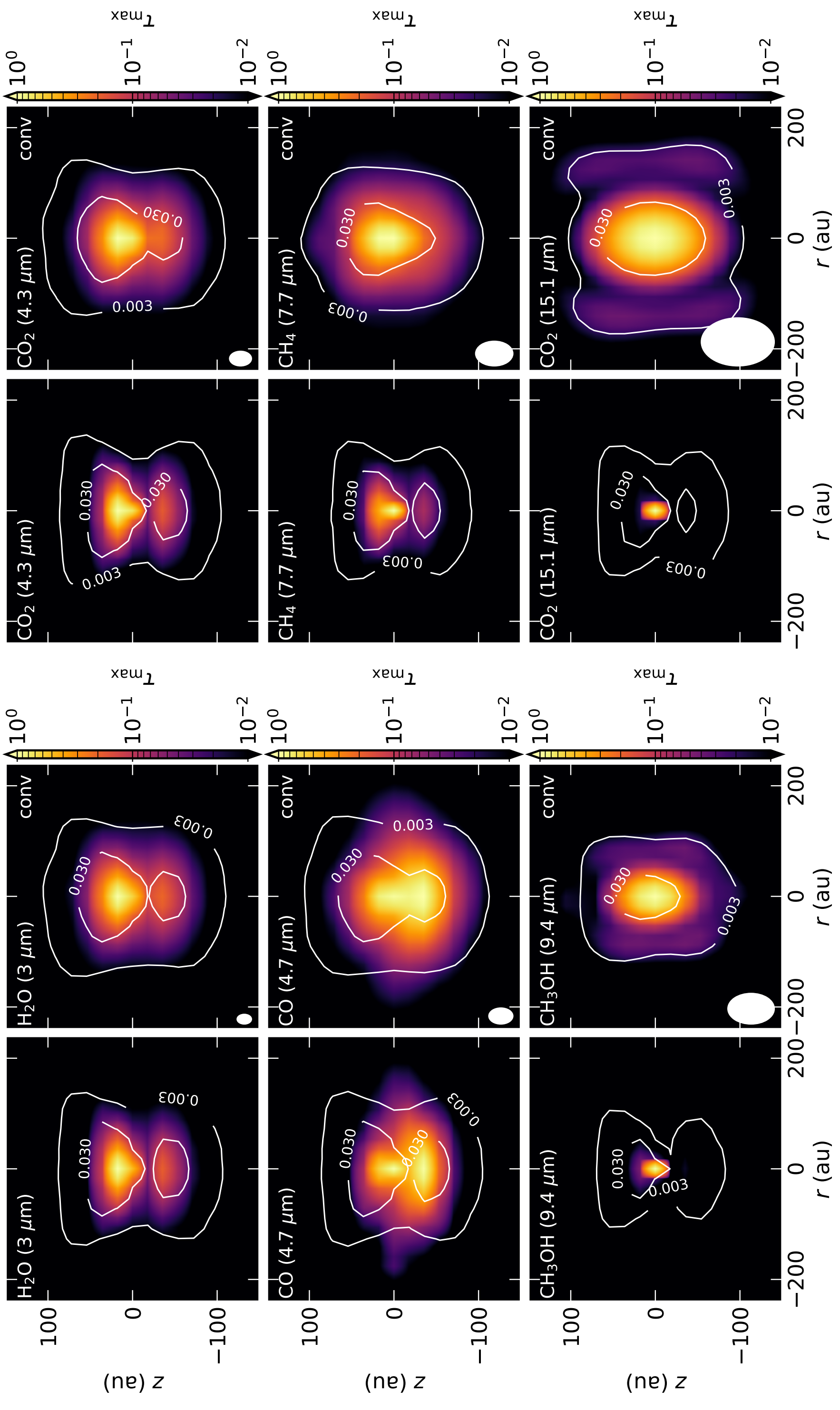

Figure 5.B.1: Same as Fig. 5.4, but weighted with the continuum emission and normalized to the peak contribution. This figure illustrates what part of the disk contributes mostly to the disk averaged spectrum or the radial slabs presented in Figs 5.B.2, 5.B.3, and 5.B.4.

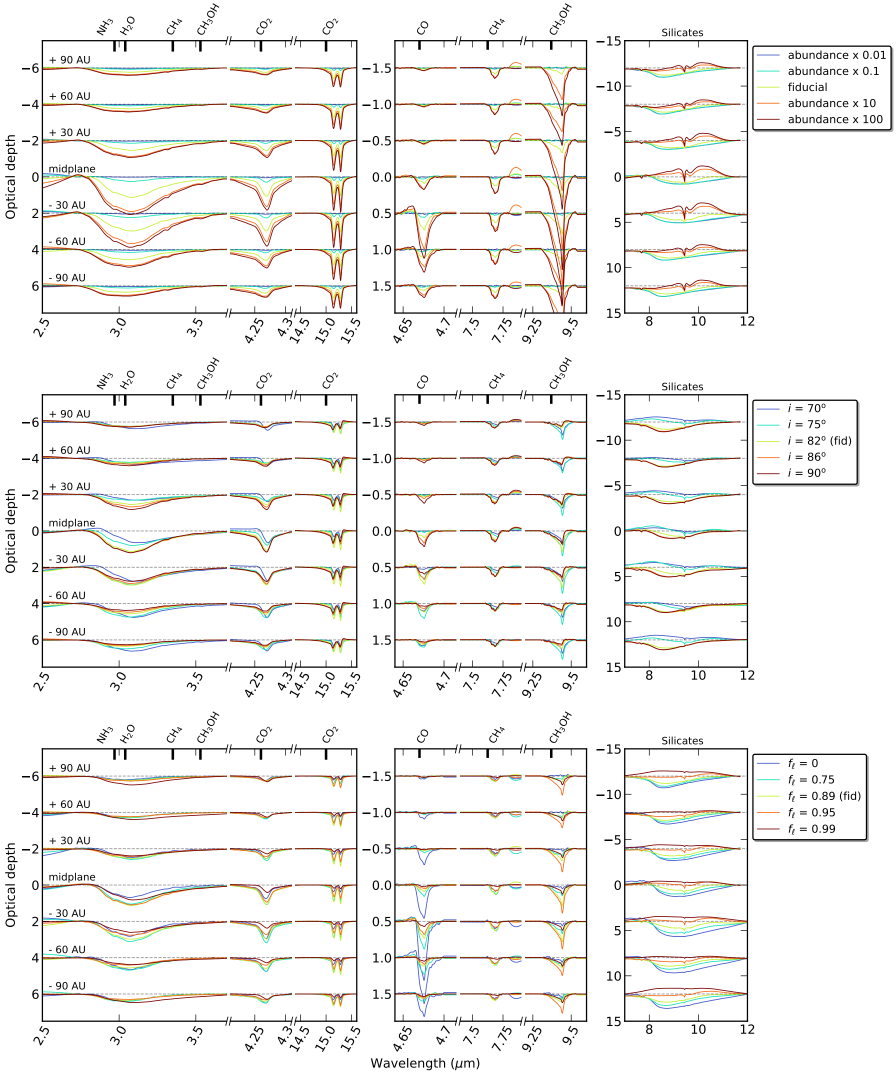

Figure 5.B.2: Dependence of the ice optical depth on the ice abundance, the inclination and the fraction of settled large grains. The modeled optical depth of the main ice features and the silicate feature are shown at 7 different vertical positions in the disk, convolved with an instrumental PSF. The resolution in height is 30 au, which corresponds to two pixels in NIRSpec/MIRI data.

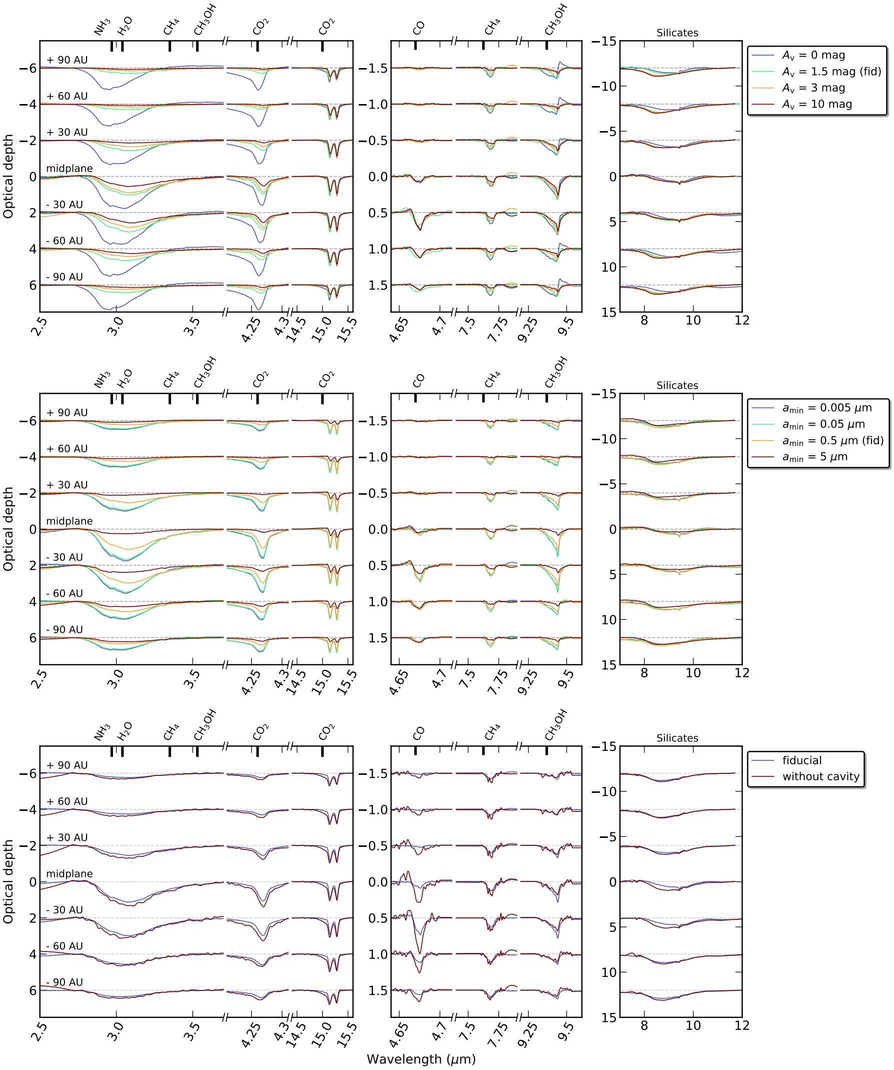

Figure 5.B.3: Same as Fig. 5.B.2, but instead varying the A_V limit and the maximum grain size, as well as with and without a dust cavity.

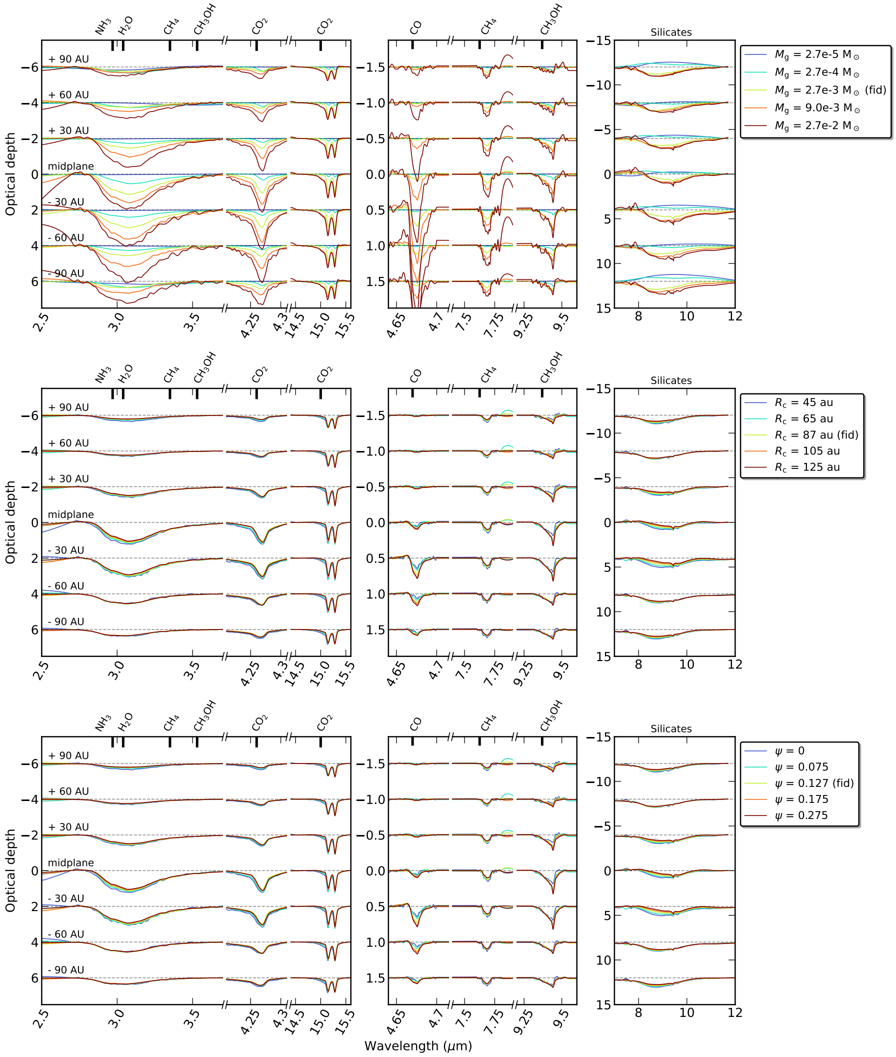

Figure 5.B.4: Same as Fig. 5.B.2, but instead varying the total disk mass and the spatial scale of the disk as a function of R_c.

Chapter 6

A JWST inventory of protoplanetary disk ices. The edge-on protoplanetary disk HH 48 NE, seen with the Ice Age ERS program

J. A. Sturm, M. K. McClure, T. L. Beck, D. Harsono, J. B. Bergner, E. Dartois, A. C. A. Boogert, J. E. Chiar, M. A. Cordiner, M. N. Drozdovskaya, S. Ioppolo, C. J. Law, H. Linnartz, D. C. Lis, G. J. Melnick, B. A. McGuire, J. A. Noble, K. I. Öberg, M. E. Palumbo, Y. J. Pendleton, G. Perotti, K. M. Pontoppidan, D. Qasim, W. R. M. Rocha, H. Terada, R. G. Urso, and E. F. van Dishoeck

A&A 679, A138 (2023)

Abstract

Ices are the main carriers of volatiles in protoplanetary disks and are crucial to our understanding of the protoplanetary disk chemistry that ultimately sets the organic composition of planets. The Director's Discretionary-Early Release Science (DD-ERS) program Ice Age on the James Webb Space Telescope (JWST) follows the ice evolution through all stages of star and planet formation. JWST's exquisite sensitivity and angular resolution uniquely enable detailed and spatially resolved inventories of ices in protoplanetary disks. JWST/NIRSpec observations of the edge-on Class II protoplanetary disk HH 48 NE reveal spatially resolved absorption features of the major ice components H_2O, CO_2, and CO, and multiple weaker signatures from less abundant ices NH_3, OCN^-, and OCS. Isotopologue $^{13}CO_2$ ice has been detected for the first time in a protoplanetary disk. Since multiple complex light paths contribute to the observed flux, the ice absorption features are filled in by ice-free scattered light. This implies that observed optical depths should be interpreted as lower limits to the total ice column in the disk and that abundance ratios cannot be determined directly from the spectrum. The $^{12}CO_2/^{13}CO_2$ integrated absorption ratio of 14 implies that the $^{12}CO_2$ feature is saturated, without the flux approaching zero, indicative of a very high CO_2 column density on the line of sight, and a corresponding abundance with respect to hydrogen that is higher than inter stellar medium values by a factor of at least a few. Observations of rare isotopologues are crucial, as we show that the $^{13}CO_2$ observation allowed us to determine the column density of CO_2 to be at least 1.6×10^{18} cm^{-2}, which is more than an order of magnitude higher than the lower limit directly inferred from the observed optical depth. Spatial variations in the depth of the strong ice features are smaller than a factor of two. Radial variations in ice abundance, for example snowlines, are significantly modified since all observed photons have passed through the full radial extent of the disk. CO ice is observed at perplexing heights in the disk, extending to the top of the CO-emitting gas layer. Although poorly understood radiative transfer effects could contribute to this, we argue that the most likely interpretation is that we observed some CO ice at high temperatures, trapped in less volatile ices such as H_2O and CO_2. Future radiative transfer models will be required to constrain the physical origin of the ice absorption and the implications of these observations for our current understanding of disk physics and chemistry.

6.1 Introduction

Life, as we know it, is largely formed from the elements C, H, O, N, and S (CHONS), which, in protoplanetary disks, are carried mostly as ices or organics on dust grains (Henning & Semenov 2013; Furuya et al. 2013; Krijt et al. 2023). These grains are accreted by newborn planets, either as they form or during a later delivery by planetesimals residing in warm or cold debris reservoirs (asteroid and Kuiper Belt analogs) in more mature systems. Such organic-rich icy grains are formed in molecular clouds and are funneled into the planet-forming regions of disks via an infalling protostellar envelope during the early stages of star formation (e.g., Visser et al. 2009; Hincelin et al. 2013; Drozdovskaya et al. 2016). During infall, some of the ices sublimate during episodic, protostellar mass accretion events (Kim et al. 2012), and they could dissociate to their atomic constituents in the gas phase before reforming and freezing out again in the disk, partly resetting the disk's ice chemistry relative to the cloud chemistry (Ballering et al. 2021). The relative amount of different ice species inherited by the disk from the cloud versus reset during this process is observationally still poorly constrained (Öberg & Bergin 2021).

Within disks, the ice species are expected to be vertically and radially segregated by 3D "snowlines", which is the point where species sublimate from the ice phase. Grain growth and gravitational settling produce a vertical dust distribution that dictates where the stellar radiation is absorbed and scattered, setting a strong vertical temperature gradient. A corresponding chemical gradient arises between the disk midplane, where planetesimals form from large, icy grains, and the disk's upper layers, where UV radiation photodesorbs the ice from the grain surface at a vertical snowsurface (Dominik et al. 2005; Kamp et al. 2018). Similarly, a radial temperature gradient gives rise to snowlines at certain distances from the central star, where inherited or reformed ices sublimate. Disk snowlines gave rise to Solar System planets, moons, and small bodies with different compositions (Bergin et al. 2015) and may have also set the bulk atmospheric properties of the planets (Öberg et al. 2011b; Madhusudhan 2019). The distribution of major CHONS ices during the initial stages of planet formation in protoplanetary disks can be inferred from comets, asteroids, and icy moons in the Solar System (e.g., with Rosetta, Hayabusa 2, OSIRIS-REx, Juice) or in situ snapshots of ices at different stages of planet formation. The latter, in particular, is critical in order to understand the variety of processes and planetary outcomes during planet formation (Krijt et al. 2023).

Individual ice species are detectable in the laboratory through fundamental vibrational modes seen in the infrared between 1 and 140 µm (e.g., Rocha et al. 2022, and references therein). These laboratory spectra can be used to identify astrophysical ices in different environments. Ices have been detected in absorption against the hot continuum provided by stars located behind cold, dense molecular clouds in protostellar envelopes, in the cold outer regions of edge-on protoplanetary disks (Boogert et al. 2015), and in emission from the midplanes of a select number of disks around T Tauri and Herbig Ae/Be stars from 44 – 63 µm with the Infrared Space Observatory (ISO) and the *Herschel* Space Observatory (Chiang et al. 2001; McClure et al. 2012, 2015; Min et al. 2016). Ice emission requires full radiative transfer modeling to be fully interpreted; however, for pure absorption spectroscopy, it has been standard practice to calculate logarithmic ice optical depths from spectroscopic data using the following:

$$\tau = -\ln\left(\frac{F_\nu}{F_{\nu,\mathrm{cont}}}\right), \tag{6.1}$$

where F_ν is the observed flux and $F_{\nu,\mathrm{cont}}$ is the flux of the fitted continuum. Then lab-measured band strengths of the ice features were used to convert the observed optical depths to column densities by

$$N = \frac{\int \tau_\nu \mathrm{d}\nu}{A}, \tag{6.2}$$

where ν is wavenumber in cm^{-1} and A is the band strength in cm molecule^{-1}. If the ice features could be assumed to come from the same absorbing region, then relative ice abundances could be derived from column densities in a model-independent way. In the past, most of the available ice spectra consisted of spatially unresolved spectroscopy of point sources; therefore, the simplifying assumptions of pure ice absorptions within the same beam seemed appropriate for ices seen toward background stars and protostars. In this manner, ice abundances relative to H_2O have been derived in a few molecular clouds using lines of sights toward background stars, many protostars, and a minimal number of edge-on disks (EODs) using the Very Large Telescope (VLT) or the *Spitzer* Space Telescope.

This assumption was known to be incorrect for ices in any source with an extended physical structure, such as a disk. However, recent work has suggested that this traditional assumption of pure ice absorption may not hold in most astrophysical environments relevant to star formation. When icy mantles grow to micrometer sizes, they are seen through a combination of both absorption and scattering, which modifies their feature profiles and may strongly impact how well column densities translate into relative abundances, even toward targets with no source structure such as stars behind molecular clouds (Dartois et al. 2022). This effect would be expected to be enhanced toward sources with an internal structure, such as protostars or disks.

For disks in particular, the observations themselves are challenging. First, ices are concentrated in the midplane, which only becomes optically thin in the far-infrared. In the absence of space-based far-infrared telescopes, the only current option to observe ices is to probe them in the mid-infrared, although this samples ices in the disk atmosphere rather than in the disk midplanes, which is optically thick in the infrared. At these wavelengths, ices have been detected by broadband, coronagraphic ground-based scattered light imaging of sufficiently bright, face-on disks, for example the Herbig Ae stars HD 142527 and HD 100546 (Honda et al. 2009, 2016), and through spectroscopy of edge-on systems ($i > 70°$). In the latter case, the optically thick midplane acts as a coronagraph to block thermal emission from the central star and hot dust in the disk's midplane at 1 – 5 au, reducing the contrast enough to detect the signatures of cold ices beyond 20 au in absorption against the faint light from the star or inner dust rim scattered through the disk's atmosphere (Pontoppidan et al. 2007; Sturm et al. 2023d). This technique allows the measurement of multiple ice species simultaneously, which is critical for determining CHONS abundances.

Previous spectroscopic studies of edge-on disks were limited by their technical capabilities and sample selection. Unresolved, single-slit ground-based spectroscopy detected water ice in a select number of disks, including CRBR 2422.8-3423, HV Tau C, HK Tau B, a couple of Orion silhouette disks, and the disks around the Herbig Ae/Be stars PDS 144 N and PDS 453 (Thi et al. 2002; Terada et al. 2007; Terada & Tokunaga 2012, 2017). However, detection of the main carbon dioxide (CO_2) and carbon monoxide (CO) ice features are limited by absorption from Earth's atmosphere and the sky background at 4 – 5 µm. Additional observations from space of edge-on disks ASR41, 2MASS J1628137-243139, HV Tau, HK Tau, UY Aur, and IRAS 04301 with AKARI (Aikawa et al. 2012) and CRBR 2422.8-3423 with *Spitzer* IRS (Pontoppidan et al. 2005) confirmed the ground-based water detections and added CO_2 detections for the latter five sources.

However, the last two systems demonstrate the second difficulty with ice measurements in disks: target selection. Without ancillary data, it can be difficult to disentangle whether the observed ice bands originate in the disk itself or in other foreground material (e.g., in a surrounding cloud or a protostellar envelope). Selecting samples of mature, envelope-free disks should solve this problem, but historically it has been difficult to identify edge-on disks a priori. Extinction, including self-extinction by their outer disks and scattering from the inner edge, can result in edge-on disks being mistaken for younger protostars due to their rising shape in the mid-infrared when identified purely based on spectral energy distributions (SEDs) (Robitaille et al. 2006; McClure et al. 2010, Figure 3). Only recently have small samples of non-embedded edge-on disks been compiled and resolved at multiple wavelengths, using optical scattered light and resolved millimeter imaging (Villenave et al. 2020). For these validated disks, the sensitivity, wavelength coverage, spectral resolution, and spatial resolution of the *James Webb* Space Telescope's (JWST) near- and mid-infrared spectrographs, NIRSpec and MIRI, now allow the 2D spatial distribution of ices in such disks to be mapped with a $0\farcs1$ to $0\farcs3$ pixel scale.

As part of the JWST Early Release Science Program, Ice Age, we observed the nearly edge-on ($i = \sim 83^\circ$ Sturm et al. 2023e) protoplanetary disk HH 48 NE around a K7 star in the Chamaeleon I star-forming region (185 pc, Gaia Collaboration et al. 2021) that has an estimated foreground-cloud visual extinction of only $A_V = 5$. A flared disk of $1\farcs3 - 1\farcs7$ diameter (120 – 160 au radius) was seen around HH 48 NE by the *Hubble* Space Telescope (HST) (Stapelfeldt et al. 2014) and by the Atacama Large (sub-)Millimeter Array (ALMA) (Villenave et al. 2020; Sturm et al. 2023e), a size that is well suited to the JWST/NIRSpec instrument's field of view. In the current study, we present the first results of these JWST/NIRSpec observations of the ices in the outer regions of HH 48 NE.

This paper describes the first complete gas and ice inventory of an edge-on protoplanetary disk observed with JWST/NIRSpec in a model-independent way.

Due to the richness and novelty of these data, new science can be gleaned directly from the data prior to radiative transfer fitting. We discuss the interpretation of disk-integrated and spatially resolved ice features, finding that multiple scattering from many regions in the disk makes the traditional metrics of optical depths and column densities meaningless. This highlights the ultimate necessity of radiative transfer for determining ice abundances in protoplanetary disks.

The paper is organized as follows: We first present the observations in Sect. 6.2. Then, in Sect. 6.3, we provide details on the detected gas and ice features in the disk-integrated spectrum, along with the spatial variations of the ice feature depth. In Sect. 6.4, we discuss the implications of the observations and pose unresolved questions for future research. Finally, Sect. 6.5 summarizes our findings and provides concluding remarks.

6.2 Observations

The protoplanetary disk around HH 48 NE was observed with NIRSpec onboard JWST on 2022 July 19, as part of the Director's Discretionary-Early Release Science (DD-ERS) program "Ice Age: Chemical evolution of ices during star formation" (ID 1309, PI: McClure). The spectroscopic data were taken with a standard 4-point dither pattern for a total integration of 2451 s, with the pointing centered on $11^{\mathrm{h}}04^{\mathrm{m}}23.56^{\mathrm{s}}$, $-77^{\circ}18'07.26''$. The disperser-filter combination used was G395H-F290LP, which covers wavelengths from 2.87 – 4.08 µm and 4.19 – 5.25 µm at a resolving power of $R \sim 2700$. Because the target is extended, target acquisition was not carried out, and HH 48 NE was blind-pointed into the NIRSpec IFU aperture for spatially resolved imaging spectroscopy across the disk and inner outflow extent. A second pointing was observed at an offset of 3 arcminutes southeast of HH 48 NE to subtract the astrophysical background from the target flux.

The data were processed through the November 2022 development version of the JWST NIRSpec pipeline (2022_2a; 1.8.3.dev26+g24aa9b1d), which included a first fix for a pronounced "ringing" throughput structure seen in the previous version of the calibrated three dimensional (3D) IFU cube product for NIRSpec. Calibration reference file database version 11.16.16 was used, which included the updated onboard flat field and throughput calibrations for absolute flux calibration accuracy estimate on the order of ∼10%. The standard steps in the JWST pipeline were carried out to process the data from the 3D ramp format to the cosmic ray corrected slope image. Further processing of the 2D slope image for WCS, flat fielding, and flux calibration were also done using standard steps in the "Level 2" data pipeline calwebb_spec2. To build the calibrated 2D IFU slice images into the 3D datacube, the "Stage 3" pipeline was run step-wise, and intermediate products were investigated for accuracy. The four dithers were combined using the "drizzle" algorithm with equal weighting and full pixel regions used. The final pipeline processed product presented here was built into 3D with the outlier bad pixel rejection step turned off, as running this over-corrected and removed target flux. As a result, clusters of bad pixels are seen in some velocity channels of the IFU cube that are flagged by hand when necessary based on the 2D spatial information.

6.3 Results

Figure 6.1 presents the spatially resolved continuum image of HH 48 NE at 4 µm together with the extended H_2 0-0 S(9) emission at 4.7 µm and the jet traced by [O I] at 0.6 µm with HST (Stapelfeldt et al. 2014). The cube is rotated by -10° using `scipy` cubic spline interpolation to align the major axis of the disk horizontally for visualization purposes. The total field of view (FOV) of the NIRSpec instrument is $3'' \times 3''$, which means that HH 48 SW (located at 2″.3; Sturm et al. 2023e) lies outside of the field, but some hints of gas emission from HH 48 SW are visible toward the southwest (see Fig. 6.1). The HH 48 NE protoplanetary disk appears spatially resolved in the NIRSpec spectral cube, with a major axis of 1″.6 (296 au) and a minor axis of 1″.1 (204 au) at 4 µm determined using a 5σ clip. The spatial resolution of the observations varies from 0″.09 at 3 µm to 0″.15 at 5 µm (17 – 28 au), which implies that the spaxels (0″.1 × 0″.1) are slightly smaller than the size of the effective PSF at the longest wavelengths. The continuum is asymmetric in the lower surface, extending further toward the west than to the east (cf. the same continuum on a log scale in the top left panel of Fig. 6.4). This pattern is consistent with the optical HST observations (Stapelfeldt et al. 2014; Sturm et al. 2023e) and may be a result of gravitational interaction between the two sources.

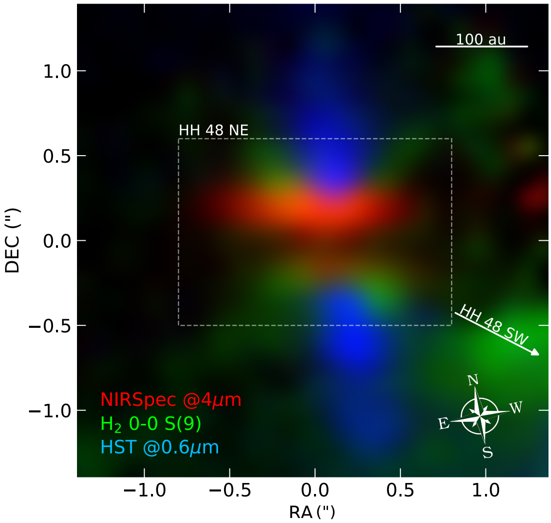

Figure 6.1: Overview of the different spatial components of the HH 48 NE system using a composition of observations. The JWST/NIRSpec disk continuum at 4 µm is shown in red, the jet is shown in blue using HST/ACS observations of the [O I] line at 0.6 µm (Stapelfeldt et al. 2014), and the vertically extended disk wind is shown in green using the H_2 0-0 S(9) transition. The region used to extract a disk-integrated spectrum is shown by the dashed rectangle. The continuum in this region is shown on a logarithmic scale in Fig. 6.4. The direction toward HH 48 SW is marked with a white arrow.

A 1D, disk-integrated spectrum is extracted within a rectangle of 1″.6 × 1″.1 around the disk, centered on $11^{h}04^{m}23.38^{s}$, $-77^{\circ}18'06.46''$ (see Fig. 6.1) by summing up the flux over the spaxels with $S/N > 5$. We estimate the noise level of the disk-integrated spectrum in a flat spectral region without gas and ice features (3.85 – 4 µm), which results in a local standard deviation of $\sigma = 0.027$ mJy, or a S/N of ∼110 on the continuum. We present the disk-integrated NIRSpec spectrum of HH 48 NE in the top panel of Fig. 6.2. The spectrum shows a fairly

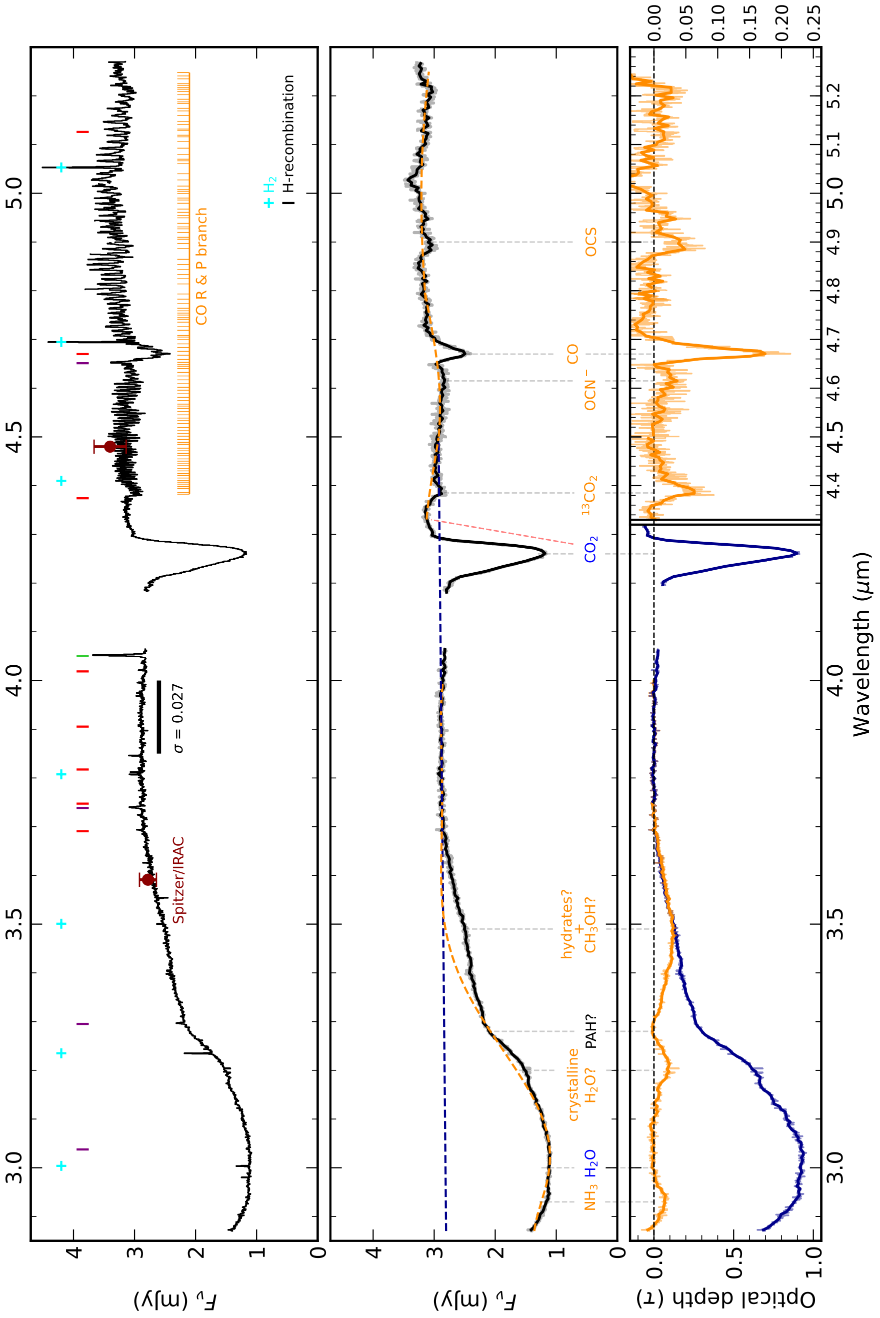

Figure 6.2: caption on next page

flat continuum of ∼3 mJy, which is consistent with the broadband *Spitzer*/IRAC fluxes calculated using a Gaussian decomposition of the two binary components (HH 48 NE and SW, separated 2″.3 from each other) by Dunham et al. (2016). This spectrum provides the total throughput of the stellar energy through the disk and has the highest achievable S/N on a spectrum in this data set for ice analysis. Several gas emission lines and ice absorption features are detected, which we present in the subsequent sections.

6.3.1 Gas inventory

Ro-vibrational molecular emission lines and hydrogen recombination lines are ubiquitously found in protoplanetary disks, arising from the warm inner disk regions (Pontoppidan et al. 2014). In edge-on disks, these - usually spatially unresolved - lines can be observed through photon scattering in a similar fashion as the thermal dust radiation. Detected gas emission lines in HH 48 NE are labeled in the upper panel of Fig. 6.2. Atomic hydrogen recombination lines are detected from the Bracket ($n = 4$), Pfund ($n = 5$), and Humphreys ($n = 6$) series. These lines are spectrally unresolved and have a constant ratio with respect to the spatially resolved scattered continuum. This indicates that the lines have a similar region of origin as the continuum emission in the inner disk, and the spatial extent of the emission is a result of photon-scattering in the outer disk. In this spectral setting, there are 7 molecular hydrogen lines from the $v = 1-0$ (O; $\Delta J = -2$) and $v = 0-0$ (S; $\Delta J = +2$) series. These lines have a slightly larger spatial extent than the disk continuum (see Fig. 6.1), and likely result from a vertically extended disk wind or outflow cavity.

Additionally, we detect many ro-vibrational lines from the CO R ($\Delta J = 1$) and P ($\Delta J =$ -1) branches, up to $J = 48$ ($E_{up} = 10{,}056$ K) and from several vibrationally excited states. These lines are broader than expected based on the instrumental resolution, which means that they may trace a warm, high-velocity

Figure 6.2: Overview of the disk-integrated JWST/NIRSpec spectrum of HH 48 NE.
Top panel: Disk-integrated JWST/NIRSpec spectrum with the main gas lines labeled. The molecular hydrogen O and S series lines are marked in cyan. Bracket, Humphreys, and Pfund recombination series of atomic hydrogen are marked in green, red, and purple, respectively. The CO R (4.3 – 4.7 µm) and P (4.7 – 5.2 µm) branches of ro-vibrational transitions are marked in orange. The two literature *Spitzer*/IRAC data points are shown in dark red for comparison. The wavelength range 4.08 – 4.19 µm is not covered in the used spectral setup.
Middle panel: Disk-integrated JWST/NIRSpec spectrum with the gas lines removed in black. The procedure for removing the CO lines is described in detail in Appendix 6.A. The positions of the main vibrational modes of the more abundant ice species are labeled, with the continua used to calculate their optical depths shown as dashed lines with corresponding colors.
Bottom panel: Optical depth of the ice features in the disk-integrated spectrum shown in the middle panel. The two different colors represent optical depths for two different continuum fits, one for the H_2O and CO_2 features in blue, and one for the weaker ice features neglecting the CO_2 and H_2O features in orange. Both corresponding continua are shown as a dashed line in the middle panel.

component in the inner disk (v ~150 km s^{-1}) or the wind-launching region. The estimated line width is consistent with high resolution VLT/CRIRES observations of similar systems (see e.g., Herczeg et al. 2011; Brown et al. 2013; Banzatti & Pontoppidan 2015) that have a range of full width at half maximum (FWHM) of 50 – 200 km s^{-1} which corresponds to an emitting radius of ~0.05 au. The spatial extent of the CO lines is similar to the continuum in the upper surface, but the contribution from the lower surface is missing (see Fig. 6.A.1). The origin of this phenomenon is unknown, but it could result from a difference in the vertical height of the CO-emitting layer compared to the continuum which could block part of the emission.

We removed the CO lines from the spectrum to accommodate a better fit of the continuum and identification of the ice absorption features, which are the main focus of this paper. For this purpose, we fit a simple LTE slab model to the lines with a constant temperature (2070 K) and column density (1.4×10^{-19} cm^{-2}), and subtracted it from the spectrum (see Appendix 6.A). Since the spatial extent of the CO emission is similar to the continuum in the upper surface, with a constant flux ratio of 10 (see Fig. 6.A.1), we assume that the propagation of photons from CO molecules is similar to the continuum emission that originates in the central regions of the disk. This implies that we detect the same CO gas component throughout the disk, and its spatial extent is the product of scattering to the outer disk. Therefore, we scale the best-fit CO spectrum with a constant scaling factor and subtract it from every spaxel that contains dust emission. Additionally, we flag the hydrogen lines and present the gas line subtracted spectrum in the middle panel of Fig. 6.2.

6.3.2 Ice inventory

The middle panel of Fig. 6.2 clearly reveals broad absorption features due to different ice species, after subtraction of the CO and other gas phase lines. We fit the continuum around the main ice absorption features with a polynomial, using the wavelength ranges and fit orders specified in Table 6.1 and show the result of the continuum fit in the middle panel of Fig. 6.2. Since the spectrum does not include the full blue wing of the water ice feature, we fit a separate linear continuum for the water (H_2O) feature that is extrapolated down to 2.87 µm. The ice spectrum is then converted to an ice optical depth[1] using Eq. 6.1. The optical depth indicates the fraction of light at each wavelength that is absorbed by the icy dust grains, on a logarithmic scale, which is linearly correlated with the ice column density encountered along the light path neglecting radiative transfer effects. The resulting spectrum is shown in blue in the bottom panel of Fig. 6.2. The integrated optical depths for the detected features are given in Table 6.1, with the same band strengths as in McClure et al. (2023) for consistency. These values cannot be used to calculate column densities directly due to the flux contributions of multiple light paths through the disk, as we will show in Sect. 6.4.2. We would like to note that the exact choice for the continuum baseline can result in an uncertainty of up to 10% in integrated optical depth.

---

[1] In edge-on disk observations, this should be interpreted as “the logarithmic fraction of light at each wavelength that reaches cold regions in the disk with ice and is absorbed there” instead of the usual “logarithmic fraction of absorbed light at specific wavelengths” with respect to a continuum background source. This implies that there is no straight-forward relationship with the column density.

We describe the major observed ice features in the next subsections. The shape and depth of ice features can be significantly altered by radiative transfer and grain growth effects, especially in scattering-dominated edge-on disks (see e.g., Dartois et al. 2022), which complicates the analysis of the ice bands. A detailed study of the ice composition, environment, and abundance requires radiative transfer modeling is therefore left for a forthcoming paper.

6.3.2.1 H_2O and NH_3: 3 µm

The 3.0 µm absorption feature is primarily attributed to the H_2O OH stretching mode and is similar to previous spectra observed toward background stars with JWST. The feature exhibits a well-defined peak with an optical depth of 0.9 and a relatively smooth shape, displaying a peak at 3.0 µm and an absorption wing on the red side. The NIRSpec filters used do not capture the blue wing of the feature below 2.8 µm. Analyzing the red wing is complicated by a potential weak emission feature of polycyclic aromatic hydrocarbons (PAH) at 3.28 µm (Draine & Lee 1984). A comparison with PAH features at MIRI wavelengths, that are strongly correlated with this feature (Draine & Lee 1984), is required to determine its actual contribution to the continuum. Currently, a continuum is fitted avoiding potential weak absorption features within the OH stretch mode of water using the wavelength ranges specified in Table 6.1, illustrated as the orange line in the middle panel of Fig. 6.2.

Other features of the 3 µm feature can be ascribed to a combination of additional species and radiative transfer effects[2]. The narrow feature centered at 2.93 µm is attributed to the ammonia NH stretch mode (Dartois et al. 2002). Its position and shape are uncertain since it is located right on the blue edge of the filter, which further complicates the exact location of the continuum. The feature at 3.2 µm is similar to those reported for the silhouetted disk 216-0939 in the M43 region and the edge-on disk around the Herbig star PDS 453 (Terada & Tokunaga 2012, 2017), and is interpreted as a result of large-particle-size (∼1 µm) crystallized water ice absorption. It is known that both larger grains and a higher degree of crystallization can cause a shift from the typical wavelength of this feature (3.1 µm) to 3.2 µm (Smith et al. 1989). The overall strength compared to the peak at 3 µm is a factor of $2 - 3$ lower than in the former sources, which suggests that the fraction of crystallized H_2O ice is lower in HH 48 NE. The broad feature at ∼3.5 µm is observed in multiple background and protostellar sources, correlating with the water ice absorption (e.g., Brooke et al. 1996, 1999; Dartois et al. 2002; Shimonishi et al. 2016). This absorption feature is often attributed to ammonia hydrates, implying an OH stretching mode absorption shifted by interaction with the nitrogen atom of ammonia embedded in water ice. The appearance and optical

---

[2] In the case of a protoplanetary disk the effect of radiative transfer on the feature shape includes contributions from the phase-dependent scattering opacity of the grains (see e.g., Dartois et al. 2022), but also includes the fact that only specific paths through the disk are viable and the fact that the absorption feature may be saturated locally in the disk.

Table 6.1: Properties of the detected ice features in the disk-integrated spectrum of HH 48 NE.

Species	λ (µm)	Continuum wavelength range (µm)	Fit order	$\int \tau_\nu d\nu$ (cm^{-1})	A (cm $molecule^{-1}$)	
H_2O	3.0	3.7 – 4, 4.42 – 4.58	1	$381^{1.}$	2.0×10^{-16}	(1)
CO_2	4.26	3.7 – 4, 4.42 – 4.58, 4.71 – 4.87, 4.95 – 5.25	5	23.0	1.1×10^{-16}	(2)
CO	4.67	"	"	2.0	1.1×10^{-17}	(1)
OCN^-	4.6	"	"	0.7	1.3×10^{-16}	(3)
OCS	4.9	"	"	0.6	1.2×10^{-16}	(4)
NH_3	2.93	2.86 – 2.9, 2.98 – 3.15, 3.27 – 3.31, 3.7 – 4.0	7	4.3	1.7×10^{-16}	(5)
$NH_3 \cdot H_2O$	3.5	"	"	27.3	2.6×10^{-17}	(6)
$^{13}CO_2$	4.39	3.65 – 4, 4.32 – 4.36, 4.43 – 4.5	5	1.0	7.1×10^{-17}	(1)

Notes: 1. This is the integrated absorption starting from 2.87 µm,

References: (1) Gerakines et al. (1995), (2) Gerakines & Hudson (2015), (3) van Broekhuizen et al. (2005), (4) Yarnall & Hudson (2022), (5) Hudson et al. (2022), (6) Dartois & d'Hendecourt (2001) depth of this mode is consistent with the detection of the NH stretch at around 2.97 µm for ammonia. Some potential additional contributions by CH stretching modes have also been presumed in this range, based on laboratory experiments using H atom irradiated carbon grains (Mennella 2010). Although the distinct, narrow peak of CH_3OH at 3.54 µm is absent (see Fig. 9 in McClure et al. 2023), a small contribution of CH_3OH cannot be excluded based solely on this feature and will be constrained better with the combined MIRI and NIRSpec data. Unfortunately, the less abundant water isotopologue, HDO, with a feature at 4.07 µm is not within the observed wavelength range, due to the NIRSpec G395H detector gap, and is therefore excluded from the analysis.

6.3.2.2 CO_2 and $^{13}CO_2$: 4.2 – 4.4 µm

The carbon dioxide (CO_2) absorption feature at 4.26 µm is detected with a similar peak optical depth as the H_2O feature. The peak position of the observed CO_2 stretching mode band is shifted compared to pure CO_2 (4.27 µm). This shift can be attributed to CO_2 in polar ice environments or by ices exposed to energetic processing at low temperatures (Ioppolo et al. 2013, 2022). The main isotopologue has a red wing in emission (see red dashed line in the middle panel of Fig. 6.2), which is likely caused by a phase scattering effect at a high degree of disk inclination involving the scattering opacity of large (>1 µm) grains (Dartois et al. 2022). The $^{13}CO_2$ isotopologue absorption band is located in this scattering wing, so for that reason we fitted the continuum for this feature separately with a local fit specified in Table 6.1. A local fit introduces further uncertainty in the derived column density, but it is necessary here as the main CO_2 feature contributes to the continuum of the $^{13}CO_2$ feature.

As for $^{12}CO_2$, the peak of the $^{13}CO_2$ feature is shifted relative to the lab-measured peak of 4.38 µm of pure $^{13}CO_2$ to 4.39 µm. Boogert et al. (2000) showed that this peak shift can be ascribed to absorption by $^{13}CO_2$ ice mixed with molecules with a large dipole moment, for example, H_2O and CH_3OH, at high concentrations. The derived $^{12}CO_2/^{13}CO_2$ ratio is low, with a ratio in peak optical depth of 14 and a ratio in the integrated optical depth of 22. Assuming that both features arise from the same region in the disk, and using the band strengths reported in Gerakines et al. (1995) and Gerakines & Hudson (2015) for $^{12}CO_2$ and $^{13}CO_2$, respectively, we find a molecular ratio of 14 compared to the local interstellar medium (ISM) ratio of 77 (Wilson 1999) and the local dark cloud ratio of 69 – 87 (McClure et al. 2023). This low $^{12}CO_2/^{13}CO_2$ ratio indicates that the main isotopologue may be saturated[3] at certain positions along the line of sight, a point to which we return in Sect. 6.4.2.

6.3.2.3 CO, OCN^-, and OCS: 4.4 – 5 µm

The right hand side of the bottom panel of Fig. 6.2 shows the spectrum in the range 4.32 – 5.24 µm, where features attributed to CO at 4.67 µm and $^{13}CO_2$ at 4.39 µm are detected. The main CO stretch feature at 4.67 µm is detected at a peak optical depth of 0.2. The feature shows signs of a potential red wing in emission, very similar to that observed for the CO_2 feature. The absorption feature appears asymmetric and the total observed FWHM of the feature (12.4 cm^{-1}) is also broader than expected from pure CO (3 cm^{-1}; Palumbo et al. 2006). This may indicate the presence of an additional component of a CO mixture with CO_2 or H_2O, similar to Pontoppidan et al. (2003) and Öberg et al. (2011a). Meanwhile, ^{13}CO is not detected, but the 3σ upper limit obtained (τ <0.03) results in a $^{12}C/^{13}C$ ratio lower limit of 6, which is consistent with the observed ratio of 14 for CO_2.

---

[3] Saturation in the context of scattered light implies that the strength of the absorption (or optical depth) is dominated by the fraction of light that makes it through icy, cold regions of the disk, instead of the column density of ice along the light path. In protoplanetary disks, saturation happens without the observed flux approaching 0.

The observed CO ro-vibrational gas lines produce in some places a quasi-continuum by line overlap. We have corrected for this effect as much as possible by subtracting a slab model (see Appendix 6.A), but the remaining systematic error of this method is hard to determine. Residual weak ice absorption should therefore be treated with care. The feature at 4.61 µm is consistent with lab measurements of the cyanate anion OCN^- (e.g., Grim & Greenberg 1987; Hudson et al. 2001). This feature is observed in a variety of sources, including low- and high-mass YSOs (e.g., Pendleton et al. 1999; van Broekhuizen et al. 2004a; Boogert et al. 2015) and it is consistent with the OCN^- band observed in laboratory analogs after UV-photolysis, ion bombardment, and thermal processing of various icy mixtures (e.g., Palumbo et al. 2000; van Broekhuizen et al. 2004a). The feature centered at 4.9 µm is consistent with OCS ice. A comparison with laboratory data suggests that the feature arises from OCS embedded in mixed ices and in regions of the disk at different temperatures (Palumbo et al. 1995, 1997; Ferrante et al. 2008; Garozzo et al. 2010; Boogert et al. 2022).

6.3.3 Spatial variation in ice features

Since the disk is resolved in both vertical and the radial directions, we can map the strength of the ice features spatially for the first time in a protoplanetary disk. In Fig. 6.3 we present three normalized spectra across the disk along the major axis (middle panel) and the minor axis (right panel). The overall structure of the spectrum is similar at all locations of the disk. Along both the major and the minor axis, there is no big difference in the ice features and in the CO ro-vibrational lines. Spectra extracted further away from the central source along the major axis show a steeper slope in the water ice feature at ∼3.3 µm, which may indicate that the relative amount of PAH emission increases in the outer disk. The spectrum extracted from the lower surface shows an increased slope of the continuum, likely as a result of the radiative transfer effects for the disk that has an inclination of 83°.

We fit the same continua as for the disk-integrated spectrum (see Table 6.1) in each spaxel with a continuum signal >5σ, estimated between 3.85 – 4 µm. We subsequently fit a Gaussian for each absorption feature, leaving amplitude, position, and FWHM as free parameters to determine the "peak optical depth" or ice feature amplitude in every spaxel. The resulting maps for the strong ice features (H_2O, CO_2, and CO) are presented in Fig. 6.4. We note that the parameters (r, z) denote projected horizontal and vertical coordinates on the sky rather than intrinsic properties of the disk. Since the disk is not exactly edge-on, but rather

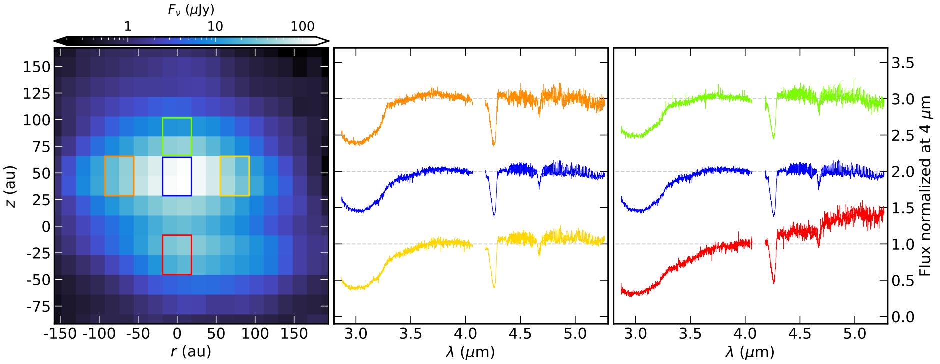

Figure 6.3: Spatial variations in the spectrum along the major and minor axes of the disk.
Left: Continuum flux of HH 48 NE at 4 µm on a logarithmic scale. The colored squares mark the regions used to extract the spectra in corresponding colors in the middle and right panel.
Middle: Three spectra extracted along the major axis of the disk at radial distances of -70, 0 and 70 au with respect to the center.
Right: Three spectra extracted along the minor axis of the disk at heights of -25, 50 and 80 au with respect to the dark lane.

inclined at ∼83° (Sturm et al. 2023e), the upper surface of the disk ($z > 0$) is different from the lower surface ($z < 0$) in terms of absolute flux.

The peak optical depth maps consistently show a butterfly pattern, with the optical depth increasing toward the midplane in the vertical direction and outwards in the radial direction. The magnitude of the variations is only minor (<50%) considering the multiple orders of magnitude difference in the continuum flux (blue panel in the top left of Fig. 6.4) and dust column density along a pencil beam[4] (note that the color bar is truncated at a peak optical depth of 0.6 for H_2O and CO_2). There are some potential east-west asymmetries in the disk's lower surface, that could be mainly attributed to a higher continuum flux on the west side, which means that we can trace the ice features further out on that side (see discussion in beginning of Sect. 6.3). Within the range where continuum emission is detected toward the east, there is no significant difference between the east and west side in any of the ice features. Overall, vertical and radial cuts through the disk follow similar trends everywhere in the disk, but vary independent from each other. In the subsequent sections, we will describe the variations in optical depth with the height and radius of the disk independently.

6.3.3.1 Radial variations

To highlight the radial trend in the ice optical depth, we took the median of the peak optical depth along the major axis of the disk, see bottom left panel of Fig. 6.4. The 1σ variations on this radial profile across the vertical extent of the

---

[4] A pencil beam is defined as the direction along a straight line at the position of every pixel, neglecting the fact that photons originate from the source in the center.

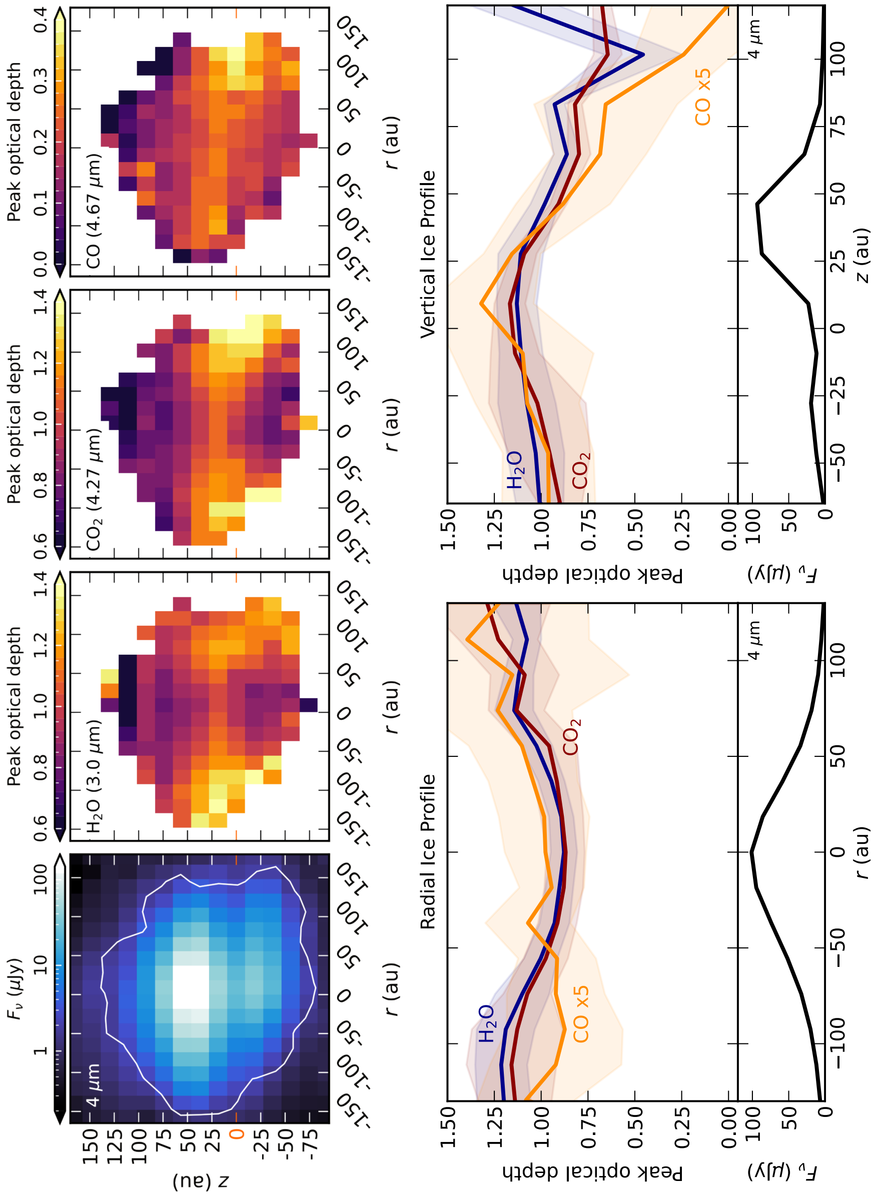

Figure 6.4: caption on next page

disk are marked as a shaded region around the median for reference. Surprisingly, the shape is similar throughout the vertical extent of the disk. The overall trend is that the optical depth increases with radius with an increase by 20% at 100 au with respect to the center. H_2O, CO_2 and CO show identical spatial profiles within the uncertainty, with CO a constant factor of ∼5 weaker relative to H_2O and CO_2. The ice absorption is in general symmetric in both sides of the disk. The slight asymmetry in the CO profile could be a result of the low S/N and the low number of pixels per bin at larger distances (see top right panel). The radial profile cannot be directly translated into a radially resolved column density profile due to complex radiation transfer, including the fact that because of the edge-on geometry of the disk all sightlines sample the full radial extent of the disk. We will return to this point in Sect. 6.4.3.

6.3.3.2 Vertical variations

To highlight the vertical variations in the ice optical depth, we took the median of the peak optical depth along the minor axis of the disk (see bottom right panel of Fig. 6.4). The 1σ variations on this profile across the radial extent of the disk are marked as a shaded region around the median. We note that the shape is similar throughout the radial extent of the disk. The overall trend in the three major ice species is that the vertical profiles peak around the dark lane and decrease quicker on the upper surface than on the lower surface. We note that the origin is taken as the dark lane, which coincides with the highest peak optical depths, but the stellar position could likely be slightly above the dark lane due to projection effects. The three major ice species (H_2O, CO_2 and CO) have identical profiles within the uncertainty from −70 au in the lower surface till 80 au in the upper surface. We will return to the interpretation of this result in Sect. 6.4.3.

Figure 6.4: Overview of the variations in the relative strength of the three strongest ice features, H_2O, CO_2, and CO.
Top left panel: Continuum flux of HH 48 NE at 4 µm on a logarithmic scale. The white line denotes the 5σ detection limit on the continuum, determined in a featureless part of the spectrum, namely the 3.85 – 4 µm region. This field of view is the same as the dashed rectangle in Fig. 6.1
Other panels in the top row: Peak optical depth per spaxel of H_2O, CO_2, and CO ice, respectively, determined using a Gaussian fit to the optical depth spectrum of each spaxel.
Bottom left panel: Median combined radial profile of the peak optical depth with the 1σ spread around this line at different disk heights as a shaded region. The black line underneath shows the radial profile of the continuum at 4 µm at z = 50 au.
Bottom right panel: Median combined vertical profile of the peak optical depth with 1σ spread around this line at different disk radii as a shaded region. The black line underneath shows the vertical profile of the continuum at 4 µm at r = 0 au. We note that z=0 is chosen as the dark lane between the upper and lower surface: in this frame, the star is located at z ∼10 au due to projection effects.

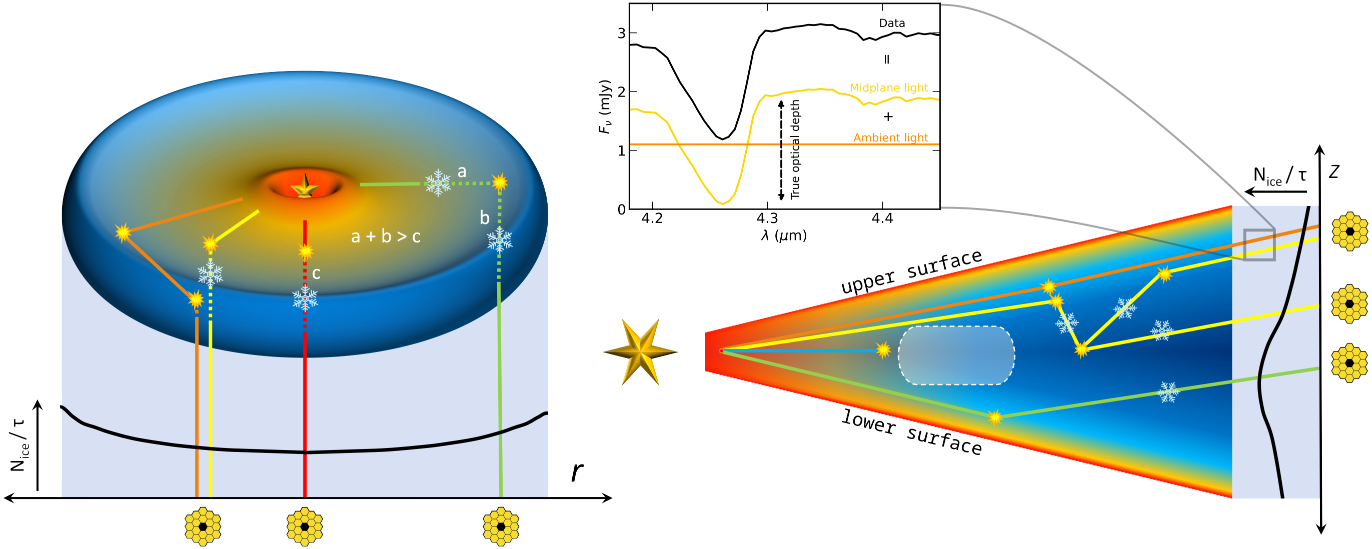
a
b
a + b > c
c
N_{ice} / τ
r
Data
=
Midplane light
+
Ambient light
True optical depth
F_ν (mJy)
0
1
2
3
4.2
4.3
4.4
λ (μm)
upper surface
lower surface
N_{ice} / τ
Z

Figure 6.5: caption on next page

6.4 Discussion

Observations of ices in protoplanetary disks are crucial to understanding the chemistry that sets the composition of planetesimals and planetary atmospheres, and we show that with JWST we can trace the ice directly in late-stage edge-on disks. Traditionally, the observed ices were believed to come from the regions that were simultaneously cold enough for particular ice species to freeze out but also sufficiently high up in the optically thin disk atmosphere to absorb stellar light scattered into the outer disk. Under these assumptions, the column densities of these ices would have provided relative measurements of CHONS-rich ice abundances in the disk layers just above the planet-forming midplane. However, the observations presented in this work reveal a low $^{12}CO_2/^{13}CO_2$ ratio, suggesting that the $^{12}CO_2$ feature is saturated, even though the minimum flux is significantly above JWST/NIRSpec's sensitivity limit. This raises the question of whether ratios between column densities, calculated from the observed optical depths using Eq. 6.2, are at all meaningful proxies for relative ice abundances. Additionally, contrary to our expectations, only minor spatial variations are observed in the strength of the ice absorption features. This leads to a second question of which disk region(s) the observations are really sampling. In the subsequent sections, we explore which fundamental constraints on the answers to these questions can be extracted from such spatially resolved observations in a model-independent fashion.

Figure 6.5: Cartoon of the physical origin of the radial (left) and vertical (right) profiles of the ice optical depths.
Left: Since we observe ice absorption against the warm inner regions of a (close to) edge-on disk, all lines of sight trace ice along the full radial extent of the disk. This results in a largely constant optical depth profile along the radial direction. Since the path of the green photon trace is longer in the ice-rich outer disk (a + b) than the direct path (c), the traced ice column densities increase with radial separation of the observation.
Right: Direct lines of sight (blue) toward the star and warm inner disk are blocked by the optically thick disk midplane (white region). The observed light follows therefore a specific path through the optically thin disk regions, including one or multiple scattering events. The flux in a JWST spaxel is composed of photons with different paths (orange and yellow), that have not necessarily crossed equal lengths in the cold parts of the disk. This means that photon paths that cross large parts of the ice-rich regions of the disk can be saturated locally, even though the optical depth of the combined contributions is a defined, small number (see inset). The optical depth increases toward the midplane, because the light paths through the cold disk layers are more likely compared to paths higher up in the disk (green). Since the scattered light from the lower surface is tilted toward the cold midplane, and similarly, light from the upper surface is tilted away from the cold midplane, the profile is asymmetric with deeper ice features in the lower surface.
Inset: Qualitative schematic of the different flux contributions in the spectrum. The spectrum always has a contribution from light that passes through little ice (ambient light continuum; orange line) and light that passes through the cold regions of the disk, usually requiring multiple scattering events along the way (yellow line). The ratio of the contributions determines the optical depth in the observations if the feature is saturated. Photons with a single scattering event are less likely to reach regions with ice in the disk than photons with multiple scattering events (see also Fig. 3 in Sturm et al. 2023d).

6.4.1 Where in the disk do these ice features originate?

The radiative transfer in edge-on disks is complicated, as only very specific light paths reach the observatory. In contrast to the pencil beam scenario, e.g. background star observations behind a dark cloud, all of the observed photons come from a similar region in the warm inner disk, before they are scattered into our line of sight (see Sturm et al. 2023d, for a deconstruction of the continuum). Fig. 6.5 illustrates examples of the photon propagation that could explain the observed absorption features and spatial variations. Most of the photons emitted by the star and the warm inner disk are absorbed along the way or scattered out of the line-of-sight. Therefore, the observed ice absorption features may represent both the optically thin regions above and beyond the optically thick disk midplane (see right panel Fig. 6.5) and potentially some part of the disk midplane itself, depending on the number of times each photon is scattered. Since the disk is axisymmetric, this means that all of the light that we observe has traveled through a similar radial extent of the disk, independent of the projected disk radius at which the light appears on the 2D JWST/NIRSpec array. The slight increase of optical depth with radius (seen in the bottom left panel of Fig. 6.4) can be understood as a geometric effect: the further away we look from the star, the longer the light has traveled on average through the disk which effectively increases the ice column density along the light path (path a + b > c in the left panel of Fig. 6.5) and the more likely the light has encountered ice along the way.

The light that we observe at every height in the disk took a complex path with one or more scattering events in-between (right panel of Fig. 6.5). The closer the light appears to come from the outer disk midplane (the dark lane at $z = 0$ au), the greater the chance that the light has scattered through cold parts of the disk. This explains why we see a peak in the optical depth values at a height of ~10 au above the midplane (bottom right panel of Fig. 6.4). Since the disk is not exactly edge-on, but rather inclined at ~83°, light that has traveled through the lower surface has a longer path through the cold midplane compared to light that traveled through the upper surface. This results in slightly elevated optical depths on the lower surface compared to the upper surface, as seen in the bottom right panel of Fig. 6.4. A final important result from Fig. 6.4 is that there are no clear vertical cut-offs - or snowlines - visible in the ice feature depths, indicating that ices may extend up to 100 au in the disk, as discussed in Sect. 6.4.3.

6.4.2 Optical depths do not trace total ice column in outer disk

Our data analysis suggests that ice feature optical depths, and by extension formal column densities, in protoplanetary disks, cannot be used to derive relative ice abundances in a straight-forward way. We have illustrated in the previous section (Sect. 6.4.1) that the observed absorption features are likely not representative of the full extent of the disk, but trace only optically thin regions above the midplane and in the outer disk. In addition, multiple light paths are combined in one line of sight, which implies that each spaxel contains multiple light contributions with different levels of ice absorption (see the inset panel of Fig. 6.5 for an illustration of this concept). This means that there may be an ambient-light continuum underneath the ice features with much less ice absorption that fills in the ice absorption features, which has important consequences for the data analysis. CO_2, H_2O, and potentially CO are locally saturated along the light path, indicating that light scattered through the cold parts in the disk is saturated in the ice absorption features (yellow line in the inset panel of Fig. 6.5). The ice optical depth is then fully determined by the fraction of light scattered through the icy regions in the disk, relative to the light scattered through the ice-free regions (i.e., the ratio of orange to yellow flux in the inset panel of Fig. 6.5); the measured optical depths do not represent the total column density of ice along the light path.

Increasing the amount of ice in the cold regions of the disk will not have a significant effect on the measured optical depth: the depth of the ice feature in the inset of Fig. 6.5 is determined primarily by the level of the orange line rather than the depth of the yellow line. This effect was already predicted using radiative transfer models of HH 48 NE in Sturm et al. (2023d), where we studied the sensitivity of the ice features on the physical disk parameters. We used a model tailored to HH 48 NE with constant ice abundances throughout the disk (taken as 80, 22, and 99 ppm for H_2O, CO_2, and CO respectively), assuming that all molecules are frozen out below their desorption temperature and below a UV threshold of $A_V = 1.5$ mag. Varying the abundances in the model, we find that similar peak optical depth values of $\sim 0.9 - 1.2$ for H_2O and CO_2 in HH 48 NE models require abundances of $2 - 100$ times the assumed ISM values: high enough to saturate these ice absorption features locally in the disk. An accurate column density can only be determined if we know what fraction of the light is scattered through regions without ice in the disk; i.e. we must determine the ambient light flux indicated by the orange line in the inset of Fig. 6.5, which yields the zero point for the flux of the yellow line. The radiative transfer models of HH 48 NE show that photons with a single scattering event - and therefore less ice absorption than photons with multiple scattering events - account for $\sim 1/3$ of the flux at NIRSpec wavelengths, which is comparable with the ambient light contribution observed (see Fig. 3 in Sturm et al. 2023d). The fraction of ambient scattered light is impossible to know without modeling the radiative transfer through the disk. Therefore, column densities derived using Eq. 6.2 should be interpreted as lower limits.

An important implication of this is that naive ice column density ratios, calculated by multiplying the observed integrated optical depth in source integrated spectra with the band strength, do not necessarily correspond to similar relative ice abundance ratios in the disk. The region where molecules are frozen out is different for every molecule, and therefore there are also differences between the ratio of ambient scattered light to scattered light that encounters locally high column densities of each ice species. Since the ambient light continuum is similar for the CO_2 and H_2O bands - due to their proximity in wavelength, and their similar snowline location in the disk - this results in comparable optical depths in the two features ($\sim$0.9), even though their actual relative abundance may be very different. The ratio of light that reaches the ices near the midplane will be even more different for volatile species like CO.

With these caveats in mind, we calculate formal column densities, presenting them as lower limits, to enable comparison with literature observations. The lower limits on the column of H_2O, CO_2, and CO are $>1.9 \times 10^{18}$ cm^{-2}, $>2.1 \times 10^{17}$ cm^{-2} and $>2.3 \times 10^{17}$ cm^{-2}, respectively. The detection of $^{13}CO_2$ with a column density of $>1.3 \times 10^{16}$ cm^{-2} is crucial, as this allows us to determine the actual CO_2 column density, using ISM assumption for the $^{12}C/^{13}C$ isotope ratio. Since the main isotopologue is locally saturated and we know that $^{12}CO_2$ and $^{13}CO_2$ should be located in the same region in the disk, we can correct for the ice-free ambient-light continuum for the $^{13}CO_2$ feature by removing a constant flux (orange line in the inset panel of Fig. 6.5) underneath the peak of the CO_2 feature. Removing the ice-free ambient-light continuum results in an increase of the peak optical depth of $^{13}CO_2$ from 0.06 to 0.010 and an increase in the integrated optical depth by a factor of 1.6. The estimated $^{13}CO_2$ column density using this approach is 2.1×10^{16} cm^{-2}. If we assume the ISM $^{12}C/^{13}C$ ratio of (77 Wilson 1999), then we can find an estimate of the actual $^{12}CO_2$ column density of 1.6×10^{18} cm^{-2}.

We note that this estimated column density is one order of magnitude higher than the lower limit found from multiplication of the observed integrated optical depth of the $^{12}CO_2$ feature with the band strength, illustrating the importance of detecting the less abundant isotopologues with JWST. Inferring molecular abundances from the main isotopologue ice features, as traditionally done in the literature, may drastically underestimate the amount of ice present and should be avoided. Therefore, it is critical to observe either less optically thick, rare isotopologues like HDO, $^{13}CO_2$ and ^{13}CO or a disk of sufficiently low mass in order to determine the correct order of magnitude for the column densities of ices in the comet-forming regions of disks.

6.4.3 Excess ice in disk atmosphere?

Assuming that the ice absorption takes place in the optically thin disk outer regions, the vertical snow surfaces caused by thermal desorption and photo-desorption should produce a noticeable drop in the peak optical depth with disk height (z in Fig. 6.4), as explained in Sect. 6.4.1. However, the three most prominent ice features H_2O, CO_2, and CO extend vertically over 125 au with only a minor decrease in strength. This is especially curious for CO ice, which is thought to sublimate thermally at ∼20 K in protoplanetary disks (Collings et al. 2003; Pinte et al. 2018; Minissale et al. 2022, and references therein) and is therefore limited to about one hydrostatic scale height, which lies at $z/r \sim 0.15$ (Pinte et al. 2018, Law et al. 2021 and see Sturm et al. 2023d). The observed CO ice is even seen at similar maximum height as the CO $J = 2-1$ gas observations reported in Sturm et al. (2023e) (see Fig. 6.6), which corresponds to temperatures of >50 K.

There are four potential scenarios that could result in a similar resolved profile for the three main ice features. Here, we describe the possibilities and identify the one that is the most viable, given what is known about this particular source.

First, the extra absorption provided by a foreground cloud or envelope with high ice column densities could explain the relatively constant peak optical depths. In that case, the whole disk would function as the light source, and all the emission that is scattered from the disk would pass through a similar cloud, which would give a relatively similar ice absorption at each spaxel across the disk. However,

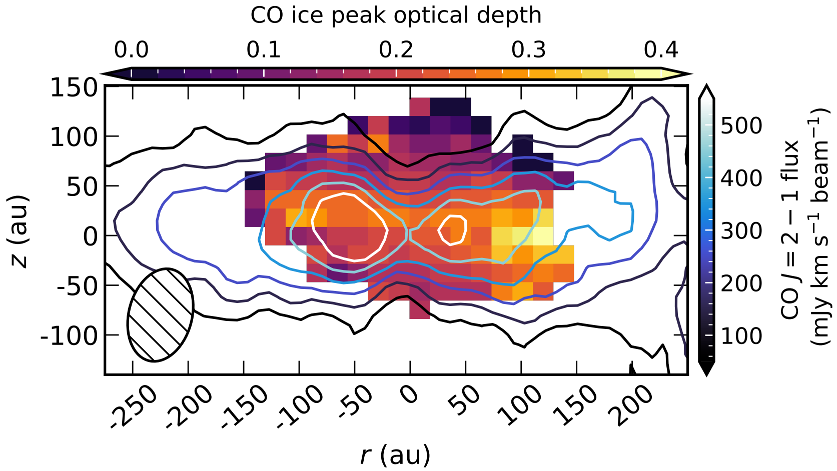

Figure 6.6: Spatial variations in the CO ice peak optical depth (colorscale) compared to ALMA CO $J = 2 - 1$ observations presented in Sturm et al. (2023e) (contours). The beam of the ALMA observations (0.″51 × 0.″31) is shown in the bottom left corner. The JWST/NIRSpec observations have an effective resolution of 28 au or 1.5 spaxels.

this option is unlikely given the measured visual extinction toward stars in the neighborhood (A_V ~3 mag) by GAIA (Gaia Collaboration et al. 2021) and the low visual extinction derived from the constraints on the disk geometry and stellar properties (A_V ~5 mag Sturm et al. 2023e). The integrated optical depths of the ice features (Table 6.1) are a factor of 5 above the observed trend with A_V toward background stars (Boogert et al. 2015), which means that a potential foreground cloud contributes <20% of the total depth to the ice absorption. Additionally, we find that the absorption features of CO_2 and H_2O are saturated at a flux >0, which is only possible if absorption in the disk dominates. If a foreground cloud dominates the absorption, the absorption features would saturate at 0 due to the lack of ice-free ambient-light continuum. The observed optical depths at $z = 125$ au are therefore likely not due to a foreground cloud.

Second, the observed profile could be a result of radiative transfer in the disk. If most of the ice absorption happens in regions relatively close to the star, and the observed features are scattered through the disk in a similar way as the continuum, the vertical distribution could be uniform. This is, however, not in line with our current knowledge of the temperature structure of the disk (Sturm et al. 2023e), because the CO snowline is estimated to be at r ~50 au, comparable to observed snowlines in other systems (Qi et al. 2013; van't Hoff et al. 2020; Podio et al. 2020; Zhang et al. 2021a) and the scattering of the ice band should therefore be inherently different than the continuum light from the warm inner disk and the CO_2 and H_2O features. Alternatively, light could have previously been scattered down below the CO snow surface, before scattering into the disk atmosphere and then again into the line-of-sight toward us (yellow line in the right panel of Fig. 6.5). However, radiative transfer models including such anisotropic scattering show layered disk ice segregation as a result of temperature gradients and photo-desorption (Ballering et al. 2021; Arabhavi et al. 2022; Sturm et al. 2023d). Even though photon packages may have encountered multiple scattering events along the light path (see also Sturm et al. 2023d), there is no reason to assume that scattering to deeper layers is more efficient than scattering through the upper layers alone, which would still result in noticeable vertical differences.

Third, a fraction of the CO ice could be trapped in ice with a much higher desorption temperature, and therefore survive at much higher temperatures than that expected of a pure CO ice. Laboratory experiments of CO and CO_2 desorption with H_2O show that CO deposited on top of a H_2O ice base layer can diffuse into the H_2O matrix, remaining trapped due to structural changes of the H_2O ice while heated, and effectively co-desorbs at the crystallization temperature of H_2O (150 K; e.g., Collings et al. 2003; Palumbo et al. 2006; Fayolle et al. 2011; Lauck et al. 2015). Similar diffusion is also seen for CO deposited onto CO_2 (Palumbo et al. 2006; Simon et al. 2019), where the diffusion into CO_2 is more efficient than into H_2O, and CO can also be trapped in a CH_3OH ice matrix (Ligterink et al. 2018). Entrapment of part of the CO in ices with a higher desorption temperature would still be in line with observations of gas-phase CO that show that most of the CO desorbs at ∼20 K, given that the features are saturated (see the discussion in Sect. 6.4.2). The hypothesis that CO is trapped in the ice matrix is supported by the width of the CO feature, which is broader than that of pure CO, and also by shifts in the peak wavelengths of the $^{12}CO_2$ and $^{13}CO_2$ features, which can occur due to a H_2O or CO rich environment. Such profile signatures were seen by McClure et al. (2023) in the CO and CO_2 ice toward background stars in the same star-forming region, and ultimately found to originate in mixed ices, after comparison with laboratory data. Due to the complicated and extended disk geometry, a detailed retrieval of the ice mixtures from the profiles must be done in conjunction with a full radiative transfer model, which we reserve for a future paper.

The trapping of CO in mixed ices would not explain the lack of snow surfaces for CO_2 and H_2O, though, unless there is a mechanism for those ices to remain trapped in a less volatile material on the grain surface. However, chemical modeling including vertical turbulent mixing and diffusion shows that icy grains can reach the observable disk surface in turbulent disks, effectively mixing ices upward faster than they can be photo-desorbed in the upper layers (Semenov et al. 2006, 2008; Furuya et al. 2013; Furuya & Aikawa 2014; Woitke et al. 2022). The grain sizes of the icy grains inferred from the H_2O and CO_2 features ($>1\mu m$; see Sect. 6.3.2), that are thought to trace mainly the disk atmosphere, could be a direct result of mixing ice rich micron-sized dust grains to the disk upper layers. While the timescales for thermal desorption are short, this could potentially explain the lack of a clear CO_2 and H_2O snowsurface. Regardless of the mechanism, if it is confirmed that a fraction of the ice survives up to the disk surface, this would have major consequences on the disk chemistry and models of planet formation, as we discuss in Section 6.4.4 below.

6.4.4 Implications for the outer disk chemistry

Using the initial ice radiative transfer models of HH 48 NE presented in Sturm et al. (2023d) and described in more detail in Sect. 6.4.2, a first order estimate of the molecular abundance can be derived using the relation between the peak optical depth of the absorption feature and the molecular abundance. We find that abundances should be significantly higher than the ISM abundance (taken as 80, 22, and 99 ppm for H_2O, CO_2, and CO respectively) in order to reproduce the observed optical depths of the three main ice species and the level of saturation traced with the $^{13}CO_2$ ice observation. Additionally, the observed ice features are stronger than anticipated based on current chemical models (e.g. Ballering et al. 2021; Arabhavi et al. 2022). This could mean that ices are efficiently inherited from the pre-stellar cloud stage (Ballering et al. 2021). However, the results suggest that there is even more ice ($>2\times$) than can be explained by inheritance from the pre-stellar phase alone.

If more ices are frozen out at the disk midplane than expected, this could impact the interpretation of the CO, C, and H_2O gas depletion seen in the outer regions of some disks with ALMA (e.g., van Zadelhoff et al. 2001; Miotello et al. 2017; Sturm et al. 2023b; Du et al. 2017; van Dishoeck et al. 2021b). Efficient conversion from volatile gas to the ice phase has long been suggested as an explanation for the CO and H_2O depletion in the outer disk gas, requiring a combination of freezeout, chemical conversion, grain growth, settling, radial drift, and vertical mixing (Bosman et al. 2018; Schwarz et al. 2018; Krijt et al. 2018, 2020). The non-detection of CH_3OH in our data suggests that, if chemical conversion is the primary depletion mechanism, CO is more likely converted into CO_2 than in more complex molecules like CH_3OH.

The co-existence of CO ice in the emitting layer of CO gas due to entrapment in less volatile ices, as discussed in Sect. 6.4.3, could be a another mechanism contributing to the low CO abundances measured in the gas phase of a large population of T Tauri stars. However, lab measurements suggest that entrapment could only result in CO gas depletion by less than a factor of 2 (Simon et al. 2019), which is insufficient to explain the 2 orders of magnitude depletion observed in older systems like TW Hya and DL Tau (Kama et al. 2016b; Sturm et al. 2022); in several T Tauri systems, the inner disk is also depleted in atomic C, which is still best explained by efficient trapping of icy dust grains at the edges of disk gaps (McClure 2019; McClure et al. 2020).

Determining which of these mechanisms is operating in HH 48 NE will be essential for procedures that measure disk gas masses using volatiles like CO, as the CO gas mass is frequently used as one proxy for the bulk H_2 gas mass in disk surveys, in the absence of better tracers like HD (Bergin et al. 2013; McClure et al. 2016; Sturm et al. 2023b). As one of the most fundamental properties of disks around young stars, good constraints on the total gas mass are crucial to understanding disk evolution and the potential of any given disk to form planets.

Finally, the observed low $^{12}CO_2/^{13}CO_2$ ratio of 14 compared to the ISM ratio of 77 (Wilson 1999), is interpreted in Sect. 6.4.2 to be likely a result of local saturation of the main feature. However, isotopic ratios in protoplanetary disks can be used as tracers of chemical fractionation processes during planet formation that are reflected in observed planetary atmospheres (see e.g., Zhang et al. 2021b; Yoshida et al. 2022). If future radiative transfer modeling suggests that the $^{12}CO_2/^{13}CO_2$ isotopic ratio is genuinely lower than in the ISM, rather than deriving from local saturation effects, then this could indicate fractionation or isotope-selective destruction processes at work in this disk (Boogert et al. 2000). In that event, edge-on disks could represent an exciting new avenue to explore solid-state fractionation in a way that is comparable to sample return missions to Solar System bodies.

6.4.5 Comparison with previous observations

In this paper, we present the first detection of $^{13}CO_2$ ice in a Class II disk, along with the first firm localization of CO ice to the disk, and the tentative identification of trace ice species OCN^-, OCS, and NH_3. While CO ice was previously detected toward a disk line of sight with VLT (Thi et al. 2002), it was later shown that the majority of the CO ice must be present in intervening cloud material (Pontoppidan et al. 2005). With AKARI, CO and ^{13}CO ice were only seen toward younger, embedded sources (Aikawa et al. 2012).

A qualitative comparison with previous observations reveals that the near-IR spectrum of HH 48 NE is remarkably similar to IRAS 04302, an edge-on Class I protostar, but bears less resemblance to the other sources observed by AKARI (Aikawa et al. 2012). This includes the absorption signatures near 2.9 and 3.1 µm, seen in HH 48 NE and IRAS 04302, but not in other systems, and the extent of the scattering versus hydrate contribution in the 3 µm red wing. The red scattering wing and relative optical depths of the CO_2 and CO features are also similar. This similarity is somewhat surprising given that IRAS 04302 has an additional envelope component (Wolf et al. 2003) that is not seen in HH 48 NE (Sturm et al. 2023e). It may suggest that the envelope of IRAS 04302 is tenuous enough not to contribute to the near-infrared ice features, or it may indicate that the envelope ices in Class I sources are similar to disk ices in Class II sources.

6.4.6 Future prospects and outlook

Clearly, observations of additional edge-on systems are needed to understand the relative importance of intrinsic disk properties vs. viewing geometry in setting the near-IR spectrum. Including more sources in the sample will help to constrain which properties are inherent to protoplanetary disks, and which should be attributed to source-specific properties like age, envelope material, and dynamical interaction with a binary component. Future comparison of HH 48 NE's near-infrared with the comparable NIRSpec spectrum from the neighboring edge-on protostar Ced 110 IRS 4, also observed as part of the Ice Age JWST ERS program, will enable us to quantify the similarity of ices between the Class I and Class II stages.

Additionally, many ice species discussed in this work have corresponding absorption features in the JWST/MIRI wavelength range, 5 – 28 µm. Longer wavelengths may trace different regions in the disk due to differences in scattering and there could be a significant contribution from direct thermal dust emission at longer wavelengths (see Fig. A.1. in Sturm et al. 2023d). However, a future comparison between NIRSpec and MIRI observations will help to constrain the strength of the potential PAH emission feature at 3.28 µm, since that feature correlates with the features at 6 and 8 µm. Additionally, it could confirm our conclusions about the presence of NH_3 and lack of CH_3OH, as both of these species have stronger absorption features at 9.0 and 9.7 µm, respectively.

In this work, we have clearly demonstrated that neglecting the role of radiative transfer in the interpretation of ice observations toward sources with substantial physical structure, like edge-on protoplanetary disks, can lead to incorrect abundances that could be off by an order of magnitude, in the case of CO_2. Due to the radiative transfer, absorption feature shapes and depths are affected, which complicates determination of abundance ratios and ice environments. In forthcoming papers, we will study the degree to which the effect of the radiative transfer on the feature shape can be disentangled from the effects of the chemical environment of the ices, based on the results of this paper. Additionally, we will use these observations to improve our already existing ice model (Sturm et al. 2023d) to study the spatial variations in ice optical depth and molecular abundances in more detail and derive an ice to silicate ratio using the additional JWST/MIRI spectra.

6.5 Conclusions

We have presented the first spatially resolved observations of the main ice species in a mature, envelope-free edge-on Class II protoplanetary disk, HH 48 NE, using JWST/NIRSpec. These results demonstrate the novel capabilities of JWST for revealing the ice inventories of disks. After analyzing the observed ice features and spatially resolved trends, we can conclude the following:

- A variety of ice features are detected including the major ice components H_2O, CO_2, and CO and multiple weaker signatures from less abundant ices, NH_3, OCN^-, and OCS. Additionally, we detected the isotopologue $^{13}CO_2$ ice absorption feature for the first time in a protoplanetary disk.

- The combination of an integrated absorption ratio of $^{12}CO_2/^{13}CO_2 = 14$, in contrast to the ISM value of 77, plus similar peak optical depths of H_2O and CO_2 indicates that the main $^{12}CO_2$ and H_2O features are saturated, despite an excellent S/N at the bottom of both features. Their saturation implies that the spectrum has a strong contribution from an ice-free ambient scattered-light continuum, which reduces the apparent optical depth, despite the high ice column densities encountered by light paths through the cold disk regions. Using the $^{13}CO_2$ absorption feature, we show that the naive calculation of column densities from the observed integrated optical depth of the $^{12}CO_2$ feature results in an underestimation of the total ice column in the disk by more than one order of magnitude. Detecting the less abundant isotopologues with JWST is therefore crucial for measuring molecular abundance ratios in the ice.

- The shape of the crystallized water ice feature and the red shoulder of the CO_2 feature indicate that a significant fraction of the probed dust grains along the photon path are larger than ∼1 µm.

- Radial variations in ice composition and abundance are hard to trace in edge-on disks due to the complex radiative transfer effects, assuming that all light originates from the warm inner disk and travels through the entire radial extent at all observed projected radii on the sky. A slight increase in feature depth with projected radial separation from the star is interpreted as a result of an increased light path length through the cold regions in the outer disk.

- Vertical variations in ice optical depth are also small and H_2O, CO_2, and CO reveal similar distributions, although these molecules have significantly different desorption temperatures. While a contribution from ices in a foreground cloud and complicated radiative transfer scattering making the ice features appear to come from higher layers cannot be excluded entirely, we find that CO ice likely survives higher up in the disk than expected based on their desorption temperature of $\sim$20 K. This may be due to the entrapment of CO in less volatile ices such as H_2O and CO_2.

- The ice features are deeper than anticipated from radiative transfer modeling assuming typical interstellar ice abundances with respect to hydrogen. The high column densities of ice observed in HH 48 NE suggest that we see a result of gaseous CO and H_2O conversion to ices, confirming the impact of earlier proposed mechanisms to explain the observed low CO gas fluxes. If it is verified, by modeling of the ice profiles, that part of the CO ice is trapped in CO_2 and H_2O ice and survives high up in the disk, then CO diffusion into the ice could also contribute to the CO depletion seen in the gas phase.

Understanding the gas/ice ratio of important volatiles is crucial in our understanding of the chemistry in planet-forming regions and the physical properties of protoplanetary disks such as the gas mass. Many of the features of these resolved ice observations and their implications on the chemistry and physics of protoplanetary disks can be readily understood in a model-independent way, as demonstrated in this work. Future comparison over the full wavelength coverage of JWST, including MIRI data, will further constrain some of the ice abundances, as well as the ice/rock ratio. However, the spatial origin of some observed signatures remains uncertain and will require advanced radiative transfer modeling, as well as a larger sample of edge-on disk observations, to fully extract relevant information about the birthplace of planets and comets.

6.6 Acknowledgments

Astrochemistry in Leiden is supported by the Netherlands Research School for Astronomy (NOVA), by funding from the European Research Council (ERC) under the European Union's Horizon 2020 research and innovation programme (grant agreement No. 101019751 MOLDISK). M.K.M. acknowledges financial support from the Dutch Research Council (NWO; grant VI.Veni.192.241). D.H. is supported by Center for Informatics and Computation in Astronomy (CICA) grant and grant number 110J0353I9 from the Ministry of Education of Taiwan. D.H. acknowledges support from the National Technology and Science Council of Taiwan through grant number 111B3005191. E.D. and J.A.N. acknowledge support from French Programme National 'Physique et Chimie du Milieu Interstellaire' (PCMI) of the CNRS/INSU with the INC/INP, co-funded by the CEA and the CNES. M.N.D. acknowledges the Swiss National Science Foundation (SNSF) Ambizione grant no. 180079, the Center for Space and Habitability (CSH) Fellowship, and the IAU Gruber Foundation Fellowship. Part of this research was carried out at the Jet Propulsion Laboratory, California Institute of Technology, under a contract with the National Aeronautics and Space Administration (80NM0018D0004). S.I., E.F.vD, and H.L. acknowledge support from the Danish National Research Foundation through the Center of Excellence "InterCat" (Grant agreement no.: DNRF150). M.A.C. was funded by NASA's Fundamental Laboratory Research work package and NSF grant AST-2009253.

Appendix

6.A CO ro-vibrational gas line fitting

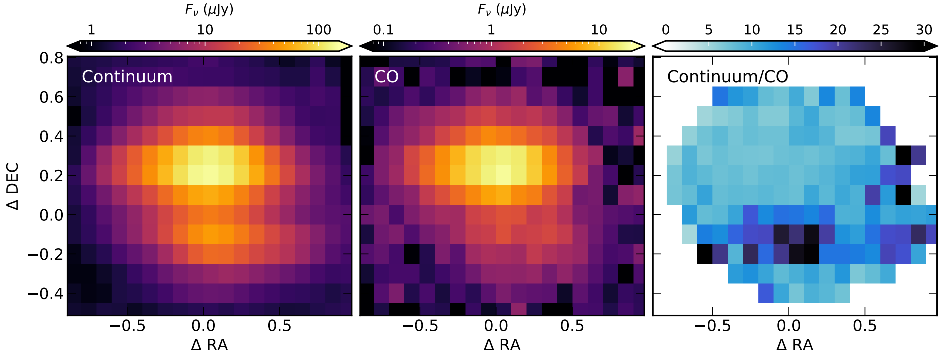

Figure 6.A.1: Comparison between the spatial distribution of the CO emission and the continuum emission.
Left: Spatial distribution of the median continuum flux in the region with CO gas emission (4.36 – 5.2 µm).
Middle: Spatial distribution of the median of the peak fluxes of the CO gas emission lines.
Right: Ratio of the left two panels showing a constant ratio in the upper surface, but a higher ratio in the lower surface due to missing CO flux.

The HH 48 NE observations include a forest of ro-vibrational CO lines from 4.3 µm to 5.28 µm that are spectrally overlapping and therefore create a quasi-continuum underneath the lines. This results in uncertainty on the continuum for the analysis of the ice absorption bands. In an attempt to remove the gas lines, we followed a similar approach as in Grant et al. (2023) by fitting a LTE slab model to the observed spectrum with a constant temperature, column density and emitting area. First, we estimated the continuum by selecting regions in the brightest CO lines and selecting regions with the least amount of line overlap and ice absorption features (see the purple dots and gray areas in Fig. 6.A.2, respectively). Next, we fitted LTE slab models to the lines in the regions marked with a gray horizontal line in the middle panel of Fig. 6.A.2 using a grid of models varying the column density, excitation temperature and linewidth. Since we observe an unknown small fraction of the CO line flux scattered through the outer disk, we normalize the fitted spectrum to the observed spectrum minimizing the reduced χ^2 value.

The best-fitting model has an excitation temperature of 2070 K, a column density of 1.4×10^{19} cm^{-2}, with a line FWHM of 150 km s^{-1}. We note that these values result in a model that fits the CO emission lines well and improves the quality of the continuum, but that these values should not be trusted to imply physical quantities or regions of origin. The radiative transfer can have a significant impact on the line ratios over the spectral region that is used for the line fitting. We can conclude that the emitting area has to be warm ($>$1500 K) to fit the lines with high $E_{\rm up}$ and that the lines are spectrally resolved indicating high velocities.

The continuum-subtracted CO emission follows a similar spatial distribution as the continuum at similar wavelengths (see Fig. 6.A.1), which indicates that the CO likely comes from the obscured inner disk or jet launching region and is scattered through the outer disk in our line of sight in a similar way as the continuum. The CO gas emission is less prominent in the lower surface, which indicates that the emitting region may be higher up than the emitting region of the continuum. We used the ratio of the CO lines to the continuum (right panel of Fig. 6.A.1) to scale the best-fitting CO spectrum and remove the lines from the continuum in every individual spaxel.

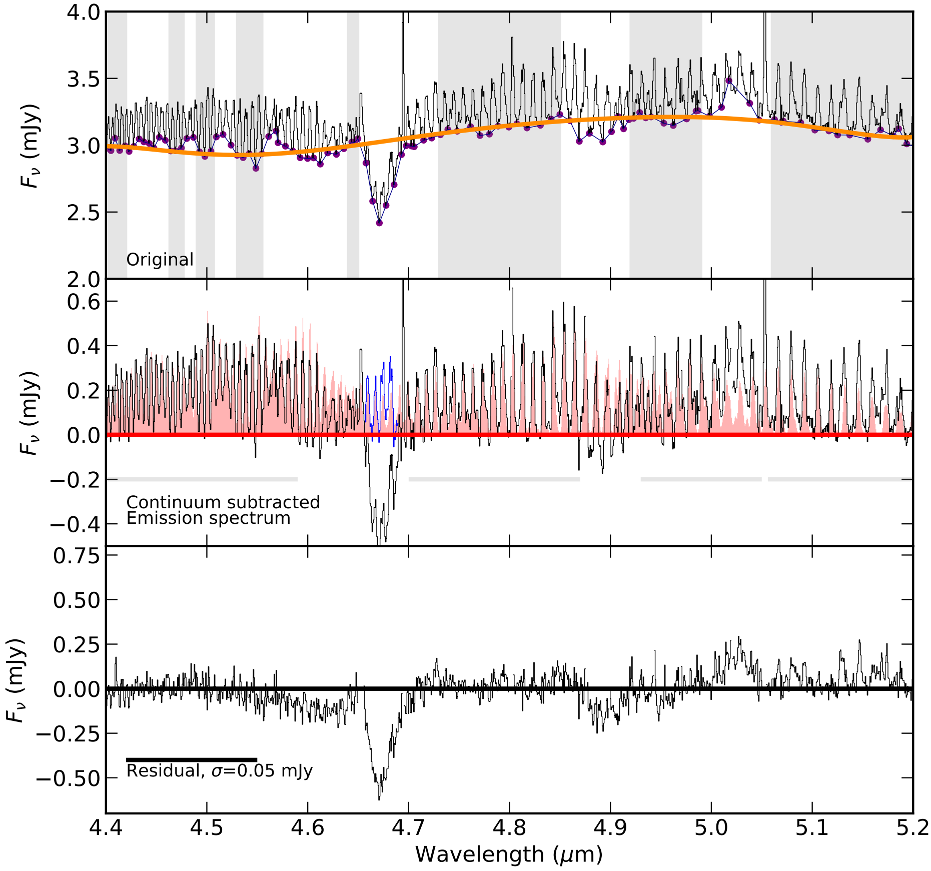

Figure 6.A.2: Overview of the CO gas line fitting procedure following the steps described in the text.
Top panel: Observed source integrated spectrum of HH 48 NE with selected troughs in between the emission lines in purple. Regions used to fit the continuum underneath the lines are marked in gray.
Middle panel: Continuum subtracted CO emission spectrum, corrected for the optical depth in the CO ice feature (blue region). The best fitting model is shown in red, regions taken into account in the fitting are marked with a gray horizontal line.
Bottom panel: Residual spectrum of subtracting the model from the data. The standard deviation over this region is 0.05 mJy, compared to 0.27 mJy in the CO line-free continuum at ∼4 µm (see Fig. 6.2).

Chapter 7

A JWST/MIRI analysis of the ice distribution and PAH emission in the protoplanetary disk HH 48 NE

J. A. Sturm, M. K. McClure, D. Harsono, J. B. Bergner, E. Dartois,
A. C. A. Boogert, M. A. Cordiner, M. N. Drozdovskaya, S. Ioppolo,
C. J. Law, D. C. Lis, B. A. McGuire, G. J. Melnick, J. A. Noble,
K. I. Öberg, M. E. Palumbo, Y. J. Pendleton, G. Perotti, W. R. M. Rocha, R. G. Urso, and E. F. van Dishoeck,

Accepted for publication in A&A

Abstract

Context. Ice-coated dust grains provide the main reservoir of volatiles that play an important role in planet formation processes and may become incorporated into planetary atmospheres. However, due to observational challenges, the ice abundance distribution in protoplanetary disks is not well constrained. With the advent of the James Webb Space Telescope (JWST) we are in a unique position to observe these ices in the near- to mid-infrared and constrain their properties in Class II protoplanetary disks.

Aims. We present Mid-InfraRed Imager (MIRI) observations of the edge-on disk HH 48 NE as part of the Director's Discretionary Early Release Science program Ice Age, completing the ice inventory of HH 48 NE by combining the MIRI data (5 – 28 µm) with that of NIRSpec (2.7 – 5 µm).

Methods. We used radiative transfer models tailored to the system, including silicates, ices, and polycyclic aromatic hydrocarbons (PAHs) to reproduce the observed spectrum of HH 48 NE with a parameterized model. The model was then used to identify ice species and constrain spatial information about the ices in the disk.

Results. The mid-infrared spectrum of HH 48 NE is relatively flat with weak ice absorption features. We detect CO_2, NH_3, H_2O and tentatively CH_4 and ${NH_4}^+$. Radiative transfer models suggest that ice absorption features are produced predominantly in the 50 – 100 au region of the disk. The CO_2 feature at 15 µm probes a region closer to the midplane ($z/r = 0.1 - 0.15$) than the corresponding feature at 4.3 µm ($z/r = 0.2 - 0.6$), but all observations trace regions significantly above the midplane reservoirs where we expect the bulk of the ice mass to be located. Ices must reach a high scale height ($z/r \sim 0.6$; corresponding to modeled dust extinction $A_\mathrm{v} \sim 0.1$), in order to be consistent with the observed vertical distribution of the peak ice optical depths. The weakness of the CO_2 feature at 15 µm relative to the 4.3 µm feature and the red emission wing of the 4.3 µm CO_2 feature are both also consistent with ices at high elevation in the disk. The retrieved NH_3 and CH_3OH abundances with respect to H_2O are significantly lower than in the ISM, but consistent with observations of comets. The contrast of the PAH emission features with the continuum is stronger than for similar face-on protoplanetary disks, which is likely a result of the edge-on system geometry. Modeling based on the relative strength of the emission features suggests that the PAH emission originates in the disk surface layer rather than the ice absorbing layer.

Conclusions. Full wavelength coverage is required to properly study the abundance distribution of ices in disks. To explain the presence of ices at high disk altitudes, we propose two possible scenarios: a disk wind that entrains sufficient amounts of dust, thus blocking part of stellar UV radiation, or vertical mixing that cycles enough ices into the upper disk layers to balance ice photodesorption from the grains.

7.1 Introduction

The composition of planetesimals, comets, and eventually planets is determined in large part by the composition of their building blocks: ice-coated dust grains. Ices are the dominant carriers of volatiles in planet-forming regions (Pontoppidan et al. 2014; Walsh et al. 2015), and set for a large part the spatial distribution of volatiles in the disk (McClure 2019; Banzatti et al. 2020; Sturm et al. 2022; Banzatti et al. 2023). Ices not only play a crucial role in the disk chemistry, but for example, are also thought to play a crucial role in planet formation processes (e.g., Öberg & Bergin 2016; Drążkowska et al. 2016). Unlike the gas present in the protoplanetary disk, ices are directly incorporated into the cores of planets, comets, and icy moons (Oberg et al. 2023). Mapping ices in disks at different stages of their evolution is therefore important to understand the initial building blocks available for planet formation.

With the advent of the James Webb Space Telescope (JWST) we are in the unique position to target the ice absorption bands in the mid-infrared (2 – 15 µm) with sufficient angular resolution to search for spatial variations in protoplanetary disk ices in nearby star-forming regions. The earlier stages of the star formation sequence, when the natal cloud or envelope has high line-of-sight A_{V} (Molecular clouds, Class 0 protostars, Class I protostars), ices have been readily observed in detail with ISO, Spitzer (Boogert et al. 2015), Akari (Aikawa et al. 2012; Noble et al. 2013), ground based observatories, and JWST (Yang et al. 2022; McClure et al. 2023; Rocha et al. 2024; Brunken et al. 2024). However, in late-stage protoplanetary disks after the envelope has dissipated (Class II systems), the contrast of these ice species with respect to the continuum from the warm inner disk is only detectable if the star and bright inner disk is blocked by the disk. This is the case for edge-on disks, which makes them ideal laboratories to study ices in Class II systems (Pontoppidan et al. 2005, 2007; Terada et al. 2007; Schegerer & Wolf 2010; Terada & Tokunaga 2012; Terada et al. 2012; Terada & Tokunaga 2017). Since these sources require high sensitivity to be observed, due to their edge-on nature, JWST is the first observatory that allows for spatially resolved, sensitive observations of these systems with full wavelength coverage in the near- and mid-infrared. An initial analysis of Near-Infrared Spectrograph (NIRSpec Jakobsen et al. 2022b) data of the edge-on disk HH 48 NE detected spatially resolved ice features for the first time in a disk, including the trace species NH_3, OCS, OCN^-, and $^{13}CO_2$, and revealed a surprisingly large vertical extent of H_2O, CO_2, and CO ice absorption (Sturm et al. 2023c). In this paper, we present new Mid-InfraRed Imager (MIRI Rieke et al. 2015b) observations of the same source to complete the inventory of ice features observable with JWST.

Our radiative transfer models and interpretation of JWST NIRSpec observations have shown that the complex scattering light path through edge-on disks precludes a straightforward analysis of the ice features, so that ice abundance distributions can only be constrained by radiative transfer modeling of multi-wavelength observations (Sturm et al. 2023d,c). Ice feature profiles become distorted by scattering (Dartois et al. 2024), and their optical depths do not depend linearly on the column density along a direct line-of-sight toward the star because the multiple light paths through the disk partially ‘dilute’ the absorption profiles. Additional modeling diagnostics of the different ice absorbing regions are necessary in order to understand the spatial distribution of abundances in disks.

Another important element of protoplanetary disks are the Polycyclic Aromatic Hydrocarbons (PAHs). Those big molecules (that in many aspects resemble small dust grains) play a crucial role in the charge balance, chemistry, and heating/cooling of the disk and could contain a significant fraction of the available carbon (Tielens 2008; Kamp 2011). PAHs can be excited by UV radiation and cool efficiently through mid-infrared emission features. These features are attributed to the stretching of C–H (3.3 µm) and C–C (6.23, 7.7 µm) bonds, in-plane (8.4 µm) and out-of-plane (11.27 µm) C–H bending motions or a combination of both (5.4, 5.65 µm). The shape and comparative strength of the features can vary depending on the excitation state, charge, size distribution and hydrogenation (Draine & Li 2007; Boersma et al. 2009; Geers et al. 2009; Maaskant et al. 2014). The distribution and excitation of PAHs in protoplanetary disks has been actively studied (Habart et al. 2006; Visser et al. 2007; Geers et al. 2007; Boutéraon et al. 2019; Kokoulina et al. 2021). Modeling shows that K–M stars ($T_* < 4200$ K) lack UV flux to excite the PAHs (Geers et al. 2009). PAH features have been detected in numerous Herbig Ae/Be stars, but not in T Tauri systems with a spectral type later than G8 (Geers et al. 2006; Tielens 2008; Maaskant et al. 2014; Lange et al. 2023b), except for the edge-on disk around Tau 042021 (Arulanantham et al. 2024). The authors suggest that the unique geometry of edge-on systems, which obstructs the thermal emission from the inner disk, enables the detection of the comparatively weaker PAH emission from T Tauri stars at mid-infrared wavelengths.

The paper is organized as follows: we first describe the details of the observations in Sect. 7.2 and the results that can be directly inferred from the observations in Sect. 7.3. Then we describe the model setup for simulating observations of ices in protoplanetary disks in Sect. 7.4 and use these models to interpret the ice composition, and abundance distribution of the HH 48 NE disk in Sect. 7.5. Finally, we discuss the implications of our findings and the prospects of analyzing ices in edge-on protoplanetary disks in Sect. 7.6. We summarize our findings in Sect. 7.7.

7.2 Description of observations

We present new observations of the HH 48 system using MIRI/MRS onboard JWST, taken on 2023 March 23, as part of the Director’s Discretionary Early Release Science (DD-ERS) program “Ice Age: Chemical evolution of ices during star formation” (ID 1309, PI: McClure). The spectroscopic data were taken with a standard 4-point dither pattern for a total integration of 1665 s, with the pointing centered on $11^{\mathrm{h}}04^{\mathrm{m}}23.18^{\mathrm{s}}$, $-77^\circ18'06.75''$. No target acquisition was taken because of the extended nature of the source. A second, emission-free pointing was observed at $11^{\mathrm{h}}04^{\mathrm{m}}24.48^{\mathrm{s}}$ $-77^\circ18'38.77''$ with similar integration time to subtract the astrophysical background from the target flux. The data were processed through JWST pipeline version 1.11.4 (Bushouse et al. 2023), which includes the time-dependent correction for the throughput of channel 4. The calibration reference file database versions 11.16.21 and jwst_1119.pmap was used, which includes

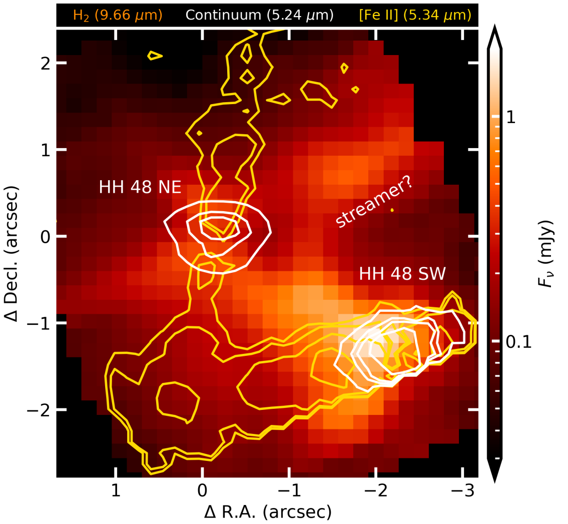

Figure 7.1: Overview of the HH 48 system at MIRI wavelengths. The continuum subtracted H$_2$ $V = 0 - 0$, $J = 5 - 3$ line emission (9.66 µm) is shown in color tracing a complex structure of outflows and potential infall. The continuum at 5.24 µm is shown in white contours at 20, 60, 100, and 300 µJy, tracing the scattered light from the two protoplanetary disks. The [Fe II] line at 5.34 µm is shown in the yellow contours at 5, 10, 30, and 100 µJy tracing the jets of both protostars. The primary, HH 48 SW and secondary, HH 48 NE are labeled in white.

updated onboard flat-field and throughput calibrations for an absolute flux calibration accuracy estimate of 5.6 ± 0.7% (Argyriou et al. 2023). The standard steps in the JWST pipeline were carried out to process the data from the 3D ramp format to the cosmic ray corrected slope image. The scientific background is subtracted after the "Level 1" run. Further processing of the 2D slope image for assigning pixels to coordinates, flat fielding, and flux calibration was also done using standard steps in the "Level 2" data pipeline calwebb_spec2. To build the calibrated 2D IFU slice images in the 3D datacube, the "Stage 3" pipeline was run. The final pipeline processed product presented here was built into 3D with the outlier bad pixel rejection step turned off, as running this over-corrected and removed target flux.

Each spectrum was extracted using a conical extraction, increasing the circular aperture with wavelength by employing a radius of 2.5 resolution elements and a minimum radius of $1\farcs25$. Since the target is a binary, we extracted spectra from both sources at the same time, centered on $11^{\mathrm{h}}04^{\mathrm{m}}23.1806^{\mathrm{s}}$ $-77°18'04.744''$ (HH 48 NE) and $11^{\mathrm{h}}04^{\mathrm{m}}23.186^{\mathrm{s}}$ $-77°18'06.939''$ (HH 48 SW). Due to the increasing size of the point spread function (PSF) with wavelength, the sources spatially overlap at wavelengths $>$ 12 µm. To make sure that our target of interest, HH 48 NE, is the least contaminated by the binary component, HH 48 SW, the mask of HH 48 SW was used to deselect the contaminated region on the mask of HH 48 NE (see Fig. 7.B.1). The masks overlap at wavelengths $>$12 µm, but the brightest core of HH 48 NE's disk remains resolved up to ∼25 µm. The 12 sub-channels are then scaled according to the median of the overlapping region in between the sub-channels starting from the shortest wavelengths (NIRSpec) to the longest sub-channels. The correction is in all cases less than 5%. For channel 4 ($\lambda > 18$ µm) we did not use any scaling because the difference in pixel size in combination with the double mask during extraction would result in sudden jumps

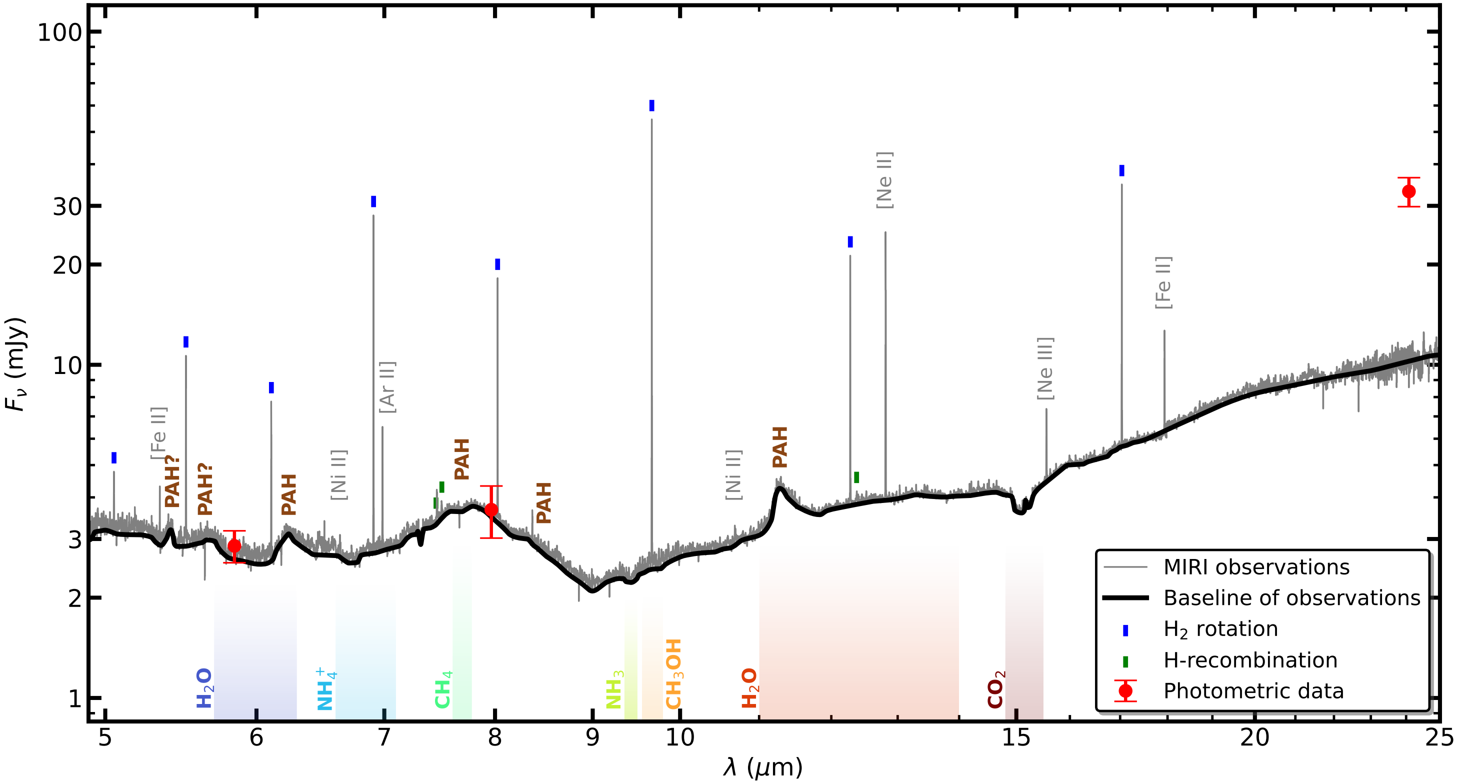

Figure 7.2: Integrated MIRI spectrum of HH 48 NE. The continuum baseline underneath the gas emission lines is shown as a black line. Gas features are labeled accordingly, molecular and recombination hydrogen lines are marked with colored tick marks. Absorption wavelength regions for important ices are marked on the bottom. Pre-JWST photometric data points are shown in red.

in the spectrum.

7.3 Observational results

An overview of the HH 48 system is presented in Fig. 7.1 where we show the spatial extent of the continuum subtracted H_2 $V = 0 - 0, J = 5 - 3$ line with contours of the continuum at 5.24 µm (white) and the continuum subtracted [Fe II] line at 5.34 µm (yellow). HH 48 is a binary of two T Tauri stars with a separation of $\sim 2\farcs3$ or 425 au. Both sources show extended continuum emission at 5.24 µm. A jet is detected in both systems in the [Fe II] line emission at 5.34 µm. The H_2 emission (background in Fig. 7.1) extends far beyond the scattered light continuum and probably traces disk winds in both protoplanetary disks. Large scale structure is detected in H_2 toward the northwest of both sources that is not connected to any of the protostars in a coherent manner and traces the asymmetric structure earlier observed in CO $J = 2 - 1$ ALMA observations (see Fig. 7.A.1 and Sturm et al. 2023e). This component only appears in low-energy H_2 lines ($E_{\rm up} < 2000$ K), which implies that the gas is cold with a high column density. A careful investigation of the region did not show any signs of an additional source, which means that the most likely origin of the large-scale structure is an infalling streamer feeding the system or an interacting large scale wind. The focus in this paper is on HH 48 NE, as it is the most inclined of the two sources, but a spectrum of HH 48 SW is shown in Appendix 7.B.

Figure 7.2 presents the source integrated spectrum MIRI spectrum of HH 48 NE. Common gas emission lines are marked in Fig. 7.2. Molecular gas emission lines (e.g., CO, H_2O) can be seen throughout the spectrum but will be analyzed later in a future article, as the main focus of this paper is on the ice absorption features. The observations are overall in good agreement with the photometric data points compiled in Sturm et al. (2023e), except for the Spitzer/MIPS data point at 24 µm. This photometric data point was based on a 2D Gaussian fit to the low-resolution *Spitzer* data, which resulted in an overestimation by a factor of 3.

To estimate the continuum baseline underneath the molecular gas emission lines, we spline-fitted a line through the troughs between the lines including the broad features from PAH and ices in the continuum. Since the placement of this continuum is uncertain, all figures include the full data as well for comparison. The spectrum shows a shallow silicate feature in absorption that peaks at 9.0 µm.

7.3.1 PAH emission

The most striking features are the PAH emission features most clearly seen at 6.23, 7.7, and 11.27 µm, but also at 5.4, 5.65, and 8.47 µm (see the PAH opacity template as the dashed line in Fig. 7.3, taken from Visser et al. 2007). The PAH emission is spatially localized at the disk (i.e., we don't detect extended emission) and shows signs of severe wavelength dependent extinction since the 3 µm feature is absent and the 6.2 µm feature is weaker than expected. This suggests that the PAHs are located in the disk atmosphere and are obscured by its edge-on nature and/or that the ultraviolet (UV)/visible part of their excitation source is strongly attenuated. Given the uncertainty of the extinction, it is difficult to compare feature ratios

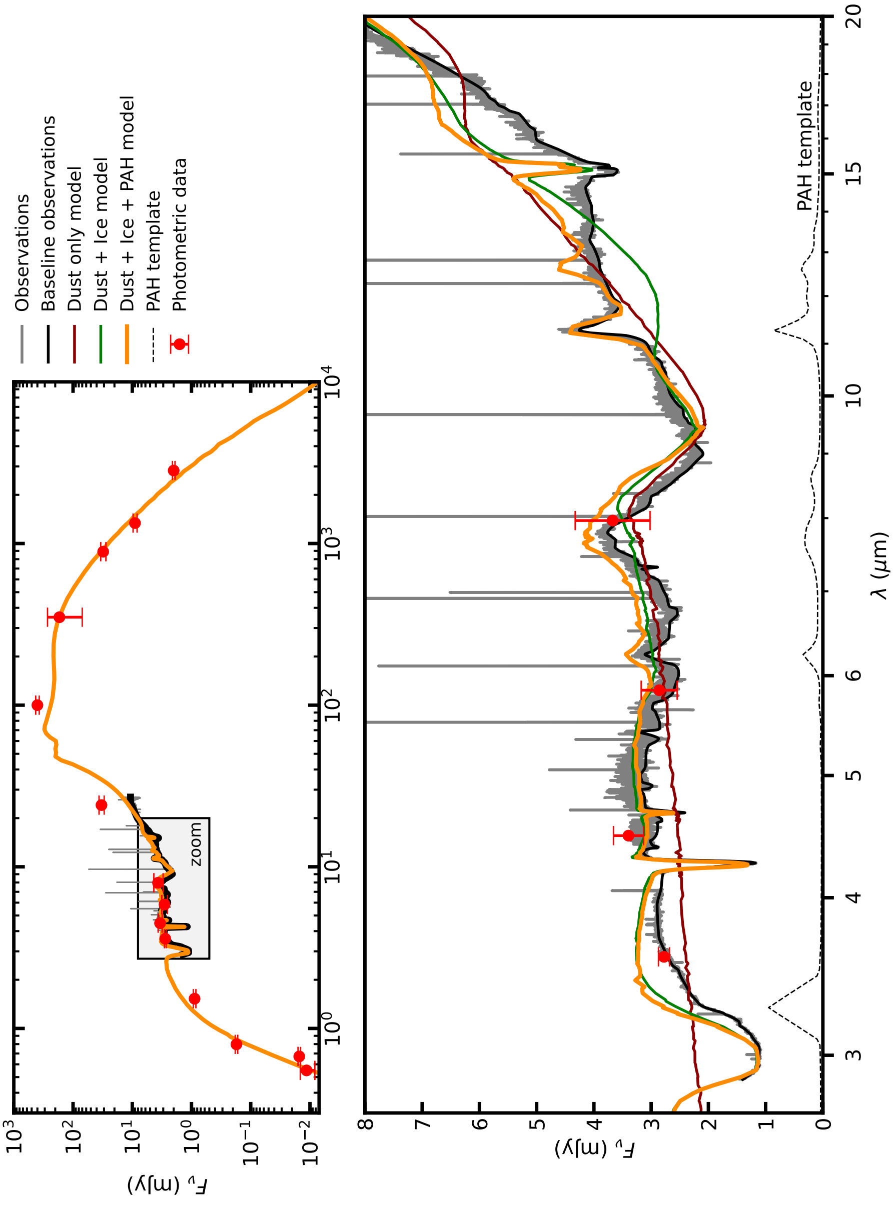

Figure 7.3: caption on next page

to constrain anything about the PAH characteristics. The peak positions do not align with the established observational classes in ISM observations in Peeters et al. (2002) that usually correlate between different features; A potential combination of the three classes' characteristics is observed concurrently, indicative of radiative transfer spectral modification or active PAH chemistry in the disk. Although the 12.6 µm feature is faint, it may be partially concealed by the H_2O libration band (as seen in the model without PAH in Fig. 7.3). The 5.4 and 5.65 µm features are more pronounced than anticipated compared to the 5.25 and 6.2 µm bands, possibly due to the presence of small PAHs with multiple hydrogen groups in trios (Boersma et al. 2009; Ricca et al. 2019). Further exploration of the origin and characteristics of the PAHs is required in the future to elucidate their significance in the physics and chemistry of regions where planets are forming, extending the analysis to less massive stars like T Tauri stars.

7.3.2 Ice features

Strong ice absorption features, such as those observed in molecular clouds or protostars, are absent from our mid-infrared MIRI observations, which we interpret as a direct result of the multiple light paths that are possible through the disk (see for more details Sturm et al. 2023c). The strongest absorption feature is the CO_2 bending mode at 15.5 µm with a peak optical depth of only 0.2. Due to the position of the PAH features and the effects of radiative transfer changing the profiles of the ice and silicate features, it is not appropriate to fit a polynomial to the continuum for ice identification and analysis. Therefore, a radiative transfer model tailored to this source is required to discriminate ice absorption features from silicate and PAH features.

7.3.3 Spatially resolved continuum emission in HH 48 NE

The left column of Fig. 7.4 presents the spatially-resolved continuum emission of the HH 48 NE disk at a range of wavelengths from optical HST observations to millimeter ALMA observations. The bowl-shaped disk with a bright lobe on top, a dark lane, and a weaker lobe at the bottom, is recognizable up to 10 µm. The disk is spatially resolved up to 15 µm, which indicates that the continuum has a significant contribution from scattered light up to 15 µm. The East-West asymmetry that was observed previously in the optical HST observations is visible to a wavelength of ∼10 µm. Normalized vertical and radial cuts through the continuum emission are shown on the right. Contributions due to HH 48 SW or

Figure 7.3: Overview of the source integrated spectrum of HH 48 NE (grey), with the continuum baseline underneath the gas lines shown in black with a zoom-in on the JWST wavelength range 2.7 – 27 µm. Different ice radiative transfer models are shown for comparison with the observations. The initial model constrained from photometric data points, HST, and ALMA observations (Sturm et al. 2023e,d) is shown in blue. A similar model was fine-tuned to the NIRSpec and MIRI spectrum with only refractory dust (red), dust and ice (green), and dust, ice, and PAHs (orange). The PAH opacity template used is shown in the bottom without extinction corrections (Visser et al. 2007).

possible dynamic interactions (Stapelfeldt et al. 2014; Sturm et al. 2023e) between the systems are masked in orange.

7.4 Model setup

Sturm et al. (2023c) show that the optical depth of the ice features in observations of edge-on protoplanetary disks is not linearly correlated with their column density and that the profiles of the ice features can be significantly altered due to the scattering opacity of the ices. Since the disk is seen in scattered light in the JWST observations, it requires detailed 3D radiative transfer modeling to interpret the observed ice features and to constrain the region that is probed in the disk.

7.4.1 Physical structure

We adopt the model setup described in Sturm et al. (2023e,d). The input spectrum is assumed to be a black body with temperature (T_s) scaled to the stellar luminosity (L_s). The density setup of the disk is parameterized with a power-law density structure and an exponential outer taper (Lynden-Bell & Pringle 1974),

$$\Sigma_\mathrm{dust} = \frac{\Sigma_\mathrm{c}}{\epsilon}\left(\frac{r}{R_\mathrm{c}}\right)^{-\gamma}\exp\left[-\left(\frac{r}{R_\mathrm{c}}\right)^{2-\gamma}\right], \tag{7.1}$$

where Σ_c is the surface density at the characteristic radius, R_c, γ is the power-law index, and ϵ is the gas-to-dust ratio. The inner radius of the disk was set to the dust sublimation radius, approximated by $r_\mathrm{subl} = 0.07\sqrt{L_\mathrm{s}/L_\odot}$, and the outer radius of the grid was set to 300 au ($1''.6$), which is consistent with the observations of the disk extent.

The vertical structure of the disk is described as

$$h = h_\mathrm{c}\left(\frac{r}{R_\mathrm{c}}\right)^{\psi}, \tag{7.2}$$

where h is the aspect ratio of the gas and small dust grains, h_c is the aspect ratio at the characteristic radius, and ψ is the flaring index. We adopted two dust size populations to mimic dust settling in the system with a Gaussian distribution,

$$\rho_\mathrm{d} = \frac{\Sigma_\mathrm{dust}}{\sqrt{2\pi}rh}\exp\left[-\frac{1}{2}\left(\frac{\pi/2-\theta}{h}\right)^{2}\right], \tag{7.3}$$

where θ is the opening angle from the midplane as seen from the central star. The aspect ratio of the large grain population is restricted to $X \cdot h$ with $X \in [0,1]$. The fraction of the total dust mass that resides in the large dust population was defined as f_ℓ. The two dust populations followed a power-law size distribution with a fixed slope of -3.5 between the minimum grain size a_min and a_max. a_min is the same for both grain populations, a_max of the large grain population is fixed at 1 mm. The dust and ice opacities were calculated using `OpTool` (Dominik et al. 2021), using the distribution of hollow spheres (DHS; Min et al. 2005) approach to account for grain shape effects with the $f_\mathrm{max} = 0.8$. The gas is assumed to follow the small dust grain population, which implies that the gas-to-dust ratio varies over the vertical extent of the disk according to the dust settling.

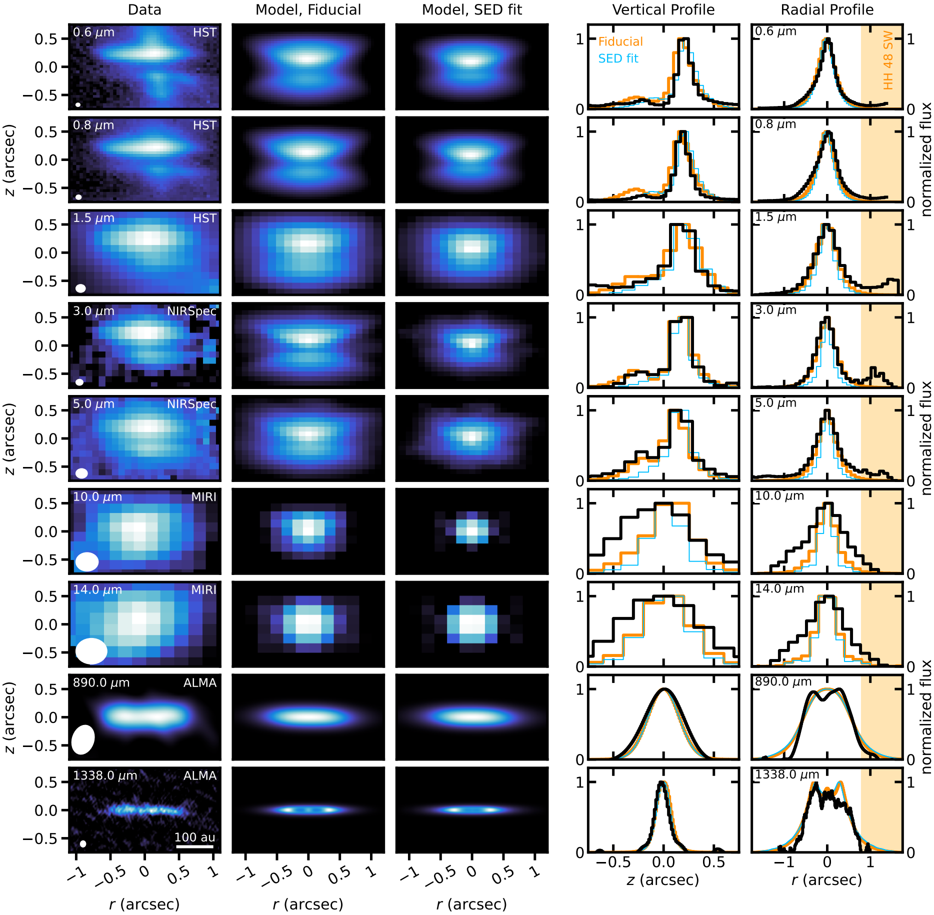

Figure 7.4: First column from the left: The spatial appearance of the continuum emission from HH 48 NE in the optical HST observations, JWST MIRI observations, and millimeter ALMA continuum observations. Second and third columns: spatial appearance of the continuum emission from the fiducial model and MIRI fit, respectively, after convolution to a representative PSF. Last two columns: median averaged vertical and radial profile of the continuum emission normalized to the peak (black) with the fiducial model (orange) and MIRI fit (blue) on top. The orange box marks the region where HH 48 SW starts dominating the continuum.

Table 7.1: Properties of the ice retrieved in the models compared to the ISM.

Ice species	E_b (K)	Disk X/H (ppm)	ISM X/H (ppm)	Disk X/H_2O (%)	ISM X/H_2O (%)	Comet X/H_2O (%)	67P X/H_2O (%)
H_2O	5705	30	80	100	100	100	100
CO_2:CO 3:1	3196	6					
– CO_2 fraction		4.5	22	15	13	2.0 – 30	4.7
– CO fraction		1.5	28	5	28	0.4 – 30	3.1
CH_4	1232	3.6	3.6	<12	1.9	0.4 – 1.6	0.34
NH_3	5362	0.5	4.8	1.7	5.0	0.2 – 1.4	0.67
CH_3OH	6621	<0.5	4.8	<1.7	3.8	0.2 – 7.0	0.21

Only CO_2 and CO are considered to be mixed in this work. The ISM ice abundances relative to hydrogen are taken from the inheritance model in Ballering et al. (2021), the ISM ice abundances relative to water are taken from the background stars published in McClure et al. (2023), cometary ice abundances relative to water are taken from Rubin et al. (2019).

7.4.2 Ice distribution

The ices are initially distributed at a constant abundance with respect to hydrogen within the expected ice surfaces, with the initial abundances taken from the inheritance model in Ballering et al. (2021), based on observations summarized in Boogert et al. (2015). The model has an increasing number of ices towards the midplane, based on their binding energy and a photodesorption limit. The thermal desorption ice line of each system is determined using the approach described in Hasegawa et al. (1992), that is the point where there is more ice than gas available of a given molecular species

$$\frac{n_{\mathrm{ice}}}{n_{\mathrm{gas}}} = \frac{\pi a_{\mathrm{d}}^2 n_{\mathrm{d}} S \sqrt{3k_{\mathrm{B}}T/M_{\mathrm{n}}}}{e^{-E_{\mathrm{b}}/T}\sqrt{2k_{\mathrm{B}}N_{\mathrm{ss}}E_{\mathrm{b}}/(\pi^2 m_i)}} > 1, \tag{7.4}$$

where n_{ice} is the number density of molecules in the ice phase, n_{gas} is the number density of molecules in the gas phase, a_{d} is the characteristic dust grain size, n_{d} is the dust number density, S is the sticking coefficient which is assumed to be 1, k_{B} is the Boltzmann constant, T is the dust temperature, M_{n} is the molecular mass of the species, E_{b} is the binding energy, N_{ss} is the number of binding sites per surface area assumed to be 8×10^{14} cm^{-2} (Visser et al. 2011), m_i is the mass of the species i. The region where ice is abundant is vertically truncated by a limit that is initially put at $A_{\mathrm{V}} = 1.5$ mag, motivated by the onset of water ice in dark cloud observations (Boogert et al. 2015), which corresponds to $z/r \sim 0.3$. Inside and above this limit, the model consists of bare grains without ice mantles. This limit is an approximation of the photodesorption limit and the slightly higher dust temperatures at low A_{V} that keeps the grains ice free.

The average density of the dust and ice composite was then calculated in every region using

$$\rho_{\mathrm{ice}} = \rho_{\mathrm{gas}} \frac{x_{\mathrm{ice}} M_{\mathrm{ice}}}{x_{\mathrm{gas}} M_{\mathrm{gas}}}, \tag{7.5}$$

where x is the abundance with respect to total hydrogen, and M the mean molecular weight. The gas predominantly consists of H_2 and He and has an abundance of $x_{\mathrm{gas}} = 0.64$ and a mean molecular weight of 2.44. The ice is distributed throughout the small and large grain population according to their surface area assuming smooth spheres, following the description in Ballering et al. (2021),

$$f_{\mathrm{ice},\ell} = \frac{f_{\mathrm{dust},\ell}}{\sqrt{a_{\mathrm{max},\ell}/a_{\mathrm{max,s}}}\,(1 - f_{\mathrm{dust},\ell}) + f_{\mathrm{dust},\ell}}. \tag{7.6}$$

In each of the two dust populations, the ice is distributed over the grains assuming a constant dust core - ice mantle mass ratio assuming efficient dust growth in the disk after initial freeze out in early phases of the star forming process.

The additional mass of the ice is not added to the dust model, to keep the physical structure of the disk the same independent of the ice distribution. This implies that we effectively used a gas-to-solid ratio of 100 that includes silicates, amorphous carbon, and ice, instead of a gas-to-dust ratio of 100. Depending on the choice of definition of settling (dust only, or dust and ice) and gas-to-dust ratio, the actual ice mass can vary up to a factor of a few, a point we return to in Sect. 7.6.

Table 7.2: Properties of the fiducial model presented in Sturm et al. 2023e,d and the model tweaked to fit the JWST spectrum.

parameter (unit)	fiducial (Sturm et al. 2023d)	best fit (this work)
L_s ($\mathrm{L}_\odot$)	0.41	0.25
T_s (K)	4155	4200
R_c (au)	87	87
h_c	0.21	0.24
ψ	0.13	0.13
i (°)	82.3	83
γ	0.81	1
M_gas ($\mathrm{M}_\odot$)	2.7×10^{-3}	3.2×10^{-3}
f_ℓ	0.89	0.97
X	0.2	0.2
a_min (µm)	0.4	0.3
$a_\mathrm{max,s}$ (µm)	7	12.6
$a_\mathrm{max,l}$ (µm)	1000	1000
R_cav (au)	55	50
δ_cav	1.6×10^{-2}	3.5×10^{-3}
photodesorption limit	$A_\mathrm{V} = 1.5$ ($z/r \sim 0.3$)	$z/r = 0.6$ ($A_\mathrm{v} \sim 0.1$)

7.4.3 PAHs

The spectrum shows clear signs of PAH emission, as described in Sect. 7.3, and without properly considering its emission, it is difficult to identify and characterize the ice features. The PAH emission is spatially localized to the disk, and the relative strengths of the different features suggest that the PAHs are obscured, which means that they are emitting from within the protoplanetary disk. Therefore, we model the PAHs in a simplistic way, including a population of PAHs in the model using the opacities from Visser et al. (2007) using a size distribution from 5 to 100 Å and a power law slope of 3.5. For the PAHs, we assumed the same temperature as for the dust; stochastic heating by UV photons was not taken into account. The PAHs are limited to the regions in the model where ices are absent due to either thermal desorption or photodesorption. The mass of PAHs required to match the strengths of the features in the observations is 175 ppm of the disk mass, or 17% of the available carbon, which is consistent with ISM abundances and above previously modeled abundance that predict a depletion by orders of magnitude in Herbig Ae/Be stars (Sloan et al. 2005; Visser et al. 2007; Geers et al. 2009; Lange et al. 2023b).

7.5 Modeling results

As a starting point, we adopted the physical structure from Sturm et al. (2023d). Initial ice abundances were established based on the average of their measurements relative to H_2O ice in Boogert et al. (2015), with the H_2O abundance at 8×10^{-5} following the reasoning in Ballering et al. (2021) and consistent with Sturm et al. (2023d) (see Table 7.1). This model is a good fit to the spatial extent of optical HST scattered light observations, ALMA millimeter continuum observations, and the SED (see Fig. 7.4,7.B.2 and Sturm et al. 2023e). The model reproduces the observed JWST spectrum reasonably well, except for the silicate feature and the flux at wavelengths >20 µm. The main reason for this is the change of origin of the continuum emission as, in the models, the direct warm emission from the disk starts dominating over the scattered light of the warm inner disk in that particular region. Since the initial model is already close to the data, we perturbed the parameters of the fiducial model using the MCMC setup presented in Sturm et al. (2023e) with L_s, h_c, ψ, M_gas, f_ℓ, a_min, $a_\mathrm{max,s}$, and δ_cav as free parameters without waiting for conversion. The best fitting model to the spectrum is given in Table 7.2) with only minor changes in the setup. Details on the outcome of the overall modeling and identified ices are presented in Sect 7.5.1, and the effect of changing the size of the region in the disk where ices are included is investigated in Sect 7.5.2.

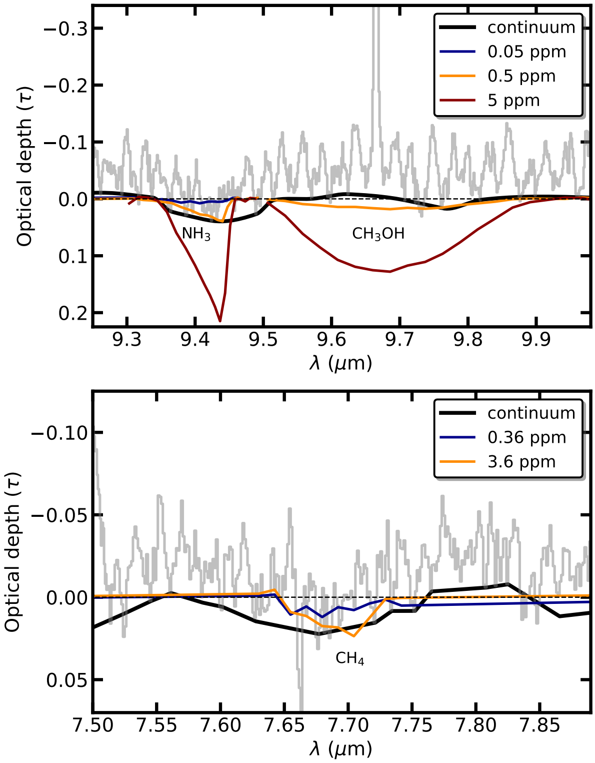

Figure 7.5: Optical depth representation of the NH_3 and CH_3OH features (top) and the CH_4 feature (bottom) with modeled features overlayed at different abundances. The black line indicates the continuum underneath the gas emission features including ices.

7.5.1 Ice identification

In the NIRSpec spectrum (2.8 – 5.3 µm), we identified the major ice components H_2O, CO_2, and CO, and multiple weaker signatures from less abundant ices NH_3, OCN^-, and OCS and the $^{13}CO_2$ isotopologue. Ice identification in the MIRI spectrum (5 – 28 µm) requires comparison with a model to correctly predict the location of the ice features and distinguish the PAH emission. Fig. 7.3 presents the comparison between the source-integrated spectrum of the observations and the best fitting model including dust, ice, and PAHs (orange line). The model is overall a good representation of the spectrum with a few wavelength regions that are over-predicted.

7.5.1.1 H_2O

The bending mode of H_2O at 6 µm is present in both the observations and the models, but is weak compared to the OH-stretch mode at 3 µm. Due to the PAH emission feature at 6.25 µm it is hard to tell whether the discrepancy between the model and the observations is a result of the continuum being slightly too high or if the feature is stronger in the observations than in the model; other molecules could contribute to the absorption feature. The libration mode of H_2O at 12 µm is not observed in the spectrum, but the model without PAH emission (green vs. orange in Fig. 7.3) illustrates that the feature can also be hidden under the 11 and 12 µm PAH emission features.

7.5.1.2 CO_2

The bending mode of CO_2 at 15 µm is weaker than expected from the CO_2 stretch feature at 4.3 µm (see Fig. 7.B.2), and has the characteristic double-peaked profile of partially segregated CO_2 ice (see e.g., Boogert et al. 2015, for a review). In addition, the bending mode has a broad contribution that is not accounted for in the model. The best-fitting model includes one component of CO_2:CO at 20 K in a 3:1 ratio at an abundance of 6 ppm with respect to hydrogen. This ice mixture was chosen to accommodate CO to be high up in the disk, and because it dominates the CO profile fit in Bergner (in prep.). Using more mixtures could improve the fit to individual ice features in the MIRI range, but we refer to Bergner (in prep.) for a detailed analysis of the ice profiles in the NIRSpec wavelength range. The models show that we can roughly reproduce the strength and shape of the CO_2 feature and the CO feature with this single component. We revisit fitting the strength of both CO_2 features in Sect. 7.5.2.2.

7.5.1.3 7 µm region

The 6.8 µm absorption feature commonly found in protostars and dark clouds, usually attributed to NH_4^+, is only weakly detected. Due to the PAH features at 6.25 µm and 7 – 9 µm, it is difficult to study this region in detail. However, the models suggest that there is an additional absorption feature centered at 6.8 µm that is currently not taken into account in the modeling, which could be due to the NH_4^+ complex (Keane et al. 2001; Boogert et al. 2008, 2015). Ice absorption features of other species, for example SO_2 and CH_4, are also known to occur at ~7.6 – 7.7 µm, the wavelength where the PAH feature is expected. The PAH feature shows a dent at the peak, which can be reproduced with the addition of

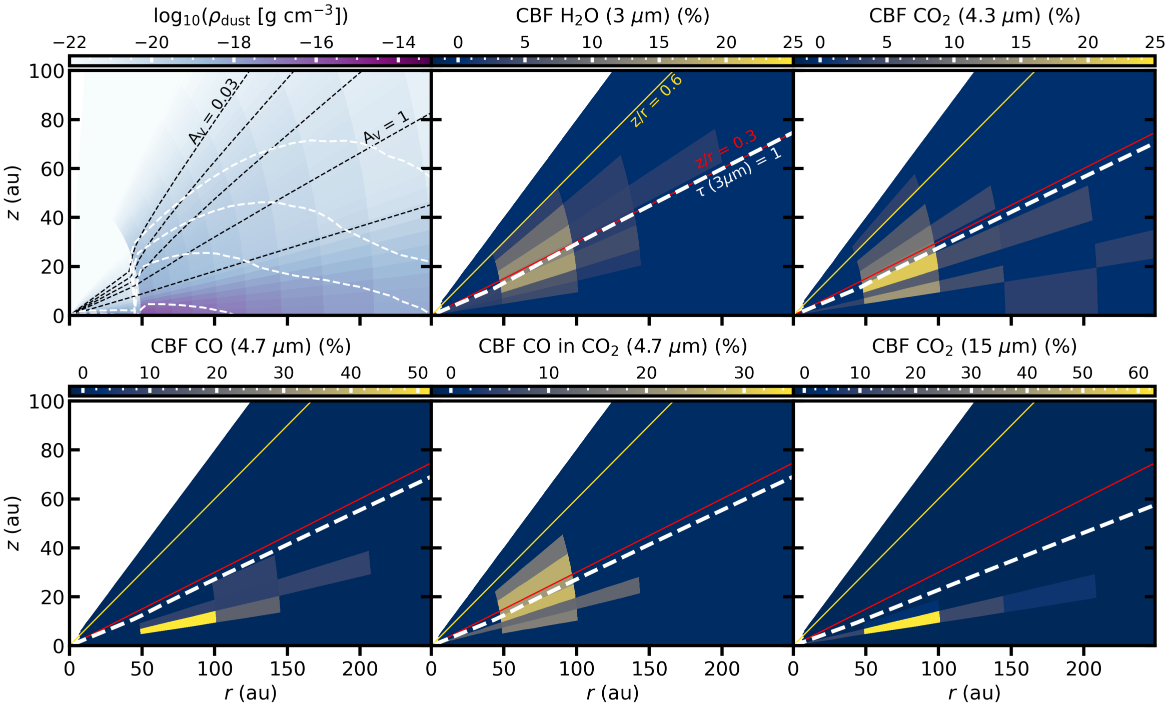

Figure 7.6: Top left: total dust density distribution in the model with internal shielding (radial A_V; black dashed) at 0.03, 0.1, 0.3, 1, and 10 mag and external shielding (vertical A_V; white dashed) at 0.01, 0.03, 0.1, and 1 mag from top to bottom. The other panels show the contribution function (CBF), i.e., the contribution of a specific region to the total absorption of the ice feature in percentages. The pure CO ice at high abundance is added for reference, but we argue in the main text that this component is not observed. The absorbing area is the region in the disk that contribute significantly to the total absorption. The red and yellow lines indicate the fiducial and best fit photodesorption snow surface, respectively, for reference. The thick, dashed, white line shows the $\tau = 1$ surface at the ice feature wavelength. We would like to note that viewing angle is really important and is 83° in this case

CH_4 ice to the model at ISM abundance (3.6 ppm, Ballering et al. 2021) with respect to hydrogen, but a component including, for example SO_2, cannot be excluded (see Fig. 7.2,7.5). OCN^- has a feature in this range as well and is weakly detected at 4.6 µm in the NIRSpec spectrum (Sturm et al. 2023c), but given the much weaker band strength at 7.6 µm, the contribution is most likely negligible (van Broekhuizen et al. 2004b). Since the shape of the PAH feature is relatively unconstrained, we leave a detailed analysis of this ice feature to a future project.

7.5.1.4 NH_3 and CH_3OH

Ammonia, NH_3, is detected at 9.3 µm at a strength consistent with the feature found at 2.93 µm (see Fig. 7.5). This feature is reproduced with a component of pure NH_3 in the model with an abundance of 0.5 ppm with respect to hydrogen, a factor 10 lower than the abundance assumed in the ISM. There is no clear sign of methanol, CH_3OH, in the spectrum: there is no sign of the 9.7 µm CH_3OH feature and the red wing of the H_2O feature at 3.4 µm shows no sign of the narrow 3.53 µm CH_3OH feature (Sturm et al. 2023c; Terwisscha van Scheltinga et al. 2018), even though it cannot be excluded that there is a minor contribution (cf. the discussion in Bergner in prep.). Given that the binding energy of methanol is higher than that of CO_2, this places tight constraints on the abundance in the disk regions that are traced with these observations. The maximum abundance of pure CH_3OH in the model that is consistent with the observations is 0.5 ppm. We return to this in Sect. 7.6.

7.5.2 Locating the measured ice

Due to the complex radiative transfer between the emission and detection of the light, our observations do not trace the bulk ice reservoir in the midplane of the disk. The presence of PAH emission complicates this further. Furthermore, we have shown in Sturm et al. (2023c) that the spatially resolved information from the ice absorption is not directly related to the ice column density along the line of sight. The main reason for these results can be attributed to the position of the light source in our observations, which is situated at the center of the source rather than behind the disk as for background star observations. Consequently, we examine the ice characteristics along the multiple trajectories of the photons that scatter within the disk's atmosphere, rather than along a narrow beam passing through the disk. In this section, we explore what regions our observations trace in the models, and constrain the region where the observed ices are located in the disk.

7.5.2.1 Contribution function

To constrain the region probed by our observations, contribution functions were generated for the ice absorption in the model. Due to scattering, it is not possible to deduce the regional contribution from a single model, since it requires storing the complete trajectory of every emitted photon, which is not practical. Therefore, we rerun the same model multiple times, each time with the ices removed in the disk except for a specific region to test the contribution to the absorption in the source-integrated spectrum of that specific region. The disk is divided into five radial bins with edges at 0, 50, 100, 150, 200, and 300 au and 11 vertical bins at

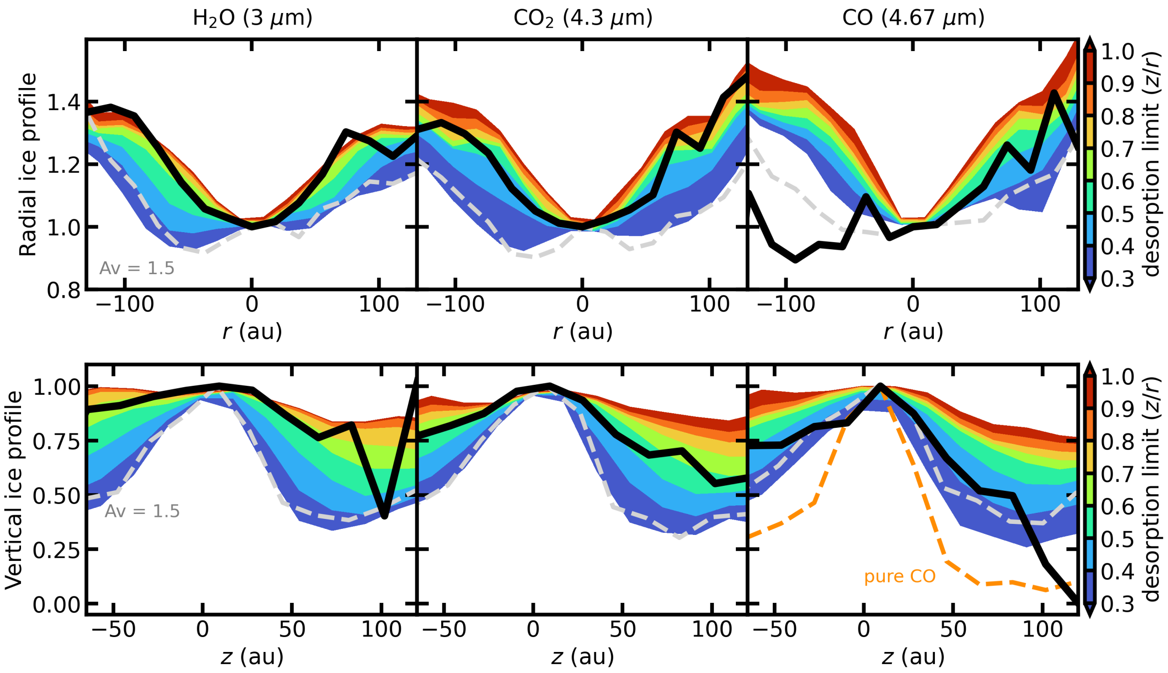

Figure 7.7: Median averaged profiles of the peak optical depths in radial direction (top) and vertical direction (bottom). The data are displayed in black and models with varying vertical photodesorption threshold in z/r are shown in the colors specified in the colorbar. The gray dashed line shows the fiducial model with a photodesorption limit of $A_V = 1.5$ mag and the orange dashed line indicates the vertical profile of the CO ice if pure CO ice is considered with a binding energy of 830 K.

z/r of 0, 0.1, 0.15, 0.2, 0.25, 0.3, 0.4, 0.5, 0.6, 0.7, 0.8, and 0.9, which results in a total of 55 models. The course gridding is necessary to have sufficient S/N on the ice feature in the source-integrated spectrum in a reasonable computation time. Note that we neglected photodesorption in this case to show what the contribution of ices to the total absorption would be at all positions in the disk. The regional contribution to the absorption of the different ice features in the source-integrated spectrum is displayed in Fig. 7.6. We included a model with one component of CO mixed in CO_2 as given in Table 7.1, and a separate model with one component of pure CO with a binding energy of 830 K.

By comparing the contribution functions in Fig. 7.6, we can identify three different categories. First, we see that the H_2O and CO_2 features in the NIRSpec wavelength range (3 and 4.3 µm, respectively) are dominated by a region between a radius of 50 and 100 au and significantly above the midplane ($z/r = 0.2 - 0.5$). The source of continuum at these wavelengths is the warm inner disk (Sturm et al. 2023d), scattered through the atmospheric layers of the disk. Ice absorption is dominated by layers that are optically thin enough to dust so that not all the light is absorbed but have enough ice mass to absorb a significant amount of light in the ice feature. The disk midplane is too optically thick to let photons escape, and the disk atmosphere ($z/r \simeq 0.5$) and outer disk ($r > 100$ au) have too low ice mass to significantly contribute to the total absorption in the spectrum. There is a significant contribution from below the $\tau = 1$ layer at the absorption feature wavelength (white dashed line), which is a result of the fact that a large fraction of the photons encounter multiple scattering and could scatter downward (cf. Sturm et al. 2023d,c).

Second, pure CO ice absorption would be dominated by a region in the model close to the midplane because of its physical location. Assuming a binding energy of 830 K (Noble et al. 2012) the pure CO ice is restricted to $z/r < 0.15$, which is reached by only a small fraction of the light. Due to the small fraction of light that reaches the CO ice-rich layer, the optical depths in the model cannot reproduce the data even for a very high CO abundance (c.f. Sturm et al. 2023d). Instead, CO is mixed with CO_2 or H_2O (see Sturm et al. 2023c and Sect. 7.5.2), leaving little room for pure CO (Bergner in prep.). CO mixed in the CO_2 matrix shows similar results as the CO_2 feature, which is no surprise given the small difference in feature wavelength.

Third, the CO_2 feature at 15 µm traces a region close to the midplane between z/r of 0.1 and 0.15. The probed region with these features is closer to the midplane because of the longer wavelength of the features, which means that photons can penetrate further in the disk. Additionally, the dominant source of continuum changes at these wavelengths from scattering to thermal dust emission in the models (see Sturm et al. 2023d), which means that the layer with the highest density that is still optically thin will produce the strongest absorption in the integrated spectrum.

7.5.2.2 Locating elevated ices

There are three pieces of evidence indicating that the ices in the disk are elevated (located higher above the midplane) with respect to our model predictions assum-

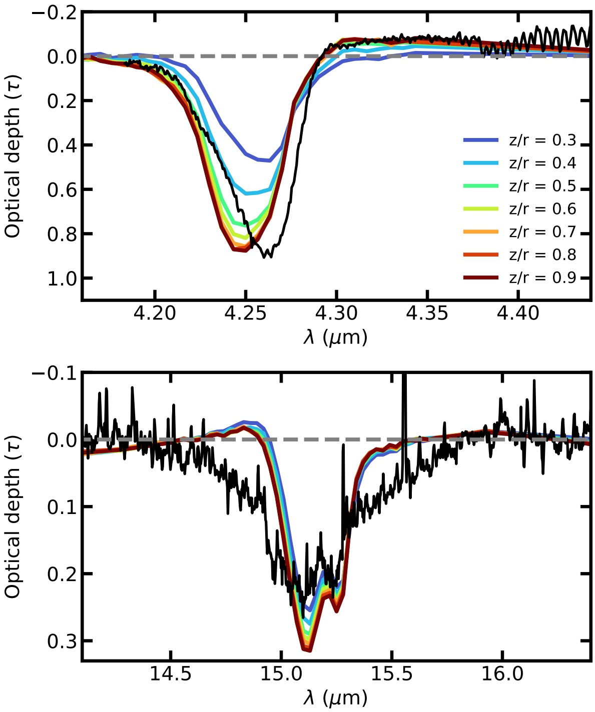

Figure 7.8: Comparison between the 4.3 μm CO_2 stretch feature and the 15 μm bending mode in the observations (black) and models with different vertical photodesorption limits (colored lines). The relative strengths of the features change with the photodesorption threshold due to a different spatial origin of the absorption (see Sect. 7.5.2.1). The shape of the 4.3 μm and especially the red emission wing at 4.30 – 4.35 μm is also dependent on the height of the photodesorption limit due to geometric effects (see Fig. 7.9). No detailed fit to ice absorption profiles was performed, which could significantly improve the fit at 15 μm (see Bergner in prep., for a fit of the 4.3 μm feature).

ing a photodesorption limit of $A_\mathrm{v} = 1.5$ mag. First, as discussed in Sturm et al. (2023c), the vertical dependence on the absorption strength in the H_2O, CO_2, and CO features is less steep than expected if the ices were physically confined near the midplane. In Fig. 7.7, we present the median averaged dependence of the peak optical depth as a function of both horizontal and vertical positions in the disk. These profiles are normalized to the absorption at $r = 0$ and $z = 0$. Unfortunately, the CO_2 feature at 15 μm is not spatially resolved, and the signal-to-noise ratio for the other ice features is insufficient for a comparable analysis. To determine the vertical extent of the ices, we conducted simulations with different photodesorption limits based on an ice destruction constraint in z/r. Subsequently, we convolved each wavelength point with the corresponding NIRSpec PSF using the `WebbPSF` package (Perrin et al. 2012) and calculated the median dependence of the optical depth in both horizontal and vertical directions similar to the observations. The modeled profiles are depicted in Fig. 7.7. The gray line represents the standard model with a photodesorption limit of $A_\mathrm{V} = 1.5$ mag, while the colored regions display the outcomes for different desorption limits. Even with the standard photodesorption limit, there are absorption features at high altitudes ($z > 50$ au) caused by photons undergoing multiple scattering events, although this is insufficient to account for the observed profile. The best fitting model features a photodesorption threshold of $z/r = 0.6$, corresponding to A_V ~0.1 mag as observed from the star. The observed absorption profile for CO can only be

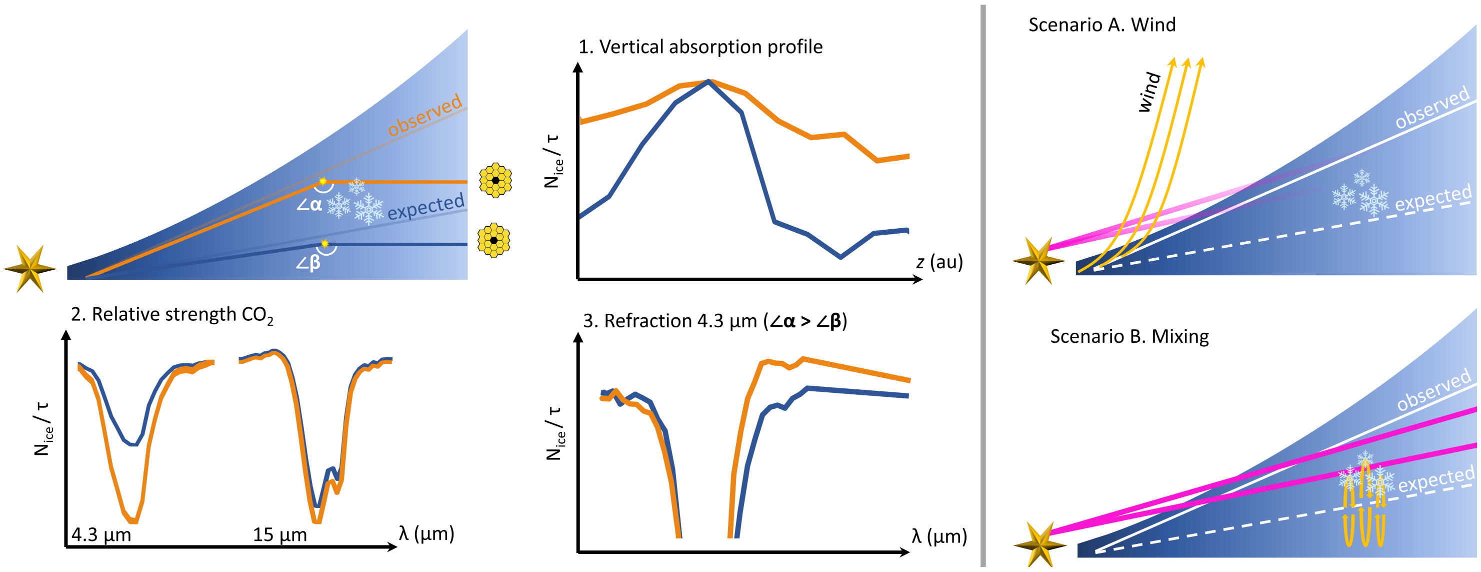
observed
∠α
expected
∠β
1. Vertical absorption profile
N_ice / τ
z (au)
2. Relative strength CO₂
N_ice / τ
4.3 µm
15 µm
λ (µm)
3. Refraction 4.3 µm (∠α > ∠β)
N_ice / τ
λ (µm)
Scenario A. Wind
wind
observed
expected
Scenario B. Mixing
observed
expected

Figure 7.9: Sketch of the three pieces of evidence for elevated ices in HH 48 NE. The orange line demonstrates the effect of including the ices high up in the disk on the vertical absorption profile (panel 1.), the relative strength of the 4.3 to 15 µm CO_2 features (panel 2.), and the scattering wing of the 4.3 µm CO_2 feature (panel 3.). Two scenarios are proposed: a dusty disk wind blocking part of the UV emission from the star (Scenario A.) or vertical mixing stirring up ice to the surface (Scenario B.).

explained by a component of CO mixed within a matrix with a higher desorption temperature, as pure CO is confined near the midplane due to its low desorption temperature, resulting in a sharp peak without a significant contribution from photons undergoing multiple scattering events ($z > 50$ au).

The radial profiles yield similar outcomes, although care has to be taken as these profiles are more sensitive to the source structure compared to the vertical profiles. One interpretation of our results would suggest that the CO_2 feature aligns more closely with a photodesorption threshold of $z/r = 0.5$, and the CO feature with a photodesorption threshold of $z/r = 0.4$. However, given the uncertainties, we assume similar snow surfaces for all three molecules.

The second piece of evidence for elevated ices in the atmosphere of the disk is the weak absorption of the bending mode of CO_2 at 15 µm in comparison to the stretching mode at 4.3 µm. The intensity of the ice absorption feature correlates with the extent of the disk area impacted by ice absorption. The contribution function (shown in Fig. 7.6) indicates that the majority of the absorption at 4.3 µm originates from a height between $z/r = 0.2 – 0.5$, whereas the absorption at 15 µm is predominantly from regions near the disk midplane ($z/r = 0.1 - 0.15$). The standard model, with a photodesorption limit of $A_V = 1.5$ mag, successfully replicates the 15 µm bending mode but fails to predict the CO_2 stretch mode at 4.3 µm by a factor of two (see Fig. 7.8). By expanding the region of absorption in the disk atmosphere by raising the photodesorption limit, the absorption at 4.3 µm increases significantly more than that at 15 µm, supporting a photodesorption limit at $z/r = 0.6$. Alternatively, increasing the abundance of CO_2 in the model by about an order of magnitude in the $z/r = 0.2 - 0.5$ region, as probed by the 4.3 µm feature, could simultaneously account for both features with the fiducial photodesorption limit of $A_V = 1.5$ mag. This would be consistent with some chemical models (e.g., Drozdovskaya et al. 2016; Arabhavi et al. 2022), but contradicts others (e.g., Ballering et al. 2021).

Finally, the shape of the ice features lends support to the notion of ice being located higher up in the disk because of geometric considerations. Apart from the importance of the extinction coefficient of ices, the refractive index of the ice also significantly influences the shape of the ice absorption features due to anisotropic scattering. In particular, additional absorption or emission wings are observed on either the blue or red side of the strong ice features (see also Dartois et al. 2022). In the NIRSpec observations of HH 48 NE, apparent emission wings are detected on the red side and absorption on the blue side of both the CO_2 and CO features at 4.3 and 4.67 µm, respectively. This is opposite to the distortion observed in background star observations (e.g., Dartois et al. 2022; McClure et al. 2023; Dartois et al. 2024) because of the source structure. For observations of background stars, the continuum is a consequence of direct emission from the star, and photons that scatter off the path on icy grains are not collected. However, for observations of disks viewed edge-on, the continuum is a result of scattered light, implying that photons that scatter from icy grains at a certain angle might be included in the observations. These wings become more prominent when the photons scatter at extreme angles, indicating the presence of ice at higher elevations in the disk (see the sketch in Fig. 7.9). Fig. 7.8 demonstrates that ice at $z/r \sim 0.6$ is required to

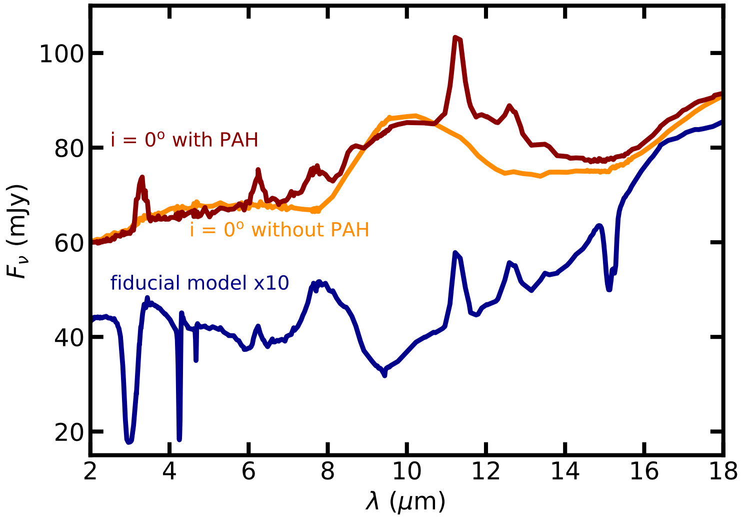

Figure 7.10: Comparison of the fiducial model (blue; $i = 83°$) with face on disk models ($i = 0°$) at similar opacities with (red) and without (orange) PAHs. The PAH emission is predicted to be strong in the face-on case as well, which is contradictory to literature observations of less inclined T Tauri systems.

explain the absorption at 4.18 – 4.21 µm and apparent emission at 4.29 – 4.4 µm.

7.6 Discussion

7.6.1 PAHs in edge-on protoplanetary disks

Protoplanetary disks that are observed face-on typically exhibit minimal or no indication of PAH emission, particularly within T Tauri star systems (see e.g., Geers et al. 2006; Visser et al. 2007; Henning et al. 2024). This absence is commonly understood to suggest a significant depletion of gas-phase PAHs by several orders of magnitude, combined with a lack of UV photons to excite them for stars with a spectral type later than G8 (Geers et al. 2006; Tielens 2008; Geers et al. 2009; Maaskant et al. 2014; Lange et al. 2023b). We find mounting evidence that edge-on systems regularly show strong 8 and 11 µm PAH features (see also the spectrum of Tau 042021 in Arulanantham et al. 2024).

The fact that we see PAH emission in edge-on but not face-on disks suggests a localized origin of this emission. However, our best-fit model of HH 48 NE disk, if oriented face-on, still predicts strong PAH emission which is inconsistent with these previous observations (see Fig. 7.10). The way in which we implemented PAHs in the model is simplistic and did not include stochastic visible/UV excitation, but we expect the resulting differences to be minor (Woitke et al. 2016) and should not affect the conclusion that the PAH emission should be visible in face-on observations if they are equally distributed over the disk. The inferred cavity in the HH 48 NE disk (Sturm et al. 2023e) might enhance the PAH emission due to reduced UV absorption by dust grains, thereby facilitating greater excitation of PAHs (Geers et al. 2009; Maaskant et al. 2014). Additional modeling is required to explain this dichotomy in the observations between the two inclination classes. Resolved observations of PAHs in edge-on and face-on systems would help constrain the properties of PAHs in disks (Lange et al. 2023a).

Bright PAH emission significantly complicates the analysis of ice features, as they dominate the continuum between 6 and 10 µm. Therefore, we limit ourselves to the strongest ice features, and leave a search for the 6.8 µm NH_4^+ feature and potential complex organic molecule signatures at 7.2 and 7.4 µm (see e.g., McClure et al. 2023; Rocha et al. 2024) to a future study.

7.6.2 Ices at high elevation in protoplanetary disks

We have shown using three different observables that at least part of the ice in HH 48 NE is located at a height of up to $z/r = 0.6$. The different methods are illustrated and explained in Fig. 7.9. Our snow surface for the main ice species is well above the photodesorption threshold of $A_V = 1.5$, and is significantly above the thermal desorption threshold for CO. As an additional check for the position of the snow surface, we ran thermochemical DALI models (Bruderer et al. 2012; Bruderer 2013) with the same physical structure and dust opacities as in the RADMC-3D model. This approach takes the full chemistry and molecular UV shielding (e.g. H_2O lines) into account and is therefore a better representation than our simplified approach assuming a photodesorption cut-off based on dust extinction. We used the standard network that is based on the UMIST 06 network (Woodall et al. 2007) to solve for steady-state chemistry. Figure 7.11 presents the location of the snow surface, defined as the place where $X_{\rm ice} = X_{\rm gas}$, for the three main ice species. The snow surface for H_2O and CO_2 in DALI is consistent with our simple parametrization of $A_V = 1.5$ mag, and agrees well in the region between 50 and 100 au which is the dominant region that is probed by our observations (see Fig. 7.6).

We consider two scenarios that could explain why the ices are elevated above a molecule's snow surface. In the first scenario, part of the UV radiation is blocked by a dusty wind which protects the ices in the disk atmosphere (see Fig. 7.9). Both a magnetically driven wind and a photoionized wind (Olofsson et al. 2009; Owen et al. 2011; Panoglou et al. 2012; Booth & Clarke 2021; Pascucci et al. 2023) do have the potential to loft submicrometer-sized grains high into the atmosphere. We do see evidence of H_2 emission above the disk that likely originates in a disk wind, and found that the disk atmosphere is poor in sub-micrometer-sized dust grains, which could be because they are actively transported away from the atmosphere by the wind (Sturm et al. 2023e). Additionally, the system has an inner cavity which is depleted in dust and gas, which could be a result of internal photoevaporation. In the case of a magnetohydrodynamic (MHD) disk wind, models suggest that a high accretion rate of 10^{-7} $M_\odot yr^{-1}$ is necessary to sufficiently block the disk from UV radiation (Panoglou et al. 2012). Unfortunately, we do not have a reliable estimate of the mass accretion rate in the system because of the edge-on nature of the source, which blocks most of the emission coming from the inner disk. However, considering the strong atomic jet and the potential streamer, it is not unlikely that the system is still strongly accreting. It has been proposed before that a dusty disk wind might account for the elevated A_V values observed in a substantial sample of disks using the Ly alpha line, relative to the optical and infrared measurements (McJunkin et al. 2014). Further discussion on the implications and supporting evidence can be found in (Pascucci et al. 2023). If this scenario is true, it would have a significant impact on the interpretation of observations and models of protoplanetary disks, as UV radiation is in many cases a dominant driver of the chemistry (e.g., Bergner et al. 2019, 2021; Calahan et al. 2023) and can excite PAHs (Visser et al. 2007; Geers et al. 2009).

In an alternative scenario, the UV photons penetrate into the disk atmosphere as usual, but efficient mixing recycles the ices at higher altitude (see Fig. 7.9). Chemical modeling including vertical turbulent mixing and diffusion shows that icy grains can reach the observable disk surface in turbulent disks, effectively mixing ices upward faster than they can be photodesorbed in the upper layers (Semenov et al. 2006, 2008; Furuya et al. 2013; Furuya & Aikawa 2014; Woitke et al. 2022). The grain sizes of the icy grains inferred from the H_2O and CO_2 features ($>$1µm; see Dartois et al. 2022 and Sturm et al. 2023c), which are thought to trace mainly the atmosphere of the disk, could be a direct result of mixing ice-rich micrometer-sized dust grains into the upper layers of the disk. If this scenario is the case, we expect to see enhanced effects of UV-driven chemistry in the outer disk as a result of UV reaching a significant fraction of the ices in the disk (Ciesla & Sandford 2012; Woitke et al. 2022), which could be tested with (sub-)millimeter (e.g., ALMA or NOEMA) observations.

Additional analysis on a larger sample of sources is required to constrain which of these scenarios is most likely. Future directions could involve including a better description of photodesorption using the stellar UV field and interstellar radiation field, and including molecular shielding for example by H_2O (Bosman et al. 2022a). Currently, external radiation is disregarded based on the assumption that sufficient residual cloud material shields the disk from such radiation; however, should it exert an influence, it would likely be counterproductive.

7.6.3 Chemical implications

The molecular abundances that we need to include in the model to match the observations are listed in Table 7.1. The retrieved abundances relative to hydrogen are considerably reduced, up to ten times less, when compared to earlier results reported in Sturm et al. (2023c) and Bergner (in prep.). This is a direct result from the elevated snow surface which spreads the ices needed to reproduce the observed line depths over a larger disk volume compared to the fiducial photodesorption limit. The presented abundances are a starting point for comparing observations with chemical models, including surface chemistry and vertical mixing. Our absolute abundances are in general lower than ISM abundances taken from the inheritance model in Ballering et al. (2021), this could be because we trace the ices in the disk atmosphere rather than in the midplane where the bulk of the ices reside. Combining multiple features of the same molecular species would allow us to study the ice composition and abundance in different regions of the disk; however, as shown in Sect. 7.5.2.2 knowing the physical location of the snow surface beforehand is crucial as these properties are degenerate. Comparing the height of the snow surface derived with JWST with high resolution ALMA observations (for example of CO, H_2CO, Podio et al. 2020) could help in this regard, but these are currently not available for this system. If sequestered ice is responsible for the gas-phase molecular depletion of CO and H_2O (see e.g., Krijt et al. 2020; Sturm et al. 2022), then it is located in the midplane, where we cannot trace it with edge-on disk observations.

In Table 7.1 we compare the ice ratios with respect to water in the protoplanetary disk with the background star observations in McClure et al. (2023). The latter observations probe the ices in the molecular cloud stage in absorption against the continuum of a background star. Since the HH 48 NE observations are taken not far from the molecular cloud, the initial conditions of the disk were likely very similar to the background star observations. The overall H_2O/CO_2 column density ratio is consistent with the background star observations, although the individual mixtures have changed (Bergner in prep.). CO appears significantly less abundant in the protoplanetary disk, compared to background star observations. However, it is very likely that the disk observations only probe the CO that is trapped in the CO_2 or H_2O matrix and therefore survives high up in the disk, while the bulk of the CO ice is closer to the midplane where it cannot be probed by edge-on disk observations. CH_4 is tentatively detected at the location of a PAH emission features, which makes the observed optical depth uncertain. Combined with the low binding energy, which indicates that the majority of the ice is located close to the midplane, the observed abundance is unreliable. CH_4 is expected to be abundant in protoplanetary disks due to the active carbon chemistry (Bruderer 2013; Woitke et al. 2016; Krijt et al. 2020; Öberg et al. 2023), which is in line with the observations, but would be an order of magnitude higher than observed in comets and the ISM (see Table 7.1). Both NH_3 and CH_3OH are significantly depleted ($\times 3$ and $>\times 3$, respectively) in the disk with respect to the dark cloud (McClure et al. 2023). Both of these molecules are not efficiently formed in protoplanetary disks, but predicted to be inherited predominantly from the natal cloud (Drozdovskaya et al. 2016; Ballering et al. 2021; Booth et al. 2021). Their low abundance suggests that at least part of the ice is reset and/or processed upon entering the protoplanetary disk. Alternatively, inherited ice ends up mostly in the midplane, and the ice we observe is formed locally in the disk. The low abundance of NH_3 and CH_3OH with respect to water is consistent with the observed abundances in comets. Presumably, comets are formed in the midplane, so in the midplane the CH_3OH abundance should be low as well, and thus favoring some reset. We would like to note, however, that comets trace the history of the protosun which may not have been formed in an environment like HH 48 NE, so one-to-one comparison is non-trivial and will require ice observations in a larger sample of disks around solar-like stars.

7.6.4 Limitations and future outlook

We have shown that we can approximately reproduce the NIRSpec and MIRI spectrum with a relatively simple parameterized model including dust, PAHs, and ices. In this section we will discuss the main observables that can be used to

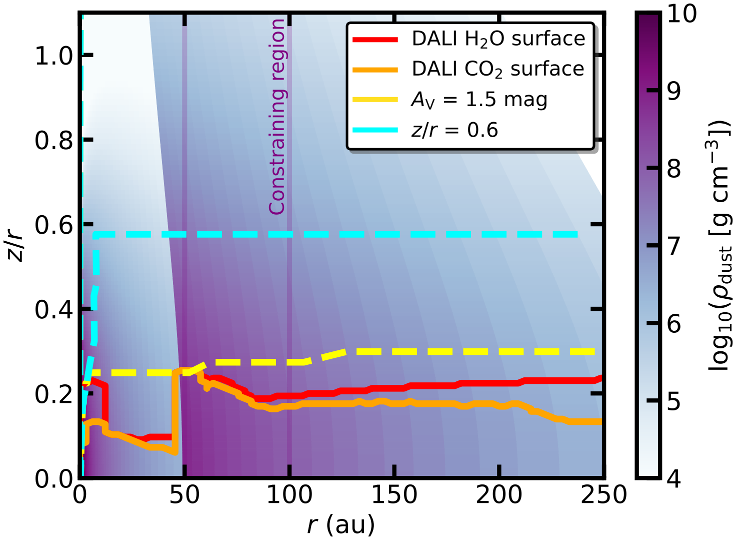

Figure 7.11: The snow surface as modeled with the simplified approach of $A_V = 1.5$ mag (yellow) and the required height (cyan). The other lines indicate the snow surfaces of H_2O (red) and CO_2 (orange) in DALI models with a similar physical structure. The region that is predominantly probed by our ice observations (see Fig. 7.6) is marked with purple lines.

constrain ice properties from the observations and give a future outlook to the possibilities.

7.6.4.1 Ice observables

Due to the complex radiative transfer in edge-on disk observations, constraining properties of the ices is not trivial. Directly using the optical depth of the ice features to derive column densities can lead to errors of several orders of magnitude, which should be avoided (Sturm et al. 2023c). There are a few observables that can be used to compare with models to learn more about the source structure, ice abundance and composition from the ice features.

1. The strength of ice absorption features is related to the size of the absorbing region in the disk and the ice abundance.

2. The vertical distribution of the peak optical depths of the ice can be used to locate ice vertically in the disk. In this work, we have shown that the ices in HH 48 NE are limited vertically by photodesorption, but a similar analysis can be done on thermal snow surfaces if, for example, pure CO ice is detected. Comparing the vertical dependence of the absorption in the 15 µm CO_2 feature with that of the 4.3 µm feature will give additional constraints on the source structure, as this will allow to probe the extent of the absorbing area at this wavelength (see Fig. 7.6).

3. Modeling observations of multiple features from the same species (e.g., H_2O and CO_2) will allow constraining the abundance and composition in different regions in the disk. Moreover, their comparative intensities can serve as a gauge for determining the extent of the area that absorbs.

4. The isotopic ratios (e.g. $^{13}CO_2$, ^{13}CO) with the main isotopologue give information on the level of saturation in the main isotopologue, assuming a $^{12}C/^{13}C$ value. We have shown that our models can explain the strong $^{13}CO_2$ absorption, but other isotopologues were unfortunately not detected. If, for example, ^{13}CO had been detected, this would hint at a small absorbing area with a high abundance of CO instead of being mixed in CO_2 and therefore widespread in the disk.

5. Ice profile shapes can be used to constrain the chemical environment of the ice which is done in a separate paper (Bergner in prep.). Combining multiple features can give insights into the vertical segregation of ice mixtures. This is only possible with high spectral resolution mid infrared instruments like MIRI.

6. We have shown that scattering wings can be used to put constraints on the source structure and the scale height of the ice, taking the geometry of the system into account. Additionally, these features can be used to constrain the grain size distribution (cf. Dartois et al. 2022, 2024).

In the end, a combination of these observables will result in the best constrained source structure in the model and the best constraints on ice properties.

7.6.4.2 Future prospects

In this study, we have demonstrated the feasibility of fitting JWST observations using a relatively straightforward approach. All relevant observables discussed in Sect.7.6.4.1 are simultaneously matched in the model. Expanding the sample size is the next logical step to compare our results for HH 48 NE with other disks; currently, only this particular source has been thoroughly examined, and it may be an outlier due to its proximity to the companion HH 48 SW. The methodology employed presents a practical means to model a broader array of disks and gather data on the composition and distribution of ice in protoplanetary disks. If other sources validate that the observed ices share a similar snowsurface as a result of photodesorption and ice mixtures, a reasonable simplification in the fitting process is a model featuring only three dust populations: small dust particles without ice, small dust particles with ice, and large dust particles with ice. This streamlines computational efforts significantly and allows for further adjustments or the inclusion of ices in MCMC or χ^2 fitting.

One drawback of using edge-on disks to investigate ices is that it does not capture the bulk of the ice mass in the disk midplane, but rather focuses on regions in the disk's atmosphere (see Fig. 7.6). Disks with lower masses have the potential to reveal a higher proportion of their ice content, with features being less likely to be saturated. Nevertheless, observed edge-on disks typically possess substantial mass by nature (Angelo et al. 2023), which complicates the analysis of ices.

If it is indeed the case that the contrast of the PAHs in the disk is intensified due to the high inclination of this source, identifying subtle features will prove to be quite challenging. A more sophisticated incorporation of PAHs, including quantum heating, is essential to make any assertions regarding their abundance and distribution within the disk. Furthermore, future endeavors should focus on comparing the results with ALMA data to differentiate between various scenarios. The scarcity of high-resolution ALMA observations of molecules in edge-on disks necessitates further exploration to impose additional constraints on the physical disk structure and chemistry.

7.7 Conclusion

We presented new JWST/MIRI data to complete the ice inventory of the edge-on protoplanetary disk HH 48 NE. Radiative transfer models are fitted to the data to constrain abundances and the regions that are probed with the observations. We therefore conclude the following.

- Edge-on disks are promising laboratories for studying ices in protoplanetary disks, as we find clear evidence for various newly-detected disk ice features including CO_2, NH_3 and tentatively CH_4. JWST spectra can be fitted well with 3D radiative transfer models using a relatively simple setup, which enables detailed analysis of their abundance and physical location in the disk.

- Ices are located unexpectedly high up in the disk, up to $z/r \sim 0.6$ and $A_V \sim 0.1$. This result is determined based on the vertical dependence of the absorption, the ratio of the 4.3 and 15 µm CO_2 features, and the scattering wings of the 4.3 µm feature. We suggest two possible scenarios: (1) Entrained dust in a disk wind is blocking the stellar UV radiation, so ice may survive higher up in the disk, but this would have strong implications for the gas-phase chemistry as well. (2) Alternatively, the icy material is efficiently elevated in the disk by vertical mixing, continuously replenishing the ice reservoir in the upper disk atmosphere.

- JWST NIRSpec probes the ices in a higher layer in the disk than MIRI due to a change in scattering properties and the origin of the continuum. This complicates the analysis since the abundance and mixture of ices may change spatially in the disk, but with sufficient wavelength coverage, we can study multiple disk regions simultaneously.

- The absence of a methanol feature and the faint NH_3 feature indicates that some of the ice from the original cloud is destroyed during earlier phases, reset upon entering the protoplanetary disk or remains concealed in the optically thick midplane.

- The PAH emission contrast to the continuum is strong in HH 48 NE, but is extincted by the disk, which implies that it must be localized to the disk itself. Current models cannot explain why the contrast in edge-on systems is so much different than in less inclined systems. This suggests that PAHs can be more abundant than previously thought, but only in specific regions in the disk probed by these observations. The spectrum of PAH emission bands hinders the analysis of ice features due to its strong, widespread impact on the continuum location.

JWST provides a unique opportunity to study ices and PAHs in protoplanetary disks in unprecedented detail. Full NIRSpec and MIRI coverage is required to understand and constrain the full ice inventory in protoplanetary disks. The application of the analysis presented here to additional protoplanetary disks will allow a more global understanding of the composition and distribution of ices in these regions, which is important in the context of the evolution of planetary systems.

7.8 Acknowledgments

Astrochemistry in Leiden is supported by the Netherlands Research School for Astronomy (NOVA), by funding from the European Research Council (ERC) under the European Union's Horizon 2020 research and innovation programme (grant agreement No. 101019751 MOLDISK). M.K.M. acknowledges financial support from the Dutch Research Council (NWO; grant VI.Veni.192.241). Support for C.J.L. was provided by NASA through the NASA Hubble Fellowship grant No. HST-HF2-51535.001-A awarded by the Space Telescope Science Institute, which is operated by the Association of Universities for Research in Astronomy, Inc., for NASA, under contract NAS5-26555. D.H. is supported by Center for Informatics and Computation in Astronomy (CICA) grant and grant number 110J0353I9 from the Ministry of Education of Taiwan. D.H. acknowledges support from the National Technology and Science Council of Taiwan through grant number 111B3005191. E.D. and J.A.N. acknowledge support from French Programme National 'Physique et Chimie du Milieu Interstellaire' (PCMI) of the CNRS/INSU with the INC/INP, co-funded by the CEA and the CNES. M.N.D. acknowledges the Holcim Foundation Stipend. Part of this research was carried out at the Jet Propulsion Laboratory, California Institute of Technology, under a contract with the National Aeronautics and Space Administration (80NM0018D0004). S.I. and E.F.vD. acknowledge support from the Danish National Research Foundation through the Center of Excellence "InterCat" (Grant agreement no.: DNRF150). M.A.C. was funded by NASA's Fundamental Laboratory Research work package and NSF grant AST-2009253.

Appendix

7.A Streamer

The H_2 emission shows, apart from the disk winds in both systems, an additional emission component to the North-West that is not correlating with the orientation of any of the sources' outflow. A comparison with the Moment 0 map of the CO $J = 2 - 1$ emission presented in Sturm et al. (2023e) shows that it is co-located with a asymmetric piece of redshifted CO emission, indicating that it is most likely an infalling stream of material falling on HH 48 NE. Unfortunately, the tail of HH 48 SW to the South-West is not observed because of the smaller MIRI field of view.

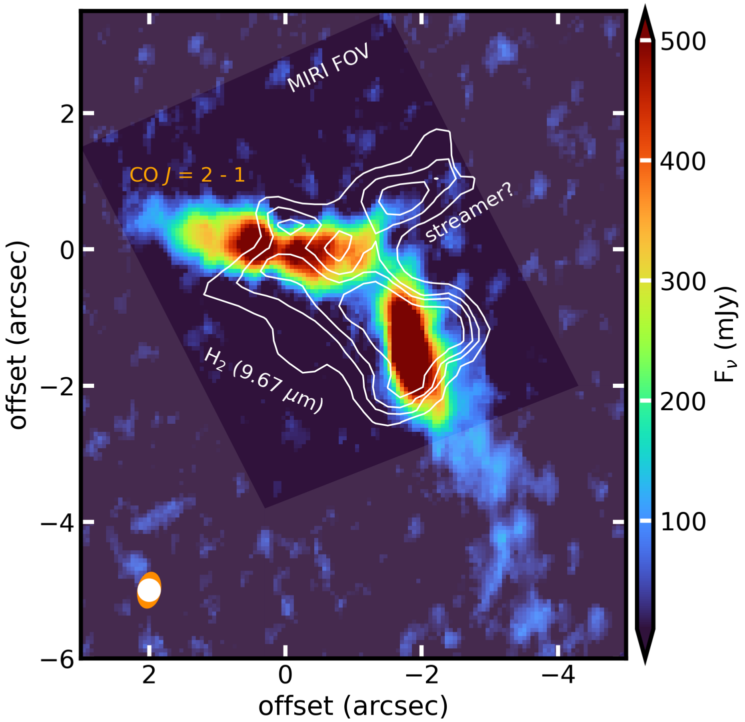

Figure 7.A.1: Overview of the asymmetric emission in the HH 48 system. The colored image shows the integrated CO $J = 2 - 1$ emission map of HH 48 NE (Sturm et al. 2023e). The contours indicate the spatial extent of the low energy H_2 emission line at 9.67 µm. The ALMA beam (orange) and MIRI PSF size at 9.7 µm (white) are shown in the bottom right.

7.B Spectral extraction

The source integrated spectrum is extracted using a conical extraction, increasing the mask with wavelength according to the resolution, to get as much S/N on the spectrum as possible. To avoid contamination from the binary component, we used the mask of the primary source, HH 48 SW, as a negative mask on the mask for HH 48 NE (see Fig. 7.B.1).

7.C Model improvements

The current best-fitting model agrees well with the observed spectrum, with most discrepancies being less than 20%. This is an improvement over the model constrained pre-JWST (see Fig. 7.B.2,7.4 for a comparison). There are a few instances

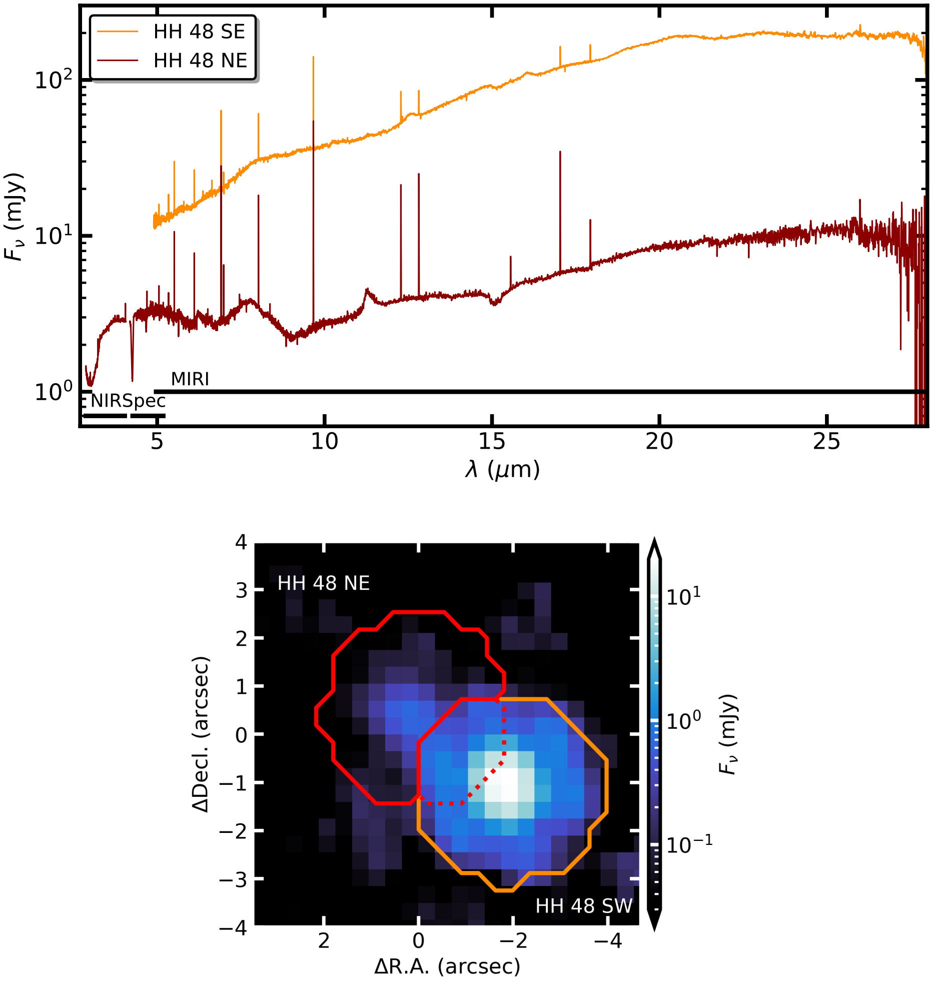

Figure 7.B.1: Left: The integrated spectrum of HH 48 NE (red) and HH 48 SW (orange). NIRSpec data of HH 48 SW are not available as a result of the smaller field of view of the NIRSpec instrument compared to MIRI. Right: Continuum image of the HH 48 system at 24 µm with the masks used to extract the source integrated spectrum shown on the left.

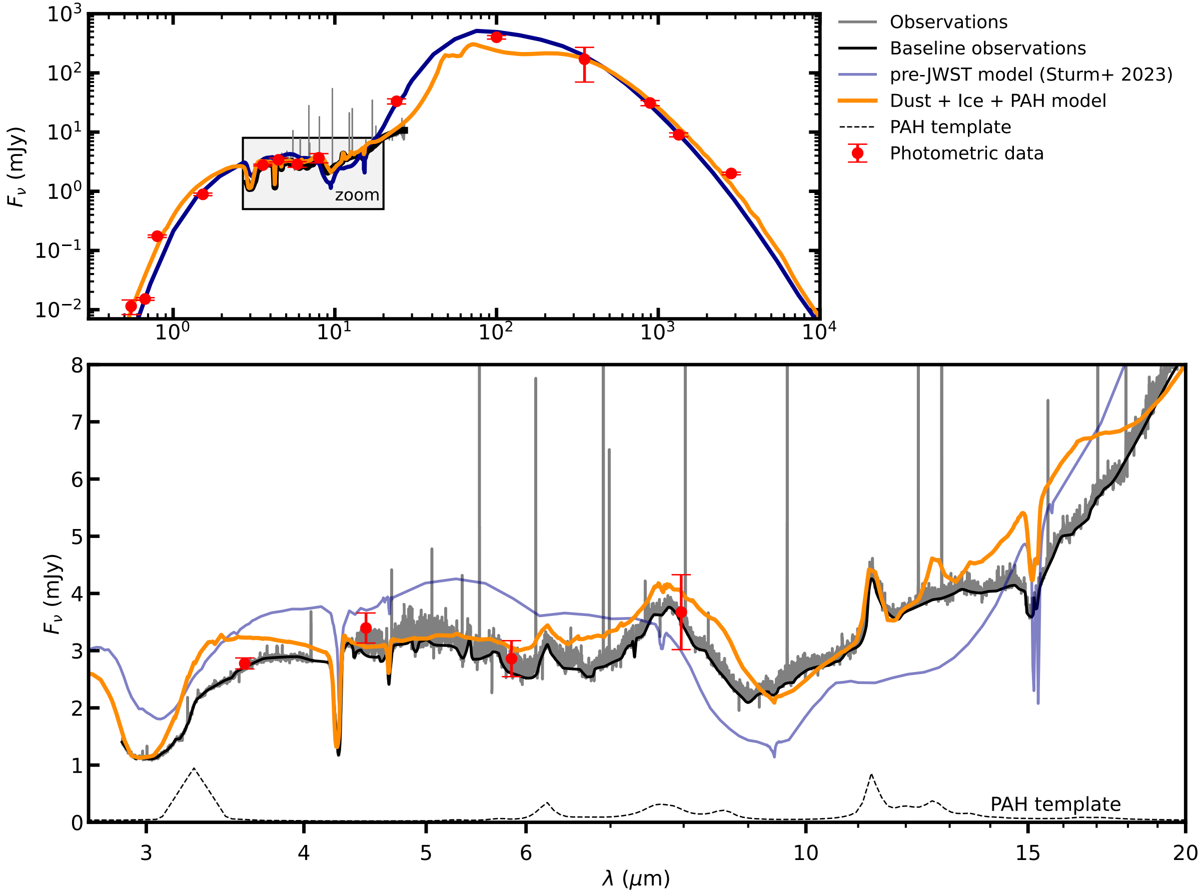

Figure 7.B.2: Same as Fig. 7.3 but with a comparison between the best fitting model and the pre-JWST model published in Sturm et al. (2023d)

where the model overestimates the flux (by less than 50%), particularly in the red wing of the water band at 3 µm. This overestimation could be due to an absorption component from ammonia hydrates ($NH_3 \cdot H_2O$) around 3.5 µm, which is not accounted for in the model. The scattering wing in emission on the red side of the feature resembles the CO_2 feature, further exacerbating the difference. The regions around the silicate features (8 – 9 µm and 13 – 18 µm) are overestimated by 50%, possibly due to the source structure and the dust scattering characteristics in the system. The disk's edge-on orientation suggests that the silicate features may have a scattered emission component from the warm inner disk and an absorption component from the cold outer disk. The ratio of these components is highly sensitive to the source structure, and they may not necessarily reflect similar grain compositions. The observations extending beyond the model's spatial extent suggest that the model's continuum source is mainly direct dust emission rather than scattered emission, indicating a need for a higher placement of the scattering surface. An analysis using a two-component Gaussian fit to the radial profile of the continuum emission reveals a discrepancy in the ratio of scattering to direct emission between the models (1:10) and the observations (1:2). While boosting scattering at these wavelengths is not straightforward, it likely involves a combination of source structure and grain composition. Investigating the inclusion of a third dust population with micron-sized grains in future studies could offer potential benefits. Maintaining a constant grain composition helps constrain the number of free parameters and speed up model computation. Future models and JWST observations are expected to provide new insights into grain composition around silicate features, which can be leveraged to improve the model accuracy in the future.

Improvements can also be made by incorporating foreground cloud absorption in the modeling process. While the current model spectrum is scaled with the extinction curve based on A_V, potential ice absorption in an envelope or foreground cloud is not considered. In particular models of younger sources may need to account for this. Uncertainties exist regarding the distribution of ices over dust grains, which can significantly influence measured abundances. The assumed system-averaged gas-to-dust ratio of 100 is consistent with most observations. Molecular abundances relative to hydrogen are integrated into the dust grains without altering the total mass in the region, effectively assuming an effective gas-to-solids ratio instead of a gas-to-dust ratio. Changes in the mass distribution can alter the physical structure and continuum significantly. Therefore, discussing ice-to-rock ratios in relevant disk regions is recommended over abundances when comparing with other systems due to the lack of precise constraints on the vertical gas distribution.

Bibliography

Aikawa, Y. & Herbst, E. 1999, A&A, 351, 233

Aikawa, Y., Kamuro, D., Sakon, I., et al. 2012, A&A, 538, A57

Alarcón, F., Teague, R., Zhang, K., Bergin, E. A., & Barraza-Alfaro, M. 2020, ApJ, 905, 68

Anderson, D. E., Blake, G. A., Bergin, E. A., et al. 2019, ApJ, 881, 127

Anderson, D. E., Cleeves, L. I., Blake, G. A., et al. 2022, ApJ, 927, 229

Andrews, S. M., Huang, J., Pérez, L. M., et al. 2018a, ApJ, 869, L41

Andrews, S. M., Rosenfeld, K. A., Kraus, A. L., & Wilner, D. J. 2013, ApJ, 771, 129

Andrews, S. M., Terrell, M., Tripathi, A., et al. 2018b, ApJ, 865, 157

Andrews, S. M., Wilner, D. J., Espaillat, C., et al. 2011, ApJ, 732, 42

Andrews, S. M., Wilner, D. J., Zhu, Z., et al. 2016, ApJ, 820, L40

Angelo, I., Duchene, G., Stapelfeldt, K., et al. 2023, ApJ, 945, 130

Ansdell, M., Williams, J. P., Trapman, L., et al. 2018, ApJ, 859, 21

Ansdell, M., Williams, J. P., van der Marel, N., et al. 2016, ApJ, 828, 46

Anthonioz, F., Ménard, F., Pinte, C., et al. 2015, A&A, 574, A41

Arabhavi, A. M., Woitke, P., Cazaux, S. M., et al. 2022, A&A, 666, A139

Argyriou, I., Glasse, A., Law, D. R., et al. 2023, A&A, 675, A111

Arulanantham, N., McClure, M. K., Pontoppidan, K., et al. 2024, arXiv e-prints, arXiv:2402.12256

Asplund, M., Grevesse, N., Sauval, A. J., & Scott, P. 2009, ARA&A, 47, 481

Astropy Collaboration, Price-Whelan, A. M., Sipőcz, B. M., et al. 2018, AJ, 156, 123

Astropy Collaboration, Robitaille, T. P., Tollerud, E. J., et al. 2013, A&A, 558, A33

Bai, X.-N. & Stone, J. M. 2010, ApJ, 722, L220

Bailer-Jones, C. A. L., Rybizki, J., Fouesneau, M., Mantelet, G., & Andrae, R. 2018, AJ, 156, 58

Ballering, N. P., Cleeves, L. I., & Anderson, D. E. 2021, ApJ, 920, 115

Bally, J. 2016, ARA&A, 54, 491

Banzatti, A., Pascucci, I., Bosman, A. D., et al. 2020, ApJ, 903, 124

Banzatti, A. & Pontoppidan, K. M. 2015, ApJ, 809, 167

Banzatti, A., Pontoppidan, K. M., Carr, J. S., et al. 2023, ApJ, 957, L22

Baraffe, I., Chabrier, G., Allard, F., & Hauschildt, P. H. 1998, A&A, 337, 403

Baratta, G. A., Accolla, M., Chaput, D., et al. 2019, Astrobiology, 19, 1018

Barnard, E. E. 1919, ApJ, 49, 1

Barranco, J. A., Pei, S., & Marcus, P. S. 2018, ApJ, 869, 127

Benisty, M., Dominik, C., Follette, K., et al. 2022, arXiv e-prints, arXiv:2203.09991

Bergin, E. A., Blake, G. A., Ciesla, F., Hirschmann, M. M., & Li, J. 2015, Proceedings of the National Academy of Science, 112, 8965

Bergin, E. A., Cleeves, L. I., Crockett, N., & Blake, G. A. 2014, Faraday Discussions, 168, 61

Bergin, E. A., Cleeves, L. I., Gorti, U., et al. 2013, Nature, 493, 644

Bergin, E. A., Du, F., Cleeves, L. I., et al. 2016, ApJ, 831, 101

Bergin, E. A., Hogerheijde, M. R., Brinch, C., et al. 2010, A&A, 521, L33

Bergner. in prep.

Bergner, J. B., Öberg, K. I., Bergin, E. A., et al. 2020, ApJ, 898, 97

Bergner, J. B., Öberg, K. I., Bergin, E. A., et al. 2019, ApJ, 876, 25

Bergner, J. B., Öberg, K. I., Guzmán, V. V., et al. 2021, ApJS, 257, 11

Birnstiel, T., Fang, M., & Johansen, A. 2016, Space Sci. Rev., 205, 41

Birnstiel, T., Ormel, C. W., & Dullemond, C. P. 2011, A&A, 525, A11

Bisschop, S. E., Fraser, H. J., Öberg, K. I., van Dishoeck, E. F., & Schlemmer, S. 2006, A&A, 449, 1297

Bisschop, S. E., Fuchs, G. W., van Dishoeck, E. F., & Linnartz, H. 2007, A&A, 474, 1061

Blum, J. 2018, Space Sci. Rev., 214, 52

Boersma, C., Mattioda, A. L., Bauschlicher, C. W., J., et al. 2009, ApJ, 690, 1208

Boogert, A. C. A., Brewer, K., Brittain, A., & Emerson, K. S. 2022, ApJ, 941, 32

Boogert, A. C. A., Ehrenfreund, P., Gerakines, P. A., et al. 2000, A&A, 353, 349

Boogert, A. C. A., Gerakines, P. A., & Whittet, D. C. B. 2015, ARA&A, 53, 541

Boogert, A. C. A., Pontoppidan, K. M., Knez, C., et al. 2008, ApJ, 678, 985

Booth, A. S. & Ilee, J. D. 2020, MNRAS, 493, L108

Booth, A. S., Walsh, C., Ilee, J. D., et al. 2019, ApJ, 882, L31

Booth, A. S., Walsh, C., Terwisscha van Scheltinga, J., et al. 2021, Nature Astronomy, 5, 684

Booth, R. A. & Clarke, C. J. 2021, MNRAS, 502, 1569

Booth, R. A., Clarke, C. J., Madhusudhan, N., & Ilee, J. D. 2017, MNRAS, 469, 3994

Bosman, A. D., Alarcón, F., Bergin, E. A., et al. 2021a, ApJS, 257, 7

Bosman, A. D., Alarcón, F., Zhang, K., & Bergin, E. A. 2021b, ApJ, 910, 3

Bosman, A. D. & Banzatti, A. 2019, A&A, 632, L10

Bosman, A. D., Bergin, E. A., Calahan, J., & Duval, S. E. 2022a, ApJ, 930, L26

Bosman, A. D., Bergin, E. A., Loomis, R. A., et al. 2021c, ApJS, 257, 15

Bosman, A. D., Bruderer, S., & van Dishoeck, E. F. 2017, A&A, 601, A36

Bosman, A. D., Trapman, L., Sturm, A., et al. 2022b, Research Notes of the American Astronomical Society, 6, 176

Bosman, A. D., Walsh, C., & van Dishoeck, E. F. 2018, A&A, 618, A182

Boutéraon, T., Habart, E., Ysard, N., et al. 2019, A&A, 623, A135

Brooke, T. Y., Sellgren, K., & Geballe, T. R. 1999, ApJ, 517, 883

Brooke, T. Y., Sellgren, K., & Smith, R. G. 1996, ApJ, 459, 209

Brown, J. M., Pontoppidan, K. M., van Dishoeck, E. F., et al. 2013, ApJ, 770, 94

Bruderer, S. 2013, A&A, 559, A46

Bruderer, S., van der Marel, N., van Dishoeck, E. F., & van Kempen, T. A. 2014, A&A, 562, A26

Bruderer, S., van Dishoeck, E. F., Doty, S. D., & Herczeg, G. J. 2012, A&A, 541, A91

Bruggeman, D. A. G. 1935, Annalen der Physik, 416, 636

Brunken, N. G. C., Rocha, W. R. M., van Dishoeck, E. F., et al. 2024, A&A, 685, A27

Bushouse, H., Eisenhamer, J., Dencheva, N., et al. 2023, JWST Calibration Pipeline

Calahan, J. K., Bergin, E., Zhang, K., et al. 2021, ApJ, 908, 8

Calahan, J. K., Bergin, E. A., Bosman, A. D., et al. 2023, Nature Astronomy, 7, 49

Calvet, N. & Gullbring, E. 1998, ApJ, 509, 802

Cardelli, J. A., Clayton, G. C., & Mathis, J. S. 1989, ApJ, 345, 245

Cardelli, J. A., Meyer, D. M., Jura, M., & Savage, B. D. 1996, ApJ, 467, 334

Cazzoletti, P., van Dishoeck, E. F., Visser, R., Facchini, S., & Bruderer, S. 2018, A&A, 609, A93

Chambers, J. E. 2009, ApJ, 705, 1206

Chapillon, E., Guilloteau, S., Dutrey, A., & Piétu, V. 2008, A&A, 488, 565

Charnley, S. B., Tielens, A. G. G. M., & Millar, T. J. 1992, ApJ, 399, L71

Chevance, M., Krumholz, M. R., McLeod, A. F., et al. 2023, in Astronomical Society of the Pacific Conference Series, Vol. 534, Protostars and Planets VII, ed. S. Inutsuka, Y. Aikawa, T. Muto, K. Tomida, & M. Tamura, 1

Chiang, E. I., Joung, M. K., Creech-Eakman, M. J., et al. 2001, ApJ, 547, 1077

Ciesla, F. J. & Sandford, S. A. 2012, Science, 336, 452

Cieza, L. A., Casassus, S., Tobin, J., et al. 2016, Nature, 535, 258

Cleeves, L. I., Bergin, E. A., Öberg, K. I., et al. 2017, ApJ, 843, L3

Cleeves, L. I., Öberg, K. I., Wilner, D. J., et al. 2018, ApJ, 865, 155

Collings, M. P., Dever, J. W., Fraser, H. J., McCoustra, M. R. S., & Williams, D. A. 2003, ApJ, 583, 1058

Coutens, A., Loison, J. C., Boulanger, A., et al. 2022, A&A, 660, L6

Cridland, A. J., Facchini, S., van Dishoeck, E. F., & Benisty, M. 2023, A&A, 674, A211

Cuppen, H. M., van Dishoeck, E. F., Herbst, E., & Tielens, A. G. G. M. 2009, A&A, 508, 275

Cuppen, H. M., Walsh, C., Lamberts, T., et al. 2017, Space Sci. Rev., 212, 1

Currie, T., Marois, C., Cieza, L., et al. 2019, ApJ, 877, L3

D'Alessio, P., Calvet, N., Hartmann, L., Franco-Hernández, R., & Servín, H. 2006, ApJ, 638, 314

Dartois, E. 2010, Molecular Physics, 108, 2273

Dartois, E. 2021, MNRAS, 504, 4369

Dartois, E. & d'Hendecourt, L. 2001, A&A, 365, 144

Dartois, E., d'Hendecourt, L., Thi, W., Pontoppidan, K. M., & van Dishoeck, E. F. 2002, A&A, 394, 1057

Dartois, E., Noble, J. A., Caselli, P., et al. 2024, Nature Astronomy

Dartois, E., Noble, J. A., Ysard, N., Demyk, K., & Chabot, M. 2022, A&A, 666, A153

Dominik, C., Ceccarelli, C., Hollenbach, D., & Kaufman, M. 2005, ApJ, 635, L85

Dominik, C., Min, M., & Tazaki, R. 2021, OpTool: Command-line driven tool for creating complex dust opacities, Astrophysics Source Code Library, record ascl:2104.010

Draine, B. T. 2003, ARA&A, 41, 241

Draine, B. T. & Lee, H. M. 1984, ApJ, 285, 89

Draine, B. T. & Li, A. 2007, ApJ, 657, 810

Drążkowska, J., Alibert, Y., & Moore, B. 2016, A&A, 594, A105

Drążkowska, J., Bitsch, B., Lambrechts, M., et al. 2023, in Astronomical Society of the Pacific Conference Series, Vol. 534, Protostars and Planets VII, ed. S. Inutsuka, Y. Aikawa, T. Muto, K. Tomida, & M. Tamura, 717

Drozdovskaya, M. N., Walsh, C., van Dishoeck, E. F., et al. 2016, MNRAS, 462, 977

Du, F., Bergin, E. A., Hogerheijde, M., et al. 2017, ApJ, 842, 98

Dullemond, C. P. & Dominik, C. 2004, A&A, 421, 1075

Dullemond, C. P., Dominik, C., & Natta, A. 2001, ApJ, 560, 957

Dullemond, C. P., Juhasz, A., Pohl, A., et al. 2012, RADMC-3D: A multi-purpose radiative transfer tool, Astrophysics Source Code Library, record ascl:1202.015

Dunham, M. M., Offner, S. S. R., Pineda, J. E., et al. 2016, ApJ, 823, 160

Dutrey, A., Guilloteau, S., Piétu, V., et al. 2017, A&A, 607, A130

Dutrey, A., Guilloteau, S., & Simon, M. 2003, A&A, 402, 1003

Earl, D. J. & Deem, M. W. 2005, Physical Chemistry Chemical Physics (Incorporating Faraday Transactions), 7, 3910

Ehrenfreund, P., Boogert, A. C. A., Gerakines, P. A., Tielens, A. G. G. M., & van Dishoeck, E. F. 1997, A&A, 328, 649

Eisner, J. A., Hillenbrand, L. A., & Stone, J. M. 2014, MNRAS, 443, 1916

Eistrup, C., Walsh, C., & van Dishoeck, E. F. 2016, A&A, 595, A83

Eistrup, C., Walsh, C., & van Dishoeck, E. F. 2018, A&A, 613, A14

Endres, C. P., Schlemmer, S., Schilke, P., Stutzki, J., & Müller, H. S. P. 2016, Journal of Molecular Spectroscopy, 327, 95

Ercolano, B. & Pascucci, I. 2017, Royal Society Open Science, 4, 170114

Espaillat, C., D'Alessio, P., Hernández, J., et al. 2010, ApJ, 717, 441

Espaillat, C. C., Macías, E., Hernández, J., & Robinson, C. 2019, ApJ, 877, L34

Facchini, S., Benisty, M., Bae, J., et al. 2020, A&A, 639, A121

Facchini, S., Birnstiel, T., Bruderer, S., & van Dishoeck, E. F. 2017, A&A, 605, A16

Facchini, S., Pinilla, P., van Dishoeck, E. F., & de Juan Ovelar, M. 2018, A&A, 612, A104

Favre, C., Cleeves, L. I., Bergin, E. A., Qi, C., & Blake, G. A. 2013, ApJ, 776, L38

Fayolle, E. C., Öberg, K. I., Cuppen, H. M., Visser, R., & Linnartz, H. 2011, A&A, 529, A74

Fedoseev, G., Chuang, K. J., Ioppolo, S., et al. 2017, ApJ, 842, 52

Fernández-López, M., Zapata, L. A., Rodríguez, L. F., et al. 2020, AJ, 159, 171

Ferrante, R. F., Moore, M. H., Spiliotis, M. M., & Hudson, R. L. 2008, ApJ, 684, 1210

Flaherty, K., Hughes, A. M., Simon, J. B., et al. 2020, ApJ, 895, 109

Flores, C., Duchêne, G., Wolff, S., et al. 2021, AJ, 161, 239

Foreman-Mackey, D., Hogg, D. W., Lang, D., & Goodman, J. 2013, PASP, 125, 306

Francis, L. & van der Marel, N. 2020, ApJ, 892, 111

Fung, J. & Chiang, E. 2016, ApJ, 832, 105

Furlan, E., Luhman, K. L., Espaillat, C., et al. 2011, ApJS, 195, 3

Furuya, K. & Aikawa, Y. 2014, ApJ, 790, 97

Furuya, K., Aikawa, Y., Nomura, H., Hersant, F., & Wakelam, V. 2013, ApJ, 779, 11

Gaia Collaboration, Brown, A. G. A., Vallenari, A., et al. 2021, A&A, 649, A1

Gaia Collaboration, Prusti, T., de Bruijne, J. H. J., et al. 2016, A&A, 595, A1

Galli, P. A. B., Bouy, H., Olivares, J., et al. 2021, A&A, 646, A46

Garozzo, M., Fulvio, D., Kanuchova, Z., Palumbo, M. E., & Strazzulla, G. 2010, A&A, 509, A67

Geers, V. C., Augereau, J. C., Pontoppidan, K. M., et al. 2006, A&A, 459, 545

Geers, V. C., van Dishoeck, E. F., Pontoppidan, K. M., et al. 2009, A&A, 495, 837

Geers, V. C., van Dishoeck, E. F., Visser, R., et al. 2007, A&A, 476, 279

Gerakines, P. A. & Hudson, R. L. 2015, ApJ, 808, L40

Gerakines, P. A. & Hudson, R. L. 2020, ApJ, 901, 52

Gerakines, P. A., Schutte, W. A., Greenberg, J. M., & van Dishoeck, E. F. 1995, A&A, 296, 810

Goldreich, P. & Tremaine, S. 1979, ApJ, 233, 857

Goldreich, P. & Tremaine, S. 1980, ApJ, 241, 425

Grant, S. L., van Dishoeck, E. F., Tabone, B., et al. 2023, ApJ, 947, L6

GRAVITY Collaboration, Eupen, F., Labadie, L., et al. 2021, A&A, 648, A37

Grim, R. J. A. & Greenberg, J. M. 1987, ApJ, 321, L91

Grudić, M. Y., Guszejnov, D., Offner, S. S. R., et al. 2022, MNRAS, 512, 216

Guillet, V., Jones, A. P., & Pineau Des Forêts, G. 2009, A&A, 497, 145

Guilloteau, S., Bachiller, R., Fuente, A., & Lucas, R. 1992, A&A, 265, L49

Guilloteau, S., Di Folco, E., Dutrey, A., et al. 2013, A&A, 549, A92

Guilloteau, S., Piétu, V., Chapillon, E., et al. 2016, A&A, 586, L1

Habart, E., Natta, A., Testi, L., & Carbillet, M. 2006, A&A, 449, 1067

Hacar, A., Clark, S. E., Heitsch, F., et al. 2023, in Astronomical Society of the Pacific Conference Series, Vol. 534, Protostars and Planets VII, ed. S. Inutsuka, Y. Aikawa, T. Muto, K. Tomida, & M. Tamura, 153

Hacar, A., Tafalla, M., Kauffmann, J., & Kovács, A. 2013, A&A, 554, A55

Harsono, D., Jørgensen, J. K., van Dishoeck, E. F., et al. 2014, A&A, 562, A77

Hartmann, L., Herczeg, G., & Calvet, N. 2016, ARA&A, 54, 135

Hasegawa, T. I., Herbst, E., & Leung, C. M. 1992, ApJS, 82, 167

Hendler, N., Pascucci, I., Pinilla, P., et al. 2020, ApJ, 895, 126

Henning, T., Kamp, I., Samland, M., et al. 2024, arXiv e-prints, arXiv:2403.09210

Henning, T. & Semenov, D. 2013, Chemical Reviews, 113, 9016

Herbst, E. & van Dishoeck, E. F. 2009, ARA&A, 47, 427

Herczeg, G. J., Brown, J. M., van Dishoeck, E. F., & Pontoppidan, K. M. 2011, A&A, 533, A112

Hildebrand, R. H. 1983, QJRAS, 24, 267

Hincelin, U., Wakelam, V., Commerçon, B., Hersant, F., & Guilloteau, S. 2013, ApJ, 775, 44

Hogerheijde, M. R., Bergin, E. A., Brinch, C., et al. 2011, Science, 334, 338

Hollenbach, D., Kaufman, M. J., Bergin, E. A., & Melnick, G. J. 2009, ApJ, 690, 1497

Hollenbach, D. J. & Tielens, A. G. G. M. 1999, Rev. Mod. Phys., 71, 173

Honda, M., Inoue, A. K., Fukagawa, M., et al. 2009, ApJ, 690, L110

Honda, M., Kudo, T., Takatsuki, S., et al. 2016, ApJ, 821, 2

Hudson, R. L., Gerakines, P. A., & Yarnall, Y. Y. 2022, ApJ, 925, 156

Hudson, R. L., Moore, M. H., & Gerakines, P. A. 2001, ApJ, 550, 1140

Hunter, J. D. 2007, Computing in Science & Engineering, 9, 90

Ilee, J. D., Walsh, C., Booth, A. S., et al. 2021, ApJS, 257, 9

Ioppolo, S., Noble, J. A., Traspas Muiña, A., et al. 2022, Journal of Molecular Spectroscopy, 385, 111601

Ioppolo, S., Sangiorgio, I., Baratta, G. A., & Palumbo, M. E. 2013, A&A, 554, A34

Ioppolo, S., van Boheemen, Y., Cuppen, H. M., van Dishoeck, E. F., & Linnartz, H. 2011, MNRAS, 413, 2281

Isella, A., Pérez, L. M., & Carpenter, J. M. 2012, ApJ, 747, 136

Jakobsen, P., Ferruit, P., Alves de Oliveira, C., et al. 2022a, A&A, 661, A80

Jakobsen, P., Ferruit, P., Alves de Oliveira, C., et al. 2022b, A&A, 661, A80

Jeans, J. H. 1902, Philosophical Transactions of the Royal Society of London Series A, 199, 1

Jeans, J. H. 1919, MNRAS, 79, 408

Jin, S., Isella, A., Huang, P., et al. 2019, ApJ, 881, 108

Johansen, A. & Lambrechts, M. 2017, Annual Review of Earth and Planetary Sciences, 45, 359

Johansen, A., Ronnet, T., Bizzarro, M., et al. 2021, Science Advances, 7, eabc0444

Kaeufer, T., Woitke, P., Min, M., Kamp, I., & Pinte, C. 2023, arXiv e-prints, arXiv:2302.04629

Kama, M., Bruderer, S., Carney, M., et al. 2016a, A&A, 588, A108

Kama, M., Bruderer, S., van Dishoeck, E. F., et al. 2016b, A&A, 592, A83

Kama, M., Folsom, C. P., & Pinilla, P. 2015, A&A, 582, L10

Kama, M., Trapman, L., Fedele, D., et al. 2020, A&A, 634, A88

Kamp, I. 2011, in EAS Publications Series, Vol. 46, EAS Publications Series, ed. C. Joblin & A. G. G. M. Tielens, 271–283

Kamp, I., Scheepstra, A., Min, M., Klarmann, L., & Riviere-Marichalar, P. 2018, A&A, 617, A1

Kanagawa, K. D., Hashimoto, J., Muto, T., et al. 2021, ApJ, 909, 212

Kanwar, J., Kamp, I., Woitke, P., et al. 2024, A&A, 681, A22

Keane, J. V., Tielens, A. G. G. M., Boogert, A. C. A., Schutte, W. A., & Whittet, D. C. B. 2001, A&A, 376, 254

Kenyon, S. J. & Hartmann, L. 1995, ApJS, 101, 117

Kim, H. J., Evans, Neal J., I., Dunham, M. M., Lee, J.-E., & Pontoppidan, K. M. 2012, ApJ, 758, 38

Kokoulina, E., Matter, A., Lopez, B., et al. 2021, A&A, 652, A61

Kratter, K. & Lodato, G. 2016, ARA&A, 54, 271

Kraus, A. L. & Ireland, M. J. 2012, ApJ, 745, 5

Kraus, S., Hofmann, K. H., Benisty, M., et al. 2008, A&A, 489, 1157

Krijt, S., Bosman, A. D., Zhang, K., et al. 2020, ApJ, 899, 134

Krijt, S., Kama, M., McClure, M., et al. 2023, in Astronomical Society of the Pacific Conference Series, Vol. 534, Astronomical Society of the Pacific Conference Series, ed. S. Inutsuka, Y. Aikawa, T. Muto, K. Tomida, & M. Tamura, 1031

Krijt, S., Schwarz, K. R., Bergin, E. A., & Ciesla, F. J. 2018, ApJ, 864, 78

Kunimoto, M. & Matthews, J. M. 2020, AJ, 159, 248

Kurtovic, N. T., Pérez, L. M., Benisty, M., et al. 2018, ApJ, 869, L44

Kwon, W., Looney, L. W., Mundy, L. G., & Welch, W. J. 2015, ApJ, 808, 102

Lada, C. J. & Lada, E. A. 1991, in Astronomical Society of the Pacific Conference Series, Vol. 13, The Formation and Evolution of Star Clusters, ed. K. Janes, 3–22

Lange, K., Dominik, C., & Tielens, A. G. G. M. 2023a, arXiv e-prints, arXiv:2311.12794

Lange, K., Dominik, C., & Tielens, A. G. G. M. 2023b, A&A, 674, A200

Langer, W. D. 2009, in Astronomical Society of the Pacific Conference Series, Vol. 417, Submillimeter Astrophysics and Technology: a Symposium Honoring Thomas G. Phillips, ed. D. C. Lis, J. E. Vaillancourt, P. F. Goldsmith, T. A. Bell, N. Z. Scoville, & J. Zmuidzinas, 71

Langer, W. D., Velusamy, T., Kuiper, T. B. H., et al. 1997, ApJ, 480, L63

Lauck, T., Karssemeijer, L., Shulenberger, K., et al. 2015, ApJ, 801, 118

Law, C. J., Teague, R., Loomis, R. A., et al. 2021, ApJS, 257, 4

Lazareff, B., Berger, J. P., Kluska, J., et al. 2017, A&A, 599, A85

Le Gal, R., Brady, M. T., Öberg, K. I., Roueff, E., & Le Petit, F. 2019, ApJ, 886, 86

Lebouteiller, V., Barry, D. J., Spoon, H. W. W., et al. 2011, ApJS, 196, 8

Lebreuilly, U., Commerçon, B., & Laibe, G. 2020, A&A, 641, A112

Leemker, M., Booth, A. S., van Dishoeck, E. F., et al. 2022a, arXiv e-prints, arXiv:2204.03666

Leemker, M., Booth, A. S., van Dishoeck, E. F., et al. 2022b, A&A, 663, A23

Lesur, G., Ercolano, B., Flock, M., et al. 2022, arXiv e-prints, arXiv:2203.09821

Lesur, G. R. J. & Latter, H. 2016, MNRAS, 462, 4549

Ligterink, N. F. W., Walsh, C., Bhuin, R. G., et al. 2018, A&A, 612, A88

Lin, D. N. C. & Papaloizou, J. 1985, in Protostars and Planets II, ed. D. C. Black & M. S. Matthews, 981–1072

Lissauer, J. J. & Stevenson, D. J. 2007, in Protostars and Planets V, ed. B. Reipurth, D. Jewitt, & K. Keil, 591

Liu, B. & Ji, J. 2020, Research in Astronomy and Astrophysics, 20, 164

Lodders, K. 2010, Astrophysics and Space Science Proceedings, 16, 379

Long, F., Herczeg, G. J., Harsono, D., et al. 2019, ApJ, 882, 49

Long, F., Herczeg, G. J., Pascucci, I., et al. 2017, ApJ, 844, 99

Long, F., Pinilla, P., Herczeg, G. J., et al. 2020, ApJ, 898, 36

Long, F., Pinilla, P., Herczeg, G. J., et al. 2018, ApJ, 869, 17

Loomis, R. A., Öberg, K. I., Andrews, S. M., et al. 2020, ApJ, 893, 101

Loomis, R. A., Öberg, K. I., Andrews, S. M., et al. 2018, AJ, 155, 182

Luhman, K. L. 2007, ApJS, 173, 104

Luhman, K. L., Allen, L. E., Allen, P. R., et al. 2008, ApJ, 675, 1375

Lynden-Bell, D. & Pringle, J. E. 1974, MNRAS, 168, 603

Maaskant, K. M., Min, M., Waters, L. B. F. M., & Tielens, A. G. G. M. 2014, A&A, 563, A78

Madhusudhan, N. 2019, ARA&A, 57, 617

Madlener, D., Wolf, S., Dutrey, A., & Guilloteau, S. 2012, A&A, 543, A81

Malfait, K., Waelkens, C., Waters, L. B. F. M., et al. 1998, A&A, 332, L25

Malygin, M. G., Kuiper, R., Klahr, H., Dullemond, C. P., & Henning, T. 2014, A&A, 568, A91

Manara, C. F., Ansdell, M., Rosotti, G. P., et al. 2023, in Astronomical Society of the Pacific Conference Series, Vol. 534, Protostars and Planets VII, ed. S. Inutsuka, Y. Aikawa, T. Muto, K. Tomida, & M. Tamura, 539

Manara, C. F., Fedele, D., Herczeg, G. J., & Teixeira, P. S. 2016, A&A, 585, A136

Manara, C. F., Testi, L., Herczeg, G. J., et al. 2017, A&A, 604, A127

Manigand, S., Jørgensen, J. K., Calcutt, H., et al. 2020, A&A, 635, A48

Manoj, P., Kim, K. H., Furlan, E., et al. 2011, ApJS, 193, 11

Marton, G., Calzoletti, L., Perez Garcia, A. M., et al. 2017, arXiv e-prints, arXiv:1705.05693

Martonchik, J. V., Orton, G. S., & Appleby, J. F. 1984, Applied Optics, 23, 541

Mayor, M. & Queloz, D. 1995, Nature, 378, 355

McClure, M. 2009, ApJ, 693, L81

McClure, M. K. 2019, A&A, 632, A32

McClure, M. K., Bergin, E. A., Cleeves, L. I., et al. 2016, ApJ, 831, 167

McClure, M. K., Calvet, N., Espaillat, C., et al. 2013, ApJ, 769, 73

McClure, M. K., Dominik, C., & Kama, M. 2020, A&A, 642, L15

McClure, M. K., Espaillat, C., Calvet, N., et al. 2015, ApJ, 799, 162

McClure, M. K., Furlan, E., Manoj, P., et al. 2010, ApJS, 188, 75

McClure, M. K., Manoj, P., Calvet, N., et al. 2012, ApJ, 759, L10

McClure, M. K., Rocha, W. R. M., Pontoppidan, K. M., et al. 2023, Nature Astronomy, 7, 431

McGuire, B. A. 2022, ApJS, 259, 30

McJunkin, M., France, K., Schneider, P. C., et al. 2014, ApJ, 780, 150

McMullin, J. P., Waters, B., Schiebel, D., Young, W., & Golap, K. 2007, in Astronomical Society of the Pacific Conference Series, Vol. 376, Astronomical Data Analysis Software and Systems XVI, ed. R. A. Shaw, F. Hill, & D. J. Bell, 127

Mennella, V. 2010, ApJ, 718, 867

Mesa, D., Ginski, C., Gratton, R., et al. 2022, A&A, 658, A63

Meyer, D. M., Jura, M., & Cardelli, J. A. 1998, ApJ, 493, 222

Mie, G. 1908, Annalen der Physik, 330, 377

Millar, T. J., Walsh, C., Van de Sande, M., & Markwick, A. J. 2024, A&A, 682, A109

Min, M., Bouwman, J., Dominik, C., et al. 2016, A&A, 593, A11

Min, M., Hovenier, J. W., & de Koter, A. 2005, A&A, 432, 909

Min, M., Waters, L. B. F. M., de Koter, A., et al. 2007, A&A, 462, 667

Minissale, M., Aikawa, Y., Bergin, E., et al. 2022, ACS Earth and Space Chemistry, 6, 597

Miotello, A., Bruderer, S., & van Dishoeck, E. F. 2014, A&A, 572, A96

Miotello, A., Facchini, S., van Dishoeck, E. F., & Bruderer, S. 2018, A&A, 619, A113

Miotello, A., Facchini, S., van Dishoeck, E. F., et al. 2019, A&A, 631, A69

Miotello, A., Kamp, I., Birnstiel, T., Cleeves, L. C., & Kataoka, A. 2023, in Astronomical Society of the Pacific Conference Series, Vol. 534, Protostars and Planets VII, ed. S. Inutsuka, Y. Aikawa, T. Muto, K. Tomida, & M. Tamura, 501

Miotello, A., van Dishoeck, E. F., Kama, M., & Bruderer, S. 2016, A&A, 594, A85

Miotello, A., van Dishoeck, E. F., Williams, J. P., et al. 2017, A&A, 599, A113

Monnier, J. D. & Millan-Gabet, R. 2002, ApJ, 579, 694

Morbidelli, A., Szulágyi, J., Crida, A., et al. 2014, ICARUS, 232, 266

Mordasini, C., Alibert, Y., Benz, W., Klahr, H., & Henning, T. 2012, A&A, 541, A97

Mousis, O. & Schmitt, B. 2008, ApJ, 677, L67

Müller, H. S. P., Schlöder, F., Stutzki, J., & Winnewisser, G. 2005, Journal of Molecular Structure, 742, 215

Muzerolle, J., D'Alessio, P., Calvet, N., & Hartmann, L. 2004, ApJ, 617, 406

Noble, J. A., Congiu, E., Dulieu, F., & Fraser, H. J. 2012, MNRAS, 421, 768

Noble, J. A., Fraser, H. J., Aikawa, Y., Pontoppidan, K. M., & Sakon, I. 2013, ApJ, 775, 85

Öberg, K. I. & Bergin, E. A. 2016, ApJ, 831, L19

Öberg, K. I. & Bergin, E. A. 2021, Phys. Rep., 893, 1

Öberg, K. I., Boogert, A. C. A., Pontoppidan, K. M., et al. 2011a, ApJ, 740, 109

Öberg, K. I., Facchini, S., & Anderson, D. E. 2023, ARA&A, 61, 287

Öberg, K. I., Murray-Clay, R., & Bergin, E. A. 2011b, ApJ, 743, L16

Öberg, K. I., Qi, C., Fogel, J. K. J., et al. 2010, ApJ, 720, 480

Öberg, K. I., Qi, C., Fogel, J. K. J., et al. 2011c, ApJ, 734, 98

Oberg, N., Cazaux, S., Kamp, I., et al. 2023, A&A, 672, A142

Oh, D., Hashimoto, J., Tamura, M., et al. 2016, PASJ, 68, L3

Olofsson, J., Augereau, J. C., van Dishoeck, E. F., et al. 2009, A&A, 507, 327

Ormel, C. W. 2017, in Astrophysics and Space Science Library, Vol. 445, Formation, Evolution, and Dynamics of Young Solar Systems, ed. M. Pessah & O. Gressel, 197

Owen, J. E., Ercolano, B., & Clarke, C. J. 2011, MNRAS, 411, 1104

Padgett, D. L., Brandner, W., Stapelfeldt, K. R., et al. 1999, AJ, 117, 1490

Palumbo, M. E., Baratta, G. A., Collings, M. P., & McCoustra, M. R. S. 2006, Physical Chemistry Chemical Physics (Incorporating Faraday Transactions), 8, 279

Palumbo, M. E., Geballe, T. R., & Tielens, A. G. G. M. 1997, ApJ, 479, 839

Palumbo, M. E., Strazzulla, G., Pendleton, Y. J., & Tielens, A. G. G. M. 2000, ApJ, 534, 801

Palumbo, M. E., Tielens, A. G. G. M., & Tokunaga, A. T. 1995, ApJ, 449, 674

Pan, L. & Yu, C. 2020, ApJ, 898, 7

Panoglou, D., Cabrit, S., Pineau Des Forêts, G., et al. 2012, A&A, 538, A2

Parvathi, V. S., Sofia, U. J., Murthy, J., & Babu, B. R. S. 2012, ApJ, 760, 36

Pascucci, I., Cabrit, S., Edwards, S., et al. 2023, in Astronomical Society of the Pacific Conference Series, Vol. 534, Protostars and Planets VII, ed. S. Inutsuka, Y. Aikawa, T. Muto, K. Tomida, & M. Tamura, 567

Peeters, E., Hony, S., Van Kerckhoven, C., et al. 2002, A&A, 390, 1089

Pegues, J., Öberg, K. I., Bergner, J. B., et al. 2020, ApJ, 890, 142

Pendleton, Y. J., Tielens, A. G. G. M., Tokunaga, A. T., & Bernstein, M. P. 1999, ApJ, 513, 294

Perrin, M. D., Soummer, R., Elliott, E. M., Lallo, M. D., & Sivaramakrishnan, A. 2012, in Society of Photo-Optical Instrumentation Engineers (SPIE) Conference Series, Vol. 8442, Space Telescopes and Instrumentation 2012: Optical, Infrared, and Millimeter Wave, ed. M. C. Clampin, G. G. Fazio, H. A. MacEwen, & J. Oschmann, Jacobus M., 84423D

Pickles, A. J. 1998, PASP, 110, 863

Piétu, V., Dutrey, A., Guilloteau, S., Chapillon, E., & Pety, J. 2006, A&A, 460, L43

Piétu, V., Guilloteau, S., Di Folco, E., Dutrey, A., & Boehler, Y. 2014, A&A, 564, A95

Pineda, J. E., Arzoumanian, D., Andre, P., et al. 2023, in Astronomical Society of the Pacific Conference Series, Vol. 534, Protostars and Planets VII, ed. S. Inutsuka, Y. Aikawa, T. Muto, K. Tomida, & M. Tamura, 233

Pinilla, P., Benisty, M., & Birnstiel, T. 2012, A&A, 545, A81

Pinte, C., Dent, W. R. F., Ménard, F., et al. 2016, ApJ, 816, 25

Pinte, C., Ménard, F., Duchêne, G., et al. 2018, A&A, 609, A47

Pirovano, L. M., Fedele, D., van Dishoeck, E. F., et al. 2022, A&A, 665, A45

Podio, L., Garufi, A., Codella, C., et al. 2020, A&A, 642, L7

Pontoppidan, K. M., Dullemond, C. P., van Dishoeck, E. F., et al. 2005, ApJ, 622, 463

Pontoppidan, K. M., Fraser, H. J., Dartois, E., et al. 2003, A&A, 408, 981

Pontoppidan, K. M., Salyk, C., Bergin, E. A., et al. 2014, in Protostars and Planets VI, ed. H. Beuther, R. S. Klessen, C. P. Dullemond, & T. Henning, 363

Pontoppidan, K. M., Stapelfeldt, K. R., Blake, G. A., van Dishoeck, E. F., & Dullemond, C. P. 2007, ApJ, 658, L111

Powell, D., Gao, P., Murray-Clay, R., & Zhang, X. 2022, Nature Astronomy, 6, 1147

Prasad, S. S. & Tarafdar, S. P. 1983, ApJ, 267, 603

Qasim, D., Fedoseev, G., Lamberts, T., et al. 2019, ACS Earth and Space Chemistry, 3, 986

Qi, C., Öberg, K. I., Espaillat, C. C., et al. 2019, ApJ, 882, 160

Qi, C., Öberg, K. I., Wilner, D. J., et al. 2013, Science, 341, 630

Ricca, A., Roser, J. E., Peeters, E., & Boersma, C. 2019, ApJ, 882, 56

Rieke, G. H., Wright, G. S., Böker, T., et al. 2015a, PASP, 127, 584

Rieke, G. H., Wright, G. S., Böker, T., et al. 2015b, PASP, 127, 584

Robberto, M., Spina, L., Da Rio, N., et al. 2012, AJ, 144, 83

Robitaille, T. P. 2011, A&A, 536, A79

Robitaille, T. P., Whitney, B. A., Indebetouw, R., Wood, K., & Denzmore, P. 2006, ApJS, 167, 256

Rocha, W. R. M., Rachid, M. G., Olsthoorn, B., et al. 2022, A&A, 668, A63

Rocha, W. R. M., van Dishoeck, E. F., Ressler, M. E., et al. 2024, A&A, 683, A124

Rodgers-Lee, D., Scholz, A., Natta, A., & Ray, T. 2014, MNRAS, 443, 1587

Rosotti, G. P., Teague, R., Dullemond, C., Booth, R. A., & Clarke, C. J. 2020, MNRAS, 495, 173

Rubin, M., Altwegg, K., Balsiger, H., et al. 2019, MNRAS, 489, 594

Sallum, S., Follette, K. B., Eisner, J. A., et al. 2015, Nature, 527, 342

Salyk, C., Blake, G. A., Boogert, A. C. A., & Brown, J. M. 2009, ApJ, 699, 330

Sauter, J., Wolf, S., Launhardt, R., et al. 2009, A&A, 505, 1167

Schegerer, A. A. & Wolf, S. 2010, A&A, 517, A87

Schöier, F. L., van der Tak, F. F. S., van Dishoeck, E. F., & Black, J. H. 2005, A&A, 432, 369

Schwarz, K. R., Bergin, E. A., Cleeves, L. I., et al. 2016, ApJ, 823, 91

Schwarz, K. R., Bergin, E. A., Cleeves, L. I., et al. 2018, ApJ, 856, 85

Semenov, D., Pavlyuchenkov, Y., Henning, T., Wolf, S., & Launhardt, R. 2008, ApJ, 673, L195

Semenov, D., Wiebe, D., & Henning, T. 2006, ApJ, 647, L57

Shakura, N. I. & Sunyaev, R. A. 1973, A&A, 24, 337

Shimonishi, T., Dartois, E., Onaka, T., & Boulanger, F. 2016, A&A, 585, A107

Shu, F., Najita, J., Ostriker, E., et al. 1994, ApJ, 429, 781

Shu, F. H., Adams, F. C., & Lizano, S. 1987, ARA&A, 25, 23

Siess, L., Dufour, E., & Forestini, M. 2000a, A&A, 358, 593

Siess, L., Dufour, E., & Forestini, M. 2000b, A&A, 358, 593

Simon, A., Öberg, K. I., Rajappan, M., & Maksiutenko, P. 2019, ApJ, 883, 21

Sloan, G. C., Keller, L. D., Forrest, W. J., et al. 2005, ApJ, 632, 956

Smith, R. G., Sellgren, K., & Tokunaga, A. T. 1989, ApJ, 344, 413

Sossi, P. A., Stotz, I. L., Jacobson, S. A., Morbidelli, A., & O'Neill, H. S. C. 2022, Nature Astronomy, 6, 951

Squire, J. & Hopkins, P. F. 2018, MNRAS, 477, 5011

Stapelfeldt, K. R., Duchêne, G., Perrin, M., et al. 2014, in Exploring the Formation and Evolution of Planetary Systems, ed. M. Booth, B. C. Matthews, & J. R. Graham, Vol. 299, 99–103

Sturm, J. A., Booth, A. S., McClure, M. K., Leemker, M., & van Dishoeck, E. F. 2023a, A&A, 670, A12

Sturm, J. A., Booth, A. S., McClure, M. K., Leemker, M., & van Dishoeck, E. F. 2023b, A&A, 670, A12

Sturm, J. A., McClure, M. K., Beck, T. L., et al. 2023c, A&A, 679, A138

Sturm, J. A., McClure, M. K., Bergner, J. B., et al. 2023d, A&A, 677, A18

Sturm, J. A., McClure, M. K., Harsono, D., et al. 2022, A&A, 660, A126

Sturm, J. A., McClure, M. K., Law, C. J., et al. 2023e, A&A, 677, A17

Swings, P. & Rosenfeld, L. 1937, ApJ, 86, 483

Szulágyi, J., Binkert, F., & Surville, C. 2022, ApJ, 924, 1

Szulágyi, J., Masset, F., Lega, E., et al. 2016, MNRAS, 460, 2853

Tabone, B., Bettoni, G., van Dishoeck, E. F., et al. 2023, Nature Astronomy, 7, 805

Tabone, B., Cabrit, S., Pineau des Forêts, G., et al. 2020, A&A, 640, A82

Tabone, B., Rosotti, G. P., Lodato, G., et al. 2022, MNRAS, 512, L74

Tafalla, M. & Santiago, J. 2004, A&A, 414, L53

Takeuchi, T. & Lin, D. N. C. 2002, ApJ, 581, 1344

Tazaki, R., Murakawa, K., Muto, T., Honda, M., & Inoue, A. K. 2021, ApJ, 921, 173

Tazzari, M., Testi, L., Ercolano, B., et al. 2016, A&A, 588, A53

Teague, R. 2019, The Journal of Open Source Software, 4, 1220

Teague, R. & Foreman-Mackey, D. 2018, Research Notes of the American Astronomical Society, 2, 173

Teague, R., Jankovic, M. R., Haworth, T. J., Qi, C., & Ilee, J. D. 2020, MNRAS, 495, 451

Terada, H. & Tokunaga, A. T. 2012, ApJ, 753, 19

Terada, H. & Tokunaga, A. T. 2017, ApJ, 834, 115

Terada, H., Tokunaga, A. T., Kobayashi, N., et al. 2007, ApJ, 667, 303

Terada, H., Tokunaga, A. T., Pyo, T.-S., et al. 2012, AJ, 144, 175

Terebey, S., Shu, F. H., & Cassen, P. 1984, ApJ, 286, 529

Terwisscha van Scheltinga, J., Ligterink, N. F. W., Boogert, A. C. A., van Dishoeck, E. F., & Linnartz, H. 2018, A&A, 611, A35

Thalmann, C., Janson, M., Garufi, A., et al. 2016, ApJ, 828, L17

Thi, W. F., Pontoppidan, K. M., van Dishoeck, E. F., Dartois, E., & d'Hendecourt, L. 2002, A&A, 394, L27

Tielens, A. G. G. M. 2008, ARA&A, 46, 289

Tielens, A. G. G. M. & Hagen, W. 1982, A&A, 114, 245

Tobin, J. J., Looney, L. W., Li, Z.-Y., et al. 2016, ApJ, 818, 73

Trapman, L., Bosman, A. D., Rosotti, G., Hogerheijde, M. R., & van Dishoeck, E. F. 2021, A&A, 649, A95

Trapman, L., Facchini, S., Hogerheijde, M. R., van Dishoeck, E. F., & Bruderer, S. 2019, A&A, 629, A79

Trapman, L., Miotello, A., Kama, M., van Dishoeck, E. F., & Bruderer, S. 2017, A&A, 605, A69

Trapman, L., Zhang, K., van't Hoff, M. L. R., Hogerheijde, M. R., & Bergin, E. A. 2022, ApJ, 926, L2

Tychoniec, Ł., Manara, C. F., Rosotti, G. P., et al. 2020, A&A, 640, A19

Ubach, C., Maddison, S. T., Wright, C. M., et al. 2012, MNRAS, 425, 3137 van Broekhuizen, F. A., Keane, J. V., & Schutte, W. A. 2004a, A&A, 415, 425

van Broekhuizen, F. A., Keane, J. V., & Schutte, W. A. 2004b, A&A, 415, 425

van Broekhuizen, F. A., Pontoppidan, K. M., Fraser, H. J., & van Dishoeck, E. F. 2005, A&A, 441, 249

van der Marel, N. 2022, arXiv e-prints, arXiv:2210.05539

van der Marel, N., Bosman, A. D., Krijt, S., Mulders, G. D., & Bergner, J. B. 2021, A&A, 653, L9

van der Marel, N. & Mulders, G. D. 2021, AJ, 162, 28

van der Marel, N., van Dishoeck, E. F., Bruderer, S., Pérez, L., & Isella, A. 2015, A&A, 579, A106

van der Marel, N., Williams, J. P., & Bruderer, S. 2018, ApJ, 867, L14

van der Marel, N., Williams, J. P., Picogna, G., et al. 2022, arXiv e-prints, arXiv:2204.08225

van der Tak, F. F. S., Lique, F., Faure, A., Black, J. H., & van Dishoeck, E. F. 2020, Atoms, 8, 15

van der Walt, S., Colbert, S. C., & Varoquaux, G. 2011, Computing in Science & Engineering, 13, 22

van Dishoeck, E. F. 2014, Faraday Discussions, 168, 9

van Dishoeck, E. F., Blake, G. A., Jansen, D. J., & Groesbeck, T. D. 1995, ApJ, 447, 760

van Dishoeck, E. F., Kristensen, L. E., Mottram, J. C., et al. 2021a, A&A, 648, A24

van Dishoeck, E. F., Kristensen, L. E., Mottram, J. C., et al. 2021b, A&A, 648, A24

van 't Hoff, M. L. R., Walsh, C., Kama, M., Facchini, S., & van Dishoeck, E. F. 2017, A&A, 599, A101

van Zadelhoff, G. J., van Dishoeck, E. F., Thi, W. F., & Blake, G. A. 2001, A&A, 377, 566

van't Hoff, M. L. R., Harsono, D., Tobin, J. J., et al. 2020, ApJ, 901, 166

Villenave, M., Benisty, M., Dent, W. R. F., et al. 2019, A&A, 624, A7

Villenave, M., Ménard, F., Dent, W. R. F., et al. 2020, A&A, 642, A164

Villenave, M., Stapelfeldt, K. R., Duchêne, G., et al. 2022, ApJ, 930, 11

Visser, R., Bruderer, S., Cazzoletti, P., et al. 2018, A&A, 615, A75

Visser, R., Doty, S. D., & van Dishoeck, E. F. 2011, A&A, 534, A132

Visser, R., Geers, V. C., Dullemond, C. P., et al. 2007, A&A, 466, 229

Visser, R., van Dishoeck, E. F., Doty, S. D., & Dullemond, C. P. 2009, A&A, 495, 881

Wakelam, V., Herbst, E., Loison, J. C., et al. 2012, ApJS, 199, 21

Walsh, C., Nomura, H., & van Dishoeck, E. 2015, A&A, 582, A88

Warren, S. G. 1984, Appl. Opt., 23, 1206

Warren, S. G. 1986, Applied Optics, 25, 2650

Warren, S. G. & Brandt, R. E. 2008, Journal of Geophysical Research (Atmo-

spheres), 113, D14220
Weidenschilling, S. J. 1977, MNRAS, 180, 57
Weinberg, W. H. 1996, Accounts of Chemical Research, 29, 479
Weingartner, J. C. & Draine, B. T. 2001, ApJ, 548, 296
Williams, J. P. & Best, W. M. J. 2014, ApJ, 788, 59
Williams, J. P. & Cieza, L. A. 2011, ARA&A, 49, 67
Wilson, R. W., Jefferts, K. B., & Penzias, A. A. 1970, ApJ, 161, L43
Wilson, T. L. 1999, Reports on Progress in Physics, 62, 143
Windmark, F., Birnstiel, T., Güttler, C., et al. 2012, A&A, 540, A73
Winston, E., Cox, N. L. J., Prusti, T., et al. 2012, A&A, 545, A145
Woitke, P., Arabhavi, A. M., Kamp, I., & Thi, W. F. 2022, A&A, 668, A164
Woitke, P., Min, M., Pinte, C., et al. 2016, A&A, 586, A103
Wolf, S., Padgett, D. L., & Stapelfeldt, K. R. 2003, ApJ, 588, 373
Wolff, S. G., Duchêne, G., Stapelfeldt, K. R., et al. 2021, AJ, 161, 238
Wolff, S. G., Perrin, M. D., Stapelfeldt, K., et al. 2017, ApJ, 851, 56
Woodall, J., Agúndez, M., Markwick-Kemper, A. J., & Millar, T. J. 2007, A&A, 466, 1197
Xu, Y., Reid, M., Dame, T., et al. 2016, Science Advances, 2, e1600878
Yang, H., Herczeg, G. J., Linsky, J. L., et al. 2012, ApJ, 744, 121
Yang, Y.-L., Green, J. D., Pontoppidan, K. M., et al. 2022, ApJ, 941, L13
Yarnall, Y. Y. & Hudson, R. L. 2022, ApJ, 931, L4
Yoshida, T. C., Nomura, H., Furuya, K., Tsukagoshi, T., & Lee, S. 2022, ApJ, 932, 126
Youdin, A. N. & Goodman, J. 2005, ApJ, 620, 459
Zhang, K., Bergin, E. A., Schwarz, K., Krijt, S., & Ciesla, F. 2019, ApJ, 883, 98
Zhang, K., Blake, G. A., & Bergin, E. A. 2015, ApJ, 806, L7
Zhang, K., Booth, A. S., Law, C. J., et al. 2021a, ApJS, 257, 5
Zhang, K., Bosman, A. D., & Bergin, E. A. 2020a, ApJ, 891, L16
Zhang, K., Schwarz, K. R., & Bergin, E. A. 2020b, ApJ, 891, L17
Zhang, Y., Snellen, I. A. G., Bohn, A. J., et al. 2021b, Nature, 595, 370
Zsidi, G., Manara, C. F., Kóspál, Á., et al. 2022, A&A, 660, A108
Zucker, C., Battersby, C., & Goodman, A. 2015, ApJ, 815, 23

Nederlandse samenvatting

“Papa, mag ik op de ladder klimmen om de zon vanachter de wolken te halen?” vroeg mijn tweejarige zoontje onlangs naïef. De enorme afstanden en tijdschalen in het heelal zijn moeilijk te bevatten voor een kind en nauwelijks minder voor volwassenen. Eeuwenlang werd daarom gedacht dat het heelal statisch en onveranderlijk was. Dankzij verbeterende waarneemtechnieken krijgen we een steeds beter begrip van afstanden en de snelheid van veranderingen in het heelal. Hierdoor weten we nu dat sterren en planeten geen eeuwige lichtpuntjes zijn, maar een product van turbulente processen, die na verloop van lange tijd ook weer kunnen verdwijnen.

Planeten kunnen allerhande chemische samenstellingen en fysische omstandigheden hebben. In ons eigen zonnestelsel hebben we bijvoorbeeld de met water bedekte Aarde met haar zuurstofrijke atmosfeer, de moordend hete Venus met haar verstikkende atmosfeer vol koolstofdioxide en zwavelzuur, de kale rots Mercurius, de stoffige, ijle Mars, de enorme gasreuzen Jupiter en Saturnus en de ijsreuzen Uranus en Neptunus. Sinds het begin van dit millennium worden ook planeten rond andere sterren veelvuldig geobserveerd, met een ongekende variatie aan grootte, temperatuur en samenstelling. De oorsprong van deze variaties ligt

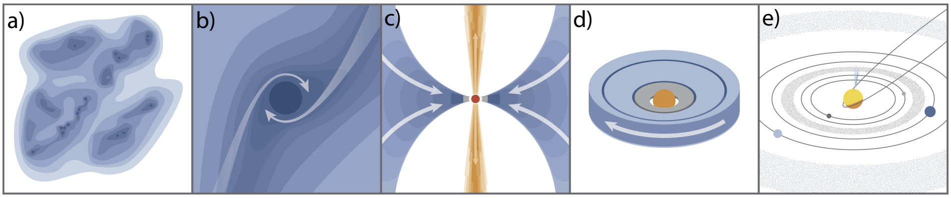

Figuur 1: Schema van de verschillende stadia van ster- en planeetvorming.
a: Sterren ontstaan in de dichte kernen van gas- en stofwolken in het heelal.
b: Stervorming begint wanneer de dichtheid zo hoog wordt dat de druk en turbulentie niet meer opwegen tegen de groeiende zwaartekracht van het systeem.
c: Door het ineenstorten van de wolk warmt het centrum op en ontstaat een protoster. Het resterende invallende materiaal vormt een schijf door het behoud van draaimoment. Deze schijf, die enkele miljoenen jaren kan bestaan, vormt de kraamkamer van steenachtige planeten zoals de Aarde. Deze fase wordt ook gekenmerkt door de uitstroom van materiaal via een wind of straalstroom loodrecht op het vlak van de schijf.
d: Nadat de gaswolk uiteen is gevallen, blijft alleen de ster over met een schijf eromheen. Planeten in de schijf blijven groeien door stof aan te trekken vanuit de schijf. Als ze groot genoeg worden, trekken ze ook gas aan. Het gas in de schijf verdwijnt na ongeveer 2 tot 10 miljoen jaar, waarna gasaccretie op de planeet niet meer mogelijk is.
e: Planeten kunnen nog rotsachtig en ijzig material gebruiken om te groeien gedurende ongeveer 100 miljoen jaar, waarna een volledig gevormd planetair systeem zoals ons zonnestelsel is gevormd. Deze figuur is overgenomen van K. Peek.

in het vormingsproces van planeten. Dit proces wordt actief bestudeerd binnen de wetenschap, om een beter begrip te krijgen welke omstandigheden en mechanismen bijdragen aan de verschillende uitkomsten. Dit proefschrift richt zich op een specifiek aspect daarvan: de verdeling van chemische elementen in de geboorteplaats van planeten, de protoplanetaire schijf.

Ster- en planeetvorming

Het ster- en planeetvormingsproces is schematisch weergegeven in Figuur 1. De ruimte tussen de sterren is niet leeg, maar is gevuld met een ijl gas wat voornamelijk uit waterstof en helium bestaat, maar ook sporen van zwaardere elementen zoals koolstof, zuurstof en stikstof bevat. In dit gas bevinden zich kleine stofdeeltjes die ongeveer 1% van de totale massa bevatten. Dit gas is altijd in beweging door de invloed van druk, turbulentie, sterwinden en dergelijke. Als genoeg materie zich ophoopt, stort de wolk ineen onder zijn eigen zwaartekracht, waarna een ster gevormd wordt in het centrum. Het resterende materiaal stroomt via een afgeplatte schijf richting de ster. In deze schijf kunnen planeten ontstaan door de samenklontering van stofdeeltjes. Daarom wordt deze schijf ook wel protoplanetaire schijf genoemd.

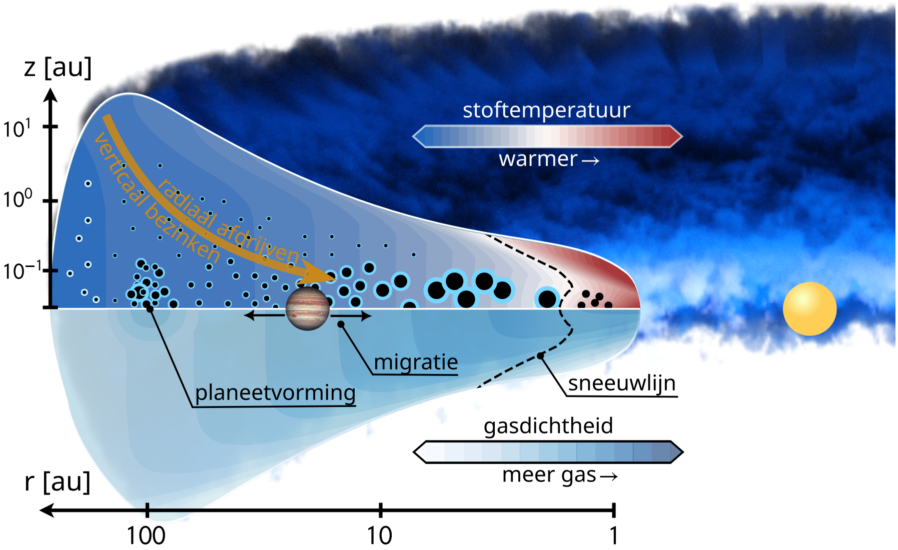

Figuur 2: Schematische weergave van de structuur van een protoplanetaire schijf. Door de energie van de vormende ster in het centrum is de schijf warmer aan het oppervlak en dicht bij de ster, wat resulteert in koude gebieden dieper in de schijf waar moleculen zoals water en koolstof(di)oxide bevriezen op de stofdeeltjes. Planeten ontstaan door het samenklonteren van zulk ijshoudend stof, waarna ze nog kunnen migreren door de schijf door interacties met het gas. Deze figuur is aangepast overgenomen van Miotello et al. (2023).

Het eindresultaat van het planeetvormingsproces wordt bepaald door de structuur en chemische samenstelling van de protoplanetaire schijf. Zoals weergegeven in Figuur 2, neemt de dichtheid in de schijf toe in de richting van de ster en wordt het steeds warmer door de constante straling van de ster. Dit resulteert in gebieden in de schijf waar veelvoorkomende moleculen zoals water en koolstof(di)oxide bevriezen op het oppervlak van de aanwezige stofdeeltjes[1]. Omdat water (H_2O) wel zuurstof (O) bevat, maar geen koolstof (C), en koolstofdioxide (CO_2) twee keer zoveel zuurstof bevat als koolstof, verandert de elementaire samenstelling in het gas in gebieden waar deze moleculen bevriezen. De locatie waar een planeet zich vormt ten opzichte van de verschillende sneeuwlijnen, bepaalt dus voor een groot deel wat de chemische samenstelling van een dergelijke planeet wordt.

IJs vervult meerdere belangrijke rollen in een protoplanetaire schijf. Het vermeerdert de vaste-stof-massa en laat stofdeeltjes gemakkelijker aan elkaar plakken, waardoor het planeetvormingsproces efficiënter kan plaatsvinden. Daarnaast kunnen moleculen op die manier gemakkelijk getransporteerd worden door de protoplanetaire schijf, waardoor blijvende verschuivingen in de chemische samenstelling kunnen optreden. Helaas is er over het ijs in protoplanetaire schijven momenteel nog erg weinig bekend, omdat de waarnemingen en interpretatie ervan lastig zijn.

Waarneemtechnieken

Protoplanetaire schijven kunnen bestudeerd worden met behulp van meerdere waarneemtechnieken. De hoofdbestanddelen van het gas, waterstof en helium, stralen geen licht uit in het grootste deel van de schijf, maar andere atomen en moleculen hebben rijke spectra aan emissielijnen die gebruikt kunnen worden om de temperatuur, dichtheid en chemische samenstelling van het gas te bepalen. Het stof in protoplanetaire schijven reflecteert sterlicht en kan daardoor waargenomen worden met conventionele telescopen. Daarnaast straalt het stof zelf ook warmtestraling uit, wat geobserveerd kan worden met behulp van radioantennes. Aan de hand hiervan kunnen de fysieke structuur en de eigenschappen van het aanwezige stof bepaald worden.

IJs kan worden waargenomen met behulp van absorptiespectroscopie waarbij specifieke golflengtes van het licht worden absorbeerd, afhankelijk van het type molecuul. Hierdoor laat het een unieke vingerafdruk achter in het waargenomen licht. In het optische spectrum is ijs moeilijk te analyseren vanwege de beperkte lichtdoorlaatbaarheid, maar in het infrarood vertoont het duidelijke absorptiebanden voor de meeste moleculen. IJs in protoplanetaire schijven kan alleen worden waargenomen als het directe sterlicht, dat niet door het ijs wordt geabsorbeerd, zoveel mogelijk wordt geblokkeerd door de schijf. Dit is mogelijk bij schijven die zo zijn georiënteerd dat we ze van de zijkant zien, waardoor alleen het licht zichtbaar is dat door de ijsrijke schijf wordt weerkaatst. Dergelijke objecten zijn echter zeldzaam en lichtzwak, wat ze moeilijk detecteerbaar maakt.

Onze atmosfeer is grotendeels ondoorzichtig voor infraroodgolflengtes, waardoor ruimteobservatoria noodzakelijk zijn voor gedegen ijsstudies. Satellietobservatoria hebben echter aanzienlijke ruimtelijke beperkingen en zijn technisch complex om te ontwikkelen. Na de Infrared Space Observatory (ISO; 1995 – 1998) en de Spitzer Space Telescope (2003 – 2020) duurde het tot 2022 voordat de James Webb Space Telescope (JWST) werd gelanceerd. De JWST is een telescoop van een nieuw kaliber, die nauwkeurige spectrale waarnemingen met hoge gevoeligheid in het infrarood mogelijk maakt, en is daardoor ideaal voor het waarnemen van ijs.

---

[1] Omdat de overgang van gas naar ijs zo abrupt is, worden deze transities ook wel sneeuwlijnen genoemd, in analogie aan de verticale transities van eeuwige sneeuw op de bergen op Aarde.

Modelleren en simuleren

Het interpreteren van waarnemingen is niet gemakkelijk, omdat deze vaak slechts een tweedimensionale projectie bieden en een enkele tijdsopname van een bepaald aspect. Fysische en chemische modellen spelen een cruciale rol bij het begrijpen van de condities en processen die aan waarnemingen ten grondslag liggen. Deze modellen bootsen relevante processen na, met ondersteuning van laboratoriummetingen. Door de resultaten te vergelijken met waarnemingen, kunnen verbanden en mechanismen beter worden bestudeerd.

In dit proefschrift maak ik gebruik van fysisch-chemische modellen om op basis van de straling van de ster en de structuur van de schijf te simuleren in welke verhouding een bepaald molecuul aanwezig is en hoeveel licht het uitstraalt. Daarnaast worden stralingstransportmodellen gebruikt om het weerkaatsen, breken en absorberen van licht in een protoplanetaire schijf te simuleren. Met behulp van deze modellen probeer ik de verdeling van chemische elementen in de protoplanetaire schijf over verschillende gebieden en moleculaire fases te begrijpen.

Dit proefschrift

Deze dissertatie onderzoekt indirecte (Hoofdstuk 2 – 3) en directe methoden (Hoofdstuk 5 – 7) om de samenstelling en locatie van ijs in protoplanetaire schijven te onderzoeken aan de hand van waarnemingen. Indirecte methoden maken gebruik van gaswaarnemingen om de invloed van bewegende stof- en ijsdeeltjes op de elementaire samenstelling van het gas te onderzoeken, terwijl directe methoden JWST-waarnemingen van ijs in schijven vanuit een zijaanzicht omvatten. De dubbele betekenis van de titel “Het breken van het ijs” verwijst naar het nieuwe inzicht dat deze studie biedt in ijs in protoplanetaire schijven. Het verkennende werk van het Ice Age-programma met JWST (Hoofdstuk 4 – 7) heeft veel nieuwe mechanismen onthuld die essentieel zijn voor verdere studies van schijven in zijaanzicht met JWST.

Overzicht per hoofdstuk

In de volgende paragrafen wordt per hoofdstuk een korte samenvatting gegeven van de belanrijkste resultaten.

Hoofdstuk 2: Dit hoofdstuk onderzoekt de afname van koolstof in de gasfase als een mogelijke indicator voor het cumulatief uitvriezen van koolstofmonoxide in protoplanetaire schijven van verschillende leeftijden. Met behulp van de Atacama Compact Array worden atomaire koolstoftransities bestudeerd op submillimeter golflengtes. Fysisch-chemische modellen worden gebruikt om de hoeveelheid koolstof ten opzichte van de hoeveelheid waterstof (C/H-verhouding) te bepalen in het buitenste deel van de schijf rond drie verschillende sterren. Alle waardes uit de literatuur vergelijkend, identificeren we een evolutionaire trend die suggereert dat gasvormig koolstof een geschikte indicator kan zijn voor de opbouw van ijs in de middenlaag van de schijf. Daarnaast vinden we bewijs dat dit ijsvormige koolstof doorgaans effectief door de schijf richting de ster wordt getransporteerd en daar weer in de gasfase verschijnt.

Hoofdstuk 3: Het gebruik van atomair koolstof om de C/H-verhouding te bepalen is gelimiteerd, omdat de lijnsterkte in dergelijke waarnemingen ook beïnvloed wordt door de totale massa van het systeem. In dit hoofdstuk wordt een nieuwe methode geïntroduceerd om de C/H-verhouding te bepalen, onafhankelijk van de totale massa van het systeem. Hierbij wordt gebruik gemaakt van de anti-correlatie tussen koolstofmonoxide en het distikstofkation (N_2H^+). Door middel van Atacama Large (sub-)Millimeter Array (ALMA) en NOrthern Extended Millimeter Array (NOEMA) waarnemingen van de protoplanetaire schijf LkCa 15 wordt aangetoond dat de schijf slechts weinig minder koolstof en zuurstof in de gasfase heeft dan verwacht, wat wijst op de invloed van zowel de fysieke structuur als de leeftijd van de schijf op de koolstofverhouding.

Hoofdstuk 4: Dit hoofdstuk introduceert een nieuwe modelopstelling om stralingstransport in een protoplanetaire schijf te analyseren. Dit model is specifiek aangepast om zoveel mogelijk te lijken op HH 48 NE, een protoplanetaire schijf in het sterrenbeeld Kameleon, gezien vanuit een zijaanzicht. HH 48 NE is onderdeel van een studie van de eerste resultaten van de JWST genaamd 'Ice Age' (ijstijd), waarbij vergelijkbare modellen nodig zijn om de resultaten te interpreteren. Het model, afgestemd op gegevens van Hubble Space Telescope, ALMA en fotometrie, biedt inzicht in de schijfstructuur, stofgrootteverdeling en karakteristieken van de ster in het centrum. De studie toont onder meer aan dat kleine korrels (<0.1 µm) grotendeels uit de schijfatmosfeer verdwenen zijn en dat het merendeel van het stof is bezonken naar het middenvlak van de schijf. Dit model geldt als een opzet voor het model met ijsabsorptie gepresenteerd in Hoofdstuk 5.

Hoofdstuk 5: In dit hoofdstuk worden de modellen uit Hoofdstuk 4 uitgebreid met ijs om het verband tussen de schijfstructuur en de sterkte van de verschillende absorptiebanden te onderzoeken. De resultaten geven aan dat ijscompositie en verhouding ten opzichte van gasvormig waterstof kunnen worden bepaald, mits bepaalde aannames over de schijfstructuur geldig zijn. Dit hoofdstuk biedt een belangrijk kader waarbinnen ijswaarnemingen in zijdelings georiënteerde schijven kunnen worden geanalyseerd.

Hoofdstuk 6: Dit hoofdstuk presenteert het eerste nabij-infrarode JWST-ijsspectrum in een protoplanetaire schijf, waarbij belangrijke ijscomponenten zoals water, koolstofdioxide en koolstofmonoxide worden geïdentificeerd, samen met het minder voorkomende ammoniak (NH_3), cyanaat (OCN^-), koolstofoxysulfide (OCS) en een zwaardere koolstofdioxide isotoop ($^{13}CO_2$). De ruimtelijk opgeloste waarnemingen van ijs in schijven blijken complex vanwege lichtbreking en -verstrooiing. Stralingstransportmodellen zijn daarom vereist voor een nauwkeurige bepaling van de ijssamenstelling en verdeling in de schijf. Bovendien vinden we aanwijzingen dat koolstofmonoxide op onverwacht grote hoogten bij hoge temperaturen in de schijf aanwezig is, wat suggereert dat het mogelijk gevangen zit in de structuren van water- of koolstofdioxide-ijs, die pas bij hogere temperaturen sublimeren. Deze conclusies kunnen belangrijke implicaties hebben voor ons begrip van de locatie van sneeuwlijnen in protoplanetaire schijven en de samenstelling van planeetatmosferen.

Hoofdstuk 7: Dit hoofdstuk presenteert het mid-infrarode JWST MIRI-ijsspectrum van dezelfde protoplanetaire schijf als in Hoofdstuk 4 – 6, waarbij de detectie van koolstofdioxide-ijs, ammoniakijs en mogelijk andere ijssoorten wordt beschreven. Daarnaast observeren we sterke signalen van aromatische koolwaterstoffen die ontbreken in vergelijkbare schijven met een lagere inclinatie. We laten zien dat de modellen, die gebaseerd zijn op pre-JWST meetgegevens, goed overeenkomen met de waarnemingen en tonen aan dat de ijssamenstelling in de protoplanetaire schijf goed overeenkomt met de ijssamenstelling van kometen in ons zonnestelsel. De vergelijking met de modellen bevestigt niet alleen dat koolstofmonoxide-ijs zich op onverwacht grote hoogten in de schijf bevindt, maar ook dat water en koolstofdioxide zich op grotere hoogten bevinden dan verwacht op basis van de sublimerende ultraviolette straling van de ster. Dit suggereert dat iets, zoals een wind vanaf het schijfoppervlak, de energierijke straling van de ster tegenhoudt, of dat het ijs in de bovenste regionen constant wordt aangevuld vanuit het koude middenvlak van de schijf door turbulente bewegingen.

Toekomstperspectief

Deze dissertatie markeert een belangrijke stap in ons begrip van de verdeling van chemische elementen in protoplanetaire schijven. Vergelijkbare studies met een groter aantal objecten zullen essentieel zijn om statistisch significante verbanden te identificeren. Toekomstige indirecte methoden zoals programma's op ALMA of NOEMA, zullen inzichten bieden in de evolutie en oorsprong van de gasvormige C/H-verhouding. Directe methoden, zoals aanvullende waarnemingen van schijven in zijdelings georiënteerde systemen, zullen cruciaal zijn om de ijsdistributie nauwkeuriger te bepalen. Het combineren van gedetailleerde ALMA- en JWST-waarnemingen van schijven in zijaanzicht zal helpen bij het oplossen van ambiguïteiten in modellen en het nauwkeuriger vaststellen van de locatie van ijs ten opzichte van het moleculaire gas binnen de schijf. Ver-infrarood ruimtetelescopen die gericht zijn op ijs-emissiekenmerken op 40 – 100 µm zouden ook aanzienlijk bijdragen aan het uitbreiden van onze kennis van de bestudeerde schijfregio's. De toekomst voor ijswaarnemingen in protoplanetaire schijven ziet er veelbelovend uit, en ik hoop dat deze dissertatie bijdraagt aan het begrip van de verdeling van chemische elementen en de resulterende planetaire samenstelling door voortdurend 'het ijs te breken'.

Publications

First authored

1. **Sturm, J. A.**, McClure, M. K., Harsono, D., Bergner, J. B., Dartois, E., Boogert, A. C. A., Cordiner, M. A., Drozdovskaya, M. N., Ioppolo, S., Law, C. J., Lis, D. C., McGuire, B. A., Melnick, G. J., Noble, J. A., Öberg, K. I., Palumbo, M. E., Pendleton, Y. J., Perotti, G., Rocha, W. R. M., Urso, R. G., and van Dishoeck, E. F.,

   A JWST/MIRI analysis of the ice distribution and PAH emission in the protoplanetary disk HH 48 NE,

   Accepted for publication in A&A (Chapter 7)

2. **Sturm, J. A.**, McClure, M. K., Beck, T. L., Harsono, D., Bergner, J. B., Dartois, E., Boogert, A. C. A., Chiar, J. E., Cordiner, M. A., Drozdovskaya, M. N., Ioppolo, S., Law, C. J., Linnartz, H., Lis, D. C., McGuire, B. A., Melnick, G. J., Noble, J. A., Öberg, K. I., Palumbo, M. E., Pendleton, Y. J., Perotti, G., Pontoppidan, K. M., Qasim, D., Rocha, W. R. M., Terada, H., Urso, R. G., and van Dishoeck, E. F.,

   A JWST inventory of protoplanetary disk ices. The edge-on protoplanetary disk HH 48 NE, seen with the Ice Age ERS program,

   A&A, 679, A138, 2023d (Chapter 6)

3. **Sturm, J. A.**, McClure, M. K., Bergner, J. B., Harsono, D., Dartois, E., Drozdovskaya, M. N., Ioppolo, S., Öberg, K. I., Law, C. J., Palumbo, M. E., Pendleton, Y. J., Rocha, W. R. M., Terada, H., and Urso, R. G.,

   The edge-on protoplanetary disk HH 48 NE. II. Modeling ices and silicates,

   A&A, 677, A18, 2023c (Chapter 5)

4. **Sturm, J. A.**, McClure, M. K., Law, C. J., Harsono, D., Bergner, J. B., Dartois, E., Drozdovskaya, M. N., Ioppolo, S., Öberg, K. I., Palumbo, M. E., Pendleton, Y. J., Rocha, W. R. M., Terada, H., and Urso, R. G.,

   The edge-on protoplanetary disk HH 48 NE. I. Modeling the geometry and stellar parameters,

   A&A, 677, A17, 2023b (Chapter 4)

5. **Sturm, J. A.**, Booth, A. S., McClure, M. K., Leemker, M., and van Dishoeck, E. F.,

   Disentangling the protoplanetary disk gas mass and carbon depletion through combined atomic and molecular tracers,

   A&A, 670, A12, 2023a (Chapter 3)

6. **Sturm, J. A.**, McClure, M. K., Harsono, D., Facchini, S., Long, F., Kama, M., Bergin, E. A., and van Dishoeck, E. F.,

   Tracing pebble drift and trapping using radial carbon depletion profiles in protoplanetary disks,

   A&A, 660, A126, 2022 (Chapter 2)

7. **Sturm, J. A.**, Rosotti, G. P., and Dominik, C.,

   Dust dynamics in planet-driven spirals,

   A&A, 643, A92, 2020 (not included in this thesis)

Co-authored

1. Arulanantham, N. L., McClure, M. K., Pontoppidan, K. M., Beck, T. L., **Sturm, J. A.**, Harsono, D., Boogert, A. C. A., Cordiner, M., Dartois, E., Drozdovskaya, M. N., Espaillat, C., Melnick, G. J., Noble, J. A., Palumbo, M. E., Pendleton, Y. J., Terada, H., and van Dishoeck, E. F.

   JWST MIRI MRS images of disk winds, water, and CO in an edge-on protoplanetary disk

   ApJ, 965, L13, 2024

2. Dartois, E., Noble, J. A., Caselli, P., Fraser, H. J., Jiménez-Serra, I., Maté, B., McClure, M. K., Melnick, G. J., Pendleton, Y. J., Shimonishi, T., Smith, Z. L., **Sturm, J. A.**, Taillard, A., Wakelam, V., Boogert, A. C. A., Drozdovskaya, M. N., Erkal, J., Harsono, D., Herrero, V. J., Ioppolo, S., Linnartz, H., McGuire, B. A., Perotti, G., Qasim, D., and Rocha, W. R. M.

   Spectroscopic sizing of interstellar icy grains with JWST

   Nature Astronomy, 2024, 8 359

3. McClure, M. K., Rocha, W. R. M., Pontoppidan, K. M., Crouzet, N., Chu, L. E. U., Dartois, E., Lamberts, T., Noble, J. A., Pendleton, Y. J., Perotti, G., Qasim, D., Rachid, M. G., Smith, Z. L., Sun, F., Beck, T. L., Boogert, A. C. A., Brown, W. A., Caselli, P., Charnley, S. B., Cuppen, H. M., Dickinson, H., Drozdovskaya, M. N., Egami, E., Erkal, J., Fraser, H., Garrod, R. T., Harsono, D., Ioppolo, S., Jiménez-Serra, I., Jin, M., Jörgensen, J. K., Kristensen, L. E., Lis, D. C., McCoustra, M. R. S., McGuire, B. A., Melnick, G. J., Öberg, K. I., Palumbo, M. E., Shimonishi, T., **Sturm, J. A.**, van Dishoeck, E. F., and Linnartz, H.

   An Ice Age JWST inventory of dense molecular cloud ices

   Nature Astronomy, 2023, 7, 431

4. Espaillat, C. C., Thanathibodee, T., Pittman, C. V., **Sturm, J. A.**, McClure, M. K., Calvet, N., Walter, F. M., Franco-Hernández, R., and Muzerolle Page, J.

   JWST detects neon line variability in a protoplanetary disk

   ApJ, 958, L4, 2023

5. Leemker, M., Booth, A. S., van Dishoeck, E. F., Pérez-Sánchez, A. F., Szulágyi, J., Bosman, A. D., Bruderer, S., Facchini, S., Hogerheijde, M. R., Paneque-Carreño, T., and **Sturm, J. A.**

   Gas temperature structure across transition disk cavities

   A&A, 663, A23, 2022

6. Bosman, A. D., Trapman, L., **Sturm, J. A.**, Bergin, E. A., Booth, A. S., Calahan, J. K., van Dishoeck, E. F., McClure, M. K., Miotello, A., and Zhang, K.

   Hydrostatic equilibrium does not solve the $C^{18}O$ *flux problem in protoplanetary disks*

   RNAAS, 6, 2022

7. Arias, M., Botteon, A., Bassa, C. G., van der Jagt, S., van Weeren, R. J., O'Sullivan, S. P., Bosschaart, Q., Dullaart, R. S., Hardcastle, M. J., Hessels, J. W. T., Shimwell, T., Slob, M. M., **Sturm, J. A.**, Tasse, C., Theijssen, N. C. M. A., and Vink, J.

   Possible discovery of Calvera's supernova remnant

   A&A, 667, A71, 2022

8. Kennedy, G. M., Ginski, C., Kenworthy, M. A., Benisty, M., Henning, T., van Holstein, R. G., Kral, Q., Ménard, F., Milli, J., Quiroga-Nuñez, L. H., Rab, C., Stolker, T., and **Sturm, J. A.**

   A low-mass stellar companion to the young variable star RZ Psc

   MNRAS, 496, L75, 2020

Curriculum Vitae

I was born on the 26th of January 1997 in Aagtekerke, a picturesque village in Zeeland, the Netherlands. After following primary school in Aagtekerke, I went to Calvijn College in Middelburg and Goes. During high school, I developed a deep curiosity about the underlying mechanisms of the world, from the intricacies of cars and rockets to the vast wonders of nature and physics. This curiosity culminated in my graduation project ("profielwerkstuk"), where my peers and I built our own telescope, observed Jupiter's Galilean moons, and with these data calculated Jupiter's mass. This project cemented my decision to study the fundamentals of nature through a physics degree at Leiden University, where I started in 2015. Since an additional bachelor astronomy required only a few additional courses, I decided to combine the two programs. Astronomy sounded intriguing and fun, but it also had my doubts: who could have a serious job as an astronomer, right? Despite initial doubts about the practicality of a career in astronomy, I found the field more suited to my interests than physics. Even though the scales are hard to comprehend, astronomy leaves room for visualization and imagination, something that the abstract nature of physics hardly allows. Therefore, I continued with an astronomy master in 2018 at the university of Leiden. During the second year I combined this with an 'Assessor' board position at the student association Depositum Custodi in Utrecht.

After that my career path was not clear. I wanted to continue the intriguing path I had followed so far, but didn't want to move abroad. I decided to try to get a position as PhD student in Ewine van Dishoeck's group, a group I was already familiar with from my two master projects. Unfortunately, that position was filled by another candidate, fortunately, Melissa McClure joined Leiden that year and offered a position that was not earlier advertised, and I got the position. I hesitated at first. Working with James Webb Space Telescope's data sounded amazing, but earlier launch delays had made me dubious whether the project would actually work out as planned. I started with the project in September 2020. Over the past four years, my work with the James Webb Space Telescope has exceeded my expectations, allowing me to engage in international collaborations and contribute to groundbreaking research. This experience has been immensely fulfilling, both professionally and personally. I will advance in my career as a scientist at Whiffle, specializing in groundbreaking high-precision weather forecasting. I carry forward the knowledge and skills I've acquired, eager to continue satisfying my curiosity in new and diverse environments.

Acknowledgements

This work would not have been possible without the support from many people. First and foremost, I would like to thank Melissa for offering me this position and for the support throughout the journey. I cannot thank you enough. Despite being your first PhD student, you did an exceptional job! Thank you for always being open and honest, for caring about my personal life and future career steps, for the engaging discussions about nearly everything in life, and for trusting me in our collaboration and communication within Ice Age. I would also like to thank Ewine for the useful science discussions and support along the way, and for letting me join the group meetings and retreats. Your guidance and knowledge has helped a lot in shaping the outline of this thesis and the discussions of the results.

I want to express my gratitude to all my scientific collaborators here in Leiden. Alice, thank you for giving me the opportunity to analyze the LkCa 15 data and for your assistance throughout the project. Giovanni, thank you for mentoring me during my master's research project. That project was a major reason I wanted to continue in astronomy research. Harold, thank you for the insightful scientific discussions and your invaluable feedback on interpreting the ice results. I was deeply saddened to hear about your unexpected passing. You have left a tremendous void, and you will be greatly missed. Lucas, it was great 'growing up' together as PhD students. Thank you for all your help with coding, figures, graduation bureaucracy, and more. Margot, thank you for being my DALI help desk and for the many mornings we started together with coffee. Martijn and Logan, thank you for your help with the MIRI calibration and analysis of the gas lines. Will, thank you for the useful discussions during my introduction to ices and opacities and for sharing your experiences in job hunting.

I also want to thank all my other scientific collaborators. I am grateful to the Ice Age collaboration for their tremendous support in analyzing, interpreting, and writing up the observations of the edge-on disk. A special thanks to Daniel, Emmanuel, and Jenny B. for the many discussions, comparisons, and benchmarking of the radiative transfer models. Thank you, Zak, for the time we spent together and for taking over the care of the ice models. Good luck to you and Lukas with future model developments. I look forward to seeing the results!

Thanks to my office mates, Andres, Andrew, Lucas, Margot, Martijn, Łukasz, and Nicolás, for making my time in the office enjoyable. Thank you for the engaging discussions, jokes, sweets, coffees, your passive pressure to start writing, and your opinions on results or figures whenever I asked.

I also thank the rest of the Leiden-Garching group – Alex, Arthur, Benoît, Giulio, Julia, Katie, Leon, Lisa, Logan, Marina, Marissa, Milou, Nashanty, Nicolás, Pooneh, Pranjal, Sierra, Teresa, and Yuan – for the scientific discussions, shared lunches, and fun times during conferences and group retreats. A PhD position can sometimes be lonely, but your support helped me through. I appreciate the

Pangolin group for the nice presentations and discussions, especially Nienke for organizing it. Thank you, Malin, Lars, and Stijn, for letting me supervise your bachelor/master research projects. It was a lot of fun working together and seeing each of you grow in the project.

I would also like to thank everyone at the observatory, even though I can't mention you all by name. Thanks for the conversations, the nice atmosphere, and the great activities. I also thank all my friends outside the university for their support. A special thanks to the members of Societas Quaerentium Sapientiam Veram – Andries, Femmie, Gerrieke, Harm-Jan, Hildert, Marius, and Roland – for our regular discussions about science, society, and religion. These discussions have greatly influenced my thinking beyond astronomy. I look forward to many more humanity-saving discussions in the future!

Beste familie, pa en ma Sturm, pa en ma Wagenaar, broers, zussen, schoonzussen, zwagers, opa, oma's, hartelijk dank voor jullie onvoorwaardelijke steun gedurende mijn studie en promotie. Dank voor jullie interesse en de discussies! Dankjewel, Marijn, voor het fantastische ontwerp van de omslag! Lieve Elsemarie, dankjewel voor je steun en liefde tijdens mijn promotie. Dank voor het proeflezen van introducties, presentaties en het proefschrift, en voor je begrip als ik later thuis was of voor langere tijd weg was naar bijvoorbeeld conferenties. Lieve William en Hosea, ik ben heel trots op jullie! Jullie zwangerschap, geboorte en eerste levensmaanden hebben veel tijd en energie van me gevraagd, maar jullie gezelligheid, vrolijkheid en ontwikkeling hebben dit dubbel en dwars goedgemaakt!